Complexity

Solving Complex Hydrological Processes using Advanced Artificial Intelligence Models

Lead Guest Editor: Zaher Mundher Yaseen
Guest Editors: Shamsuddin Shahid and Ozgur Kisi

Solving Complex Hydrological Processes using Advanced Artificial Intelligence Models

Complexity

Solving Complex Hydrological Processes using Advanced Artificial Intelligence Models

Lead Guest Editor: Zaher Mundher Yaseen
Guest Editors: Shamsuddin Shahid and Ozgur Kisi

Contents

Hindawi
Complexity
Volume 2021, Article ID 8850243, 20 pages
https://doi.org/10.1155/2021/8850243

Research Article

Application of Artificial Intelligence Models for Evapotranspiration Prediction along the Southern Coast of Turkey

Mohammed Majeed Hameed,[1] Mohamed Khalid AlOmar,[1] Siti Fatin Mohd Razali,[2] Mohammed Abd Kareem Khalaf,[3] Wajdi Jaber Baniya,[4] Ahmad Sharafati,[5] and Mohammed Abdulhakim AlSaadi[6]

[1]*Department of Civil Engineering, Al-Maaref University College, Ramadi, Iraq*
[2]*Department of Civil Engineering, Faculty of Engineering and Built Environment, Universiti Kebangsaan Malaysia, Bangi, Selangor, Malaysia*
[3]*Iraqi Federal Board of Supreme Audit, Baghdad, Iraq*
[4]*Department of Civil Engineering, Cairo University, Cairo, Egypt*
[5]*Department of Civil Engineering, Science and Research Branch, Islamic Azad University, Tehran, Iran*
[6]*National Chair of Materials Science and Metallurgy, University of Nizwa, Nizwa, Oman*

Correspondence should be addressed to Mohamed Khalid AlOmar; mohd.alomar@yahoo.com

Received 18 August 2020; Revised 1 October 2020; Accepted 6 August 2021; Published 24 August 2021

Academic Editor: Honglei Xu

Reference evapotranspiration (ET_o) is one of the most significant factors in the hydrological cycle since it has a great influence on water resource planning and management, agriculture and irrigation management, and other processes in the hydrological sector. In this study, an efficient and local predictive model was established to forecast the monthly mean $ET_o t$ over Turkey based on the data collected from 35 locations. For this purpose, twenty input combinations including hydrological and geographical parameters were introduced to three different approaches called multiple linear regression (MLR), random forest (RF), and extreme learning machine (ELM). Moreover, in this study, large investigation was done, involving the establishment of 60 models and their assessment using ten statistical measures. The outcome of this study revealed that the ELM approach achieved high accurate estimation in accordance with the Penman–Monteith formula as compared to other models such as MLR and RF. Moreover, among the 10 statistical measures, the uncertainty at 95% (U_{95}) indicator showed an excellent ability to select the best and most efficient forecast model. The superiority of ELM in the prediction of mean monthly ET_o over MLR and RF approaches is illustrated in the reduction of the U_{95} parameter to 49.02% and 34.07% for RF and MLR models, respectively. Furthermore, it is possible to develop a local predictive model with the help of computer to estimate the ET_o using the simplest and cheapest meteorological and geographical variables with acceptable accuracy.

1. Introduction

1.1. Background. Global warming has become a great concern of researchers and world leaders. It is well known that the Earth surface temperature is increasing significantly during the last decades [1, 2]. Water storage, hydrological cycles, and, consequently, water availability are directly affected by global warming [3–5]. Thus, one of the most essential indicators of climate change is the referenced evapotranspiration (ET_o), which is considered as the most complicated element in the hydrological cycle [6–8].

ET_o mainly occurs due to two complicated processes. The first is when water evaporates from the surface of the soil, lakes, rivers, etc., and this process is called physical evaporation. The second process is the transpiration phenomenon in crops and plants, which is called biological transpiration [9, 10]. Undeniably, the evaporation process requires energy to convert water from the liquid phase to the

vapor phase. Therefore, the main parameters that affect the ET_o process is the sun radiation, wind speed and direction, air temperature, and humidity [9–11]. In conclusion, the ET_oalso represents the link between surface energy and carbon cycle [12, 13]. Based on the stated literature, a precise measurement and prediction of $ET_o$is essential for quantifying surface energy and water reserves worldwide [14–16]. Thus, providing accurate models for weather and climate change diagnosis is crucial [14, 17–21].

1.2. Literature Review. Due to the significant effect of ET_oon climate change, Earth temperature, crops and plants, water management, and runoff quantity, many researchers have studied the ET_oprediction over the last decades [9, 22–24]. The Penman–Monteith (P – M) is the most widely used model, and it is considered as a physical ET_omodel as it is an approximate linearized solution governing energy balance, thermodynamic state, vertical heat, and water-vapor diffusion [9, 23]. However, P – M requires many meteorological data to be applied, which can be considered as a drawback for this equation [25, 26]. In any case, there are many models applied to estimate the ET_oaround the world. Examples of such are the constant heat method by including heat pulse [27, 28] and the Shuttleworth–Wallace S-W method to estimate the transpiration from plants [29–31]. It is worth mentioning that the number of empirical equations for modeling the evaporation has exceeded 100 due to the importance of ET_omeasurements and the variety of meteorological data around the world. Therefore, it is impossible to decisively compare these models [32–34].

Recently, the development of artificial intelligence has received significant attention from communities in the hydrological and environmental sciences, including water treatment [35, 36], hydrology [37–41], water reservoir optimization [42–44], remote sensing applications [45, 46], etc. Consequently, due to the highly nonlinear characteristics associated with the ET_odata, AI technology presented a suitable modeling approach to solve many issues with the empirical equations that has been used before [47]. Kumar et al. utilized the artificial neural network (ANN) in 2002 for predicting ET_o, where different ANN architectures were implemented for evaporation simulation. The radial neural network yielded the best results for evaporation simulation, and it calculates the number of layers and neurons based on a trial and error process. [48]. Many researchers have followed his footprint in predicting ET_o[49–52]. In addition, an adaptive network-based fuzzy inference system (ANFIS) has been used to predict ET_o [53, 54]. The ANFIS and ANN techniques and empirical equations were used in the evapotranspiration field, and it was found that the ANFIS and ANN methods were much better than the empirical equations. [55, 56]. However, it is well established that ANN models easily get stuck in a local minimum, and, therefore, recent studies have employed new models adopting other AI techniques for ET_omodeling [47]. Many approaches have been utilized for this purpose, including support vector machine SVM [53, 57, 58]. The SVM is well known to have a basic form, but one of the drawbacks of SVM is the unknown parameter [59]. Another approach in the field of simulation ET_o data is genetic programming (GP). This approach consists of measurement programming capable of obtaining input data and producing a nonlinear interaction between data to determine the outputs [55, 60–62].

In order to enhance the ability of AI models, many algorithms were associated with different AI methodologies, including the use of wavelet transform regression model [63], wavelet coupled with ANN [64, 65], and wavelet enhanced extreme learning machine [66]. Others utilize random forest (RF) algorithm to enhance the AI techniques. Due to its success over a variety of datasets, high precision estimation, a small range of user-defined parameters, the ability to estimate relative value of the variables, and its ability to preclude overfitting, the RF approach has become extremely popular in recent years [26, 34, 67, 68]. Recently, due to its higher efficiency and much quicker calculation speed, a newly proposed machine learning technology called the extreme learning machine (ELM) has confirmed it to be a promising ET_o estimation tool [69]. First, Abdullah et al. (2015) used ELM to forecast ET_o at three Iraqi stations and concluded that the ELM model is highly efficient and computerized at high generalization speeds [70, 71]. Ever since, the ELM for ET_o predictions has been used by many studies in different climate environments [72–74]. To the best of the authors' knowledge, all models presented in the literature were established to simulate the evapotranspiration using a single model for each location or case study. Furthermore, some researchers employed modern techniques and used different case studies, but they could not produce a general model that could take into account more than one case study. In this study, an effort is being made to include a robust modeling methodology using a variety of locations along the southern coast of Turkey to create a comprehensive general model to forecast ET_o. The other objective of the study is to predict mean monthly $ET_o$from limited data, which can be easily available.

1.3. Motivation of the Study. Due to the significance of ET_o, there are numerous studies that have been conducted to estimate it, such as AI techniques and empirical models. In general, these approaches achieved a satisfactory success. However, creating one robust model for conducting local ET_othroughout a specific country based on data collected from different sites is still considered as a challenging issue that needs to be addressed. Moreover, recognizing the statistical measures that are effectively used to assess the feasibility of a certain model are also very significant in the selection of the best predictive model. Thus, in this study, a broad investigation is performed using three different approaches, multiple linear regression (MLR), random forest (RF), and extreme learning machine (ELM), based on twenty combinations of meteorological and geographical indicators constituting 60 predictive models. Moreover, there were 10 efficient statistical measures employed to assess the accuracy of the performance for each model separately in accordance

with the Penman–Monteith equation. Although the formula of Penman–Monteith is well-known in the prediction of ET_o, it does pose some issues regarding the measurement of some factors, which may not be relevant to every site such as solar radiation and sensible heat flux into the soil. Therefore, a robust local model is established in this study, which can efficiently predict the local mean monthly ET_o over the southern coast of Turkey using conveniently and inexpensively measurable parameters. Furthermore, the evaluation of the outcomes of the models will be further assessed and validated against the actual ET_ovalues, which are calculated by the Penman–Monteith equation.

2. Case Study and Data Collection

In this study, the data collected from 35 meteorological stations in Turkey are used. The geographical location of these stations covers large area located between a latitude from 36° to 38°. Figure 1 shows the location of each meteorological station separately. It can be seen that the majority of these stations are located in the south of Turkey on the coasts of the Mediterranean Sea. The data collected from the general directorate of Turkish state meteorological includes several long-term monthly meteorological data such as temperature, humidity, wind speed, and reference evapotranspiration. Furthermore, the dataset comprises of the long-term mean monthly variables covering the period from 1975 to 2010. The highest temperature is recorded at the Mut station at 46.7°C, while the lowest temperature is recorded at Goksun station at −33.5°C. Figure 2 showed the long-term monthly mean (ET_o), overall in Turkey. It can be observed that the highest value of (ET_o) occurred in July followed by June, August, and May, consecutively.

It is worth mentioning that Turkey primarily has a complex climate due to its location and topography. The Mediterranean climate in southern Turkey is predominant with warm and dry summers and wet and moderate to cold winters. Continental weather is predominant in central Turkey with warm and dry summers and cold winters. The oceanic atmosphere in northern Turkey is seen through warm and rainy summers and cold and wet winters. This study ensures that the stations chosen to measure ET_o are spread nearly uniformly across southern Turkey in order to determine spatial differences in mean monthly ET_o values and their time characteristics.

Due to the lack of ET_o data, the FAO embraced the PM equation as a standard methodology for calculating the reference ET_o. The FAO56-PM can be used on hourly or daily scales to supply the data needed for machine learning approaches. The equation is suggested for hourly time measures as expressed in the following equation [7, 75]:

$$ET_o = \frac{0.408\Delta\left(R_N - G\right) + \gamma\left(900/\left(T + 273\right)\right)U_2\left(e_a - e_d\right)}{\Delta + \gamma\left(1 + 0.34U_2\right)}, \tag{1}$$

where ET_o is the reference evapotranspiration in (mm/day), Δ represents the slope of the saturation vapor pressure function at air temperature T in $(\mathrm{kPa}^\circ \cdot \mathrm{C}^{-1})$, R_N is the net solar radiation in $(\mathrm{MJ} \cdot \mathrm{m}^{-2} \cdot \mathrm{day}^{-1})$, G is the soil heat flux density in $(\mathrm{MJ} \cdot \mathrm{m}^{-2} \cdot \mathrm{day}^{-1})$, γ is the psychometric constant in $(\mathrm{kPa}^\circ \cdot \mathrm{C}^{-1})$, T is the mean air temperature in (°C), U_2 is the average 24-hour wind speed at 2m height above the ground surface in $(\mathrm{m.s}^{-1})$, e_a is the saturation vapor pressure in (kPa), and e_d is the actual vapor pressure in (kPa). Finally, it is important to mention that the dataset is subjected to the normalization process (between 0 and 1), for all input variables and their appropriate targets. This process is very important in order to boost the predictive model performance. Later, the data are simulated using three modeling approaches, namely, RF, ELM, and MLR.

3. Methodology

3.1. Random Forest. Random Forests (RF) is an algorithm that manages regression issues of high dimensions. This method is tree-based, where all trees have random variables in the selection, and the forest is established from several trees of regression and is clustered together [34, 76]. The tree is chosen as a random subset of variables that will be used to determine the result of the prediction. Whereas, in the random forest learning process, two significant parameters are identified: the first one is the number of trees (n_{tree}) and the second one is the number of variables in each division (m_{try}). After fitting single tree into the ensemble (bagging procedure), the final decision is made by averaging the output. The bias between the bagged trees is equal to that of the single tree, while the variance is reduced as the correlation between the trees is reduced [77].

For regression-based RF formation, in order to get the tree predictor $h(X, \ominus)$ numerical value, the process starts by growing trees on the bias of a random vector $(\ominus)$. For any given numerical estimator, the mean squared generalization error can be expressed as follows [78]:

$$E_{(X,Y)} = \left(Y - h(X)^2\right). \tag{2}$$

The RF predictor is generated by taking an average over j of a single tree. Here, in this respect, the following theorems line up:

Theorem 1. *By expanding the number of trees in the forest, the error will then be expressed as follows:*

$$E_{(X,Y)}\left(\mathrm{Yav}_j h\left(X, \ominus_j\right)\right)^2 \ominus E_{X.Y}\left(Y - E_\ominus h(X, \ominus)\right)^2. \tag{3}$$

This equation's right hand demonstrates the generalization error of the forest. Similarly, the average tree generalization error can be found from the following equation:

$$\mathrm{PE} * (\mathrm{tree}) = E_\ominus E_{X,Y}\left(Y - h(X, \ominus)\right)^2. \tag{4}$$

Theorem 2. *If we assume $E_Y = E_X h(X, \ominus)$ for every $\ominus$, then*

$$\mathrm{PE} * (\mathrm{forest}) \leq \overline{p}.\mathrm{PE}(\mathrm{tree}), \tag{5}$$

where $\overline{p}$ represent the weight correlation [76].

3.2. Extreme Learning Machine (ELM). The ELM, an advanced learning algorithm, is a machine learning modeling approach assembled with single-layer feedforward neural network (SLFN) [79]. ELM's primary strength is that the weight of the input parameters is determined arbitrarily, while the output parameter weights are measured analytically using the Moore–Penrose approach (Huang et al., 2006). The SLFN function combines the hidden node additives and activation function, which can be represented mathematically as follows:

$$f(x) = \sum_{i=1}^{L} \beta_i G(a_i, b_i, x), \tag{6}$$

where $f(x)$ represents the ELM model output function; x represents the input variable, ai and bi represent the learning parameters hidden nodes, and L stands for the number of hidden nodes. The βi governs the connecting weight to the i-hidden node between the output nodes. The output vector $G(ai, bi, x)$ implies the output of the hidden node. The sigmoid activation solves the additional hidden node as follows:

$$G(a_i, b_i, x) = g(a_i.x + b_i), \tag{7}$$

where a_i and b_i represent weight and basis values for each i-node in its hidden layer. In the algorithm of ELM, the weight of the input layer and bias values are randomly generated. Figure 3 showed the basic structure of the ELM.

For the input and output variables, the arbitrary distinct sample N is denoted as (x_i, y_i). Based on the above findings, equation (6) can be rewritten as follows:

$$H\beta = T, \tag{8}$$

where the Hussain matrix (H) is represented as

$$H = \begin{bmatrix} G(a_1, b_1 + x_1) & \cdots & g_L(a_L, b_L, x_1) \\ \vdots & \ddots & \vdots \\ G(a_N, b_N + x_N) & \cdots & g_L(a_L, b_L, x_L) \end{bmatrix}_{NxL}. \tag{9}$$

In addition,

$$\beta = \begin{bmatrix} \beta_1^T \\ . \\ . \\ . \\ \beta_L^T \end{bmatrix}_{Lxm}, \qquad T = \begin{bmatrix} Y_1^T \\ . \\ . \\ . \\ Y_L^T \end{bmatrix}_{Nxm}. \tag{10}$$

G represents the activation function and in this current study, log-sigmoid transfer function is used, which is expressed as

$$G(y) = \frac{1}{1 + \exp(-y)}, \tag{11}$$

where $y = ax + b$ as indicated in equation (6).

The ELM model with independent L sets, which can result in zero learning errors, can be trained in the form of SLFN [80]. In addition, even with fewer hidden neurons (L) than the number of separate samples (N), the ELM will specify random parameters for the hidden nodes. Ultimately, the output weights can be calculated by means of pseudoinverse of H, which makes a limited error range $\varepsilon > 0$. The hidden node parameters (weights and bias) are given random values during the training phase [81].

3.3. Multiple Linear Regression. In the form of the local climatic parameters of minimum and maximum temperature, relative humidity, wind speed and sun hours, the ET_o data can be formulated using multiple linear regression (MLR) models. Herein, the ET_o is calculated by MLR. The MLR can be employed to describe the relationship between dependent and independent variables as a multivariate statistical tool described by the following equation:

$$Y = \alpha_o + \alpha_1 X_1 + \alpha_2 X_{2+\ldots} \alpha_j X_1, \tag{12}$$

where the response variables are represented by Y, which is also the predicted mean monthly ET_o.The independent variables and the predictors are represented by X_1, X_2, X_n, and the coefficients of regression are represented by $\alpha_o \alpha_1, \alpha_2, \ldots, \alpha_j$, which can be acquired by the following equations [82]:

$$\begin{aligned} e &= \sum_{i=1}^{n} (Y - y_i)^2, \\ \frac{\partial e}{\partial \alpha_o} &= 0, \\ \frac{\partial e}{\partial \alpha_1} &= 0, \\ \frac{\partial e}{\partial \alpha_2} &= 0, \\ \frac{\partial e}{\partial \alpha_j} &= 0, \end{aligned} \tag{13}$$

where the error of the estimated and real values of ET_o is represented by e and y_i, respectively.

3.4. Model Evaluation. The selection process of the best predictive model is of great importance to achieve high accurate predictions. Therefore, in this study, ten statistical parameters have been used to assess the performances of each predictive approach [83, 84]. The quantitative parameters are as follows:

(i) Mean absolute error (MAE). It can be expressed by assuming the absolute errors divided by the

number of total observations. This indicator is widely used in water resources and hydrological sectors to assess the predictive models because it provides significant information on how closely the simulated data points match with the actual ones. The mathematical expression of MAE is shown in the following equations [85, 86]:

$$e = \mathrm{ET}_{o\,i,m} - \mathrm{ET}_{o\,i,p}, \tag{14}$$

where e is the forecasted error,

$$\mathrm{MAE}\,(mm/\mathrm{month}) = \sum_{i=1}^{n} \left|\frac{e_i}{n}\right|. \tag{15}$$

(ii) Root mean square error (RMSE). It is a statistical parameter often used to compare the forecasting errors of several models. The lower RMSE value usually points out to better predictions. The RMSE can be derived using the following equation [87, 88]:

$$\mathrm{RMSE}\,(\mathrm{mm/month}) = \sqrt{\frac{1}{n}\sum_{i=1}^{n} e_i^2}. \tag{16}$$

(iii) Mean absolute relative error (MARE). This indicator can be expressed as an absolute relative computer error (difference between actual and forecasted points). When the MARE parameter is represented as a percentage, it is called the mean absolute relative error (MARE), which is expressed by the following equation:

$$\mathrm{MARE} = \frac{1}{n}\sum_{i=1}^{n} \frac{e_i}{\mathrm{ET}_{o\,i,m}}. \tag{17}$$

(iv) Root mean square relative error (RMSRE) is expressed as

$$\mathrm{RMSRE} = \sqrt{\frac{1}{n}\sum_{i=1}^{n}\left(\frac{e_i}{\mathrm{ET}_{o\,i,m}}\right)^2}. \tag{18}$$

(v) Relative root mean square error (RRMSE) can be calculated by dividing the RMSE criteria over the mean of actual data points. This parameter is very vital in assessing the accuracy of a model. In accordance to [89], the model is considered excellent if RRMSE > 10%, good if 10% < RRMSE < 20%, fair if 20% < RRMSE < 30%, and last, the model can be considered poor if RRMSE > 30%. The mathematical expression of the RRMSE is depicted as follows:

$$\mathrm{RRMSRE}\,(\%) = \sqrt{\frac{\mathrm{RMSE}}{1/n\sum_{i=1}^{n}\mathrm{ET}_{o\,i,m}}}. \tag{19}$$

(vi) Mean bias error (MBE). It discloses the tendency of a model and explains whether it overestimates the data or underestimates them and is expressed by the following equation:

$$\mathrm{MBE}\,(\mathrm{mm/month}) = \frac{1}{n}\sum_{i}^{n} e_i. \tag{20}$$

(vii) Correlation of coefficient (CC). The CC is a significant factor that can be utilized to efficiently discover the robustness of the relationship between predicted and simulated data points. The mathematical expression of CC is shown in the following equation [82, 90]:

$$\mathrm{CC} = \frac{\sum_{i=1}^{n}\left(\mathrm{ET}_{o\,i,m} - \overline{\mathrm{ET}_{o\,i,m}}\right)\left(\mathrm{ET}_{o\,i,p} - \overline{\mathrm{ET}_{o\,i,p}}\right)}{\sum_{i=1}^{n}\left(\mathrm{ET}_{o\,i,m} - \overline{\mathrm{ET}_{o\,i,m}}\right)^2 \sum_{i=1}^{n}\left(\mathrm{ET}_{o\,i,p} - \overline{\mathrm{ET}_{o\,i,p}}\right)^2}. \tag{21}$$

(viii) Maximum absolute relative error (erMAX) is expressed as

$$\mathrm{erMAX}\left(\left|\frac{e_i}{\mathrm{ET}_{o\,i,m}}\right|\right). \tag{22}$$

(ix) t-statistic ($t-$stat). This statistical test is beneficial for validating and testing the broadband models [91]. As $t-$stat indicator approaches zero, the desired model would be achieved and it is expressed by the following equation:

$$t-\mathrm{stat} = \sqrt{\frac{(n-1)\mathrm{MBE}^2}{\mathrm{MBE}^2 - \mathrm{RMSE}^2}}, \tag{23}$$

where n is the total number of observations, and $\mathrm{ET}_{o\,i,m}$ $\mathrm{ET}_{o\,i,p}$ are the i_{th} actual and estimated mean monthly reference of evapotranspiration, respectively.

(x) Uncertainty at 95% (U_{95}). This quantitative criterion is very efficient in terms of selecting an efficient predictive model among several models. The U_{95}indicator provides very useful information on the deviation of a certain model [91]. The U_{95} can be calculated by the following equation:

$$U_{95} = 1.96\left(\mathrm{SD}^2 + \mathrm{RMSE}^2\right)^{1/2}, \tag{24}$$

where SD represents the standard deviation of the difference between true and simulated data points. The value 1.96 is a coverage factor corresponding to 95% confidence level. Last, for visual evaluation, boxplots and scatter plots are presented in the Results and Discussion sections. The coefficient of determination ($R2$) is calculated based on the following equation:

$$R^2 = 1 - \frac{\sum_{i=1}^{n} e_i^2}{\sum_{i=1}^{n}\left(\mathrm{ET}_{o\,i,p} - \overline{\mathrm{ET}_{o\,i,p}}\right)^2}. \tag{25}$$

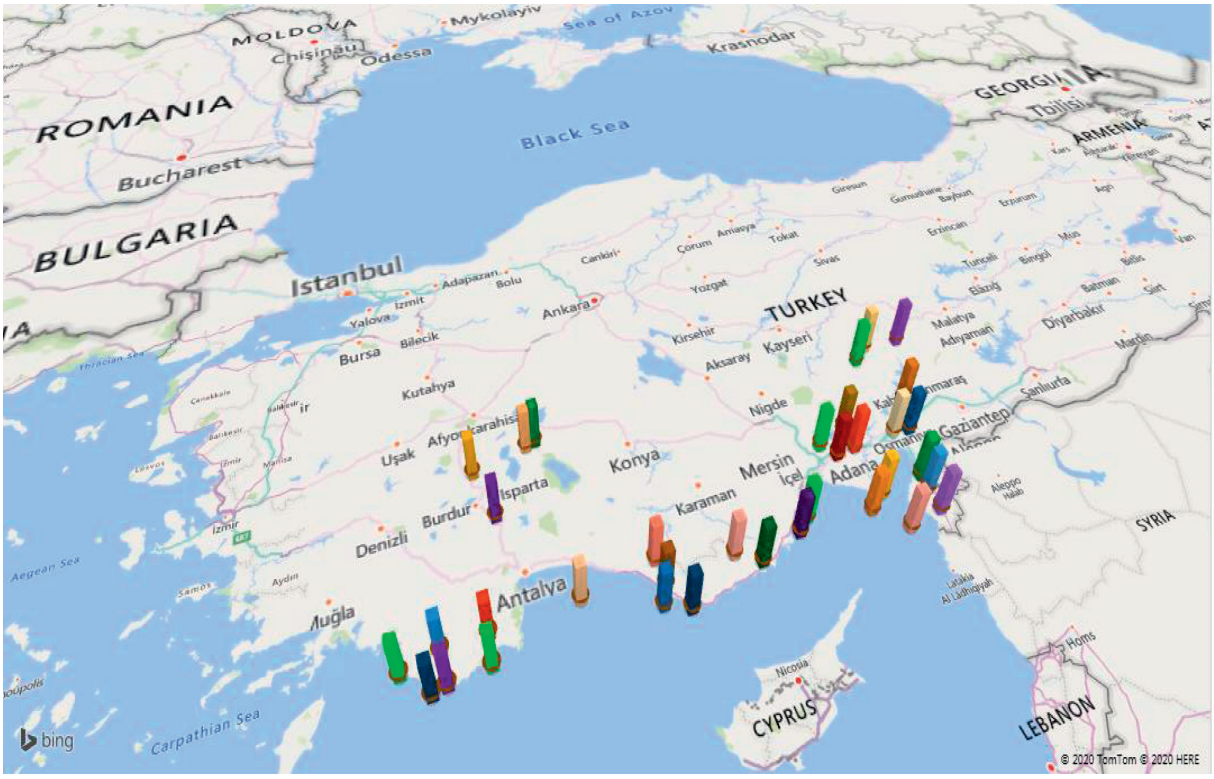

Figure 1: The distribution of meteorological stations in Turkey.

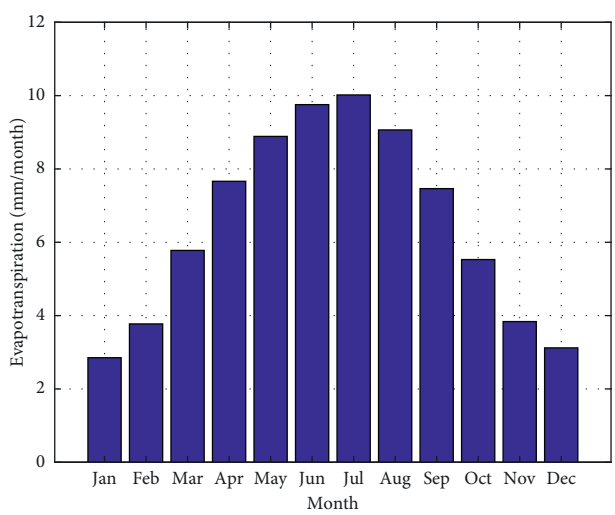

Figure 2: Distribution of the mean monthly (ET_o) over Turkey.

3.5. Model Development. To accurately predict the monthlymean ET_o, three different models were assigned called MLR, RF, and ELM approaches. In accordance with the nature of dataset collected from different locations and sites, and in addition to having different characters, it is a significant and difficult task to create a reliable predictive model. Therefore, the current work is carried out by establishing 20 different input groups for each predictive approach as shown in Table 1. The dataset is randomly divided into phases called training set and testing set. The training set is used for calibration process and model construction, while the testing set is used for examining the performance accuracy of each candidate model. Table 2 shows the statistical description of the variables used in this study. In addition, Table 3 gives information about the Pearson correlation coefficient between all variables and ET_o used in the suggested case study. As shown in the table, the maximum temperature variable has the highest correlation with $ET_o$for both training and testing datasets. The table shows that the longitude variable has the lowest correlation

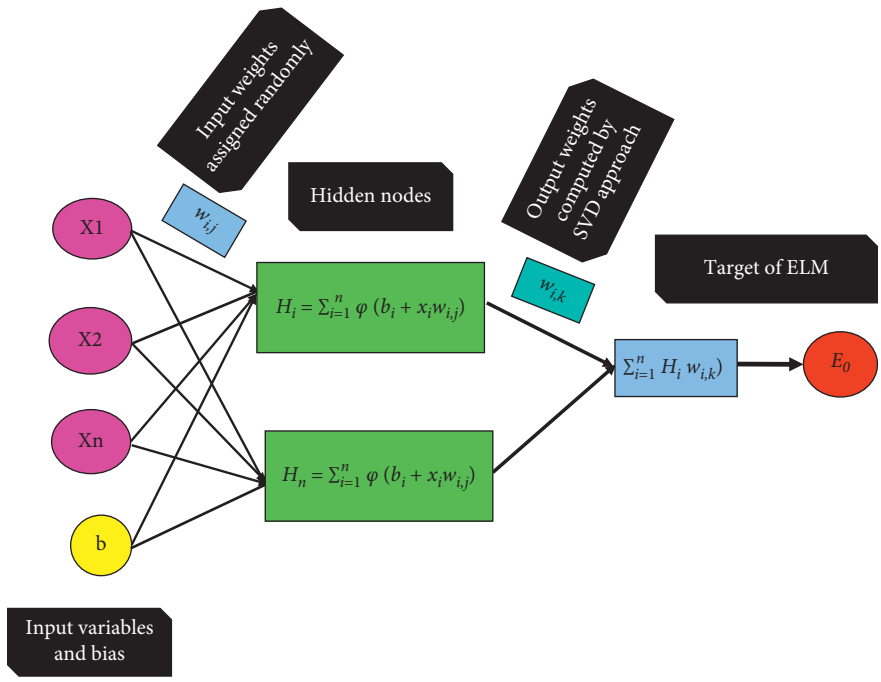

Figure 3: Fundamental structure of ELM.

Table 1: Statistical description of the predictors and evapotranspiration that used in this current study.

Variables		Unit	Max	Min	Mean	Std	Skewness	Kurtosis
Latitude	Training	—	38.21	36.05	36.8	0.69	0.89	2.44
	Testing		38.21	36.05	36.87	0.75	0.73	2.05
	Overall		38.21	36.05	36.82	0.7	0.85	2.34
Longitude	Training	—	37.11	29.07	33.37	2.57	−0.24	1.56
	Testing		37.11	29.07	33.8	2.58	−0.47	1.68
	Overall		37.11	29.07	33.48	2.58	−0.29	1.58
Elevation	Training	m	1552	3	369.35	489.37	0.97	2.33
	Testing		1552	3	426.25	528.16	0.77	1.94
	Overall		1552	3	383.57	499.32	0.92	2.22
T_{max}	Training	C^O	46.7	12.5	32.65	7.54	−0.44	2.32
	Testing		45.4	14.4	31.7	8.01	−0.17	1.84
	Overall		46.7	12.5	32.41	7.67	−0.37	2.17
T_{min}	Training	C^O	20.6	−33.5	1.46	10.27	−0.68	3.65
	Testing		17	−29.4	−0.11	11.03	−0.67	3.15
	Overall		20.6	−33.5	1.07	10.47	−0.68	3.52
T_{mean}	Training	C^O	30.2	−3.8	16.78	7.81	−0.31	2.35
	Testing		28.9	−0.5	15.73	8.25	−0.16	2.01
	Overall		30.2	−3.8	16.52	7.93	−0.27	2.25
Ws	Training	m/sec	5.6	0.7	1.97	0.76	1.46	6.2
	Testing		5.1	0.7	2.15	0.93	1.26	4.35
	Overall		5.6	0.7	2.02	0.81	1.44	5.68
RH_{max}%	Training	—	88.4	53.8	73.33	7.62	−0.39	2.52
	Testing		90.1	55.8	75.17	7.19	−0.44	2.8
	Overall		90.1	53.8	73.79	7.55	−0.41	2.59
RH_{min}%	Training	—	38	0	7.76	5.67	1.43	6.47
	Testing		26	1	7.81	5.44	0.77	3.16
	Overall		38	0	7.77	5.61	1.28	5.75
ET_O	Training	mm/month	15.98	1.5	6.47	2.79	0.27	2.59
	Testing		14.8	1.45	6.5	2.98	0.26	2.34
	Overall		15.98	1.45	6.48	2.84	0.27	2.52

Table 2: Different input combinations.

Combinations	Input parameters
C1	$E_O = f$ (Latitude, Longitude, Elevation, T_{max}, T_{min}, T_{mean}, Ws, RH_{max}, RH_{min})
C2	$E_O = f$ (Latitude, T_{max}, T_{min}, T_{mean}, Ws, RH_{max}, RH_{min})
C3	$E_O = f$ (Longitude, T_{max}, T_{min}, T_{mean}, Ws, RH_{max}, RH_{min})
C4	$E_O = f$ (Elevation, T_{max}, T_{min}, T_{mean}, Ws, RH_{max}, RH_{min})
C5	$E_O = f$ (Latitude, T_{max}, Ws, RH_{max})
C6	$E_O = f$ (Longitude, T_{max}, Ws, RH_{max})
C7	$E_O = f$ (Elevation, T_{max}, Ws, RH_{max})
C8	$E_O = f$ (Latitude, T_{min}, Ws, RH_{min})
C9	$E_O = f$ (Longitude, T_{min}, Ws, RH_{min})
C10	$E_O = f$ (Elevation, T_{min}, Ws, RH_{min})
C11	$E_O = f$ (Latitude, T_{mean}, Ws)
C12	$E_O = f$ (Longitude, T_{mean}, Ws)
C13	$E_O = f$ (Elevation, T_{mean}, Ws)
C14	$E_O = f$ (T_{max}, Ws, RH_{max})
C15	$E_O = f$ (T_{min}, Ws, RH_{max})
C16	$E_O = f$ (T_{mean}, Ws, RH_{max})
C7	$E_O = f$ (T_{mean}, Ws, RH_{min})
C18	$E_O = f$ (T_{max}, Ws, Latitude)
C19	$E_O = f$ (T_{max}, Ws)
C20	$E_O = f$ (T_{max})

coefficient with an ET_o of 0.09, while the maximum temperature is significantly correlated with $ET_o$with an R of 0.841.

The process of selecting a more accurate model is relatively tough with ten statistical matrices and three different approaches including several input combinations. Thus, the assessment process is carried out based on two stages. First, during the training set, from each approach, the best three different models (in total nine models) are being selected. In the second step, it is crucial to monitor the performance of those models, which are selected throughout the training phase, during the testing phase and to select the three most efficient models for each approach. Finally, this process would provide much information about each adopted approach, apart from providing a clear and realistic impression of the performance of each predictive model separately.

Furthermore, a robust and effective performance measure is used to assess the capability of each model. Among these statistical metrics, the uncertainty at 95% (U_{95}) has been used to assess the performance accuracy for each model and subsequently recognize the best predictive model. Figure 4 describes the prediction process of ET_o along the southern coast of Turkey. Last, it is imperative to emphasize that all input variables and their corresponding targets are normalized between 0 and 1. This process is very important to enhance the effectiveness of the predictive models [92, 93]. All models are developed using MATLAB 2017a.

4. Results and Discussion

This section of the study is dedicated to illustrating the forecast results obtained for mean monthly ET_oover Turkey via three different predictive models, namely, MLR, RF, and ELM. Twenty scenarios have been presented including different input variables and are introduced to the mentioned models. 60 predictive models are assessed and validated against the Penman–Monteith equation using ten efficient statistical indicators and graphical presentations. A qualified model is one that meets the requirements of most of the mentioned statistical parameters. The dataset collected from 35 stations is divided randomly into two sets: the training phase (75%) is used to calibrate the models, and the rest of the data is used for validation purposes.

In terms of quantitative assessment, Table 4 exhibits further information about the performances of the proposed 60 different models based on different input variables through the training phase. The three predictive modeling approaches have achieved different accuracies in accordance with statistical measures. Moreover, it is difficult to rank the models in accordance with the achieved accuracies, but the RF approach relatively showed the best accuracy predictions. However, for conducting a fair comparative analysis for each adopted approach, from each modeling technique, the best three models with different input combinations have been selected for performing further and fair comparisons.

Thus, among the 60 predictive models, only the best nine models are selected for optimally carrying out the efficient quantitative analysis. Reducing the number of models has many advantages. For instance, it ensures conducting a powerful and excellent compilation and, thereby, optimally choosing the best statistical matrices. Table 5 shows the performance accuracy of three different approaches based on several input variables.

In general, remarkably, it can be noted from Table 5 that the most frequent combination is C1, C4, and C7, consecutively. This means that the component includes all useful parameters that have effective impact on mean monthlyET_o. At a glance, it can be said that the RF models provided more accurate estimations of mean monthly ET_o than MLR and ELM approaches. Here, it is essential to mention that the uncertainty at 95% (U_{95}) indicator is the most efficient factor, which plays a major role in the evaluation process of

Table 3: Crosscorrelation matrix of the variables used in this study.

	Latitude	Longitude	Elevation	T_{max}	T_{min}	T_{mean}	WS	RH_{max}	RH_{min}	ET_O
					Training					
Latitude	1.000									
Longitude	0.206	1.000								
Elevation	0.673	−0.112	1.000							
T_{max}	−0.194	0.095	−0.301	1.000						
T_{min}	−0.468	−0.021	−0.522	0.852	1.000					
T_{mean}	−0.319	0.036	−0.393	0.943	0.954	1.000				
WS	−0.114	0.004	0.024	0.027	0.125	0.089	1.000			
RH_{max}	0.115	0.157	−0.012	−0.279	−0.341	−0.339	−0.024	1.000		
RH_{min}	0.000	−0.046	0.084	−0.143	−0.058	−0.068	0.118	0.079	1.000	
ET_O	−0.101	0.052	−0.071	0.815	0.696	0.778	0.459	−0.208	−0.065	1.000
					Testing					
Latitude	1.000									
Longitude	0.181	1.000								
Elevation	0.717	−0.068	1.000							
T_{max}	−0.168	0.166	−0.374	1.000						
T_{min}	−0.450	0.064	−0.625	0.877	1.000					
T_{mean}	−0.283	0.118	−0.493	0.958	0.951	1.000				
WS	−0.354	0.013	−0.169	0.024	0.176	0.113	1.000			
RH_{max}	0.194	0.217	0.083	−0.175	−0.268	−0.237	−0.005	1.000		
RH_{min}	0.157	−0.042	0.164	−0.279	−0.210	−0.233	0.093	0.204	1.000	
ET_O	−0.166	0.091	−0.206	0.841	0.738	0.820	0.419	−0.144	−0.208	1.000

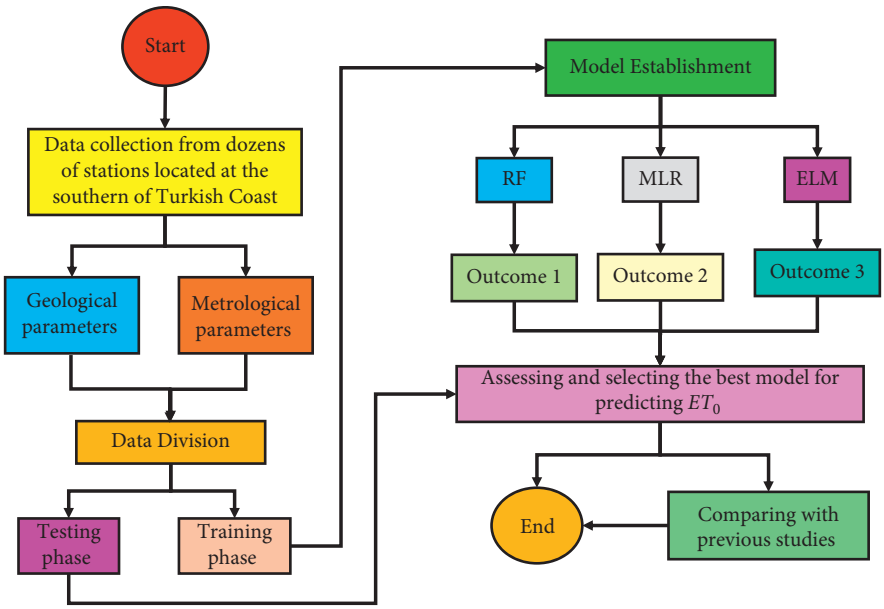

Figure 4: Prediction process of the monthly mean evapotranspiration using several AI approaches.

the best model. Furthermore, the RF-C7 produced the lowest value (1.441) of U_{95} as compared with other predictive models. Besides, the model mentioned also presented high performance based on the rest of the statistical measures. Nevertheless, the accuracy of MLR was unsatisfactory and recorded a high uncertainty with $U_{95}$of 6.077. This is due to the fact that the nonlinear relationship between predictors and their corresponding targets was not considered. Finally, the performances of ELM modeling approaches were satisfactory according to the U_{95} indicator. With respect to the ELM approach, the best model was ELM-C1, which recorded 4.126 ofU_{95}.

Essentially, it should be taken into consideration that promising estimations were obtained during the training phase, which is primarily employed to effectively calibrate the models based on the known input variables and targets. However, the testing step is vital in assessing the performance of a model since it examines the model's accuracy

Table 4: Performance skill description of each predictive model according to different input combinations: training set.

Model	MAE (mm/month)	RMSE (mm/month)	MARE	RMSRE	RRMSE (%)	CC	erMAX	MBE (mm/month)	t_stat	U_{95}(%)
MLR-C1	0.801	0.938	0.158	0.22	14.490	0.942	1.692	6.47	17.909	6.077
RF-C1	0.561	0.688	0.102	0.134	10.628	0.972	1.573	6.468	17.821	1.758
ELM-C1	0.722	0.851	0.141	0.193	13.154	0.952	1.776	6.47	17.875	4.126
MLR-C2	0.839	1.011	0.164	0.232	15.630	0.932	1.838	6.47	17.941	8.227
RF-C2	0.534	0.671	0.095	0.124	10.373	0.973	1.529	6.469	17.816	1.596
ELM-C2	0.772	0.93	0.144	0.202	14.380	0.943	1.621	6.47	17.906	5.893
MLR-C3	0.84	1.02	0.164	0.24	15.766	0.931	1.815	6.47	17.944	8.516
RF-C3	0.541	0.69	0.097	0.127	10.663	0.971	1.5	6.471	17.822	1.781
ELM-C3	0.822	0.99	0.159	0.222	15.303	0.935	1.726	6.47	17.931	7.557
MLR-C4	0.801	0.938	0.158	0.219	14.503	0.942	1.698	6.47	17.909	6.1
RF-C4	0.525	0.66	0.095	0.126	10.197	0.974	1.531	6.481	17.813	1.49
ELM-C4	0.731	0.86	0.135	0.18	13.293	0.951	1.591	6.47	17.879	4.305
MLR-C5	0.842	1.014	0.165	0.235	15.678	0.931	1.829	6.47	17.942	8.325
RF-C5	0.565	0.705	0.103	0.134	10.890	0.971	1.689	6.484	17.826	1.937
ELM-C5	0.761	0.923	0.136	0.175	14.263	0.944	1.532	6.47	17.903	5.704
MLR-C6	0.876	1.053	0.173	0.252	16.270	0.926	1.799	6.47	17.959	9.657
RF-C6	0.556	0.697	0.101	0.13	10.779	0.971	1.489	6.465	17.824	1.861
ELM-C6	0.816	0.968	0.156	0.213	14.956	0.938	1.762	6.47	17.922	6.896
MLR-C7	0.8	0.942	0.158	0.22	14.559	0.941	1.705	6.47	17.911	6.194
RF-C7	0.524	0.654	0.095	0.124	10.112	0.975	1.531	6.472	17.811	1.441
ELM-C7	0.788	0.923	0.156	0.214	14.270	0.944	1.635	6.47	17.903	5.716
MLR-C8	1.248	1.508	0.254	0.352	23.310	0.841	2.396	6.47	18.222	40.689
RF-C8	0.831	1.006	0.159	0.209	15.542	0.938	1.64	6.464	17.938	8.043
ELM-C8	1.088	1.346	0.205	0.278	20.809	0.876	2.113	6.47	18.117	25.846
MLR-C9	1.436	1.687	0.298	0.412	26.069	0.796	2.352	6.47	18.355	63.653
RF-C9	0.843	1.02	0.166	0.225	15.769	0.936	1.89	6.47	17.945	8.52
ELM-C9	1.133	1.382	0.216	0.294	21.357	0.868	2.105	6.47	18.138	28.67
MLR-C10	1.216	1.461	0.245	0.337	22.586	0.852	2.25	6.47	18.19	35.863
RF-C10	0.801	0.975	0.157	0.212	15.076	0.943	1.898	6.482	17.924	7.118
ELM-C10	1.086	1.341	0.205	0.272	20.724	0.877	1.95	6.47	18.113	25.431
MLR-C11	1.071	1.26	0.2	0.252	19.473	0.892	1.852	6.47	18.066	19.818
RF-C11	0.836	1.013	0.159	0.21	15.659	0.943	1.829	6.463	17.942	8.284
ELM-C11	1.004	1.206	0.177	0.219	18.645	0.901	1.688	6.47	18.036	16.653
MLR-C12	1.169	1.367	0.223	0.29	21.130	0.871	1.942	6.47	18.129	27.486
RF-C12	0.837	1.005	0.159	0.21	15.539	0.94	1.793	6.461	17.938	8.033
ELM-C12	0.976	1.189	0.176	0.232	18.380	0.904	1.912	6.47	18.027	15.735
MLR-C13	1.013	1.208	0.18	0.225	18.676	0.901	1.807	6.47	18.037	16.768
RF-C13	0.783	0.934	0.151	0.202	14.427	0.952	1.849	6.478	17.907	5.973
ELM-C13	0.898	1.073	0.161	0.203	16.591	0.923	1.742	6.47	17.969	10.441
MLR-C14	0.875	1.057	0.172	0.249	16.330	0.925	1.822	6.47	17.961	9.801
RF-C14	0.669	0.837	0.122	0.16	12.940	0.961	1.726	6.449	17.871	3.862
ELM-C14	0.75	0.921	0.131	0.165	14.235	0.944	1.457	6.47	17.902	5.66
MLR-C15	1.451	1.706	0.297	0.405	26.362	0.791	2.271	6.47	18.37	66.586
RF-C15	0.976	1.189	0.192	0.258	18.383	0.913	1.986	6.467	18.028	15.74
ELM-C15	1.232	1.502	0.236	0.324	23.222	0.842	2.301	6.47	18.218	40.075
MLR-C16	1.162	1.36	0.22	0.287	21.011	0.873	1.907	6.47	18.125	26.868
RF-C16	0.845	1.045	0.161	0.217	16.150	0.935	1.824	6.469	17.956	9.381
ELM-C16	0.999	1.201	0.181	0.23	18.563	0.902	1.823	6.47	18.033	16.366
MLR-C17	1.16	1.358	0.226	0.3	20.988	0.873	1.972	6.47	18.124	26.749
RF-C17	0.867	1.052	0.165	0.218	16.254	0.936	1.8	6.463	17.959	9.622
ELM-C17	1.038	1.247	0.187	0.239	19.278	0.894	1.902	6.47	18.059	19.034
MLR-C18	1.071	1.26	0.2	0.252	19.473	0.892	1.852	6.47	18.066	19.818
RF-C18	0.824	0.989	0.156	0.205	15.281	0.942	1.741	6.471	17.931	7.516
ELM-C18	0.943	1.141	0.167	0.21	17.637	0.912	1.73	6.47	18.002	13.341
MLR-C19	1.169	1.369	0.223	0.291	21.155	0.871	1.953	6.47	18.13	27.616
RF-C19	0.827	1.022	0.149	0.197	15.794	0.933	1.795	6.468	17.945	8.577
ELM-C19	1.05	1.274	0.186	0.236	19.684	0.889	1.866	6.47	18.074	20.69
MLR-C20	1.394	1.751	0.273	0.38	27.065	0.778	2.651	6.47	18.407	73.96
RF-C20	1.092	1.425	0.199	0.279	22.028	0.86	2.297	6.445	18.17	32.439
ELM-C20	1.329	1.709	0.25	0.347	26.416	0.79	2.409	6.47	18.373	67.125

Table 5: Selection of the best three models for each predictive approach through the calibration process.

Model	MAE (mm/month)	RMSE (mm/month)	MARE	RMSRE	RRMSE (%)	CC	erMAX	MBE (mm/month)	t_stat	U_{95}(%)	Rank
MLR-C1	0.801	0.938	0.158	0.22	14.490	0.942	1.692	6.47	17.909	6.077	1
MLR-C4	0.801	0.938	0.158	0.219	14.503	0.942	1.698	6.47	17.909	6.1	2
MLR-C7	0.8	0.942	0.158	0.22	14.559	0.941	1.705	6.47	17.911	6.194	3
RF-C7	0.524	0.654	0.095	0.124	10.112	0.975	1.531	6.472	17.811	1.441	1
RF-C4	0.525	0.66	0.095	0.126	10.197	0.974	1.531	6.481	17.813	1.49	2
RF-C2	0.534	0.671	0.095	0.124	10.373	0.973	1.529	6.469	17.816	1.596	3
ELM-C1	0.722	0.851	0.141	0.193	13.154	0.952	1.776	6.47	17.875	4.126	1
ELM-C4	0.731	0.86	0.135	0.18	13.293	0.951	1.591	6.47	17.879	4.305	2
ELM-C14	0.75	0.921	0.131	0.165	14.235	0.944	1.457	6.47	17.902	5.66	3

based on unseen target values. This advantage does not exist in the training set. Therefore, the reliable model should have a stable and balanced performance in both training and testing phases.

After demonstrating the performance of the models during the calibration (training) phase, it is very important to see the accuracy of the adopted models during the testing phase. Table 6 demonstrated the performance skill of each predictive model using different input parameters.

It is also important to carefully follow-up the performance of nine efficient models that were chosen in the training set (MLR-C1, MLR-C4, MLR-C7, RF-C7, RF-C4, RF-C2, ELM-C1, ELM-C4, and ELM-C14). Besides the mentioned models, there were additional three models (RF-C5, RF-C6, and ELM-C2) that have effectively provided satisfactory estimations. The heat-map diagram as presented in Figure 5 provided significant information about the best modeling performance based on ten statistical parameters.

Although RF models generated acceptable precision during the training set, it exhibited the worst accuracies as compared to ELM and MLR techniques in the testing set. Moreover, these models produced high uncertainty, and the values of U_{95} are 19.59, 27.1, 22.74, 22.35, and 26.72% for RF-C7, RF-C4, RF-C5, RF-C6, and RF-C2, respectively. Additionally, the other statistical parameters such as RMSE and RRMSE also gave further information about the weaknesses of RF models. It is undeniable that the RF approach suffers from overfitting issue. On the other hand, the MLR models showed much better performance capacity than RF models. Finally, the ELM models achieved high precision in the prediction of mean monthly ET_o in accordance with the P-M equation. Moreover, the ELM-C1 is considered the best predictive model and recorded the highest CC (0.957), lowest RMSE (1.155), MAE (0.946 mm/month), $t-$stat(10.37), RRMSE (16.54%), and U_{95}(9.989%), respectively. Moreover, among ten statistical parameters, the most efficient parameters, which can easily recognize the best predictive model are U_{95}, RMSE, and RRMSE. The supremacy of ELM approaches was evaluated in accordance with its ability of reducing the most significant statistical measures (U_{95}, RMSE, and RRMSE) throughout the testing phase. The results obtained as shown in Figure 6 illustrated the superiority of ELM-C1 over other predictive models in reducing the value of the mentioned three statistical metrics. The effectiveness of the ELM-C1 model over MLR-C1 powerfully appeared in reducing the RMSE and U_{95} parameters to 10.05% and 34.07%, respectively. Moreover, the prediction accuracy of ELM-C1 accomplished better outcome when it is compared with the RF-C7 model, where there was a significant improvement in the reduction of RMSE and U_{95} parameters, which reached 16.36% and 49.02%, respectively.

The box plot diagram, shown in Figure 7, presented the best candidate models, which were employed to predict the average monthlyET_o. It can be remarkably noted that the RF models could not perform well as compared to the other approaches such as MLR and ELM. However, the MLR models had the modest performance and poor accuracy as compared to ELM approaches. It can be said that the best performance approach in prediction average monthlyET_o is ELM, followed by MLR and RF techniques, consecutively. The ELM-C1 achieved the best estimation accuracy where the median and interquarter range (IQR) were found to be very close to the actual median and IQR.

Line graph and scatterplot of predicted and actual average monthlyET_o are provided in Figures 8(a) and 8(b) during the testing phase. The scatter plot effectively presents useful visualization information on the diversion between observed and predicted values, and the coefficient of determination (R^2) showed the determination between them. Based on Figures 8(a) and 8(b), the proposed ELM-C1 has better prediction performance than other comparative models in terms of providing a higher value of R^2 (0.915).

Considering the best ELM models, it can be noted that this approach often requires a relatively higher number of input parameters in comparison with RF and MLR approaches. The logical explanation of this phenomenon is that the data size includes 35 locations of different characteristics. Besides, the geographical factors are very important when developing local and robust models based on a dataset collected from several locations.

For further assessment, it is vital to examine the ability of the suggested model (ELM-C1) against several predictive models that were proposed in the previous studies to estimate

Table 6: Performance skill description of each predictive model according to different input combinations: testing set.

Model	MAE (mm/month)	RMSE (mm/month)	MARE	RMSRE	RRMSE (%)	CC	erMAX	MBE (mm/month)	t_stat	U_{95} (%)
MLR-C1	1.078	1.284	0.172	0.214	18.392	0.945	1.449	6.254	10.42	15.151
RF-C1	1.281	1.561	0.187	0.213	22.359	0.938	1.556	5.992	10.563	29.955
ELM-C1	**0.946**	**1.155**	0.149	0.191	**16.544**	**0.956**	1.634	6.333	**10.372**	**9.989**
MLR-C2	1.117	1.358	0.173	0.216	19.458	0.936	1.545	6.242	10.448	19.537
RF-C2	1.229	1.513	0.178	0.206	21.673	0.938	1.503	6.032	10.535	26.723
ELM-C2	0.962	1.216	**0.146**	0.18	17.417	0.95	1.422	6.322	10.392	12.574
MLR-C3	1.167	1.407	0.181	0.22	20.159	0.936	1.501	6.158	10.475	21.306
RF-C3	1.253	1.541	0.182	0.209	22.080	0.935	1.492	6.018	10.55	28.899
ELM-C3	1.111	1.357	0.168	0.203	19.444	0.946	1.456	6.131	10.458	17.33
MLR-C4	1.074	1.282	0.172	0.214	18.371	0.945	1.456	6.266	10.419	15.248
RF-C4	1.256	1.523	0.184	0.21	21.820	0.939	1.516	6.013	10.542	27.104
ELM-C4	0.999	1.248	0.147	0.177	17.884	0.955	1.467	6.228	10.409	12.848
MLR-C5	1.118	1.348	0.178	0.221	19.312	0.934	1.56	6.283	10.441	19.589
RF-C5	1.144	1.423	0.168	0.198	20.391	0.946	1.526	6.168	10.481	22.741
ELM-C5	1.052	1.269	0.163	0.19	18.186	0.952	1.447	6.197	10.419	13.441
MLR-C6	1.199	1.429	0.195	0.246	20.475	0.926	1.551	6.232	10.477	24.555
RF-C6	1.134	1.422	0.164	0.195	20.371	0.947	1.677	6.155	10.482	22.346
ELM-C6	1.066	1.282	0.174	0.218	18.367	0.95	1.496	6.197	10.423	14.126
MLR-C7	1.071	1.281	0.168	0.204	18.348	0.945	1.461	6.274	10.417	15.282
RF-C7	1.103	1.381	0.16	0.194	19.785	0.951	1.649	6.165	10.464	19.593
ELM-C7	1.047	1.253	0.164	0.199	17.947	**0.956**	1.445	6.185	10.414	12.401
MLR-C8	1.524	1.803	0.276	0.366	25.837	0.851	1.871	6.348	10.636	73.725
RF-C8	1.389	1.684	0.217	0.272	24.132	0.901	1.784	6.255	10.589	52.417
ELM-C8	1.316	1.633	0.218	0.273	23.396	0.891	1.554	6.256	10.564	45.735
MLR-C9	1.751	2.069	0.315	0.419	29.644	0.796	2.267	6.296	10.798	129.564
RF-C9	1.468	1.781	0.229	0.279	25.512	0.886	1.727	6.207	10.646	65.221
ELM-C9	1.368	1.731	0.212	0.28	24.804	0.872	2.188	6.302	10.606	60.569
MLR-C10	1.462	1.746	0.264	0.367	25.015	0.867	1.811	6.283	10.616	62.258
RF-C10	1.414	1.698	0.221	0.274	24.321	0.906	2.015	6.241	10.598	53.811
ELM-C10	1.237	1.56	0.198	0.249	22.356	0.903	1.593	6.296	10.526	38.316
MLR-C11	1.342	1.66	0.213	0.269	23.785	0.901	1.66	6.083	10.6	43.783
RF-C11	1.467	1.836	0.209	0.251	26.298	0.911	1.767	5.958	10.719	64.059
ELM-C11	1.246	1.583	0.179	0.213	22.677	0.929	1.349	5.976	10.576	31.619
MLR-C12	1.505	1.801	0.248	0.307	25.806	0.876	1.788	6.057	10.681	62.81
RF-C12	1.408	1.763	0.2	0.234	25.254	0.917	1.524	5.976	10.673	53.541
ELM-C12	1.302	1.605	0.201	0.26	22.997	0.927	1.476	5.947	10.591	32.973
MLR-C13	1.264	1.589	0.196	0.246	22.765	0.918	1.577	6.044	10.57	34.417
RF-C13	1.423	1.783	0.202	0.239	25.547	0.919	1.546	5.944	10.69	55.172
ELM-C13	1.277	1.527	0.19	0.227	21.880	0.949	1.302	5.878	10.561	23.495
MLR-C14	1.197	1.429	0.194	0.244	20.470	0.925	1.569	6.248	10.476	24.857
RF-C14	1.247	1.55	0.184	0.22	22.210	0.94	1.622	6.146	10.539	33.389
ELM-C14	1.015	1.259	0.148	0.176	18.038	0.952	1.397	6.209	10.414	13.109
MLR-C15	1.734	2.079	0.308	0.409	29.792	0.789	2.079	6.339	10.795	134.22
RF-C15	1.599	1.924	0.266	0.336	27.565	0.858	2.048	6.264	10.716	93.894
ELM-C15	1.419	1.76	0.229	0.298	25.220	0.858	1.979	6.382	10.61	67.441
MLR-C16	1.487	1.805	0.244	0.305	25.854	0.878	1.776	6.034	10.687	62.369
RF-C16	1.518	1.888	0.227	0.28	27.053	0.891	2.048	5.994	10.745	74.975
ELM-C16	1.351	1.633	0.207	0.251	23.394	0.923	1.52	5.932	10.608	35.411
MLR-C17	1.534	1.825	0.262	0.338	26.149	0.879	1.663	5.985	10.708	63.591
RF-C17	1.539	1.896	0.229	0.274	27.166	0.901	1.858	5.962	10.756	74.846
ELM-C17	1.363	1.672	0.205	0.241	23.954	0.916	1.44	5.936	10.628	40.003
MLR-C18	1.342	1.66	0.213	0.269	23.785	0.901	1.66	6.083	10.6	43.783
RF-C18	1.407	1.775	0.203	0.245	25.426	0.915	1.656	5.957	10.683	54.491
ELM-C18	1.254	1.577	0.185	0.227	22.590	0.929	1.535	5.975	10.573	31.011
MLR-C19	1.505	1.805	0.248	0.309	25.867	0.877	1.776	6.047	10.685	63.046
RF-C19	1.369	1.736	0.195	0.23	24.875	0.906	1.49	5.99	10.655	50.356
ELM-C19	1.265	1.583	0.186	0.221	22.674	0.923	1.45	6.029	10.569	33.28
MLR-C20	1.877	2.329	0.295	0.361	33.366	0.82	2.197	5.567	11.228	154.758
RF-C20	1.859	2.398	0.264	0.316	34.363	0.813	2.089	5.499	11.333	171.226
ELM-C20	1.8	2.275	0.261	0.317	32.599	0.832	2.109	5.613	11.156	142.188

Bold numbers refer to the best results.

Figure 5: Heat-map diagram illustrating the best three models for each predictive approach through the calibration process.

ET_O over different locations around the world. In this respect, the findings obtained during the test step by using the ELM-C1 model are validated against several predictive models carried out in the literature by some researchers. Khoob [94] conducted a study using ANN to predict ET_Oin Safiabad station, which is located in Southern Iran. The outcome of this study revealed that the suggested ANN model performed very well when compared with the actual values ofET_O. The most significant observation is that the accuracy of the model was very good with a high $R^2$of 0.9135. Moreover, another study was carried out using the ANN technique to predict ET_O in the Reynolds Creek Experimental Watershed in Southwestern Idaho, USA [95]. The obtained results showed that the ANN model managed to effectively estimate $ET_O$with high accuracy of prediction and fewer forecasted error reported (R^2 = 0.82). Additionally, another study was conducted in Southeast Asia using different AI models; Wu and Fan [96] introduced a comprehensive study to accurately predict ET_O over 14 stations located in China. The researchers employed eight different techniques such as ANFIS, MLP, GRNN, KNEA, SVR, XGBoost, M5Tree, and Mars. These models were developed based on the collected data, which includes precipitation and temperature variables. The outcomes of the study illustrated that the machine learning techniques could provide satisfactory prediction of $ET_O$by using only one variable (temperature). In addition, the estimated ET_O values were close to the actual ones, and the reported average R^2 indicator was equal to 0.829. On top of that, Izadifar and Elshorbagy [97] employed three data-driven models called MLR, GP, and ANN to estimate ET_O over Northern Alberta, Canada. Statistical analyses of the study revealed that the most influencing variables on ET_O were net radiation and temperature. Besides, the ANN approached trained Bayesian regularization algorithm presented more accurate results than other comparable models, which recorded the highest accuracy of prediction (R^2 = 0.82).

Significant attempts were made to increasingly constitute powerful models to accurately estimate ET_Obased on few parameters, which can easily be measured such as temperature. Zhu et al. [69] managed to develop a hybrid model called PSO-ELM to predict ET_O over five meteorological stations located at the Northwest of China. The proposed model produced more accurate estimations than other AI models and employed empirical equations. The proposed model (PSO-ELM) were built based on temperature only, in general, and produced fewer forecasted errors and higher correlation with the actual one (mean R^2 of 0.8905).

Overall, the published studies, as illustrated above, have been carried out to estimate ET_Oover several case studies. Even though researchers developed powerful approaches that attained high accuracy, the approaches mentioned could not be applied to constitute a general model instead of simulation of each case study separately. However, in this

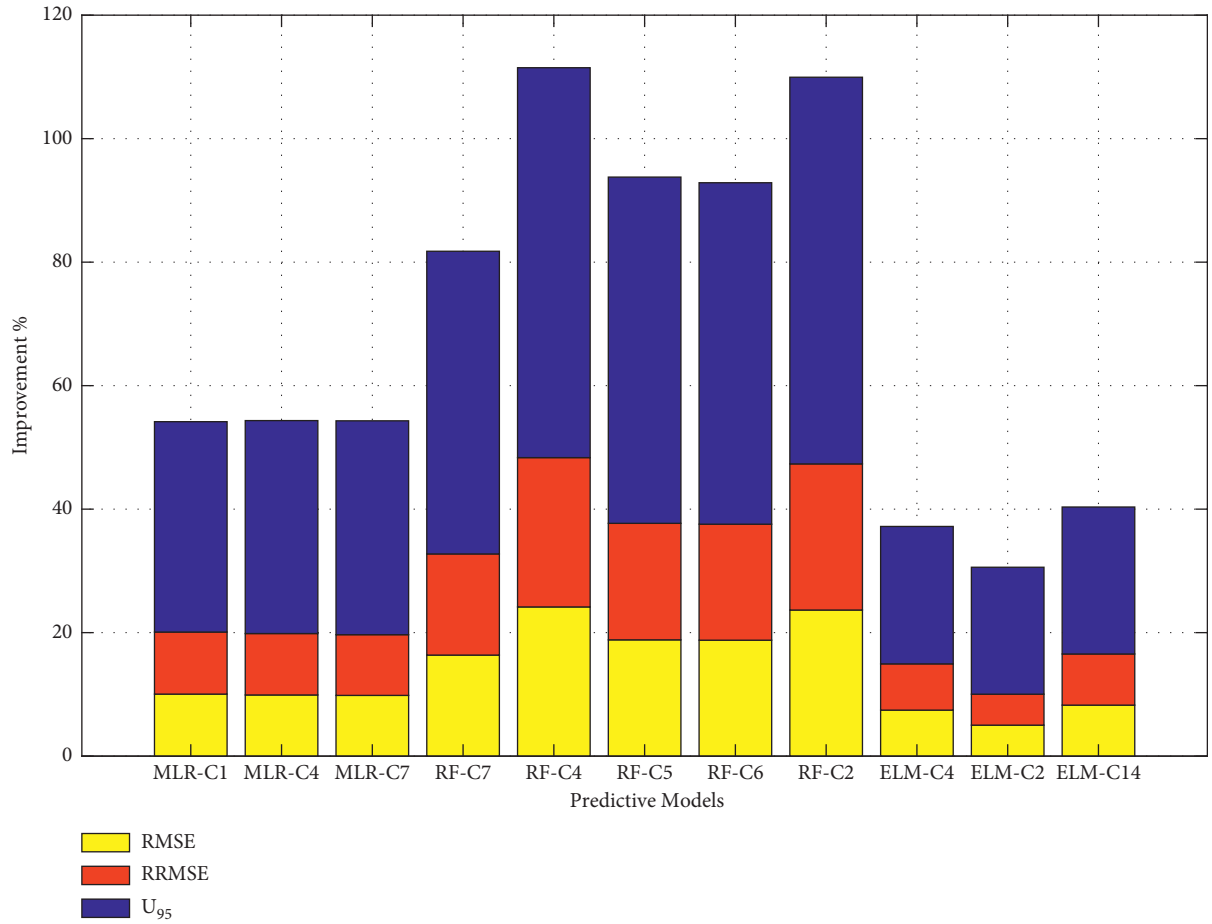

Figure 6: The enhancement percentage of the ELM-C1 predictive model over other models based on RMASE, RRMSE, and U_{59}.

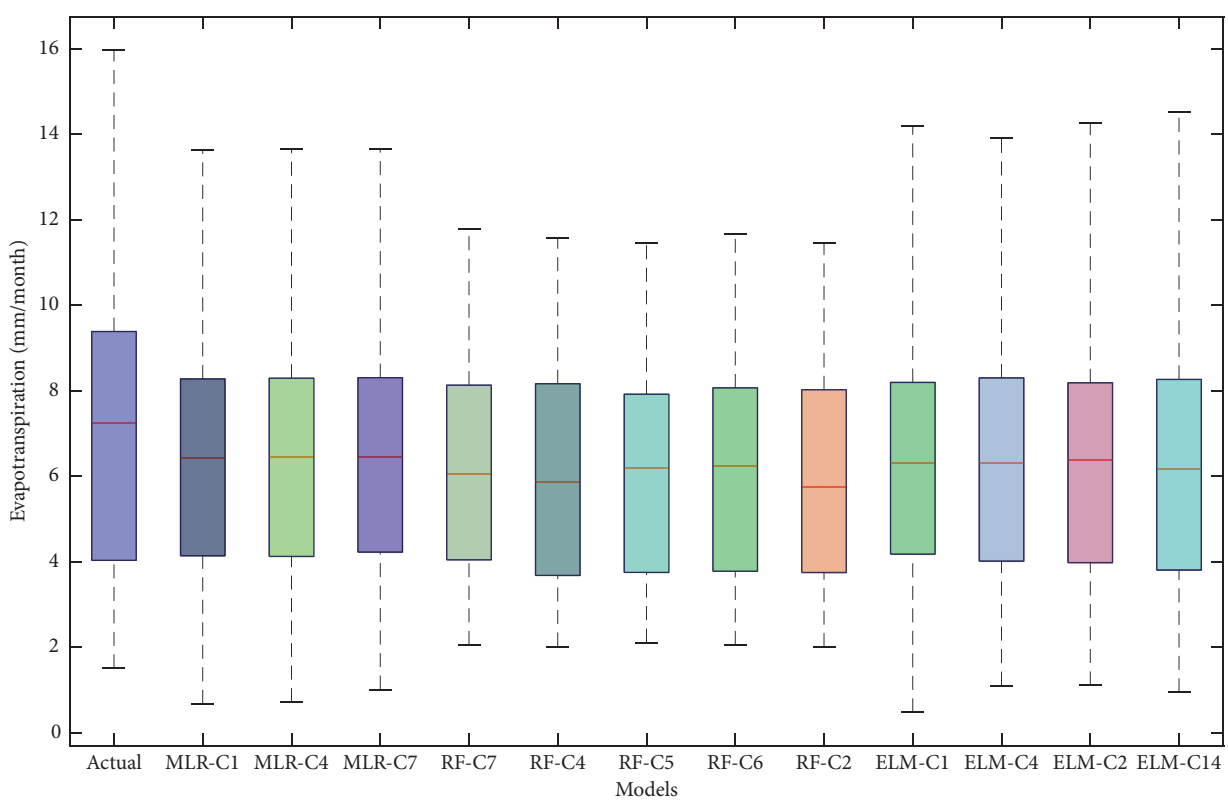

Figure 7: Boxplot diagram presented the superiority of ELM over other comparable models during the testing set.

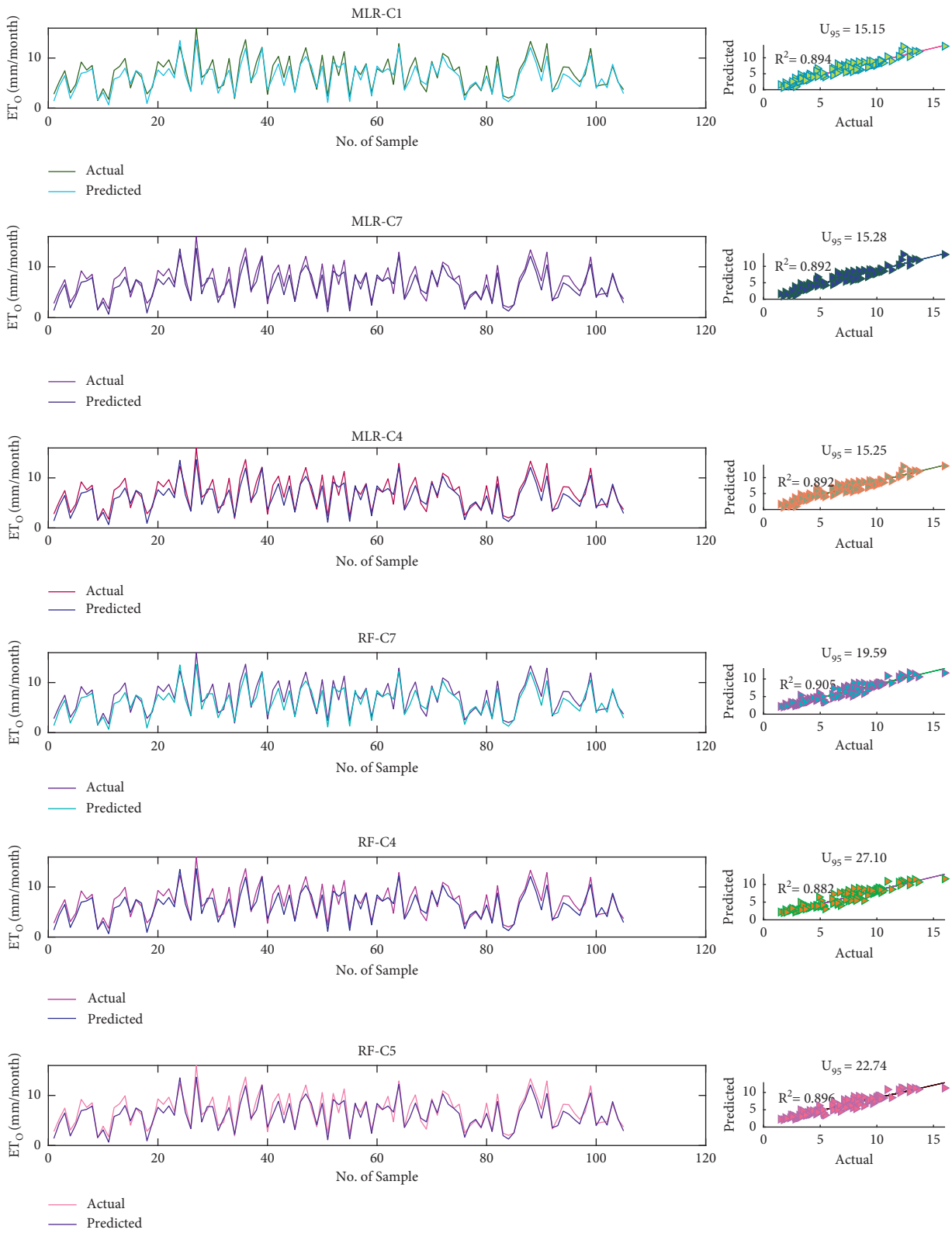

(a)

Figure 8: Continued.

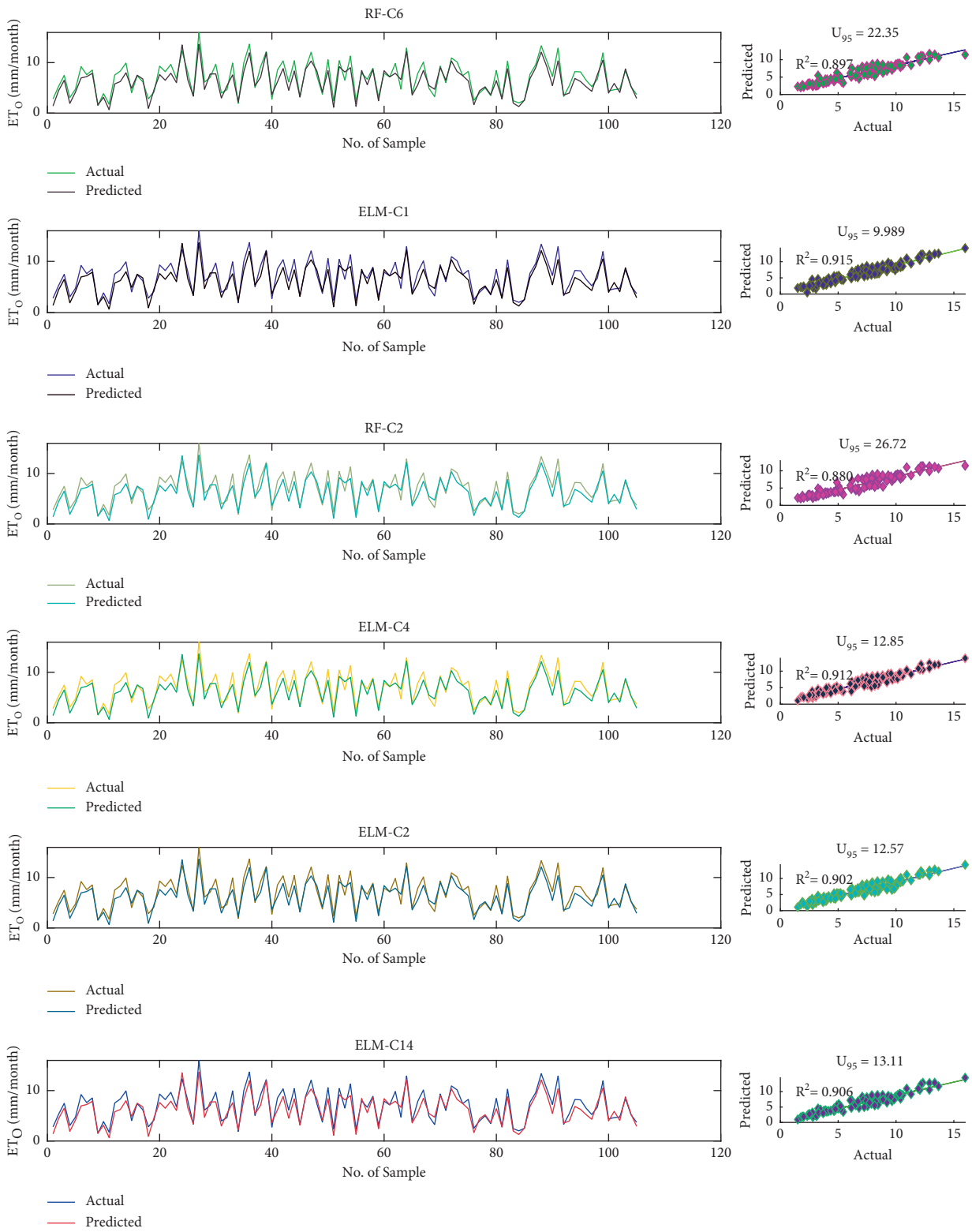

(b)

Figure 8: (a): Observed vs. predicted values of mean monthlyET_ousing different models: testing set. (b) Observed vs. predicted values of mean monthly ET_ousing different models: testing set.

current study, a single model (ELM-C1) successfully managed to simulate the ET_O based on the data collected from dozens of stations. In addition to the simulation process of 35 stations in one single model, the other interesting feature is that the predictability of the proposed model was recorded high ($R^2 > 0.91$).

5. Conclusion

Evapotranspiration is considered as one of the most significant factors in the hydrological cycle. Although the well-known Penman–Monteith equation for computing the evapotranspiration exists, there are some difficulties in accurately calculating some of its parameters such as solar radiation and sensible heat flux into the soil. Therefore, in this study, three different approaches were employed, namely, ELM, RF, and MLR, based on geographical and meteorological parameters for the prediction of the mean monthly evapotranspiration over southern Mediterranean coast of Turkey. Besides, twenty different input combinations assigned according to data collected from 35 meteorological stations were established. Ten efficient statistical parameters have been used to assess the 60 predictive models. The outcomes of this study revealed that the performance of the ELM approach outperformed the MLR and RF models. In addition, the efficiency of the proposed ELM produced less computed errors during the testing set. It is worth mentioning that the U_{95} measure played a vital role in the selection of the best model accuracy among the established 60 models in this study. The other essential observation that can be drawn is that the RF approach provided the perfect accuracy during the training phase, and when it comes to examining its performances during the testing phase, the predictions' accuracies were very poor and disappointing. Finally, this study suggested the use of ELM in building local models based on different stations and weather conditions. In addition, a study that covers the whole area of the Mediterranean Sea via one robust model is needed. For further investigation, feature selection approaches can possibly be integrated prior to the predictive learning process to extract the essential input variables for the prediction matrix [98, 99].

Abbreviations

ET_o: Reference evapotranspiration
T_{max}: Maximum monthly temperature
T_{min}: Minimum monthly temperature
T_{mean}: Average monthly temperature
Std: Standard deviation
W_s: Wind speed
RH_{max}: % Maximum relative humidity
RH_{min}: % Minimum relative humidity
MAE: Mean absolute error
e: Estimated error between actual and predicted ET_O
RMSE: Root mean square error
MARE: Mean absolute relative error
RMSRE: Root mean square relative error
RRMSE: Relative root mean square error
MBE: Mean bias error
CC: Correlation of coefficient
R^2: Correlation of determination
erMAX: Maximum absolute relative error
t – stat: t-statistic
$U95$: Uncertainty at 95%
ELM: Extreme learning machine
RF: Random Forests
MLR: Multiple-linear regression
P – M: Penman–Monteith.

Data Availability

All the data are available upon request.

Conflicts of Interest

The authors have no conflicts of interest.

Acknowledgments

The authors would like to thank AlMaaref University College (AUC) for funding this research.

References

[1] U. Maček, N. Bezak, and M. Šraj, "Reference evapotranspiration changes in Slovenia, Europe," *Agricultural and Forest Meteorology*, vol. 260-261, pp. 183–192, 2018.

[2] H. Sanikhani, R. C. Deo, P. Samui et al., "Survey of different data-intelligent modeling strategies for forecasting air temperature using geographic information as model predictors," *Computers and Electronics in Agriculture*, vol. 152, pp. 242–260, 2018.

[3] J. Hall, B. Arheimer, M. Borga et al., "Understanding flood regime changes in Europe: a state-of-the-art assessment," *Hydrology and Earth System Sciences*, vol. 18, no. 7, pp. 2735–2772, 2014.

[4] J. de Leeuw, J. Methven, and M. Blackburn, "Variability and trends in England and Wales precipitation," *International Journal of Climatology*, vol. 36, no. 8, pp. 2823–2836, 2016.

[5] S. M. Awadh, H. Al-Mimar, and Z. M. Yaseen, "Groundwater availability and water demand sustainability over the upper mega aquifers of Arabian Peninsula and West Region of Iraq," *Environment, Development and Sustainability*, vol. 23, pp. 1–21, 2021.

[6] Z. Yang, Q. Liu, and B. Cui, "Spatial distribution and temporal variation of reference evapotranspiration during 1961–2006 in the Yellow River Basin, China," *Hydrological Sciences Journal*, vol. 56, no. 6, pp. 1015–1026, 2011.

[7] K. Xiang, Y. Li, R. Horton, and H. Feng, "Similarity and difference of potential evapotranspiration and reference crop evapotranspiration - a review," *Agricultural Water Management*, vol. 232, Article ID 106043, 2020.

[8] A. Malik, A. Kumar, S. Kim et al., "Modeling monthly pan evaporation process over the Indian central Himalayas: application of multiple learning artificial intelligence model," *Engineering Applications of Computational Fluid Mechanics*, vol. 14, no. 1, pp. 323–338, 2020.

[9] F. Granata, "Evapotranspiration evaluation models based on machine learning algorithms-A comparative study," *Agricultural Water Management*, vol. 217, pp. 303–315, 2019.

[10] M. E. Jensen and R. G. Allen, *Evaporation, Evapotranspiration, and Irrigation Water Requirements*, American Society of Civil Engineers, Reston, VA, USA, 2016.

[11] M. Valipour, "Analysis of potential evapotranspiration using limited weather data," *Applied Water Science*, vol. 7, no. 1, pp. 187–197, 2017.

[12] S. Jasechko, Z. D. Sharp, J. J. Gibson, S. J. Birks, Y. Yi, and P. J. Fawcett, "Terrestrial water fluxes dominated by transpiration," *Nature*, vol. 496, no. 7445, pp. 347–350, 2013.

[13] M. Jung, M. Reichstein, P. Ciais et al., "Recent decline in the global land evapotranspiration trend due to limited moisture supply," *Nature*, vol. 467, no. 7318, pp. 951–954, 2010.

[14] K. Zhang, J. S. Kimball, and S. W. Running, "A review of remote sensing based actual evapotranspiration estimation," *WIREs Water*, vol. 3, no. 6, pp. 834–853, 2016.

[15] G. R. Diak, J. R. Mecikalski, M. C. Anderson et al., "Estimating land surface energy budgets from space: review and current efforts at the University of Wisconsin-madison and USDA-ARS," *Bulletin of the American Meteorological Society*, vol. 85, no. 1, pp. 65–78, 2004.

[16] K. Khosravi, P. Daggupati, M. T. Alami et al., "Meteorological data mining and hybrid data-intelligence models for reference evaporation simulation: a case study in Iraq," *Computers and Electronics in Agriculture*, vol. 167, p. 105041, 2019.

[17] R. A. Pielke, fnm Sr, R. Avissar et al., "Interactions between the atmosphere and terrestrial ecosystems: influence on weather and climate," *Global Change Biology*, vol. 4, no. 5, pp. 461–475, 1998.

[18] C. Schumacher, R. A. Houze Jr., and I. Kraucunas, "The tropical dynamical response to latent heating estimates derived from the TRMM precipitation radar," *Journal of the Atmospheric Sciences*, vol. 61, no. 12, pp. 1341–1358, 2004.

[19] W. J. Shuttleworth, "Putting the "vap" into evaporation," *Hydrology and Earth System Sciences*, vol. 11, no. 1, pp. 210–244, 2007.

[20] T. Stocker, *Climate Change 2013: The Physical Science Basis: Working Group I Contribution to the Fifth Assessment Report of the Intergovernmental Panel on Climate Change*, Cambridge University Press, Cambridge, UK, 2014.

[21] S. Naganna, P. Deka, M. Ghorbani, S. Biazar, N. Al-Ansari, and Z. Yaseen, "Dew point temperature estimation: application of artificial intelligence model integrated with nature-inspired optimization algorithms," *Water*, vol. 11, no. 4, p. 742, 2019.

[22] X. Lian, S. Piao, C. Huntingford et al., "Partitioning global land evapotranspiration using CMIP5 models constrained by observations," *Nature Climate Change*, vol. 8, no. 7, pp. 640–646, 2018.

[23] P. C. D. Milly and K. A. Dunne, "Potential evapotranspiration and continental drying," *Nature Climate Change*, vol. 6, no. 10, pp. 946–949, 2016.

[24] W. Jing, Z. M. Yaseen, S. Shahid et al., "Implementation of evolutionary computing models for reference evapotranspiration modeling: short review, assessment and possible future research directions," *Engineering Applications of Computational Fluid Mechanics*, vol. 13, no. 1, pp. 811–823, 2019.

[25] M. K. Saggi and S. Jain, "Application of fuzzy-genetic and regularization random forest (FG-RRF): estimation of crop evapotranspiration (ET) for maize and wheat crops," *Agricultural Water Management*, vol. 229, Article ID 105907, 2020.

[26] S. Karimi, J. Shiri, and P. Marti, "Supplanting missing climatic inputs in classical and random forest models for estimating reference evapotranspiration in humid coastal areas of Iran," *Computers and Electronics in Agriculture*, vol. 176, Article ID 105633, 2020.

[27] S. Green, B. Clothier, and B. Jardine, "Theory and practical application of heat pulse to measure sap flow," *Agronomy Journal*, vol. 95, no. 6, pp. 1371–1379, 2003.

[28] H. Chen, J. J. Huang, and E. McBean, "Partitioning of daily evapotranspiration using a modified shuttleworth-wallace model, random forest and support vector regression, for a cabbage farmland," *Agricultural Water Management*, vol. 228, Article ID 105923, 2020.

[29] S. Kang, B. Gu, T. Du, and J. Zhang, "Crop coefficient and ratio of transpiration to evapotranspiration of winter wheat and maize in a semi-humid region," *Agricultural Water Management*, vol. 59, no. 3, pp. 239–254, 2003.

[30] W. Zegada-Lizarazu and P. R. Berliner, "Inter-row mulch increase the water use efficiency of furrow-irrigated maize in an arid environment," *Journal of Agronomy and Crop Science*, vol. 197, no. 3, pp. 237–248, 2011.

[31] N. Raz-Yaseef, D. Yakir, G. Schiller, and S. Cohen, "Dynamics of evapotranspiration partitioning in a semi-arid forest as affected by temporal rainfall patterns," *Agricultural and Forest Meteorology*, vol. 157, pp. 77–85, 2012.

[32] U. S. Panu and T. Nguyen, "Estimation of mean areal evaporation in Northwestern Ontario," *Canadian Water Resources Journal*, vol. 19, no. 1, pp. 69–82, 1994.

[33] V. P. Singh and C.-Y. Xu, "Evaluation and generalization of 13 mass-transfer equations for determining free water evaporation," *Hydrological Processes*, vol. 11, no. 3, pp. 311–323, 1997.

[34] J. Shiri, "Improving the performance of the mass transfer-based reference evapotranspiration estimation approaches through a coupled wavelet-random forest methodology," *Journal of Hydrology*, vol. 561, pp. 737–750, 2018.

[35] S. S. Fiyadh, M. A. AlSaadi, M. K. AlOmar et al., "The modelling of lead removal from water by deep eutectic solvents functionalized CNTs: artificial neural network (ANN) approach," *Water Science and Technology*, vol. 76, no. 9, pp. 2413–2426, 2017.

[36] S. S. Fiyadh, M. A. AlSaadi, M. K. AlOmar, S. S. Fayaed, F. S. Mjalli, and A. El-Shafie, "BTPC-based DES-functionalized CNTs for As3+ removal from water: NARX neural network approach," *Journal of Environmental Engineering*, vol. 144, no. 8, Article ID 04018070, 2018.

[37] Z. M. Yaseen, W. H. M. W. Mohtar, A. M. S. Ameen et al., "Implementation of Univariate paradigm for streamflow simulation using hybrid data-driven model: case study in tropical region," *IEEE Access*, vol. 7, pp. 74471–74481, 2019.

[38] Z. Yaseen, I. Ebtehaj, S. Kim et al., "Novel hybrid data-intelligence model for forecasting monthly rainfall with uncertainty analysis," *Water*, vol. 11, no. 3, p. 502, 2019.

[39] H. H. Hasan, S. F. Mohd Razali, N. S. Muhammad, and A. Ahmad, "Research trends of hydrological drought: a systematic review," *Water*, vol. 11, no. 11, p. 2252, 2019.

[40] M. A. Ghorbani, R. Khatibi, V. Karimi, Z. M. Yaseen, and M. Zounemat-Kermani, "Learning from multiple models using artificial intelligence to improve model prediction accuracies: application to river flows," *Water Resources Management*, vol. 32, no. 13, pp. 4201–4215, 2018.

[41] S. Maroufpoor, E. Maroufpoor, O. Bozorg-Haddad, J. Shiri, and Z. Mundher Yaseen, "Soil moisture simulation using hybrid artificial intelligent model: hybridization of adaptive neuro fuzzy inference system with grey wolf optimizer algorithm," *Journal of Hydrology*, vol. 575, pp. 544–556, 2019.

[42] A. Ahmad, S. F. Mohd Razali, A. El-Shafie, and Z. Samba Mohamad, "Optimal timah tasoh reservoir in, perlis: an operation using the Gravitational Search Algorithm (GSA)," *Jurnal Teknologi*, vol. 77, no. 30, 2015.

[43] A. Ahmad, S. F. M. Razali, Z. S. Mohamed, and A. El-shafie, "The application of artificial bee colony and gravitational search algorithm in reservoir optimization," *Water Resources Management*, vol. 30, no. 7, pp. 2497–2516, 2016.

[44] M. F. Allawi, O. Jaafar, F. Mohamad Hamzah, S. M. S. Abdullah, and A. El-shafie, "Review on applications of artificial intelligence methods for dam and reservoir-hydro-environment models," *Environmental Science and Pollution Research*, vol. 25, no. 14, pp. 13446–13469, 2018.

[45] A. M. Muad, S. K. M. Zaki, and S. A. Jasim, "Optimizing hopfield neural network for super-resolution mapping," *Jurnal Kejuruteraan*, vol. 32, no. 1, pp. 91–97, 2020.

[46] A. Koppa and M. Gebremichael, "A framework for validation of remotely sensed precipitation and evapotranspiration based on the Budyko hypothesis," *Water Resources Research*, vol. 53, no. 10, pp. 8487–8499, 2017.

[47] Y. Feng, N. Cui, D. Gong, Q. Zhang, and L. Zhao, "Evaluation of random forests and generalized regression neural networks for daily reference evapotranspiration modelling," *Agricultural Water Management*, vol. 193, pp. 163–173, 2017.

[48] M. Kumar, N. S. Raghuwanshi, R. Singh, W. W. Wallender, and W. O. Pruitt, "Estimating evapotranspiration using artificial neural network," *Journal of Irrigation and Drainage Engineering*, vol. 128, no. 4, pp. 224–233, 2002.

[49] G. Landeras, A. Ortiz-Barredo, and J. J. López, "Comparison of artificial neural network models and empirical and semi-empirical equations for daily reference evapotranspiration estimation in the Basque Country (Northern Spain)," *Agricultural Water Management*, vol. 95, no. 5, pp. 553–565, 2008.

[50] Ö. KiŞI, "Generalized regression neural networks for evapotranspiration modelling," *Hydrological Sciences Journal*, vol. 51, no. 6, pp. 1092–1105, 2006.

[51] S. Traore, Y.-M. Wang, and T. Kerh, "Artificial neural network for modeling reference evapotranspiration complex process in Sudano-Sahelian zone," *Agricultural Water Management*, vol. 97, no. 5, pp. 707–714, 2010.

[52] N. Abrishami, A. R. Sepaskhah, and M. H. Shahrokhnia, "Estimating wheat and maize daily evapotranspiration using artificial neural network," *Theoretical and Applied Climatology*, vol. 135, no. 3, pp. 945–958, 2019.

[53] H. Tabari, O. Kisi, A. Ezani, and P. Hosseinzadeh Talaee, "SVM, ANFIS, regression and climate based models for reference evapotranspiration modeling using limited climatic data in a semi-arid highland environment," *Journal of Hydrology*, vol. 444-445, pp. 78–89, 2012.

[54] M. F. Allawi and A. El-Shafie, "Utilizing RBF-NN and ANFIS methods for multi-lead ahead prediction model of evaporation from reservoir," *Water Resources Management*, vol. 30, no. 13, pp. 4773–4788, 2016.

[55] S. Gavili, H. Sanikhani, O. Kisi, and M. H. Mahmoudi, "Evaluation of several soft computing methods in monthly evapotranspiration modelling," *Meteorological Applications*, vol. 25, no. 1, pp. 128–138, 2018.

[56] A. Moghaddamnia, M. Ghafari Gousheh, J. Piri, S. Amin, and D. Han, "Evaporation estimation using artificial neural networks and adaptive neuro-fuzzy inference system techniques," *Advances in Water Resources*, vol. 32, no. 1, pp. 88–97, 2009.

[57] Y. Yao, S. Liang, X. Li et al., "Improving global terrestrial evapotranspiration estimation using support vector machine by integrating three process-based algorithms," *Agricultural and Forest Meteorology*, vol. 242, pp. 55–74, 2017.

[58] Z. Yin, X. Wen, Q. Feng, Z. He, S. Zou, and L. Yang, "Integrating genetic algorithm and support vector machine for modeling daily reference evapotranspiration in a semi-arid mountain area," *Hydrology Research*, vol. 48, no. 5, pp. 1177–1191, 2016.

[59] M. Ehteram, V. P. Singh, A. Ferdowsi et al., "An improved model based on the support vector machine and cuckoo algorithm for simulating reference evapotranspiration," *PLoS One*, vol. 14, no. 5, Article ID e0217499, 2019.

[60] K. Parasuraman, A. Elshorbagy, and S. K. Carey, "Modelling the dynamics of the evapotranspiration process using genetic programming," *Hydrological Sciences Journal*, vol. 52, no. 3, pp. 563–578, 2007.

[61] A. Guven, A. Aytek, M. I. Yuce, and H. Aksoy, "Genetic programming-based empirical model for daily reference evapotranspiration estimation," *Clean-Soil, Air, Water*, vol. 36, no. 10-11, pp. 905–912, 2008.

[62] B. Narapusetty, "The role of atmospheric internal variability on the prediction skill of interannual North Pacific sea-surface temperatures," *Theoretical and Applied Climatology*, vol. 133, no. 1, pp. 113–121, 2018.

[63] Ö. Kişi, "Evapotranspiration modeling using a wavelet regression model," *Irrigation Science*, vol. 29, no. 3, pp. 241–252, 2011.

[64] Y. Falamarzi, N. Palizdan, Y. F. Huang, and T. S. Lee, "Estimating evapotranspiration from temperature and wind speed data using artificial and wavelet neural networks (WNNs)," *Agricultural Water Management*, vol. 140, pp. 26–36, 2014.

[65] T. Partal, "Modelling evapotranspiration using discrete wavelet transform and neural networks," *Hydrological Processes*, vol. 23, no. 25, pp. 3545–3555, 2009.

[66] O. Kisi and M. Alizamir, "Modelling reference evapotranspiration using a new wavelet conjunction heuristic method: wavelet extreme learning machine vs wavelet neural networks," *Agricultural and Forest Meteorology*, vol. 263, pp. 41–48, 2018.

[67] S. Wang, J. Lian, Y. Peng, B. Hu, and H. Chen, "Generalized reference evapotranspiration models with limited climatic data based on random forest and gene expression programming in Guangxi, China," *Agricultural Water Management*, vol. 221, pp. 220–230, 2019.

[68] C. Gonzalo-Martín, M. Lillo-Saavedra, A. Garcia-Pedrero, O. Lagos, and E. Menasalvas, "Daily evapotranspiration mapping using regression random forest models," *IEEE Journal of Selected Topics in Applied Earth Observations and Remote Sensing*, vol. 10, no. 12, pp. 5359–5368, 2017.

[69] B. Zhu, Y. Feng, D. Gong, S. Jiang, L. Zhao, and N. Cui, "Hybrid particle swarm optimization with extreme learning machine for daily reference evapotranspiration prediction from limited climatic data," *Computers and Electronics in Agriculture*, vol. 173, Article ID 105430, 2020.

[70] S. S. Abdullah, M. A. Malek, N. S. Abdullah, O. Kisi, and K. S. Yap, "Extreme Learning Machines: a new approach for prediction of reference evapotranspiration," *Journal of Hydrology*, vol. 527, pp. 184–195, 2015.

[71] M. K. AlOmar, M. M. Hameed, N. Al-Ansari, and M. A. AlSaadi, "Data-driven model for the prediction of total dissolved gas: robust artificial intelligence approach," *Advances in Civil Engineering*, vol. 2020, Article ID 6618842, 2020.

[72] J. Fan, W. Yue, L. Wu et al., "Evaluation of SVM, ELM and four tree-based ensemble models for predicting daily reference evapotranspiration using limited meteorological data in different climates of China," *Agricultural and Forest Meteorology*, vol. 263, pp. 225–241, 2018.

[73] M. Gocic, D. Petković, S. Shamshirband, and A. Kamsin, "Comparative analysis of reference evapotranspiration equations modelling by extreme learning machine," *Computers and Electronics in Agriculture*, vol. 127, pp. 56–63, 2016.

[74] D. Kumar, J. Adamowski, R. Suresh, and B. Ozga-Zielinski, "Estimating evapotranspiration using an extreme learning machine model: case study in north Bihar, India," *Journal of Irrigation and Drainage Engineering*, vol. 142, no. 9, Article ID 04016032, 2016.

[75] R. G. Allen, L. S. Pereira, D. Raes, and M. Smith, *Crop evapotranspiration-Guidelines for Computing Crop Water Requirements-FAO Irrigation and Drainage Paper 56*, FAO, vol. 300, no. 9, p. D05109, Rome, Italy, 1998.

[76] L. Breiman, "Random forests," *Machine Learning*, vol. 45, no. 1, pp. 5–32, 2001.

[77] T. Hastie, R. Tibshirani, and J. Friedman, "Random forests," in *The Elements of Statistical Learning: Data Mining, Inference, and Prediction*, pp. 587–604, Springer New York, New York, NY, USA, 2009.

[78] L. Breiman, *Machine Learning*, vol. 45, no. 1, pp. 5–32, 2001.

[79] T. Hai, A. Sharafati, A. Mohammed et al., "Global solar radiation estimation and climatic variability analysis using extreme learning machine based predictive model," *IEEE Access*, vol. 8, pp. 12026–12042, 2020.

[80] N. Nan-Ying Liang, fnm Guang-Bin Huang, P. Saratchandran, and N. Sundararajan, "A fast and accurate online sequential learning algorithm for feedforward networks," *IEEE Transactions on Neural Networks*, vol. 17, no. 6, pp. 1411–1423, 2006.

[81] Z. M. Yaseen, S. M. Awadh, A. Sharafati, and S. Shahid, "Complementary data-intelligence model for river flow simulation," *Journal of Hydrology*, vol. 567, pp. 180–190, 2018.

[82] M. M. Hameed and M. K. AlOmar, *Prediction of Compressive Strength of High-Performance Concrete: Hybrid Artificial Intelligence Technique*, Springer International Publishing, Cham, Switzerland, 2020.

[83] A. Ashrafzadeh, M. A. Ghorbani, S. M. Biazar, and Z. M. Yaseen, "Evaporation process modelling over northern Iran: application of an integrative data-intelligence model with the krill herd optimization algorithm," *Hydrological Sciences Journal*, vol. 64, no. 15, pp. 1843–1856, 2019.

[84] T. M. T. Tiyasha, T. M. Tung, and Z. M. Yaseen, "A survey on river water quality modelling using artificial intelligence models: 2000-2020," *Journal of Hydrology*, vol. 585, p. 124670, 2020.

[85] G. Zhang, Z. Hasan Ali, M. S. Aldlemy et al., "Reinforced concrete deep beam shear strength capacity modelling using an integrative bio-inspired algorithm with an artificial intelligence model," *Engineering with Computers*, 2020.

[86] K. Onyelowe, G. U. Alaneme, M. Onyia et al., "Comparative modeling of strength properties of hydrated-lime activated rice-husk-ash (HARHA) modified soft soil for pavement construction purposes by artificial neural network (ANN) and fuzzy logic (FL)," *Jurnal Kejuruteraan*, vol. 33, no. 2, pp. 365–384, 2021.

[87] Z. M. Yaseen, A. El-Shafie, H. A. Afan, M. Hameed, W. H. M. W. Mohtar, and A. Hussain, "RBFNN versus FFNN for daily river flow forecasting at Johor River, Malaysia," *Neural Computing & Applications*, vol. 27, no. 6, pp. 1533–1542, 2016.

[88] M. M. Hameed, M. K. AlOmar, W. J. Baniya, and M. A. AlSaadi, "Prediction of high-strength concrete: high-order response surface methodology modeling approach," *Engineering with Computers*, 2021.

[89] M.-F. Li, X.-P. Tang, W. Wu, and H.-B. Liu, "General models for estimating daily global solar radiation for different solar radiation zones in mainland China," *Energy Conversion and Management*, vol. 70, pp. 139–148, 2013.

[90] M. K. AlOmar, M. M. Hameed, and M. A. AlSaadi, "Multi hours ahead prediction of surface ozone gas concentration: robust artificial intelligence approach," *Atmospheric Pollution Research*, 2020.

[91] O. Behar, A. Khellaf, and K. Mohammedi, "Comparison of solar radiation models and their validation under Algerian climate—the case of direct irradiance," *Energy Conversion and Management*, vol. 98, pp. 236–251, 2015.

[92] H. A. Afan, A. El-Shafie, Z. M. Yaseen, M. M. Hameed, W. H. M. Wan Mohtar, and A. Hussain, "ANN based sediment prediction model utilizing different input scenarios," *Water Resources Management*, vol. 29, no. 4, pp. 1231–1245, 2015.

[93] M. M. Hameed, S. Sharqi, Z. M. Yaseen, and H. A. Afan, "Application of artificial intelligence (AI) techniques in water quality index prediction: a case study in tropical region, Malaysia," *Neural Computing & Applications*, vol. 28, no. 1, pp. 893–905, 2017.

[94] A. Rahimi Khoob, "Artificial neural network estimation of reference evapotranspiration from pan evaporation in a semi-arid environment," *Irrigation Science*, vol. 27, no. 1, pp. 35–39, 2008.

[95] S. K. Jain, P. C. Nayak, and K. P. Sudheer, "Models for estimating evapotranspiration using artificial neural networks, and their physical interpretation," *Hydrological Processes*, vol. 22, no. 13, pp. 2225–2234, 2008.

[96] L. Wu and J. Fan, "Comparison of neuron-based, kernel-based, tree-based and curve-based machine learning models for predicting daily reference evapotranspiration," *PLoS One*, vol. 14, no. 5, Article ID e0217520, 2019.

[97] Z. Izadifar and A. Elshorbagy, "Prediction of hourly actual evapotranspiration using neural networks, genetic programming, and statistical models," *Hydrological Processes*, vol. 24, no. 23, pp. 3413–3425, 2010.

[98] H. A. Afan, M. F. Allawi, A. El-Shafie et al., "Input attributes optimization using the feasibility of genetic nature inspired algorithm: application of river flow forecasting," *Scientific Reports*, vol. 10, no. 1, p. 4684, 2020.

[99] S. J. Hadi, S. I. Abba, S. S. Sammen, S. Q. Salih, N. Al-Ansari, and Z. M. Yaseen, "Non-linear input variable selection approach integrated with non-tuned data intelligence model for streamflow pattern simulation," *IEEE Access*, vol. 7, pp. 141533–141548, 2019.

Hindawi
Complexity
Volume 2021, Article ID 6683759, 12 pages
https://doi.org/10.1155/2021/6683759

Research Article

Forecasting Daily and Monthly Reference Evapotranspiration in the Aidoghmoush Basin Using Multilayer Perceptron Coupled with Water Wave Optimization

Fatemeh Sayyahi, Saeed Farzin, and Hojat Karami

Department of Water Engineering and Hydraulic Structures, Faculty of Civil Engineering, Semnan University, Semnan 35131-1911, Iran

Correspondence should be addressed to Saeed Farzin; saeed.farzin@semnan.ac.ir

Received 1 November 2020; Revised 20 January 2021; Accepted 2 August 2021; Published 14 August 2021

Academic Editor: Ning Cai

The aim of this study is to evaluate the ability of soft computing models including multilayer perceptron- (MLP-) water wave optimization (MLP-WWO), MLP-particle swarm optimization (MLP-PSO), and MLP-genetic algorithm (MLP-GA), to simulate the daily and monthly reference evapotranspiration (ET) at the Aidoghmoush basin (Iran). Principal component analysis (PCA) was used to find the best input combination including the lagged ETs. According to the results, the ET values with 1, 2, and 3 (days) lags as well as those with 1, 2, and 3 (months) lags were the most effective variables in the formation of the PCs. The total variance proportion of inputs and eigenvalues was used to identify the most important variables. The accuracy of the models was assessed based on multiple statistical indices such as the mean absolute error (MAE), Nash–Sutcliff efficiency (NSE), and percent bias (PBIAS). The results showed that the performance of hybrid MLP models was better than that of the standalone MLP. The findings confirmed that the MLP-WWO could precisely predict ET.

1. Introduction

Soft computing models are widely used to solve various problems in water resource management, such as reservoir operation [1, 2], flood routing [3], irrigation management [4], and drug removal modeling [5]. Reference evapotranspiration (ET) is a key parameter for hydrology [6]. The major significance of ET in estimating the water budget has been well proved. The precise estimation of ET is highly important in managing water resources. In fact, it is essential to predict ET with an acceptable level of precision in managing watersheds [7], which can help decision-makers use accurate predictions to ensure the best allocation of water resources among the stakeholders [8]. For example, models used for predicting ET in relatively humid areas may not be suitable for dry basins where the water shortage is a significant challenge [9].

However, ET is measured only at a very limited number of meteorological stations due to the high cost of the necessary equipment. The FAO-56 Penman–Monteith equation, which is widely used as a reference model for ET computation [10], requires a multitude of hydrological data, which is considered as one of its serious drawbacks. However, many hydrological modelers do not have access to accurate measurement devices to record information regularly [11]. Several empirical methods have been proposed to compute ET based on meteorological variables. The radiation-based and temperature-based ET models are widely used due to the restriction in the availability of meteorological data. A large number of studies have shown that the ET temperature-oriented models cannot achieve a high level of accuracy.

A growing body of research has examined the ability of the soft computing models in estimating ET. These computing models usually use nonlinear inputs to predict ET,

while old data-driven ET predictions mostly use statistical methods such as linear regression and autoregressive integrated moving average models [12] and are restricted by the hypothesis that the inputs are linear. Nonlinear models have received growing attention in the management of water resources using soft computing techniques, such as artificial neural network (ANN) and adaptive neuro-fuzzy interface system (ANFIS).

Shiri et al. [13] compared the performance of gene express programming (GEP) and FAO-56 Penman–Monteith (PM) in Spain. Their results indicated that the GEP model outperformed other models in most cases. In another study, Tabari et al. [14] applied ANFIS and support vector machine (SVM) to calculate potato crop evapotranspiration and found that the ANFIS had a better performance than the SVM model. In addition, Luo et al. [15] applied ANN and PM models to predict the ET and reported the superior performance of ANN in comparison to the PM model. Furthermore, Patil and Chandra Deka [16] examined the ability of the extreme learning machine (ELM) and ANN model in India and found that the ELM model provided better results.

Patil and Chandra Deka [17] applied ANFIS, wavelet ANFIS, and wavelet ANN to predict ET. Their results showed that the ANFIS-wavelet model outperformed other models. Seifi and Riahi [18] investigated the effectiveness of least square support vector machine (LSSVM), ANFIS, and ANN models in predicting ET using meteorological data. The results indicated that LSSVM model provided a more desirable prediction compared to the other models.

In this study, the MLP model was used to predict monthly and daily ET. Although the SVM models can predict hydrological variables, they have some inherent drawbacks [18]. For example, the SVM models cannot accurately estimate the target variables when the number of features is more than the number of the samples, and the input data have more noise [18]. Therefore, choosing a kernel function is not easy for the modelers. The MLP models are widely used to predict hydrological variables because they can handle multivariate inputs and have multistep forecasts. However, the MLP models have some important drawbacks [19]. The training soft computing models are a real challenge for users. The traditional training algorithms such as the backpropagation algorithm of soft computing models may trap in the local optimum. Optimization algorithms are considered as suitable alternatives for traditional training algorithms due to their advanced operators, which avoid trapping in local optimums. The optimization algorithms are widely used for training soft computing models [19–26]. The genetic algorithm (GA) and particle swarm optimizations (PSO) are powerful optimization algorithms. The positions of particles are considered as the candidate solutions. This study combines the WWO and MLP models to increase the convergence speed and accuracy. In addition, the WWO avoids trapping in local optimums by refraction operator, which increases the population diversity. Therefore, the use of this strategy avoids falling into the local optimums.

Water wave optimization (WWO), as an innovative optimization algorithm, has been recently used in various research fields such as the optimal reactive power dispatch, benchmark functions, and traveling salesman problem [27–29]. Previous research has shown that the WWO could increase the convergence speed and computation accuracy compared to PSO, GA, and other algorithms. WWO has several advantages such as a good balance between exploration and exploitation. Furthermore, it uses different operators such as refraction, propagation, and breaking operators to increase population diversity. Furthermore, the advanced operators of the WWO can reduce premature convergence. The main motivation of this paper is to develop the new hybrid MLP models for predicting ET. In addition, the new hybrid models can be used for predicting target variables in other fields. Although the different studies use different metrological data for predicting ET, this study uses the lagged ET values for predicting ET. Thus, this study is useful when the scholars do not have different climate input data for predicting ET.

In this paper, a new optimization algorithm aiming to combine within the MLP model was developed to predict monthly ET. To this end, meteorological data were collected from Aidoghmoush station in Iran. To the best of our knowledge, scanty research has examined the potential of the combination of MLP model and WWO algorithm to predict daily and monthly ET. Regarding the performance of the combined MLP-WWO, the outputs of the combined MLP-WWO are compared with the standalone MLP model, MLP-genetic algorithm (MLP-GA), and MLP-particle swarm optimization (MLP-PSO).

2. Materials and Methods

2.1. MLP Model. MLPs include a set of neurons placed in layers. Activation functions are used in each node to transform the weighted inputs to an output characteristic of the mathematical properties of the activation function. The MLP in this study was trained using the back propagation algorithm (BPA) [30]. This network includes input, hidden, and output layers. The input data are received in the first layer. Then, the information is processed in the hidden layer. Finally, the model prediction is produced by the output layer. The applied MLP model is based on the following levels:

(1) The input-out data were accidentally selected by employing the given training input data. Models with different sizes, which had the highest accuracy, were tested for training and testing levels, among which 70 and 30 of the data were selected for training and testing levels, respectively.

(2) The outputs were generated for some input patterns after being applied to the transfer function.

(3) An objective function such as root mean square error (RMSE) was selected.

(4) The connection weight was updated to obtain the lowest RMSE value.

(5) For the testing and training levels, each pair consisting of the input-output vectors was continued through levels to the extent in which there was no considerable change in the RMSE in the model (Figure 1).

2.2. Genetic Algorithm. GA is an evolutionary algorithm which finds the optimal solutions for a problem based on Darwin's principle via mutation, crossover, and selection operators. To this end, several initial solutions are generated and their corresponding objective function values are computed. The selection operation is used to choose the old population parents. Next, the new individuals are generated by the crossover operator [31]. Finally, the mutation operator is used to maintain the diversity between the current and the next generations. The algorithm ends when the stopping criteria are satisfied (Figure 2).

2.3. PSO Algorithm. PSO is widely used for different optimization problems. Similar to other optimization algorithms, this algorithm begins with a randomly initialized population of members and uses the social behaviors of the particles to obtain the best solution by setting the position of each member concerning the best position of the particle in the swarm population. Equations (1) and (2) are used to update the velocity and position of the particles [32]:

$$V_i(t+1) = V_i(t) + c_1 \cdot \text{rand} \cdot \left(l\text{best}_i - X_i\right) + c_2 \cdot \text{rand} \cdot \left(g_{\text{best}_i} - X_i\right), \tag{1}$$

$$X_i(t+1) = X_i(t) + V_i(t+1), \tag{2}$$

where $X_i(t+1)$ is the position of the iterating particle $(t+1)$, $V_i(t+1)$ denotes the velocity of the iterating particle $(t+1)$, c_1 and c_2 represent the constant value ranges 0–2, g_{best_i} shows the global best particle, l_{best_i} is local best particle, and rand denotes the random number, which is between 0 and 1. Figure 3 shows the optimization process of PSO.

2.4. WWO Algorithm. The WWO algorithm aims to enhance the exploration and exploitation of the abilities of the optimization algorithms based on propagation, refraction, and braking operators. The WWO mimics the shallow water wave theory. Every agent in the algorithm has some resemblance to the "water wave" entity with a wavelength (WL) of λ and a wave height of h. As shown in Figure 4, the objective function value of the water wave is considerably lower, its h is lower, and WL is shorter than in deep water origins [29].

2.4.1. Propagation. It is hypothesized that x represents the original water wave, and x' denotes a new one generated by the propagation operator (weights and biases of the MLP) [33].

$$x'(d) = x(d) + \text{rand}(-1,1) \cdot \lambda L(d), \tag{3}$$

where $L(d)$ is the length of the search space, $\text{rand}(-1,1)$ shows a uniformly distributed random number, $x(d)$ represents the original water wave, and $x'(d)$ denotes the new water wave. After propagating, the objective function value of x' is evaluated. Without losing generality, F is assumed as a minimization problem with fitness functions of f and F. The practical problem can be compared with the shallow water model (Figure 5).

If $f(x') < f(x)$, x' is used instead of x in the population. Then, the wave height is adjusted to maxim height ($h_{\max}$). On the contrary, the wave x is fixed, and the wave height is reduced by one to show the loss of energy. Therefore, the following equation could be used to update the wavelength [33]:

$$\lambda = \lambda.\alpha^{-\left(f(x) - f_{\min} + \varepsilon / f_{\max} - f_{\min} + \varepsilon\right)}, \tag{4}$$

where α is the wavelength reduction, $f_{\max}$ shows the maximum objective function value, $f_{\min}$ represents the minimum objective function value, and ε denotes the positive integer.

2.4.2. Refraction. In the optimization process, the refraction operation can only be conducted on the wave x, which approaches 0 in its height to prevent search stagnation. The position update is given as follows [33]:

$$x'(d) = N\left(\frac{x_d^* + x_d}{2}, \frac{\left|x^*(d) - x(d)\right|}{2}\right), \tag{5}$$

where x_d^* is the optimal solution and $N(\sigma, \mu)$ shows a Gaussian random number with the mean (μ) of 0 and standard deviation of 1 (σ). The N allows the wave x_d to learn from the best solution x_d^*.

2.4.3. Breaking. The utility of the breaking operator is to make the population diverse. K dimensions are randomly chosen, and each dimension is selected for providing each dimension of solitary wave x' [29]:

$$x'(d) = x(d) + N(0,1) \cdot \beta L(d), \tag{6}$$

where β is the breaking coefficient. If the objective function value of wave x^* is much better than the provided solitary waves, the x^* wave is kept. Figure 6 shows the optimization levels for WWO.

2.5. Optimization Algorithms for Training MLPs. It is necessary to consider two technical aspects in order to integrate the optimization algorithms with MLP, namely, the method for encoding the agents/solutions and the procedure for determining the objective function. Although the standalone MLP models have high ability, their training algorithms may have slow convergence or may trap in local optimums [21–34]. Therefore, it is essential to improve the accuracy of the MLP models. These models were trained for 1000 epochs in this study. The learning rate and momentum coefficient were 0.001 and 0.09, respectively.

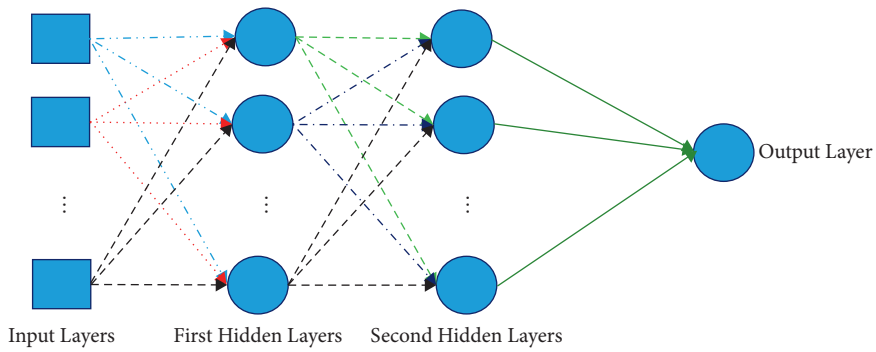

Figure 1: The schematic structure of the MLP model.

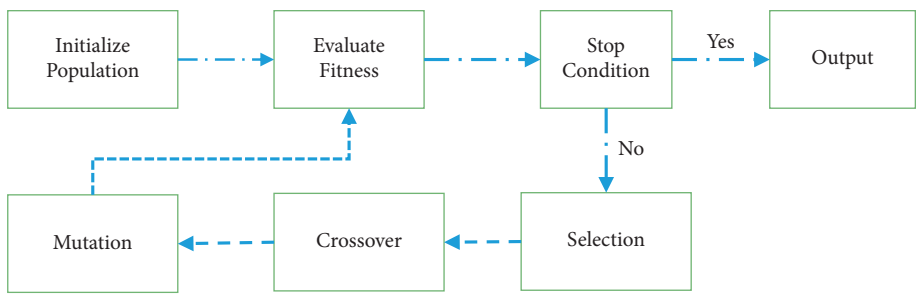

Figure 2: GA flowchart.

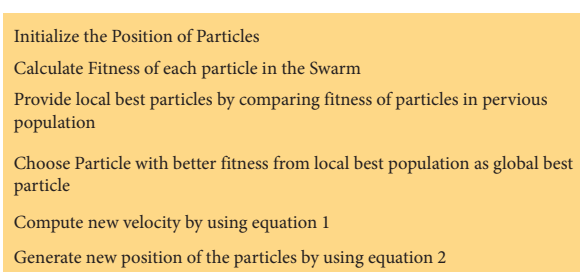

Figure 3: The optimization process of PSO.

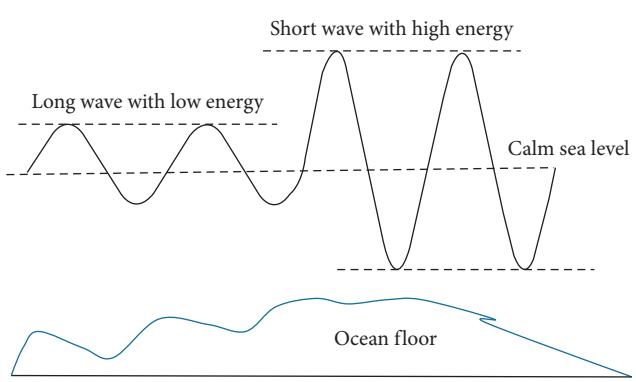

Figure 4: The details of WWO.

In evolutionary algorithms-MLP models, every dimensional vector can refer to an agent (e.g., particles (PSO), chromosomes (GA), and 'wave water' objects (WWO)), which may include random numbers in [−1, 1]. Each agent indicates a candidate MLP (Figure 7). The encoded agents contain sets of bias values and connection weights. The number of weights and biases determines the length of the vector. To compute the objective function values of the agents, all agents should be transferred to the MLP so that they could be labeled as the connection weights. RMSE is typically the applied objective function in MLP-optimization algorithms. The level of the hybrid model trainer can be explained in the following levels:

(1) The optimization algorithm-MLP model initiates the random agents
(2) The agents are mapped to some biases and weight values of a candidate MLP
(3) The quality of the MLPs is evaluated according to the RMSE
(4) The optimization algorithm-MLP model constructs the fittest MLP with the minimum RMSE
(5) The agents are updated
(6) Steps 2 to 4 are continued until the last iteration (Figure 7)

2.6. Dataset. Figure 8 shows the data obtained from the meteorological station located in the Aidoghmoush basin of Iran (37°16′ to 37°31′N; 47°33′ to 47°49′E) during 1987 to 2000.

The average discharge and the average annual rainfall are $190 * 10^6\,m^3$ per year and 340 mm, respectively. The rainy period of the year is from October to May, and August is the driest month. In addition, the peak probability for rainfall is in April, while the rainless period of the year is from June to

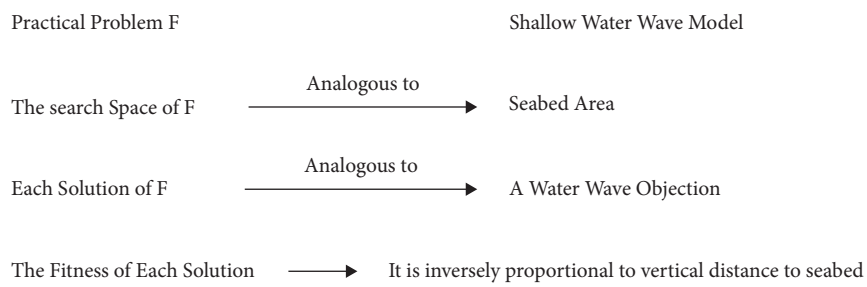

Figure 5: The detail of WWO for a practical problem.

1- Initialize random parameters and a population p of NP waves
2- While stop criterion is not satisfied do
3- For each x ∈ P do
4- Propagate x to new x′ based on equation 3
5- If (x′) < f (x*) then
6- Break x based on equation 6
7- Update x* with x′
8- End if
9- Replace with x′
10- Else
11- Decrease x.h by one
12- If x.h = 0 then
13- Refract x to a new x′ based on equation 5
14- End if
15- End if
16- Update the wavelength based on equation 4
17- End for
18- End while

Figure 6: The optimization levels for WWO.

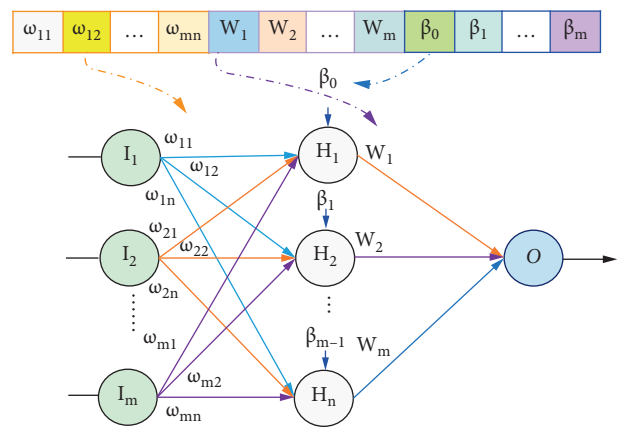

Figure 7: Solution structure in MLP-optimization model [35].

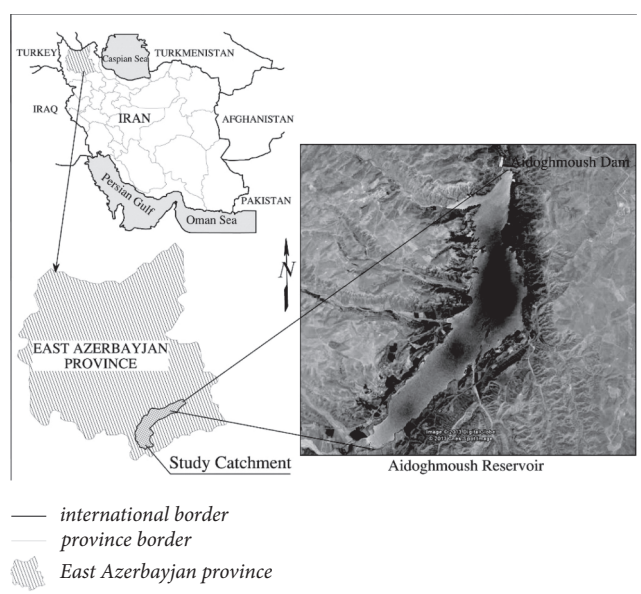

Figure 8: Location of the case study [36].

October. The brighter and darker periods are from May to August and October to February, respectively [37].

The MLP, MLP-WWO, MLP-PSO, and MLP-GA were used to forecast the daily and monthly ET. Table 1 shows the tabulation of the statistical characteristics of the input data in this study. The lagged ET values were used to estimate one month or day ahead prediction of ET. The lagged ET values were used because it aimed to evaluate the ability of the models based on the limited input data. In fact, since there was no access to the climate data, the accurate forecasting ET was an important issue.

The data were divided into 70% training and 30% testing. The lagged ET values were used as the input to soft computing models. Different sizes of data were tested, and 70 and 30 achieved the least value of the objective function. Before developing the model, principal component analysis (PCA) was performed on monthly and daily ET values to select the significant lags, that is, the lagged inputs mostly affect daily and monthly ET values. The variables lagged up to 7 days and 7 months were used as the inputs for the soft computing models to predict daily and monthly ET. PCA is a statistical model to transform a given set of n variables into a new set of PCs which are orthogonal to each other. The PCA was used to choose the best-lagged input variable to predict hydrological variables [37–39]. Previous studies indicated the superiority of PCA in comparison to other methods such as gamma test and correlation method [37–39]. The principals with eigenvalues, which are more than one, are considered as significant inputs. In addition, the most effective variables in PCs have a coefficient of ≥0.90. Thus, the principals and their variables are selected based on the aforementioned rules [37–39].

Table 1: Statistical characteristics for ET: monthly and daily values.

	ET	Maximum (mm)	Minimum (mm)	Coefficient of variation (mm)	Average (mm)
Monthly values	January	18	10	0.23	14
	February	17	12	0.20	15
	March	52	34	0.45	39
	April	89	45	0.56	52
	May	112	90	0.91	104
	June	224	209	1.01	212
	July	232	223	1.04	228
	August	145	138	0.98	142
	September	132	112	1.01	129
	October	98	91	0.65	95
	November	89	82	0.55	85
	December	67	54	0.72	59
Daily values			Train		
	Value	24	12	0.32	18
			Test		
	Value	21	14	0.45	19

Preparing the input data, computing the covariance matrix, along with the eigenvalues and vectors, as well as calculating the proportion of total variance for each PC are considered as the main levels of PCA model. The following indexes are used to assess the models.

$$\text{PBIAS} = \frac{\sum_{i=1}^{N}\left(Y_i^{\text{obs}} - Y_i^{\text{sim}}\right)}{\sum_{i=1}^{1} Y_i^{\text{obs}}}, \tag{7}$$

$$\text{NSE} = 1 - \left[\frac{\sum_{i=1}^{n}\left(Y_i^{\text{obs}} - Y_i^{\text{sim}}\right)}{\sum_{i=1}^{n}\left(Y_i^{\text{obs}} - Y^{\text{mean}}\right)^2}\right], \tag{8}$$

$$\text{MAE} = \frac{1}{n}\sum_{i=1}^{n}\left|\left(Y_i^{\text{obs}} - Y_i^{\text{sim}}\right)\right|, \tag{9}$$

where MAE is the mean absolute error, NSE shows Nash–Sutcliff efficiency, Y_i^{obs} indicates the observed data, Y^{mean} represents the average of the observed data, and Y_i^{sim} denotes the forecasted data.

3. Results and Discussion

3.1. Selection of the Inputs

3.1.1. Daily Scale. Table 2 shows the outputs of the PCA including the contribution of seven inputs to seven PCs, the described variance of each PC, and the cumulative sum of the described variance. As shown, the PC1 and the first three PCs contributed to 54% and 91% of the total variance, respectively. The results indicated that the ET values with lags 1, 2, and 3 (days) were significant and used as the inputs.

3.1.2. Monthly Scale. Based on the results, the PC1 and the first three PCS contributed to 53% and 94% of the total variance, respectively. In addition, the ET values with lags 1, 2, and 3 (month) were significant and used as the inputs to the soft computing models (Table 2).

3.2. Results of the Data Analyses for Soft Computing Models

3.2.1. Daily Scale. The random parameters of optimization algorithms are considered as influential coefficients which significantly affect the performance of the algorithms. For example, the random parameters of WWO are the population size, wavelength, wave height, and breaking coefficients. Table 3 shows other important variables. Each MLP-optimization algorithm model was tested by different values of the random parameters. A sensitivity analysis was used to find the optimal value of the parameters. The variation of the objective function was computed versus the variation of interest of parameter. When a value of the interest of parameters varies, the other parameters are fixed. The best values of the parameters minimize the objective function.

The objective function was used to compute the error of performance at the end of each iteration. Each model was run within 2000 iterations to optimize the MLP parameters. Therefore, a series MLP-optimization algorithms was conducted using various population sizes (PS), wave lengths (WL), wave heights (WH), and breaking coefficients (BC) ranging from 100 to 400, 0.1 to 1, 1 to 5, and 0.01 to 0.10, respectively. The obtained results showed that the PS: 200, WL: 0.5, WH: 2, and BC: 0.05 provided the lowest RMSE. Therefore, these values were selected as the optimum parameters in the MLP-WWO model. Regarding a similar process, the optimal parameters of the other algorithms were obtained.

Table 4 demonstrates the outputs related to the training level of the MLP models. The results shown in Tables 4 and 5 are based on the best value of random parameters obtained in Table 3.

Based on Table 4, the hybrid MLP has better and more acceptable results for modeling. In addition, the MAE of the MLP-WWO was 2.1%, 3.2%, and 4.1% lower than those of the MLP-PSO, MLP-GA, and MLP models. The PBIAS of the MLP-WWO was 0.14, while it was 0.35, 0.37, and 0.39 for the MLP-PSO, MLP-GA, and MLP models. The MLP-WWO has the highest NSE and the lowest PBIAS among other

Table 2: The daily scale of outputs in the PCA.

	Input	PC (1)	PC (2)	PC (3)	PC (1)	PC (5)	PC (6)	PC (7)
Daily scale	$E\ (d-1)$	0.94	0.93	0.92	0.62	0.55	0.43	0.42
	$E\ (d-2)$	0.90	0.92	0.91	0.59	0.54	0.47	0.42
	$E\ (d-3)$	0.89	0.91	0.90	0.55	0.52	0.40	0.39
	$E\ (d-4)$	0.65	0.62	0.69	0.49	0.58	0.47	0.42
	$E\ (d-5)$	0.62	0.45	0.42	0.42	0.45	0.40	0.39
	$E\ (d-6)$	0.54	0.34	0.31	0.29	0.41	0.36	0.35
	$E\ (d-7)$	0.43	0.29	0.27	0.25	0.32	0.30	0.29
	Explained variance %	54	22	17	3	3	0.5	0.5
	Eigen value	3.24	1.32	1.02	0.18	0.18	0.03	0.03
	Cumulative variance %	54	76	91	96	99	100	100
Monthly scale	$E\ (m-1)$	0.95	0.94	0.92	0.76	0.61	0.60	
	$E\ (m-2)$	0.94	0.92	0.91	0.69	0.55	0.52	
	$E\ (m-3)$	0.93	0.92	0.90	0.67	0.44	0.41	
	$E\ (m-4)$	0.85	0.84	0.80	0.65	0.42	0.39	
	$E\ (m-5)$	0.82	0.81	0.79	0.62	0.40	0.34	
	$E\ (m-6)$	0.80	0.79	0.77	0.55	0.38	0.36	
	Explained variance (%)	53	27	17	2	0.5	0.5	
	Eigen vale	3.18	1.62	1.02	0.12	0.03	0.03	
	Cumulative variance %	53	80	94	99	99.5	100	

Table 3: The optimal value of the random parameters.

WWO, population size: 200, wave length: 0.3, wave height: 0.5, and BC: 0.05
PSO, number of particles: 200, c_1: 2, c_2: 2, and w: 0.4
GA, number of chromosomes: 100, mutation probability: 0.01, and crossover probability: 0.3

Table 4: Training level for the statistical results related to soft computing models based on the daily scale.

Index	MAE (mm)	PBIAS	NSE
Training level			
MLP-WWO	3.12	0.14	0.94
MLP-PSO	3.19	0.35	0.91
MLP-GA	3.22	0.37	0.89
MLP	3.25	0.39	0.85
Testing level			
MLP-WWO	5.15	0.17	0.92
MLP-PSO	5.22	0.47	0.90
MLP-GA	5.28	0.49	0.87
MLP	5.32	0.51	0.84

Table 5: The training level for the statistical results related to the soft computing models based on the monthly scale.

Index	MAE (mm)	PBIAS	NSE
Training level			
MLP-WWO	0.49	0.19	0.95
MLP-PSO	0.53	0.32	0.92
MLP-GA	0.57	0.33	0.90
MLP	0.59	0.35	0.88
Testing level			
MLP-WWO	0.51	0.21	0.93
MLP-PSO	0.55	0.34	0.90
MLP-GA	0.58	0.37	0.87
MLP	0.61	0.39	0.85

models. The PBIAS of the MLP model is higher than those of the other models.

Table 4 shows the error indexes for soft computing models based on the daily scale at the testing level. As seen in this table, the MAE of the MLP-WWO is 1.3%, 2.5%, and 3.3% lower than those of the MLP-PSO, MLP-GA, and MLP models. Furthermore, the PBIAS of the MLP-GA is higher than those of the other hybrid models. The NSE of the MLP is 0.84, while it was 0.87, 0.90, and 0.92 for MLP-GA, MLP-PSO, and MLP-WWO models.

3.2.2. Monthly Scale. Based on Table 5, the hybrid MLP has better and more acceptable testing results for modeling. The PBIAS of the MLP-WWO is lower than those of the other hybrid models. The MAE of the MLP-WWO was 7.2%, 14%, and 17% lower than those of the MLP-PSO, MLP-GA, and MLP models. The highest NSE and lowest PBIAS were obtained for the MLP-WWO model.

Table 5 shows the results related to the testing level of the MLP models. As shown, the MAEs of the WWO are 7.2, 12, and 17% lower than those of the MLP-PSO, MLP-GA, and MLP models, respectively. The NSE of the MLP-PSO is higher than that of the MLP-GA and MLP models.

The results indicated that the optimization algorithms improved the accuracy of the standalone MLP model. In other words, the combination of the hybrid MLP model and preprocessing method such as PCA could be used for practical problems with different input scenarios in water resource management. The modelers may encounter with a large number of input data in estimating different hydrological variables. In addition, the standalone soft computing models may not lead to good results only. Thus, it is essential to use a hybrid framework based on preprocessing methods and optimization algorithms to ensure accurate estimations of the target variables.

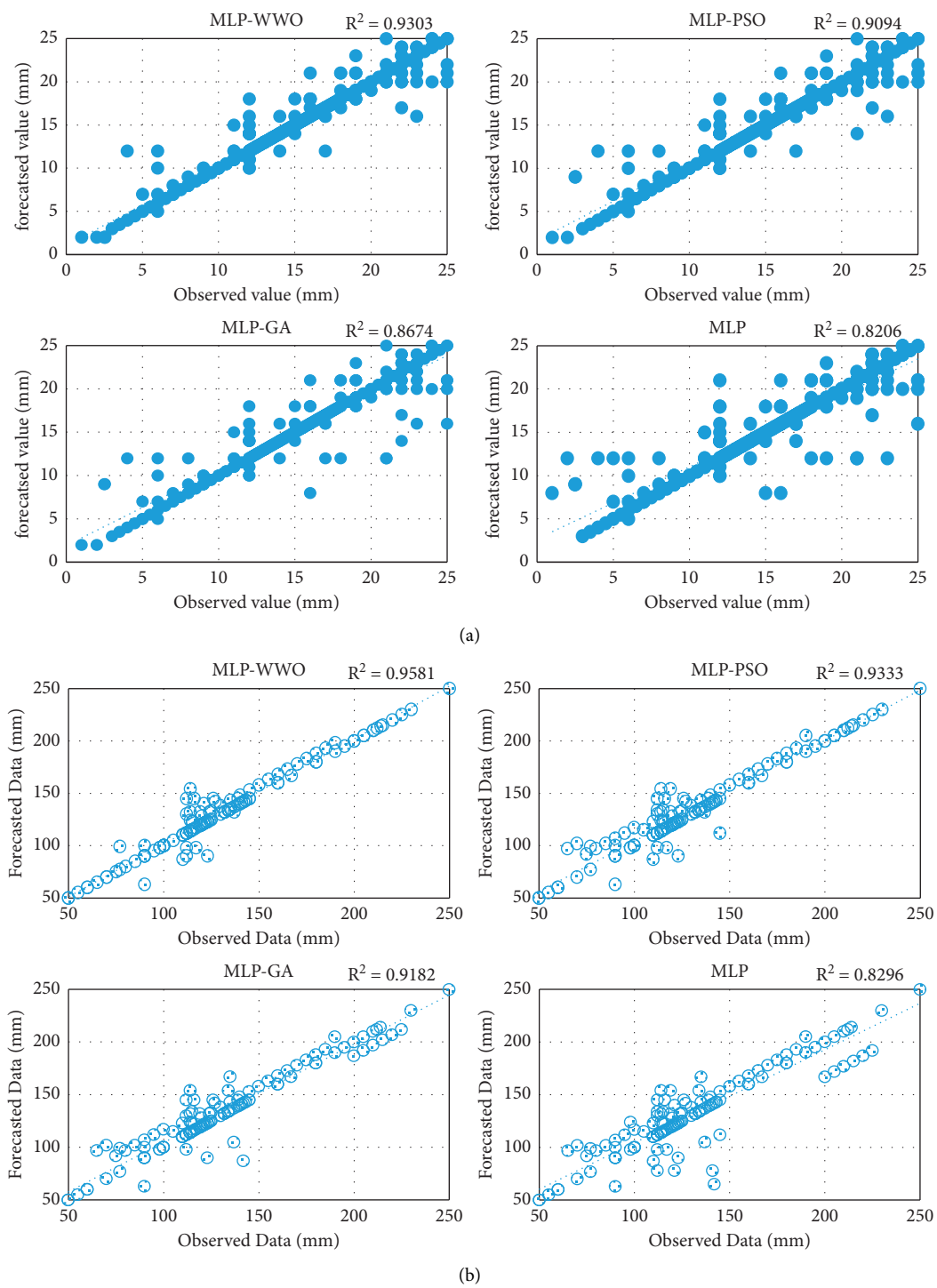

Figure 9: Scatter plots for (a) daily values and (b) monthly values.

Table 6: Classification of hydrological model [40].

Goodness of fit	The accuracy of models
$0.90 \leq \text{NSE} \leq 1$	Very good
$0.80 \leq \text{NSE} \leq 0.90$	Good
$0.65 \leq \text{NSE} \leq 0.80$	Satisfactory
$\text{NSE} \leq 0.65$	Unsatisfactory

3.3. Scatter Plots

3.3.1. Daily Scale. Figure 9 shows the scatter plots for the soft computing models.

The results indicated that the outputs related to the MLP-WWO were closer to the observed data indicating the

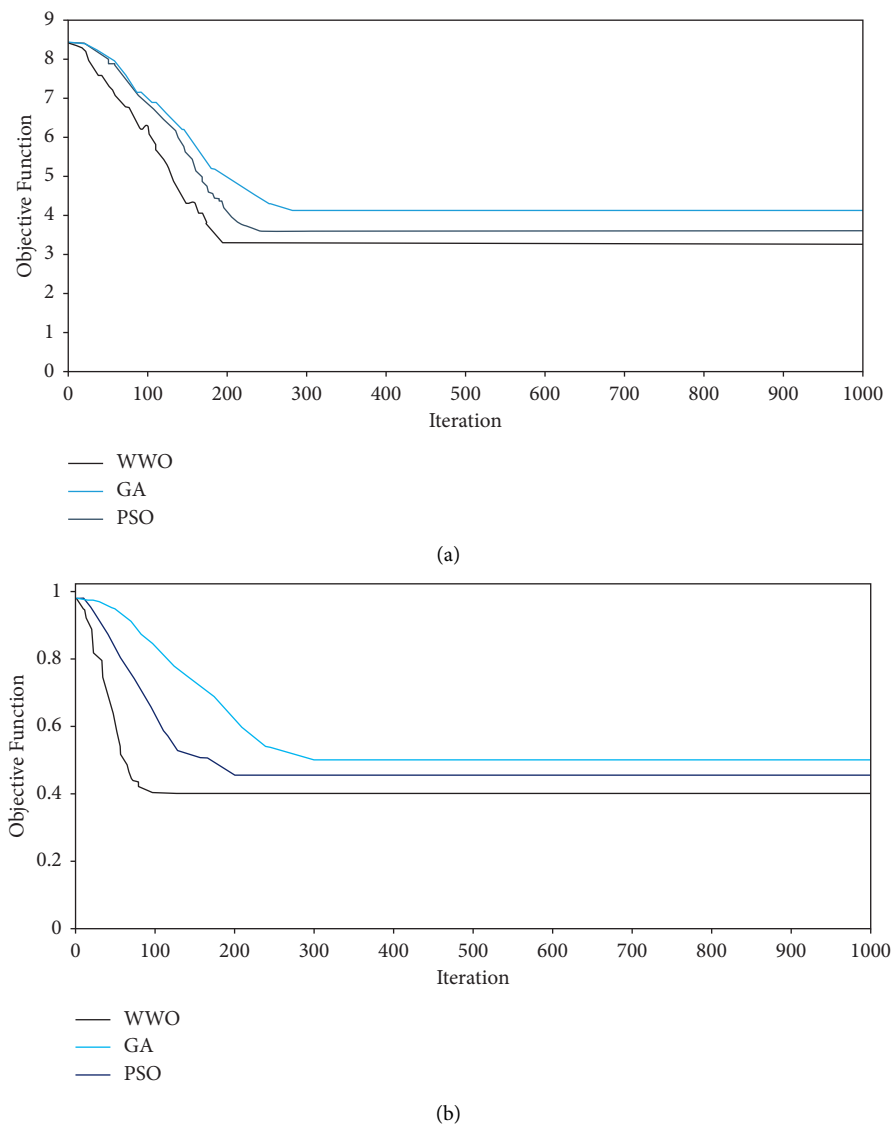

Figure 10: Convergence curve of algorithms for (a) daily scale and (b) monthly scale.

accurate performance of the combined model. Figure 9(a) demonstrates that the MLP model has the worst performance among the MLP models. Furthermore, as displayed in Figure 9(a), the MLP-PSO scatter points are closer to the 45° line in comparison to the MLP-GA scattered points.

3.3.2. Monthly Scale. The computed R^2 for soft computing models indicated that the MLP-WWO had the best performance as compared to the other models, and the PSO outperformed the GA. To sum up, the hybrid MLP models outperformed the standalone MLP model (Figure 9(b)).

3.4. Probability Distribution of NSE. The training data were randomly sampled M times with replacement to build a model and evaluate its NSE for each resample. M trained models were used to compute the NSE based on the validation data. This approach was used to perform the goodness of fit of predicted data and observed data.

The procedure may require high computational time, depending on the number of patterns. After approximating the probability distribution of NSE of the NSE, its significance was evaluated based on the 95% confidence interval (CI) (Table 6). The results were analyzed to predict the daily and monthly ET as follows:

3.4.1. Daily Scenario (NSE). Figure 10(a) displays how the probability that NSE > 0.80 is as high as 93% in the MLP-WWO model. Thus, the MLP-GA model did not achieve 0.90 NSE and decreased to 0.50 to 0.89 (Figure 11(a)). The obtained results for the MLP-PSO show that more than 60% of the CIs are above 0.80 NSE (Figure 11(a)). Based on the results, the MLP-PSO is better than the MLP-GA and MLP-WWO.

3.4.2. Monthly Scenario (NSE). Regarding the MLP-WWO, the results indicated that more than 93% of the CIs are above

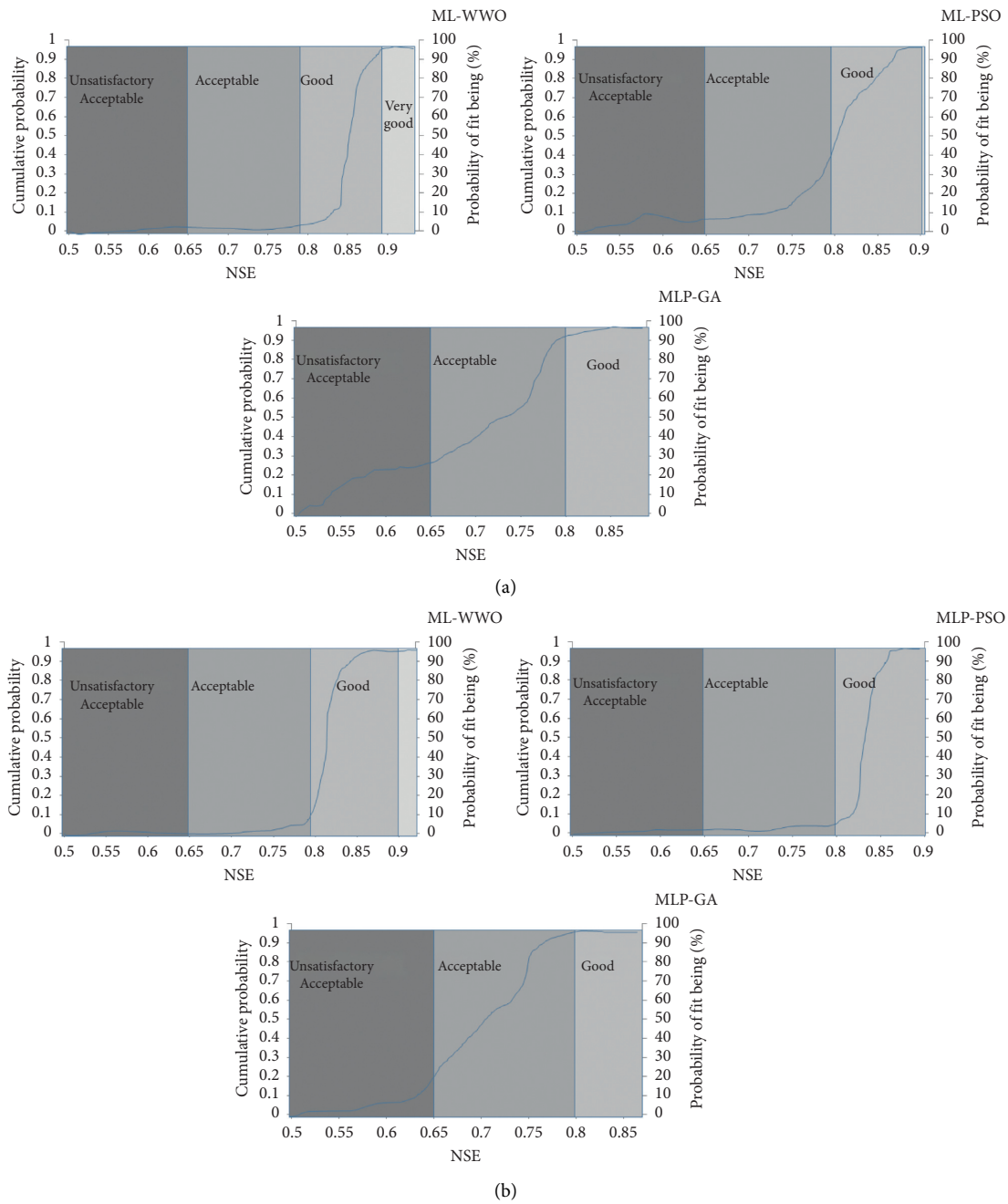

Figure 11: The probability distribution for NSE: (a) daily ET and (b) monthly ET.

0.80 NSE (Figure 11(b)). Therefore, the MLP-GA model failed to reach 0.90 NSE and decreased to 0.5 to 0.87 (Figure 11(b)).

Based on Figure 10 showing the convergence curves, the WWO converted earlier than other methods.

4. Conclusion

In this study, the soft computing models were used as the input for the soft computing models. The forecasting models were generated using the lagged ET values for Aidoghmoush basin (Iran). Then, the outputs of the soft computing models were compared, which indicated that the MLP-WWO outperformed the other MLP models. In addition, the MAE of the MLP-WWO is 1.3%, 2.5%, and 3.3% lower than those of the MLP-PSO, MLP-GA, and MLP models in the daily scale models. The MAE of the MLP-WWO was 7.2%, 14%, and 17% lower than those of the MLP-PSO, MLP-GA, and MLP models in the monthly scale. In addition, the outputs related to the MLP-WWO were closer to the observed data. Finally, it must be stated that the appropriate optimization algorithms affect the accuracy of standalone soft computing models. Thus, the

selection of a robust optimization algorithm is an important issue for developing the soft computing models. Future investigations can develop the performance of the models of this study. The proposed models can be used for predicting other hydrological variables such as rainfall, temperature, and runoff. Furthermore, the next studies can investigate the effect of uncertainty on the accuracy of the models.

Data Availability

The data used to support the findings of this study are available from the corresponding author upon reasonable request.

Conflicts of Interest

The authors certify that they have no affiliations with or involvement in any organization or entity with any financial interest in the subject matter in this article.

References

[1] V. Ramaswamy and F. Saleh, "Ensemble based forecasting and optimization framework to optimize releases from water supply reservoirs for flood control," *Water Resources Management*, vol. 34, pp. 989–1004, 2020.

[2] M. Mohammadi, S. Farzin, S. Farhad Mousavi, and H. Karami, "Investigation of a new hybrid optimization algorithm performance in the optimal operation of multi-reservoir benchmark systems," *Water Resources Management*, vol. 33, pp. 4767–4782, 2019.

[3] A. Pashazadeh and M. Javan, "Comparison of the gene expression programming, artificial neural network (ANN), and equivalent Muskingum inflow models in the flood routing of multiple branched rivers," *Theoretical and Applied Climatology*, vol. 139, no. 3-4, pp. 1349–1362, 2020.

[4] F. Banadkooki, M. Ehteram, A. N. Ahmed et al., "Enhancement of groundwater-level prediction using an integrated machine learning model optimized by whale algorithm," *Natural Resources Research*, vol. 29, pp. 3233–3252, 2020.

[5] S. Farzin, N. C. Farideh, M. V. Anaraki, and F. Mahmoudian, "Introducing a framework for modeling of drug electrochemical removal from wastewater based on data mining algorithms, scatter interpolation method, and multi criteria decision analysis (DID)," *Journal of Cleaner Production*, vol. 266, 2020.

[6] G. M. Kovoor and L. Nandagiri, "Sensitivity analysis of FAO-56 penman–monteith reference evapotranspiration estimates using Monte Carlo simulations," in *Hydrologic Modeling. Water Science and Technology Library*, V. Singh, S. Yadav, and R. Yadava, Eds., Springer, Singapore, 2018.

[7] G. Huang, L. Wu, X. Ma et al., "Evaluation of CatBoost method for prediction of reference evapotranspiration in humid regions," *Journal of Hydrology*, vol. 574, pp. 1029–1041, 2019.

[8] B. A. Kimball and K. J. Boote, "Simulation of maize evapotranspiration: an inter-comparison among 29 maize models," *Agricultural and Forest Meteorology*, vol. 271, pp. 264–284, 2019.

[9] J. Shiri, "Improving the performance of the mass transfer-based reference evapotranspiration estimation approaches through a coupled wavelet-random forest methodology," *Journal of Hydrology*, vol. 561, pp. 737–750, 2018.

[10] H. Farzanpour, J. Shiri, A. A. Sadraddini, and S. Trajkovic, "Global comparison of 20 reference evapotranspiration equations in a semi-arid region of Iran," *Hydrology Research*, vol. 50, no. 1, pp. 282–300, 2019.

[11] J. Shiri, "Modeling reference evapotranspiration in island environments: assessing the practical implications," *Journal of Hydrology*, vol. 570, pp. 265–280, 2019.

[12] M. K. Saggi and S. Jain, "Reference evapotranspiration estimation and modeling of the Punjab northern India using deep learning," *Computers and Electronics in Agriculture*, vol. 156, pp. 387–398, 2019.

[13] J. Shiri, Ö. Kişi, G. Landeras et al., "Daily reference evapotranspiration modeling by using genetic programming approach in the Basque country (northern Spain)," *Journal of Hydrology*, vol. 415, pp. 302–316, 2012.

[14] H. Tabari, C. Martinez, A. Ezani, and P. Hosseinzadeh Talaee, "Applicability of support vector machines and adaptive neurofuzzy inference system for modeling potato crop evapotranspiration," *Irrigation Science*, vol. 31, pp. 575–588, 2013.

[15] Y. Luo, S. Traore, X. Lyu et al., "Medium range daily reference evapotranspiration forecasting by using ann and public weather forecasts," *Water Resources Management*, vol. 29, 2015.

[16] A. P. Patil and P. Chandra Deka, "An Extreme learning machine approach for modeling evapotranspiration using extrinsic inputs," *Computers and Electronics in Agriculture*, vol. 121, 2016.

[17] A. P. Patil and P. Chandra Deka, "Performance evaluation of hybrid wavelet-ANN and wavelet-ANFIS models for estimating evapotranspiration in arid regions of India," *Neural Computing & Applications*, vol. 28, 2017.

[18] A. Seifi and H. Riahi, "Estimating daily reference evapotranspiration using hybrid gamma test-least square support vector machine, gamma test-ann, and gamma test-anfis models in an arid area of Iran," *Journal of Water and Climate Change*, vol. 11, 2020.

[19] M. A. Ghorbani, R. Kazempour, K. W. Chau, S. Shamshirband, and T. G. Pezhman, "Forecasting *Pan* evaporation with an integrated artificial neural network quantum-behaved particle swarm optimization model: a case study in Talesh, Northern Iran," *Engineering Applications of Computational Fluid Mechanics*, vol. 12, no. 1, pp. 724–737, 2018.

[20] Y. Guan, B. Mohammadi, Q. B. Pham et al., "A novel approach for predicting daily pan evaporation in the coastal regions of Iran using support vector regression coupled with krill herd algorithm model," *Theoretical and Applied Climatology*, vol. 142, 2020.

[21] S. Mohamadi, M. Ehteram, and A. El-Shafie, "Accuracy enhancement for monthly evaporation predicting model utilizing evolutionary machine learning methods," *International journal of Environmental Science and Technology*, vol. 17, pp. 1–24, 2020.

[22] F. B. Banadkooki, M. Ehteram, A. N. Ahmed et al., "Suspended sediment load prediction using artificial neural network and ant lion optimization algorithm," *Environmental Science and Pollution Research*, vol. 27, no. 30, pp. 38094–38116, 2020.

[23] M. Ehteram, S. Q. Salih, and Z. M. Yaseen, "Efficiency evaluation of reverse osmosis desalination plant using hybridized multilayer perceptron with particle swarm

optimization," *Environmental Science and Pollution Research*, vol. 27, pp. 5278–15291, 2020.

[24] S. Mohamadi, S. Sh Sammen, F. Panahi et al., "Zoning map for drought prediction using integrated machine learning models with a nomadic people optimization algorithm," *Natural Hazards*, vol. 104, pp. 537–579, 2020.

[25] M. Ehteram, F. Y. Teo, A. N. Ahmed et al., "Performance improvement for infiltration rate prediction using hybridized adaptive neuro-fuzzy inferences system (ANFIS) with optimization algorithms," *Ain Shams Engineering Journal*, vol. 12, pp. 1665–1676, 2020.

[26] H. Nguyen, H. Moayedi, W. A. W. Jusoh, and A. Sharifi, "Proposing a novel predictive technique using M5Rules-PSO model estimating cooling load in energy-efficient building system," *Engineering with Computers*, vol. 35, 2020.

[27] Y. Zhou, J. Zhang, X. Yang, and Y. Ling, "Optimal reactive power dispatch using water wave optimization algorithm," *Operational Research*, vol. 20, pp. 1–17, 2018.

[28] A. Hematabadi and A. A. Foroud, "Optimizing the multi-objective bidding strategy using min–max technique and modified water wave optimization method," *Neural Computing & Applications*, vol. 31, 2019.

[29] A. Liu, L. Peng, W. Sun et al., "Prediction of mechanical properties of micro-alloyed steels via neural networks learned by water wave optimization," *Neural Computing & Applications*, vol. 32, 2020.

[30] Y. Han, J. Wu, B. Zhai et al., "Coupling a bat algorithm with XGBoost to estimate reference evapotranspiration in the arid and semiarid regions of China," *Advances in Meteorology*, vol. 2019, Article ID 9575782, 2019.

[31] F. Alasali, H. Stephen, and W. Holderbaum, "Stochastic optimal energy management system for RTG cranes network using genetic algorithm and ensemble forecasts," *Journal of Energy Storage*, vol. 24, 2019.

[32] M. Li, H. Chen, X. Wang, N. Zhong, and S. Lu, "An improved particle swarm optimization algorithm with adaptive inertia weights," *International Journal of Information Technology and Decision Making*, vol. 18, no. 03, pp. 833–866, 2019.

[33] Y.-J. Zheng, "Water wave optimization: a new nature-inspired metaheuristic," *Computers & Operations Research*, vol. 55, pp. 1–11, 2015.

[34] A. Ashrafzadeh, M. A. Ghorbani, S. M. Biazar, and Z. M. Yaseen, "Evaporation process modelling over northern Iran: application of an integrative data-intelligence model with the krill herd optimization algorithm," *Hydrological Sciences Journal*, vol. 64, 2019.

[35] A. A. Heidari, Y. Yin, M. Mafarja, S. M. J. Jalali, J. S. Dong, and S. Mirjalili, "Efficient moth-flame-based neuroevolution models," *Algorithms for Intelligent Systems. In Evolutionary Machine Learning Techniques*, Springer, Singapore, 2020.

[36] P.-S. Ashofteh, O. Bozorg-Haddad, and H. A. Loáiciga, "Logical genetic programming (LGP) development for irrigation water supply hedging under climate change conditions," *Irrigation and Drainage*, vol. 66, no. 4, pp. 530–541, 2017.

[37] R. Noori, A. R. Karbassi, A. Moghaddamnia et al., "Assessment of input variables determination on the SVM model performance using PCA, gamma test, and forward selection techniques for monthly stream flow prediction," *Journal of Hydrology*, vol. 401, 2011.

[38] R. Noori, A. Khakpour, B. Omidvar, and A. Farokhnia, "Comparison of ANN and principal component analysis-multivariate linear regression models for predicting the river flow based on developed discrepancy ratio statistic," *Expert Systems with Applications*, vol. 37, 2010.

[39] J. M. Kim and J. Lee, "Time series analysis for evaluating hydrological responses of pore-water pressure to rainfall in a slope," *Hydrological Sciences Journal*, vol. 62, 2017.

[40] D. N. Moriasi, J. G. Arnold, M. W. Van Liew, R. L. Bingner, R. D. Harmel, and T. L. Veith, "Model evaluation guidelines for systematic quantification of accuracy in watershed simulations," *Transactions of the ASABE*, vol. 50, no. 3, pp. 885–900, 2007.

Hindawi
Complexity
Volume 2021, Article ID 6611848, 17 pages
https://doi.org/10.1155/2021/6611848

Research Article

Using Hybrid Wavelet-Exponential Smoothing Approach for Streamflow Modeling

Vahid Nourani,[1,2] **Hessam Najafi**,[1,3] **Alireza Babaeian Amini**,[3] **and Hitoshi Tanaka**[4]

[1]*Center of Excellence in Hydroinformatics, Faculty of Civil Engineering, University of Tabriz, P.O. Box: 51666, Tabriz, Iran*
[2]*Faculty of Civil and Environmental Engineering, Near East University, Near East Boulevard, Nicosia 99138, Cyprus*
[3]*Faculty of Civil Engineering, University of Bonab, P.O. Box: 5551761167, Bonab, Iran*
[4]*Department of Civil Engineering, Tohoku University, Sendai 980-8579, Japan*

Correspondence should be addressed to Hessam Najafi; hessamnajafi71@gmail.com

Received 11 November 2020; Revised 7 December 2020; Accepted 16 April 2021; Published 27 April 2021

Academic Editor: Rosa M. Benito

Considering the three intrinsic components (of autoregressive, seasonality, and error) of streamflow time series, the overall performance of the streamflow modeling tool is associated with the correct estimation of these components. In this study, a new hybrid method based on the wavelet transform (WT) as a multiresolution forecasting tool and exponential smoothing (ES) method, with two presented scenarios (WES_1 and WES_2), was introduced. To this end, the performance of the proposed method was investigated versus four conventional methods of the autoregressive integrated moving average (ARIMA), ES ad-hoc, artificial neural network (ANN), and wavelet-ANN (WANN) for daily and monthly streamflow modeling of West Nishnabotna and Trinity River watersheds with different hydro-geomorphological conditions. In the presented WES technique, firstly, WT is employed for decomposing the observed signal to one approximation (deterministic trend) and more diverse components of subseries (each at a specific frequency). Then, for the first scenario (WES1), only two subseries are introduced to the model as input parameters; however, for the second scenario (WES2), decomposed subseries are separately used as the inputs of ES models. The obtained results indicated that combining WT with the ES method and ANN led to more accurate modeling. The proposed methodology (WES_2) that used all decomposed subseries separately improved the efficiency of models up to 30% and 10% for the daily dataset and up to 88% and 57% for the monthly dataset, respectively, for the West Nishnabotna and Trinity Rivers.

1. Introduction

Forecasting streamflow has been investigated by several researchers [1–5] as it is a fundamental subject in hydrological modeling. As a result, many researchers are developing new models to improve streamflow modeling. For instance, recently, new models were developed for streamflow forecasting by improving artificial intelligence (AI) models [6, 7]. Accurate modeling of the streamflow is a significant step in any study for a river improvement and management of the related watershed and includes highly nonlinear and interacting components that cause complexity. Difficulties in the estimation of each component of the process causing the estimation of the streamflow become notably difficult. As a result, the black-box models can be more efficient than the physical base models due to the complexity of streamflow time series [8–12]. For instance, linear and stationary time series can be properly modeled by the classic black-box methods by using seasonal auto-regressive integrated moving average (SARIMA) [13, 14]. But such models (e.g., SARIMA) may not be a suitable model for hydrological time series that are highly nonlinear and complex. As an alternative, nonlinear AI-based methods, especially the artificial neural network (ANN), have achieved real success in modeling hydrological time series because of its significant advantages that are as follows [15]:

(i) Being black-box tools, it can be easily used in the absence of prior knowledge about the physical concepts of the process

(ii) Having inherent nonlinearity, provided through activation functions and neurons, it can handle the nonlinearity of the process

(iii) Possibility to have different input variables, thus it can consider time-space variability

Among widely adopted nonlinear models, the used time series are considered to be merely nonlinear but they may not be always purely nonlinear [16]. For practical matters, it is a challenging step to realize whether a time series is generated from a composition of some linear or nonlinear processes. So the application of such techniques with the capability of considering linear and nonlinear properties sounds a reasonable manner.

Exponential smoothing (ES) contributed to the various successful modeling techniques (considering linear and nonlinear methods). It was originally classified by McCormick's [17] taxonomy, then developed by Gardner [18], adjusted by Hyndman et al. [19], and again expanded by Taylor [20] and Gardner [21], which resulted in thirty different models. While the successful applications of the ES method have been reported widely in the field of financial studies and business areas, the available literature in the hydro-environmental applications is really limited. It is notable that only the linear models of the ES method can be taken as an example of the ARIMA approach. The linear ARIMA model may not be able to handle the nonlinear behavior of the process; in this case, the use of ES models that consider both linear and nonlinear behaviors of the process seems to be a reliable alternative. Forecasts produced using the ES method are weighted averages of past observations, with the weights decaying exponentially as the observations get older [22]. Ord et al. [23] and Hyndman et al. [19] have stressed that all ES models (including nonlinear models) could lead to optimal forecasts from the innovation of state-space models. More information can be found in Gardner [18, 21]. Demand for extensive data samples for developing nonlinear models is a well-known issue, and the pure linear ARIMA models may not also be a good choice for handling the behavior of those processes [24]. The application of ES models seems to be a more logical alternative since it is capable of considering the linear and nonlinear nature of the datasets [25].

On the contrary, due to the nonstationarity and climate variability on many time scales (diurnal, subseasonal, seasonal, low-frequency, etc.), the ability of mentioned models (i.e., ANN, SARIMA, and ES) to forecast highly nonstationary and seasonal hydrological time series (e.g., streamflow) may be restricted due to the multifrequency nature of the real hydrological process. To handle the mentioned nonstationary problem, the application of wavelet-based data preprocessing has been already proposed and used successfully in hydro-environmental modeling [26–29]. For example, Jamei et al. [27] developed wavelet-multigene genetic programming for the simulation of surface water total dissolved solids. Ahmadianfar et al. [26] developed the locally weighted linear regression with the wavelet transform (WT) for the prediction of electrical conductivity in surface water. Ni et al. [29] used a hybrid wavelet and long short-term memory (LSTM) network for monthly streamflow and rainfall forecasting and indicated the superiority of the hybrid model against conventional LSTM.

In the presence of highly nonstationary and seasonal variations, data preprocessing methods may be used to get a better model performance. The WT is a suitable approach since it is capable of discerning underlying frequencies and extracting more information from the large datasets. Thus, the hybrid wavelet-ANN (WANN) model has shown good performance and is widely applied for hydrological modelings such as rainfall runoff, groundwater, and river flows [10, 30–32].

Therefore, to the simultaneous use of WT and ES method capabilities for streamflow modeling as a complex process, the wavelet-ES (WES) method is to model the river streamflow. WES_1 and WES_2 were considered as two approaches of the WES method. The aggregated details' subseries and approximation have been used for modeling via WES_1, while the WES_2 method employed all subseries as inputs of the ES method.

This study is the first investigation into the capability of the WES technique in streamflow modeling, and therefore, the purpose of this research is to investigate the capability of the wavelet-based models (i.e., WES_1, WES_2, and WANN), ANN, ES, and SARIMA (as benchmark models) in streamflow modeling. To this end, datasets from two different watersheds (in terms of geomorphological conditions) have been used at daily and monthly scales, and the obtained results were compared together.

2. Study Area and Dataset

In the current research, the data from 2 case studies, West Nishnabotna River, a subbasin in southwestern Iowa, and Trinity River, a subbasin in California, United States, were adopted for implementing the presented techniques (see Figure 1).

The used streamflow time series were obtained from the USGS (https://waterwatch.usgs.gov/). The streamflow time series data of 35 years from 1981 to 2015 were employed in the modeling process, with 75% divided as the training dataset and the rest 25% considered as the test dataset. Table 1 presents the statistical characteristics of streamflow data of watersheds (e.g., mean, maximum, coefficient of variation, etc.).

Trinity River is one of the important tributary of the Klamath River which flows through the Coast Ranges and Klamath Mountains (in northwestern California) and located at 41° 11′ 5″ North latitude and 123°42′ 31″ West longitude. The area of the watershed is about 7800 km^2 (Figure 1(a)). The altitude of the river fluctuates between 58 m and 2709 m above sea level and contains oak, fir, and pine forests (about 92%).

The West Nishnabotna River is one of the two streams of the Nishnabotna River that rises in southwestern Carroll County, flows about 190 km long and located at 40° 34′ 00″ North latitude and 95°39′ 51″ West longitude (Figure 1(b)). The watershed area is approximately 7600 km^2 with the

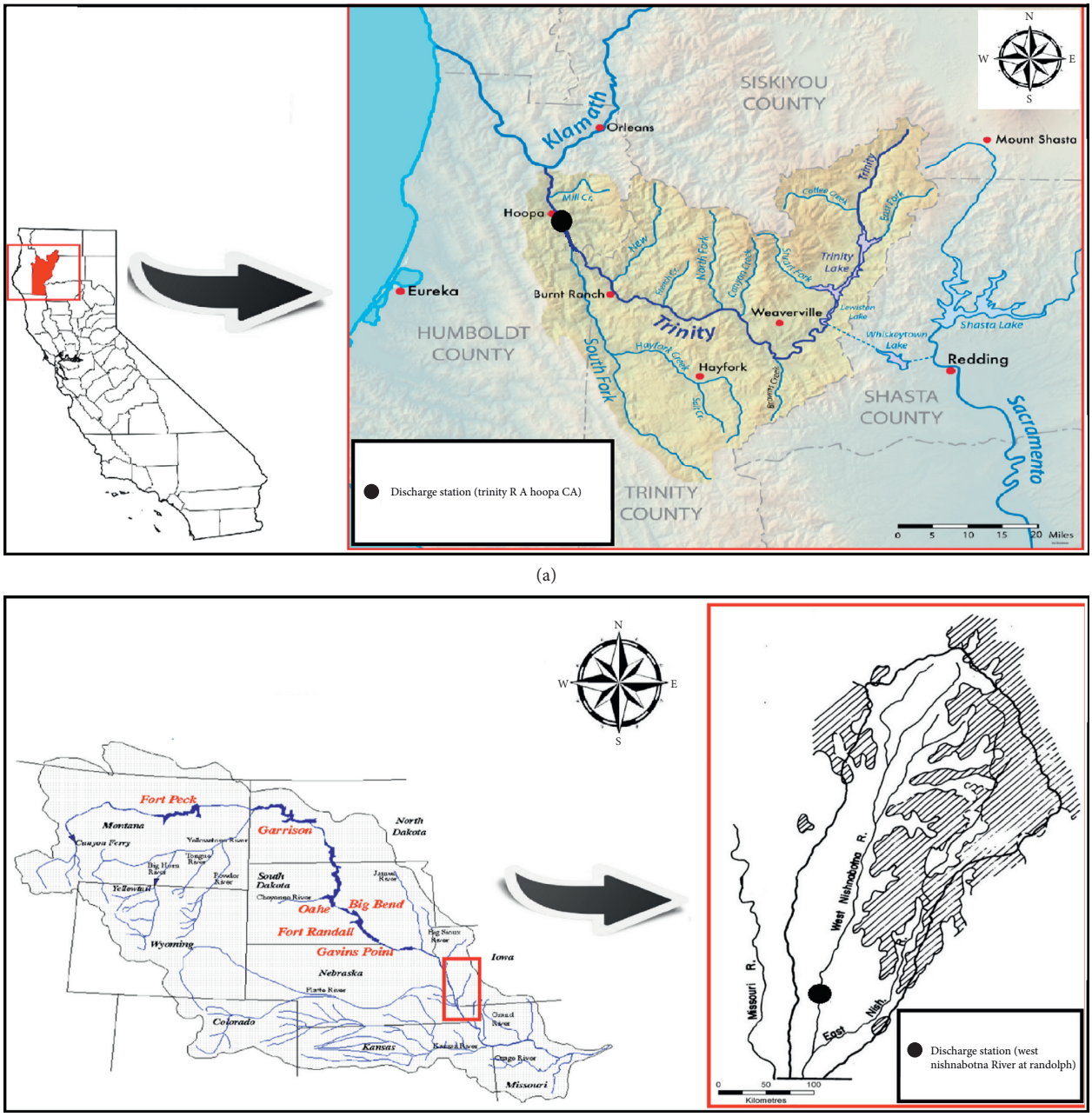

Figure 1: Rivers and stations of (a) Trinity and (b) West Nishnabotna.

field land cover. Broad and open valleys with rolling uplands form the topography of the Nishnabotna River watershed.

The studied watersheds are located at a distance of about 1460 km from each other and have different geomorphological conditions. As shown in Table 1, it is clear that the Trinity River has a greater mean monthly streamflow than that of the West Nishnabotna River. The Trinity River Watershed consists of mixed conifer and evergreen brush at the lower elevations with true fir and lodgepole pine at the higher elevation. It consists of 76 percent mixed conifer, 10 percent shrub, 6 percent mixed fir, 5 percent nonforested, and 3 percent hardwoods (Upper Trinity River Watershed Analysis, USFS, 2005). In contrast to the forest land cover of the Trinity River Watershed, the West Nishnabotna River Watershed is characterized by its field land cover within only 10 percent forest or grassland [33].

The stated autocorrelation function (ACF) shows the seasonal frequency and autoregressive properties of watersheds' time series (see Figure 2). It indicated a more regular pattern for the Trinity River since the denser land cover contributes to the regular pattern of the flow regime.

Additionally, considering the statistical characteristics of the watersheds reported in Table 1, the coefficient of variation for the West Nishnabotna River Watershed is higher than that for the Trinity River Watershed which denotes the

Table 1: Time series descriptive statistics.

Scale	Time series	Parameter	Watershed			
			Trinity River		West Nishnabotna River	
			Train	Test	Train	Test
Daily	Streamflow (m^3/s)	Mean	145.72	109.02	21.02	28.39
		Maximum	2860.00	1475.31	730.57	654.12
		Minimum	12.26	14.33	1.30	2.63
		Standard deviation	214.83	118.60	31.76	36.30
		Coefficient of variation (dimensionless)	1.47	1.09	1.51	1.28
		Sample size	9375	3126	11160	3721
Monthly	Streamflow (m^3/s)	Mean	4454.33	3326.40	641.53	859.65
		Maximum	28299.86	12895.78	5580.12	5105.81
		Minimum	377.94	232.76	56.86	123.07
		Standard deviation	5079.00	2932.42	657.64	829.08
		Coefficient of variation (dimensionless)	1.14	0.88	1.03	0.96
		Sample size	305	102	363	122

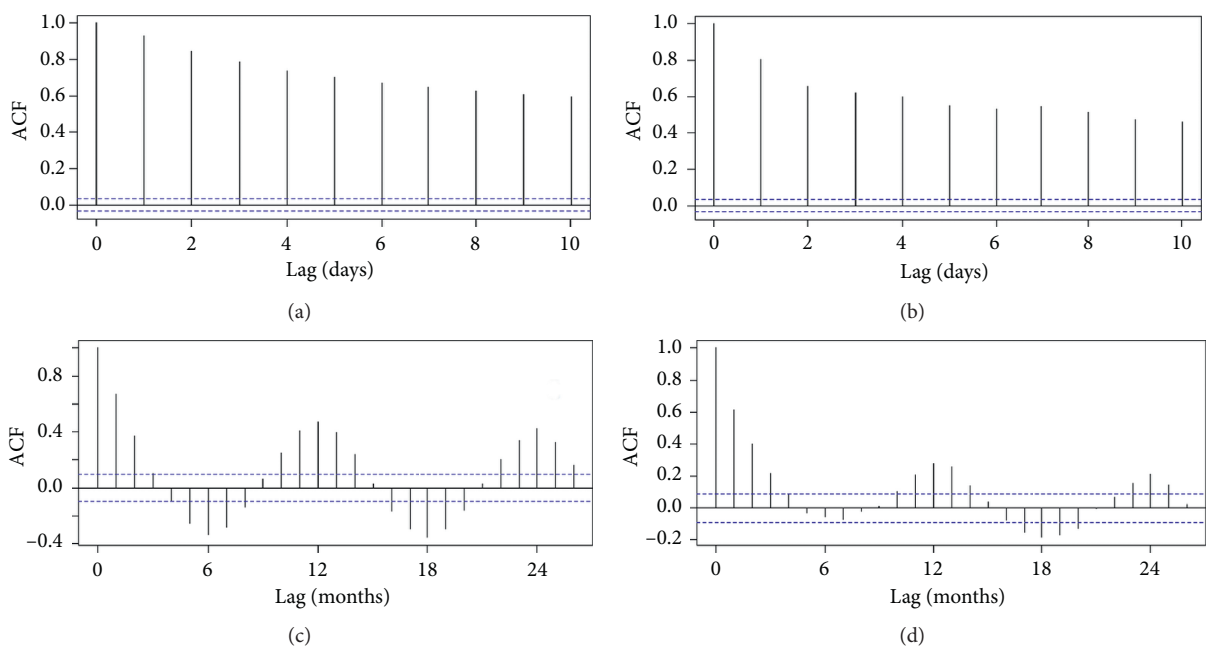

Figure 2: Time series ACF plots for (a, c) Trinity and (b, d) West Nishnabotna.

fact that the West Nishnabotna River Watershed can be considered as a wild watershed in regards with Trinity River Watershed. It can be inferred that the West Nishnabotna River Watershed experiences a more irregular and nonlinear pattern in its involved hydro-environmental processes rather than well-dominated seasonal weather. Therefore, it is expected that the modeling results for the Trinity River Watershed will be better than the Nishnabotna River. The reported results of this study confirm this claim (see Section 4).

3. Methodology

3.1. Wavelet Transform. The continuous form of WT (W) for $x(t)$ is shown as follows [34]:

$$W(m \cdot n) = \frac{1}{\sqrt{m}} \int_{-\infty}^{+\infty} M^{*}\left(\frac{t-n}{m}\right) x(t) \cdot \mathrm{d}t, \tag{1}$$

where n stands for the temporal translation of the function that helps to study the signal around n, m indicates the dilation and * corresponds to the complex conjugate, and $M(t)$ denotes the mother wavelet (wavelet function). Localizing the time scale of the process is the core objective of this transformation. For pragmatic cases, discrete-time signal approaches are more preferred by hydrologists in comparison with continuous one. A discrete mother wavelet can be expressed as follows [34]:

$$M_{a,b}(t) = \frac{1}{\sqrt{m_0^a}} M\left(\frac{t - bn_0 m_0^a}{m_0^a}\right), \tag{2}$$

where a as an integer plays a regulatory role for the wavelet dilation and b as another integer denotes the wavelet translation. The location is specified by the parameter n_0 that is a positive value, and the fined dilation step is represented by parameter m_0 that is a positive score higher than one. $n_0 = 1$ and $m_0 = 2$ are widely chosen scores. This logarithmic scaling for dilation and translation is known as *dyadic grid arrangement*, and the dyadic wavelet function is specified as follows [34]:

$$M_{a,b}(t) = 2^{-(a/2)} \times M\left(2^{-a}t - b\right) = \frac{1}{\sqrt{2^a}} M\left(\frac{t - 2^a b}{2^a}\right). \quad (3)$$

The dyadic WT for x_t as a discrete-time series becomes [34]

$$T_{a,b} = \frac{1}{\sqrt{2^a}} \sum_{t=0}^{L-1} M\left(\frac{1}{2^a} t - b\right) x_t, \quad (4)$$

where $T_{a,b}$ stands for the discrete wavelet coefficient based on the scale $m = 2^a$ and localization parameter $n = 2^a b (t = 0, 1, 2, \ldots, L-1$ and L is an integer power of 2: $L = 2^A)$. The overall trend of the signal (indicated by the smoothed part of the signal) is indicated by T. The formula for renovating the time series x_t by the inverse discrete transform is [34]

$$x_t = T(t) + \sum_{a=1}^{A} T_{a,b}(t), \quad (5)$$

where $T(t)$ is termed as the approximation series at level A. Also, $T_{a,b}(t)$ indicates the detail series with decomposition level a $(a = 1, 2, \ldots, A)$ and time dimension t $(t = 1, 2, \ldots, b)$.

3.2. Autoregressive Integrated Moving Average. As the benchmark model, ARIMA and seasonal ARIMA (SARIMA) models were examined for the streamflow modeling of watersheds, in order to compare the results of linear and nonlinear models.

SARIMA models have been employed to analyze and forecast univariate hydro-environmental time-series data [10]. The SARIMA model is a developed form of the ARIMA model, which reflects the seasonal variation of the time series, and the original time series $-Y_t-$ employs a lag operator B to process SARIMA $(p, d, q)(P, D, Q)[S]$. The SARIMA model can be formulated as follows [35]:

$$\varphi_p(B)\Phi_P\left(B^S\right)^d\left(1 - B^S\right)^D Y_t = \theta_q(B)\Theta_Q\left(B^S\right)\varepsilon_t. \quad (6)$$

In equation (6), B is the lag operator (defined as $B^k Y_t = Y_{t-k}$); $\varphi(B)$ and $\theta(B)$ are polynomials of orders p and q, respectively, $\Phi_P(B^S)$ and $\Theta_Q(B^s)$ are polynomials in B of degrees P and Q, respectively, p and d denote the order of nonseasonal auto-regression and the number of regular differences, q indicates the order of nonseasonal moving average, P, D, and Q show the order of seasonal auto-regression, the number of seasonal differences, and the order of seasonal moving average, respectively, and finally, S stands for the length of the season. Thus, for the ARIMA model, it means that the seasonality parameters (P, D, and Q) are considered to be equal to zero.

In this paper, the ARIMA and SARIMA models were applied for streamflow forecasting using the R software program. ARIMA and SARIMA models were first trained via the training dataset and then verified using the validation set.

3.3. Artificial Neural Network. ANN models are frequently utilized in dynamic nonlinear datasets' modeling and achieve accurate results, particularly for complex hydrological phenomena in which the physics of problem's variables are not entirely comprehended. In other words, ANNs are suitable for modeling the data-driven nature time series. An ANN is a composition of a set of neurons (or nodes, i.e., interconnected simple processing elements) with an attractive set of information processing characteristics such as nonlinearity, parallelism, noise tolerance, and learning and generalization capabilities.

Between the ANNs, the Feedforward Backpropagation (FFBP) Neural Network is the most common method utilized in solving different engineering problems [30, 36]. The term "Feed-Forward" means that a neuron in the input layer is only connected to other neurons in the hidden layer and neurons in the hidden layer are connected to neurons in the output layer. So there are no interconnections within each layer's neurons.

An output value's explicit expression form of a three-layered FFBP neural network is specified by [37]

$$\hat{y}_k = f_0\left[\sum_{j=1}^{M_N} w_{kj} \cdot f_h\left(\sum_{i=1}^{N_N} w_{ji} x_i + w_{jo}\right) + w_{ko}\right], \quad (7)$$

where f_0 denotes the activation function for the output neuron, w_{kj} is a weight vector in the output layer connecting the kth neuron in the output layer and the jth neuron in the hidden layer, f_h indicates the activation function of the hidden neuron, w_{ji} is the weights applied in the hidden layer connecting the jth node in the hidden layer and the ith node in the input layer, x_i is the ith input variable for the input layer, w_{jo} is the bias for the jth hidden neuron, w_{ko} is the bias for the kth output neuron, and $\hat{y}_k$ is the computed output variable. Finally, M_N and N_N are the number of nodes in the input and hidden layers, respectively. It should be noted that the data are normalized to become between 0 and 1 before feeding into the network.

Also, it is notable that, in this study for modeling streamflow via ANN tool, the MATLAB® software and its *nntool* were used.

3.4. Exponential Smoothing. ES is a practical approach for forecasting whereby the prediction is based on an exponentially weighted average of past observation [38]. Hence, by adopting the ES state-space technique, better results could be expected from the models developed for the datasets which pose nonstationary or nonlinear behavior [39].

Table 2 denotes the ES different models. For example, consider the cell (A, A) and cell (A, M) as an example; they

Table 2: The different types of ES Models [39].

	Trend component	Seasonal component		
		N (none)	A (additive)	M (multiplicative)
N	None	N, N	N, A	N, M
A	Additive	A, N	A, A	A, M
A	Additive damped	A_d, N	A_d, A	A_d, M
M	Multiplicative	M, N	M, A	M, M
M	Multiplicative damped	M_d, N	M_d, A	M_d, M

represent the "additive Holt-Winters" and the "multiplicative Holt-Winters" model, respectively. According to the literature, the Holt-Winters (HW) model which has easier formulation and simultaneously handles the autoregressive and seasonal components of time series, among different forms of ES approach, is a commonly applied model [18, 40]. There are two possible state-space models for each of the fifteen models in Table 2, one for a model with additive errors and the other corresponding to the model with multiplicative errors. In our work, the additive and multiplicative errors have been applied for streamflow simulation, and thirty class of ES models (15) × (2) have been used, and the most reliable results have been presented in the *Results and Discussion* section.

The (E, T, S) states the components of error, trend, and seasonality [39]. Therefore, e.g., the ETS (M, M, N) represents a model with multiplicative errors and a multiplicative trend with no seasonality. It should be mentioned that additive or multiplicative determines linear or nonlinear attitude.

The equations of the HW model can be expressed as follows (equations (8)–(17)), and readers can find more details about other classes of ES on Hyndman and Khandakar [39].

The HW approach includes trend and seasonal (S_t) factors with α, β, and γ as smoothing parameters where the trend factor formed from growth (B_t) and level (L_t) terms. The additive HW model is as follows [22]:

$$B_t = \beta(L_t - L_{t-1}) + (1-\beta)B_{t-1}, \tag{8}$$

$$L_t = \alpha(x_t - S_{t-c}) + (1-\alpha)(L_{t-1} + B_{t-1}), \tag{9}$$

$$S_t = \gamma(x_t - L_{t-1} - B_{t-1}) + (1-\gamma)S(t-c), \tag{10}$$

and the multiplicative HW model can be defined as follows [41]:

$$L_t = \alpha\left(\frac{x_t}{S_{t-c}}\right) + (1-\alpha)(L_{t-1} + B_{t-1}), \tag{11}$$

$$B_t = \beta(L_t - L_{t-1}) + (1-\beta)B_{t-1}, \tag{12}$$

$$S_t = \gamma\left(\frac{x_t}{L_{t-1} - B_{t-1}}\right) + (1-\gamma)S_{t-c}. \tag{13}$$

As already stated, α, β, and γ denote the smoothing parameters and, respectively, are affected by level, slope, and seasonality $(0 < \alpha, \beta, \gamma < 1)$. The parameters α, β, and γ are calculated by applicable error functions such as root mean square error (RMSE). For obtaining the seed values, the following formula can be used [41]:

$$L_0 = x_0, \tag{14}$$

$$B_0 = \frac{1}{c}\sum_{i=1}^{c}\left(\frac{x_{c+i} - x_i}{c}\right), \tag{15}$$

$$S_i = \frac{1}{N}\sum_{j=1}^{N}\frac{x_{c(j-1)+i}}{A_j}, \quad \forall i = 1, 2, \ldots, c, \tag{16}$$

since

$$A_j = \frac{1}{c}\sum_{i=1}^{c} x_{c(j-1)+i}, \quad \forall j = 1, 2, \ldots, N, \tag{17}$$

where A_j states the mean value of x in the jth cycle of data, N states the cycles number, and C states the length of the seasonal cycle.

Also, in this study for modeling streamflow via the ES method, the *R* software was used. To this end, the "ETS" function from the "forecast" package was used. The "ETS" function tests all possible ES models (see Table 2) and selects the best model by optimizing parameters based on the mean square error (MSE) criterion [39].

3.5. Proposed Methodology. To use the advantages of ES and WT methods at the same time, the hybrid WES model is adopted in the presented study. As a temporal preprocessor, the WT is employed for detecting and extracting the existed seasonality and temporal features in the streamflow time series. The WT decomposes the observed streamflow time series $(Q(t))$ into an approximation subseries $Q(t)_a$ and i detail subseries, $Q(t)_{d_1}, \ldots, Q(t)_{d_i}$, where i states the decomposition level, and each subseries implies an individual level of seasonality. Using the WT tool, the resulted subseries are fed into the univariate ES method. According to the univariate nature of the ES method, two scenarios were designed to use the WT resulted subseries. Since the WT decomposes the time series into two components, an approximation subseries and fluctuation subseries (which include several subseries representing the seasonal periods), the designed scenarios must consider both components separately. Hence, two scenarios were designed to model the approximation and fluctuation components separately, with the difference that the WES_1 models the approximate subseries and aggregated fluctuation subseries (two ES models) but WES_2 models the approximate subseries and all fluctuation subseries individually (i+1 ES models).

The developed models of WES_1 and WES_2 are stated below.

The outline of the WES_1 is described in three steps as follows (Figure 3(a)):

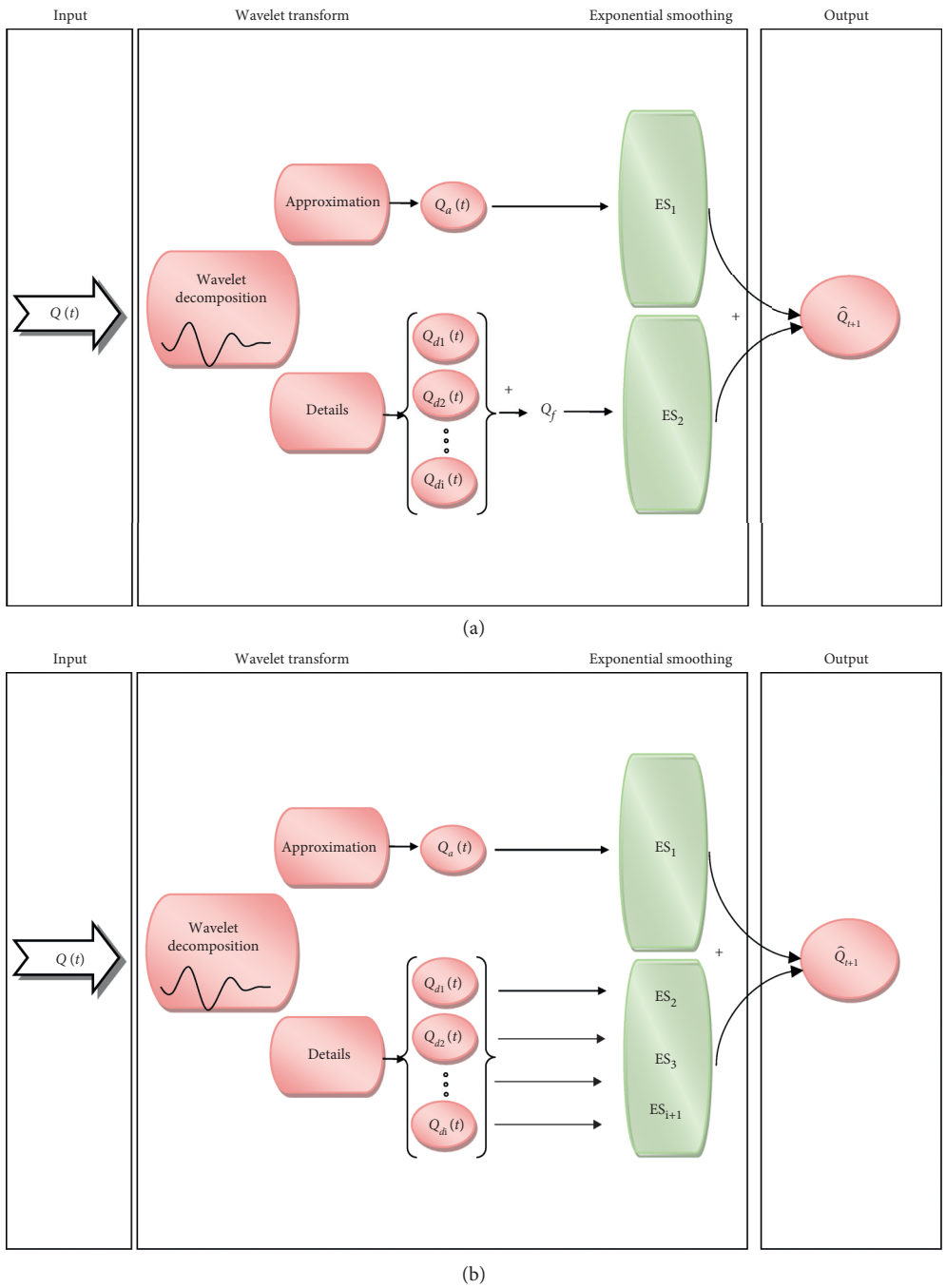

FIGURE 3: Structure of the proposed methods. (a) WES_1. (b) WES_2.

(i) The fluctuation series $(Q(t)_f)$ is computed through $Q(t)_f = Q(t) - Q(t)_a$

(ii) Employing two distinct ES models, both of approximation $(Q(t)_a)$ and fluctuation series $(Q(t)_f)$ are modeled individually; consequently, both of $\widehat{Q}(t)_a$ and $(\widehat{Q}(t)_f)$ are obtained as computed series

(iii) In the end, the overall computed streamflow $(\widehat{Q}(t))$ is achieved by $\widehat{Q}(t) = \widehat{Q}(t)_a + \widehat{Q}(t)_f$

The outline of the WES_2 is described in two steps as follows (Figure 3(b)):

(i) All of the resulted subseries are modeled individually by employing $i+1$, ES models $(ES_1, ES_2, \ldots, ES_{i+1})$. Consequently, the computed approximation series $(\widehat{Q}(t)_a)$ and detail series $(\widehat{Q}(t)_{d1}, \widehat{Q}, \ldots, \widehat{Q}(t)_{di})$ are obtained.

(ii) In the end, the computed streamflow time series $\widehat{Q}(t)$ is obtained using $\widehat{Q}(t) = \widehat{Q}(t)_a + \widehat{Q}(t)_{d_1} + \widehat{Q}(t)_{d_2} + \cdots + \widehat{Q}(t)_{d_i}$.

As it can be seen in Figure 3, the major contrast between the two WES_1 and WES_2 models is the number of utilized ES

models. The WES_1 uses two ES models for predicting the streamflow but the WES_2 uses $i+1$ models. In other words, WES_1 uses the $Q(t)_a$ and $Q(t)_f$ as the inputs, while the inputs of WES_2 are $Q(t)_a, Q(t)_{d_1}, Q(t)_{d_2} \ldots$ and $Q(t)_{d_i}$ subseries.

3.6. Efficiency Criteria. In this study, RMSE and Nash–Sutcliffe (NSE) were used as efficiency criteria. The RMSE (equation (18)) and Nash–Sutcliffe (equation (19)) are broadly employed as evaluating criteria of the efficiency performance of hydrological models [42]:

$$\mathrm{RMSE} = \sqrt{\frac{\sum_{i=1}^{N} (O_i - C_i)^2}{N}}, \tag{18}$$

$$\mathrm{NSE} = 1 - \frac{\sum_{i=1}^{N} (O_i - C_i)^2}{\sum_{i=1}^{N} (O_i - \overline{O})^2}. \tag{19}$$

In equations (18) and (19), N, O_i, C_i, and $\overline{O}$, respectively, indicate the number of samples, observed values, calculated values, and average of the observed values. Legates and McCabe [43] revealed that RMSE and NSE can evaluate the performance of the hydro-environmental models appropriately. Furthermore, considering the importance of peak values in modeling as well, equation (20) may be employed to assess the performance of the model in terms of capturing the extreme values [42]:

$$\mathrm{NSE}_{\mathrm{peak}} = 1 - \frac{\sum_{i=1}^{N_p} \left(O_{pi} - C_{pi}\right)^2}{\sum_{i=1}^{N_p} \left(O_{pi} - \overline{O_p}\right)^2}, \tag{20}$$

where $\mathrm{NSE}_{\mathrm{peak}}$ indicates the Nash–Sutcliffe criterion of peak values, N_p stands for the number of peak values, O_{p_i} indicates the observations, and C_{p_i} and $\overline{O_p}$ are computed and average of peak values, respectively.

4. Results and Discussion

In this research, the ES, ARIMA, ANN, and WANN as benchmark models were developed beside the WES method (with two considered scenarios) to one-time step ahead modeling of daily and monthly streamflow time series (see Figure 4). In the following, the results of the WES method are presented and discussed; then, a comparison with benchmark models is performed.

For each daily data and monthly data, the resolution levels of 2 to 8 and 2 to 5 were adopted, respectively. In early studies, the optimum decomposition level was usually determined through a trial-and-error process, but afterward, a formula which relates the minimum level of decomposition, L, to the number of data points within the time series N_s was introduced in the literature [30]:

$$L = \mathrm{int}\left[\log N_s\right]. \tag{21}$$

So, in this study, the initial point of view to select of the decomposition level was taken from L but since many seasonal characteristics may be embedded in hydrological signals, 2–8 resolution levels $(L \pm x)$ for the daily and 2–5 resolution levels $(L \pm x)$ for the monthly modeling were examined via the proposed WANN and WES models which, respectively, denote to the 2^2-day mode and 2^3-day mode (which is nearly weekly mode), 2^4-day mode (which is nearly semimonthly mode), 2^5-day mode (which is nearly monthly mode), 2^6-day mode, 2^7-day mode (which is nearly semi-yearly mode), and 2^8-day mode (which is nearly yearly mode) in the daily scale and 2^2-month mode, 2^3-month, 2^4-month, and 2^5-month mode in the monthly scale. Besides, the Daubechies 4 wavelet (db4) that has been frequently assessed in hydrological modeling was considered as the mother wavelet in this study. Based on the literature, in contrast to the importance of the decomposition level, the type of the mother wavelet poses a minor effect since the model can adjust the output [30]. Finally, by applying the models (ES and ANN) to the inputs obtained by wavelet decomposition, the output of hybrid models (WES and WANN) as $Q(t+1)$ can be computed. It should be mentioned that, for the daily and monthly scale, the 4th decomposition level offered better results. Thus, the outcomes of the 4th level are presented in the tables.

To increase the model efficiency regarding the multi-frequency feature of the WT, the preprocessed data by WT were introduced to the ES method (with thirty types of models). The results of WES_1 and WES_2 modeling scenarios were, respectively, presented in Tables 3 and 4 . It is obvious that, for both watersheds, the second scenario (WES_2) offers more precise results in comparison with the first scenario (WES_1) because the WES_2 uses all resulted subseries by WT as inputs but in modeling by WES_1, by aggregating the details' subseries and using only two inputs (approximation and fluctuation subseries), the effect of WT becomes weaker.

A noticeable point about the ES method parameters in Tables 3 and 4 (also in Table 5) is the values of the α as level (trend), β as the slope (trend growth), γ as seasonal, and φ as damping factors $(0 < \alpha, \beta, \gamma, \varphi < 1)$. The level index (α) gives an estimate of the local mean, the slope index (β) denotes the change between successive time points, the seasonality index (γ) estimates the deviation from the local mean due to seasonality, and finally, the damping index (φ) is related to the stationary state of the time series, meaning that if the time series do not converge to a stable value as t increases limitlessly, the time series is nonstationary and φ should get a high value (near 1). In other words, a small value of φ means that older observations in the time series are weighted markedly but values near 1 mean that the latest observations will get higher weights [25].

As aforementioned, γ parameter indicates the seasonal component of the time series. However, the WT already extracted the seasonal component (as detail subseries), and the resulted subseries by WT do not have extractable seasonal components. Therefore, as can be seen in Tables 3 and 4, the value of the γ parameter is zero or very low (especially in daily models and the approximation component in monthly models). But the approximation subseries indicates the major trend of the original time series, so the α and β parameters of its ES model take their highest value (very close to 1).

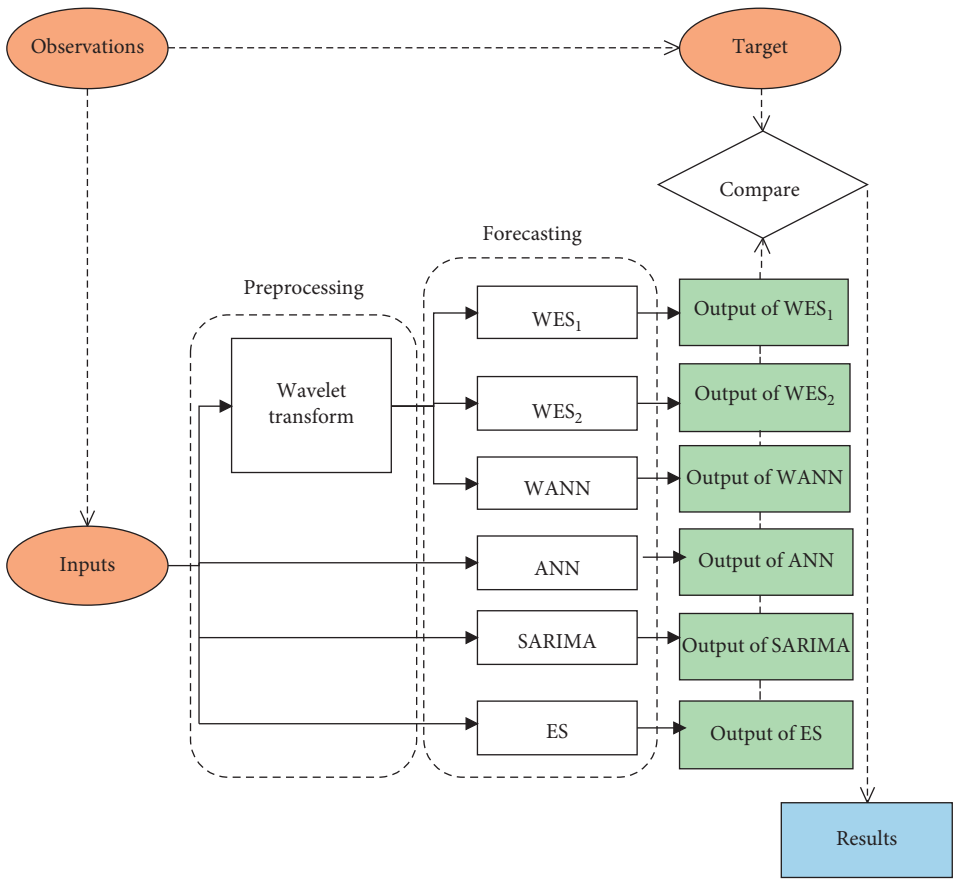

Figure 4: Research methodology flowchart.

Table 3: Performance results of the WES_1 method.

	Watersheds	Type of ES	Inputs	Structures α	β	γ	ϕ	NSE Train	NSE Test	RMSE (m^3/s) Train	RMSE (m^3/s) Test	NSE_{peak} Test
Daily	Trinity River	(A, A_d, N)	Approximation	0.9999	0.9999	—	0.9634	0.873	0.866	41.467	73.484	0.804
		(A, N, N)	Details	0.9999	—	—	—					
	West Nishnabotna River	(A, A_d, N)	Approximation	0.9999	0.9999	—	0.9635	0.655	0.645	21.365	21.636	0.538
		(A, N, N)	Details	0.5953	—	—	—					
Monthly	Trinity River	(A, A_d, N)	Approximation	0.9999	0.9999	—	0.9539	0.551	0.542	2237.014	2630.001	0.264
		(A, A_d, A)	Details	0.7654	0.0001	0.0001	0.9428					
	West Nishnabotna River	(A, A_d, N)	Approximation	0.9999	0.9999	—	0.9558	0.493	0.471	463.48	603.564	0.399
		(A, N, A)	Details	0.0001	—	0.0001	—					

The most efficient ES models of the two first levels of the resulted subseries (by WT) express the high-frequency seasonal characteristics with an insignificant trend element, so contains no β and a lower α score (see Table 4) so that modeling the first and second detail subseries within notable variations was considered a challenging step.

As the benchmark models, ANN, WANN, SARIMA, and ES were also examined for the streamflow modeling of the watersheds.

To develop the model with the ANN, up to n lag times (Q_t, Q_{t-1}, ..., Q_{t-n}) of past observations were considered as possible inputs of ANN to forecast the Q_{t+1}. Due to the selection of best inputs to modeling via AI-based models (multivariate models), the Pearson correlation coefficient (CC) and mutual information (MI) were used [44], and according to the efficiency criteria (RMSE and NSE), only the best results were reported in Table 6. Since the proper selection of input parameters and the network structure (i.e.,

Table 4: Performance results of the WES_2 method.

	Watersheds	Type of ES	Inputs	Structures				NSE		RMSE (m^3/s)		NSE_{peak}
				α	β	γ	ϕ	Train	Test	Train	Test	Test
Daily	Trinity River	(A, A_d, N)	Approximation	0.9999	0.9999	—	0.9634	0.926	0.912	35.102	52.402	0.892
		(A, N, N)	Detail 1	0.0001	—	—	—					
		(A, N, N)	Detail 2	0.0001	—	—	—					
		(A, A_d, N)	Detail 3	0.9020	0.9250	—	0.8002					
		(A, A_d, N)	Detail 4	0.9999	0.9999	—	0.8743					
	West Nishnabotna River	(A, A_d, N)	Approximation	0.9999	0.9999	—	0.9088	0.841	0.822	15.517	15.797	0.808
		(A, N, N)	Detail 1	0.0001	—	—	—					
		(A, N, N)	Detail 2	0.0001	—	—	—					
		(A, A_d, N)	Detail 3	0.9999	0.9999	—	0.8649					
		(A, A_d, N)	Detail 4	0.9999	0.9999	—	0.8778					
Monthly	Trinity River	(A, A_d, N)	Approximation	0.9999	0.9999	—	0.9539	0.831	0.79	1581.341	1977.409	0.836
		(A, N, A)	Detail 1	0.0001	—	0.0001	—					
		(A, N, A)	Detail 2	0.0001	—	0.1701	—					
		(A, N, A)	Detail 3	0.9999	—	0.0001	—					
		(A, A_d, N)	Detail 4	0.9999	0.9999	—	0.8693					
	West Nishnabotna River	(A, A_d, N)	Approximation	0.9999	0.9999	—	0.9558	0.756	0.735	358.957	501.186	0.629
		(A, N, A)	Detail 1	0.0001	—	0.0001	—					
		(A, N, A)	Detail 2	0.0001	—	0.0001	—					
		(A, N, A)	Detail 3	0.9999	—	0.0001	—					
		(A, A_d, N)	Detail 4	0.9999	0.9999	—	0.8656					

Table 5: Performance results of the ES method.

	Watersheds	Type of ES	Structure				NSE		RMSE (m^3/s)		NSE_{peak}
			Alpha	Beta	Gamma	Phi	Train	Test	Train	Test	Test
Daily	Trinity River	*(M, N, N)*	0.9999	—	—	—	0.871	0.862	39.108	70.049	0.808
	West Nishnabotna River	*(M, N, N)*	0.6322	—	—	—	0.677	0.642	19.856	19.914	0.571
Monthly	Trinity River	*(M, M, M)*	0.2676	0.0001	0.1243	—	0.596	0.582	2147.33	2545.478	0.342
	West Nishnabotna River	*(M, A, M)*	0.5337	0.0016	0.0001	—	0.526	0.509	481.016	522.556	0.36

Table 6: Performance results of AI-based models.

	Watersheds	Model	Inputs	Best structures	No. of hidden neurons	Epoch	NSE		RMSE (m^3/s)		NSE_{peak}
							Training	Test	Training	Test	Test
Daily	Trinity River	ANN	$Q(t)$, $Q(t-1)$, $Q(t-2)$	3-4-1	4	20	0.852	0.845	39.938	72.981	0.791
		WANN	$Q_a(t)$, $Q_{d2}(t)$, $Q_a(t-1)$, $Q_{d4}(t-1)$	4-7-1	7	30	0.932	0.921	30.471	51.305	0.905
	West Nishnabotna River	ANN	$Q(t)$, $Q(t-1)$, $Q(t-2)$	3-9-1	9	90	0.689	0.658	19.407	19.807	0.569
		WANN	$Q_a(t)$, $Q_{d1}(t)$, $Q_a(t-1)$, $Q_{d1}(t-1)$	4-9-1	9	40	0.823	0.812	17.022	17.326	0.765

Table 6: Continued.

	Watersheds	Model	Inputs	Best structures	No. of hidden neurons	Epoch	NSE		RMSE (m^3/s)		NSE_{peak}
							Training	Test	Training	Test	Test
Monthly	Trinity River	ANN	$Q(t)$, $Q(t-12)$	2-5-1	5	20	0.611	0.601	2123.189	2401.262	0.679
		WANN	$Q_a(t)$, $Q_{d3}(t)$, $Q_a(t-1)$, $Q_{d4}(t-1)$	4-4-1	4	10	0.85	0.822	1381.341	1877.409	0.851
	West Nishnabotna River	ANN	$Q(t)$, $Q(t-12)$	2-7-1	7	100	0.578	0.545	470.929	517.635	0.559
		WANN	$Q_a(t)$, $Q_{d4}(t)$, $Q_a(t-1)$, $Q_{d3}(t-1)$	4-8-1	8	10	0.779	0.764	258.957	411.186	0.761

Table 7: Performance results of ARIMA and SARIMA models.

	Watersheds	Model	Structures	NSE		RMSE (m^3/s)		NSE_{peak}
				Train	Test	Train	Test	Test
Daily	Trinity River	ARIMA	ARIMA (5, 0, 3)	0.849	0.835	41.868	74.696	0.783
	West Nishnabotna River	ARIMA	ARIMA (3, 1, 2)	0.623	0.621	21.5	21.914	0.545
Monthly	Trinity River	SARIMA	SARIMA (2, 0, 1) (2, 0, 0) [12]	0.517	0.502	2594.93	2855.697	0.02
	West Nishnabotna River	SARIMA	SARIMA (2, 0, 1) (0, 0, 2) [12]	0.431	0.391	496.18	646.966	0.197

number of layers, activation function, epoch number, and hidden neurons) deeply influence the AI-based model, problems such as underfitting and overfitting can be avoided by suitable selection of the network structure. The Levenberg–Marquardt backpropagation algorithm was utilized to train the network. To this end, tangent sigmoid has been used as the activation functions, and up to quadruple of the inputs were considered as the hidden neurons, and up to 500 were examined as iteration epochs' number [37]. The most efficient ANNs' outcomes are stated in Table 6.

The ability of WT in the multiresolution analysis could be used in dealing with seasonal patterns. Since the combination of WT and ANN methods reinforce the capability of the model in dealing with seasonality, in this study, for daily and monthly modeling, the WANN method was utilized. So, by using the feature selection methods (CC and MI) to select inputs and constructing the networks, $Q(t+1)$ can be predicted. The tabulated results in Table 6 show the efficient performance of WANN.

For both watersheds, ARIMA and SARIMA performed better, respectively, for daily and monthly scales (see Table 7). However, at monthly modeling for the low NSE value (<0.5), the considered models could not make a good fit on the streamflow and thus are not reliable models. The streamflow time series intrinsic nonlinear nature and its multifrequency seasonality patterns may be the reason for the lack of accuracy in modeling by linear and unifrequency analysis (SARIMA).

The performance results of the ES method are stated in Table 5. As can be seen, for all of the case studies, the ES model offered better outcomes in comparison to the ARIMA and SARIMA. But regarding the low value of NSE (≈0.5) in monthly modeling, this model did not present a good capability to model the streamflow of these rivers. The multifrequency nature of the signal may be the reason for the resulted deficiency.

The hybrid WES_2 model performed better than other single models up to 30% and 10% (daily scale) and up to 88% and 57% (monthly scale) for the West Nishnabotna and Trinity, respectively. Especially, WES_2 was more efficient in the face of the peak values for both watersheds (Figures 5–8).

The WANN and the WES_2 are the potential methods to deal with autoregressive features and seasonality fluctuations, which are widely seen components at both daily and monthly streamflow time series (see Figure 2). Hence, the WANN and WES_2 offered more reliable results in comparison with other methods such as the ARIMA (an approach that is capable of handling with the autoregressive only), the ES and SARIMA (uni-frequency analysis tools), and the WES_1 model (the detail subseries are aggregated, and two inputs are introduced to the model with a lower impact of WT), that is, because the WT method is capable of handling complicated streamflow processes due to its potential in the multiresolution analysis. Figures 5–8 depict this superiority for both watersheds at both scales. In other words, it means introducing of all the resulted subseries from decomposing the main signal using WT, as the inputs would increase the efficiency of the model since each subseries would represent a specific seasonal scale and the various seasonality characteristics would be covered in the model. As the seasonality features become more highlighted and common at the monthly scale, this process becomes more sensitive [25].

The computational cost for WANN was more than that of the WES_2 model because ANN has more parameters than the ES model (e.g., input numbers, weights, biases, hidden neurons number, and transfer functions' type), while the

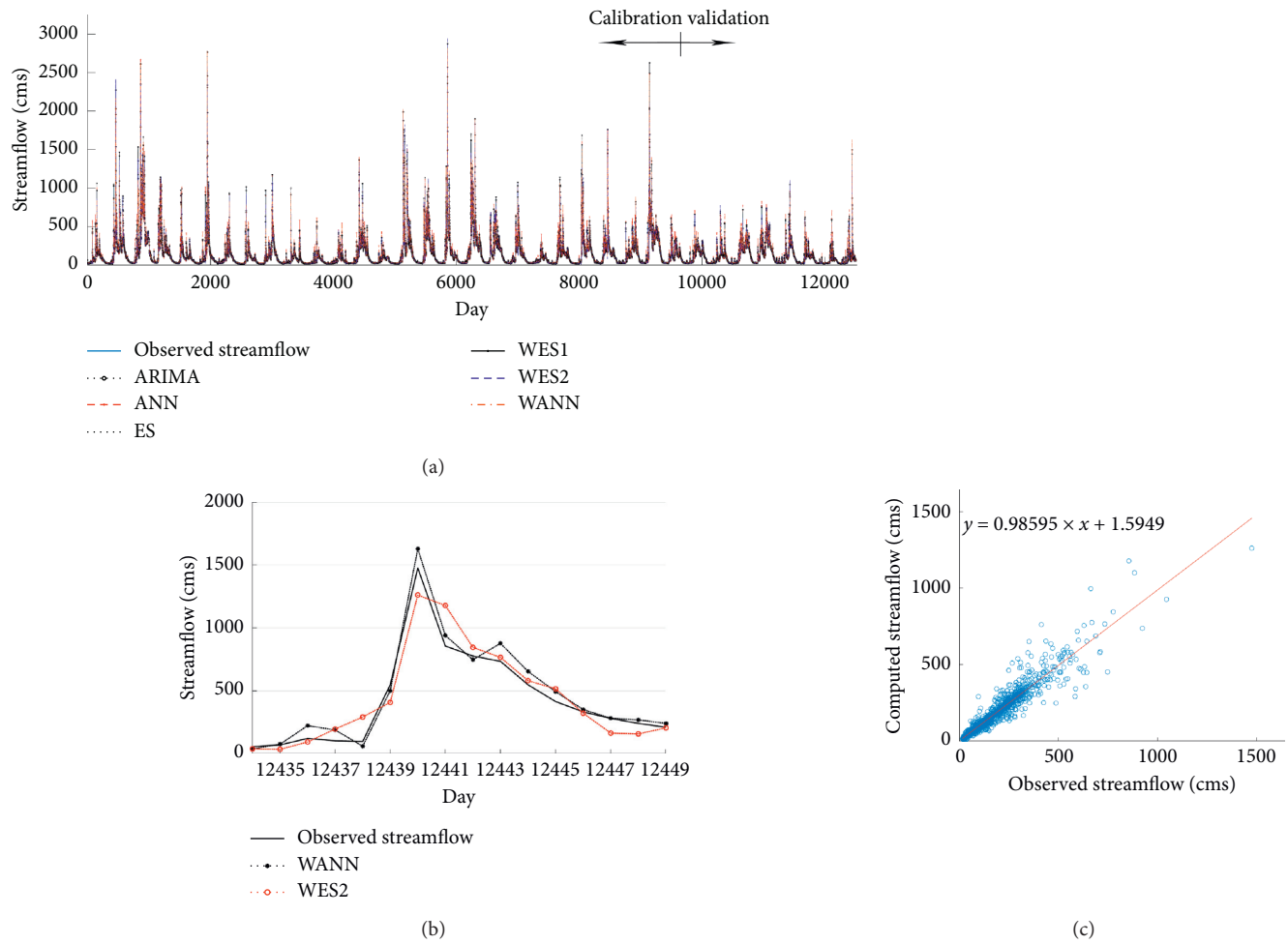

Figure 5: Observed/simulated daily streamflow of Trinity. (a) Whole. (b) Detail. (c) Verification scatter plot of WES_2.

performance of the WANN and WES_2 model was more or less in the same range; ES models offered more reliable results compared to ARIMA and SARIMA due to the comprising linear and nonlinear kernels and their capability in analyzing time series regarding the primary factors of time series (trend, seasonality, and error).

The daily ARIMA model led to reliable results (because of the autoregressive characteristic of streamflow daily time series, see Table 7); however, for the monthly time series, the SARIMA model could not gain acceptable results (see Table 7), that is, maybe because of the existence of the multifrequency pattern of the streamflow monthly time series.

For a more comprehensive presentation of the performance of the WES_2 model in streamflow modeling, a Taylor diagram (Figure 9) was developed by considering the CC, standard deviation, and RMSE between the observed and computed streamflow time series. In the Taylor diagram, the standard deviation of the pattern is proportional to the radial measured from the origin, the correlation between the two fields is given by the azimuthal position of the test field, and the centered RMSE value is proportional to the distance between the actual and the estimated fields with the same units as the standard deviation [45]. When the predicted value is closer to the observed value in the matter of CC and standard deviation, one can expect more accurate prediction results. The value of the RMSE decreases with an increase in correlation. From the result shown in Figure 9, it can be clearly seen that the WES_2 and WANN models demonstrated higher capability than the other used models for the streamflow modeling in terms of RMSE and pattern correlation (also standard deviation).

It can be concluded that, while for the time series in the monthly scale of the watershed, the WANN, WES_2, ANN, ES, WES_1, and SARIMA presented a more reliable performance; WES_2, WANN, ANN, ES, WES_1, and ARIMA models led to more acceptable outcomes in the daily scale, respectively.

From the aspect of spatial assessment, the studied watersheds' land covers have different conditions. As stated in Tables 3–7, it is obvious that, by employing various time scales, West Nishnabotna River efficiency's increase was more than Trinity River. Also, for all modeling procedures, the Trinity River got more reliable outcomes because the Trinity River Watershed has a more dense land cover (covered by forests and is not much affected by anthropogenic influences), and its reaction to rainstorm (or precipitation) is not so complex (nonlinear) as much as West Nishnabotna. Add to that, as it is clear in Figure 2, the Trinity

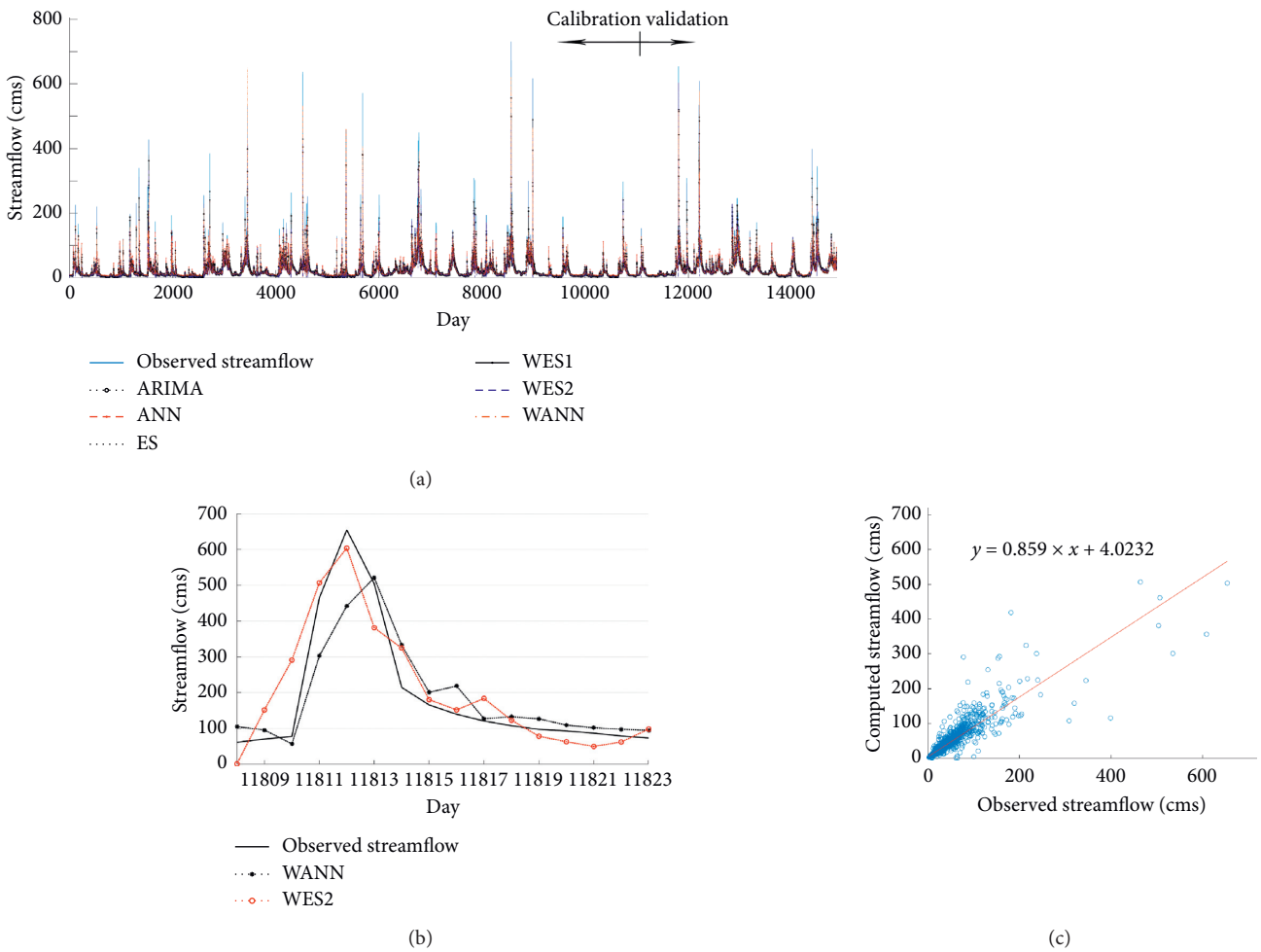

Figure 6: Observed/simulated daily streamflow of West Nishnabotna. (a) Whole. (b) Detail. (c) Verification scatter plot of WES_2.

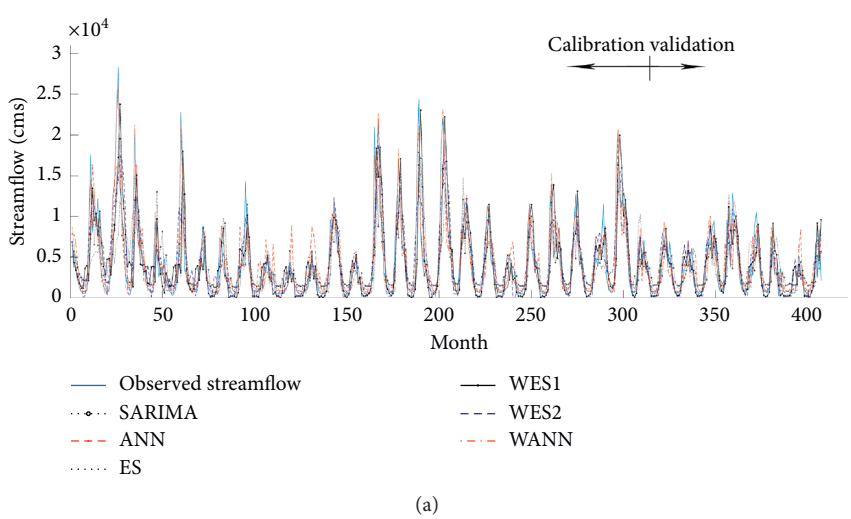

Figure 7: Continued.

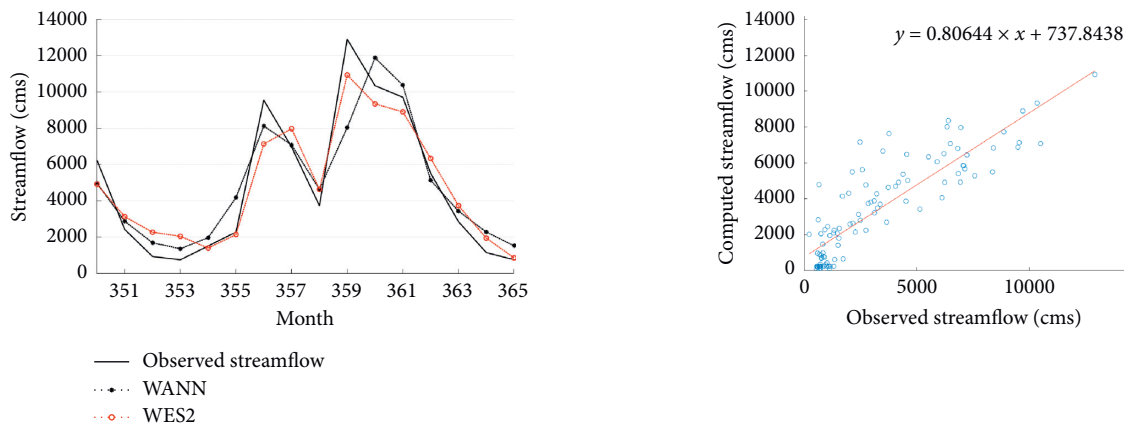

(b) (c)

Figure 7: Observed/simulated monthly streamflow of Trinity. (a) Whole. (b) Detail. (c) Verification scatter plot of WES_2.

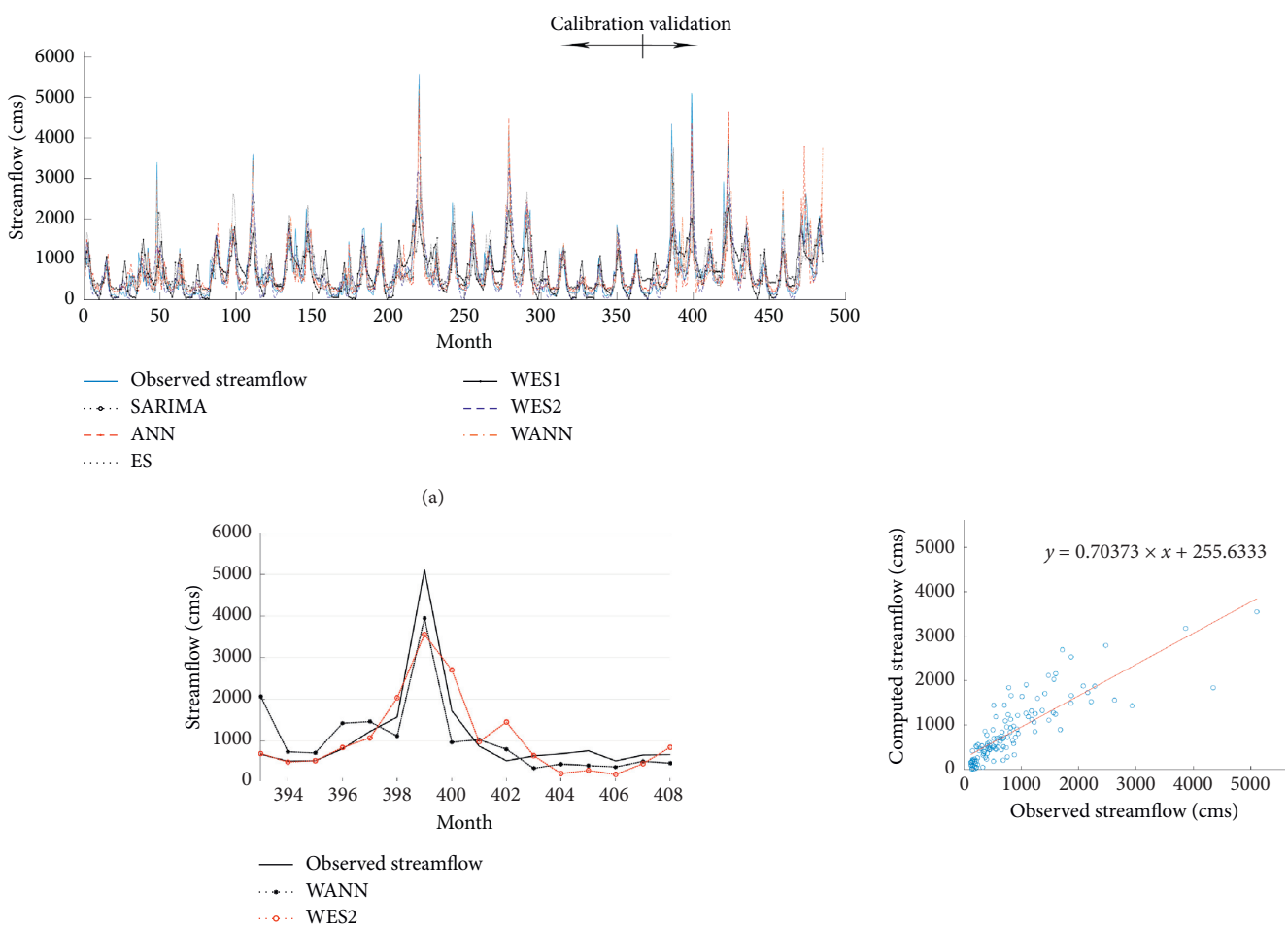

(a) (b) (c)

Figure 8: Observed/simulated monthly streamflow of West Nishnabotna. (a) Whole. (b) Detail. (c) Verification scatter plot of WES_2.

River posed a more powerful "autoregressive characteristic" than the West Nishnabotna River. In fact, time-series within moderate "autoregressive characteristic" show relatively weaker performance in the modeling process. However, it should be mentioned that WT contributes to the more enhancement of performance for the cases that have a moderate autoregressive. So, in this study, WT led to the enhancement of efficiency for West Nishnabotna River

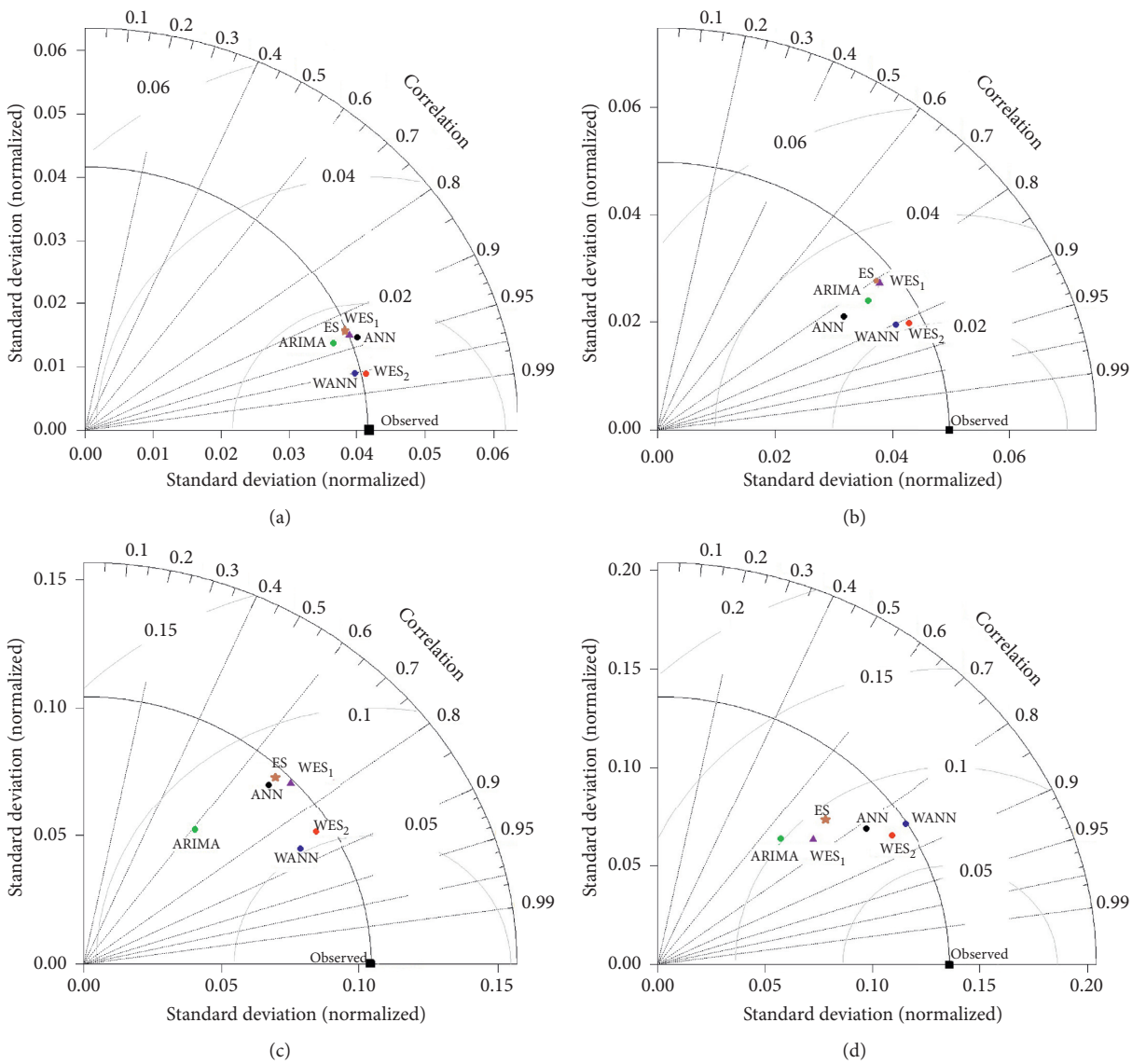

Figure 9: Taylor diagrams of the streamflow models. (a) Daily streamflow of Trinity. (b) Daily streamflow of West Nishnabotna. (c) Monthly streamflow of Trinity. (d) Monthly streamflow of West Nishnabotna.

streamflow modeling, which was more than that for the Trinity River.

The hydrological processes such as streamflow include several lumped and physical-based parameters, and it will be quite impossible to perform exact estimation of each parameter of the process. As a result, the black-box modeling can be more effective than the fully distributed models because of complex unknown and abstruse factors involved in streamflow nature. The black-box modeling (such as the present modeling) is case sensitive, and although the same methodology can be applied to other cases, the results and calibrated parameters cannot be similarly used for other cases. However, as presented in this study by applying to two different cases, it will be possible to apply the presented methodology to other watersheds by calibrating the parameters of the models. Although it seems the proposed methodology may include a high degree of freedom (the ES parameters selection, mother wavelet selection, level of decomposition, etc.), no need to calibrate all because some of them (e.g., wavelet type, mother wavelet type, and decomposition level) may be determined by prior knowledge (according to the physics of the process) or by referring to the literature [30].

Regarding the amount of data for streamflow modeling, this can be seen from two different aspects: diversity of datasets (having data from several cases and watersheds) and the length of the data itself (for each case). Referring to the aim of this study (which is to introduce a newly proposed methodology in streamflow modeling), it is revealed that at least one case study is needed to verify the applicability of the proposed model, and then, others may apply to other cases. In this way, the methodology was applied on two distinct case studies to see the performance and validity of the proposed model at different conditions. In spite of the

different hydrological natures of these two case studies, results showed the priority of the model (WES_2) and its capability in streamflow modeling. However, regarding the length of the used dataset, the dataset includes about 35 years of daily record; referring to literature in streamflow modeling, it is revealed that the length of data is suitable for the hydrological modeling [28, 46, 47]. It is noticeable that the longer period of historical records would be usually better for modeling hydrological phenomena, but the used historical records are taken due to their quality and the minimum gap existence in the records (particularly as the longest available period).

5. Conclusions

Due to the importance of hydrological time series and their complex intrinsic components (autoregressive, seasonality, and error), the performance of the hydrological models depends on their ability in dealing with these components. In this research, the capability of ARIMA (a classic autoregressive model), SARIMA (a classic autoregressive model which also considers uniperiodicity of the process), ES (a nonstationary but unifrequency modeling approach), ANN (a nonlinear model), WANN (a multifrequency preprocessed nonlinear model), and proposed WES with two different scenarios were examined for daily and monthly streamflow modeling of two different watersheds.

In the presented WES technique, after using WT for decomposing the observed time series, for the WES_1, only two input subseries were introduced to the model as input parameters, while the WES_2 used all decomposed subseries separately as the inputs of developed ES models. Finally, by aggregating the outputs of all ES models, the outputs of the streamflow modeling were obtained.

The WES_2 hybrid model performed better than other used models (single models) up to 30% and 10% (daily time scale) and up to 88% and 57% (monthly time scale), respectively, for West Nishnabotna and Trinity rivers. Also, the WES_2 in comparison with other methods presented better results in estimating the extreme points.

Comparing the results, it can be concluded that merging the capability of the WT method with ES (WES_2) and ANN (WANN) contributed to more accurate models to predict the streamflow. The performances of the WANN and WES_2 model were more or less in the same range but the computational cost for the WANN model was more that of WES_2 because ANN has more parameters than the ES model (e.g., input numbers, weights, biases, hidden neurons number, transfer functions' type, etc.).

To spatial assessment, modeling enhancement for the West Nishnabotna River was more than that of Trinity River due to its different geomorphological conditions, which was deliberated in Section 2.

The depicted reliable outcome of WES_2 application for streamflow forecasting recommends its employment for other processes such as wastewater treatment, air pollution, and groundwater. Moreover, applying the stated methodology of streamflow modeling on the other watersheds would be helpful for evaluating the impact of geomorphological conditions on the efficiency of the modeling.

Data Availability

The used streamflow time series were obtained from the USGS (https://waterwatch.usgs.gov/).

Conflicts of Interest

The authors declare that there are no conflicts of interest regarding the publication of this paper.

References

[1] L. Crochemore, M.-H. Ramos, F. Pappenberger, and C. Perrin, "Seasonal streamflow forecasting by conditioning climatology with precipitation indices," *Hydrology and Earth System Sciences*, vol. 21, no. 3, pp. 1573–1591, 2017.

[2] M. Rezaie-Balf and O. Kisi, "New formulation for forecasting streamflow: evolutionary polynomial regression vs. extreme learning machine," *Hydrology Research*, vol. 49, no. 3, pp. 939–953, 2017.

[3] L. J. Slater, G. Villarini, A. A. Bradley, and G. A. Vecchi, "A Dynamical Statistical Framework for Seasonal Streamflow Forecasting in an Agricultural Watershed," *Climate Dynamics*, vol. 53, pp. 1–17, 2017.

[4] H. Tao, A. O. Al-Sulttani, A. M. Salih Ameen et al., "Training and testing data division influence on hybrid machine learning model process: application of river flow forecasting," *Complexity*, vol. 2020, Article ID 8844367, 22 pages, 2020.

[5] Z. M. Yaseen, W. H. M. W. Mohtar, A. M. S. Ameen et al., "Implementation of univariate paradigm for streamflow simulation using hybrid data-driven model: case study in tropical region," *IEEE Access*, vol. 7, pp. 74471–74481, 2019.

[6] B. Mohammadi, F. Ahmadi, S. Mehdizadeh et al., "Developing novel robust models to improve the accuracy of daily streamflow modeling," *Water Resources Management*, vol. 34, no. 10, pp. 3387–3409, 2020.

[7] Y. Tikhamarine, D. Souag-Gamane, A. N. Ahmed, O. Kisi, and A. El-Shafie, "Improving artificial intelligence models accuracy for monthly streamflow forecasting using grey Wolf optimization (GWO) algorithm," *Journal of Hydrology*, vol. 582, Article ID 124435, 2020.

[8] J. D. Salas, J. W. Delleur, V. M. Yevjevich, and W. L. Lane, *Applied Modeling of Hydrologic Time Series*, Water Resources Publication, Littleton, Colorado, 1980.

[9] Q. Zhang, B.-D. Wang, B. He, Y. Peng, and M.-L. Ren, "Singular spectrum analysis and ARIMA hybrid model for annual runoff forecasting," *Water Resources Management*, vol. 25, no. 11, pp. 2683–2703, 2011.

[10] J. Adamowski, H. Fung Chan, S. O. Prasher, B. Ozga-Zielinski, and A. Sliusarieva, "Comparison of multiple linear and nonlinear regression, autoregressive integrated moving average, artificial neural network, and wavelet artificial neural network methods for urban water demand forecasting in Montreal, Canada," *Water Resources Research*, vol. 48, no. 1, 2012.

[11] J. Busch, D. Elixmann, P. Kühl et al., "State estimation for large-scale wastewater treatment plants," *Water Research*, vol. 47, no. 13, pp. 4774–4787, 2013.

[12] Z. M. Yaseen, H. Faris, and N. Al-Ansari, "Hybridized extreme learning machine model with salp swarm algorithm: a

novel predictive model for hydrological application," *Complexity*, vol. 2020, Article ID 8206245, 14 pages, 2020.

[13] C. D. Tankersley, W. D. Graham, and K. Hatfield, "Comparison of univariate and transfer function models of groundwater fluctuations," *Water Resources Research*, vol. 29, no. 10, pp. 3517–3533, 1993.

[14] J. V. Hansen and R. D. Nelson, "Neural networks and traditional time series methods: a synergistic combination in state economic forecasts," *IEEE Transactions on Neural Networks*, vol. 8, no. 4, pp. 863–873, 1997.

[15] T.-W. Kim and J. B. Valdés, "Nonlinear model for drought forecasting based on a conjunction of wavelet transforms and neural networks," *Journal of Hydrologic Engineering*, vol. 8, no. 6, pp. 319–328, 2003.

[16] H. Moeeni, H. Bonakdari, and I. Ebtehaj, "Integrated SARIMA with neuro-fuzzy systems and neural networks for monthly inflow prediction," *Water Resources Management*, vol. 31, no. 7, pp. 2141–2156, 2017.

[17] G. P. McCormick, "Communications to the editor-exponential forecasting: some new variations," *Management Science*, vol. 15, no. 5, pp. 311–320, 1969.

[18] E. S. Gardner, "Exponential smoothing: the state of the art," *Journal of Forecasting*, vol. 4, no. 1, pp. 1–28, 1985.

[19] R. J. Hyndman, A. B. Koehler, R. D. Snyder, and S. Grose, "A state space framework for automatic forecasting using exponential smoothing methods," *International Journal of Forecasting*, vol. 18, no. 3, pp. 439–454, 2002.

[20] J. W. Taylor, "Exponential smoothing with a damped multiplicative trend," *International Journal of Forecasting*, vol. 19, no. 4, pp. 715–725, 2003.

[21] E. S. Gardner, "Exponential smoothing: the state of the art-Part II," *International Journal of Forecasting*, vol. 22, no. 4, pp. 637–666, 2006.

[22] R. Hyndman and G. Athanasopoulos, *Forecasting: Principles and Practice: Notes*, The University of Western Australia, Perth, Australia, 2014.

[23] J. K. Ord, A. B. Koehler, R. D. Snyder, J. K. Ord, A. B. Koehler, and R. D. Snyder, "Estimation and prediction for a class of dynamic nonlinear statistical models," *Journal of the American Statistical Association*, vol. 92, no. 440, pp. 1621–1629, 1997.

[24] A. M. Melesse, S. Ahmad, M. E. Mcclain, X. Wang, and Y. H. Lim, "Suspended sediment load prediction of river systems: an artificial neural network approach," *Agricultural Water Management*, vol. 98, no. 5, pp. 855–866, 2011.

[25] E. Sharghi, V. Nourani, H. Najafi, and S. Soleimani, "Wavelet-exponential smoothing: a new hybrid method for suspended sediment load modeling," *Environmental Processes*, vol. 6, no. 1, pp. 191–218, 2019.

[26] I. Ahmadianfar, M. Jamei, and X. Chu, "A novel hybrid wavelet-locally weighted linear regression (W-LWLR) model for electrical conductivity (EC) prediction in water surface," *Journal of Contaminant Hydrology*, vol. 232, Article ID 103641, 2020.

[27] M. Jamei, I. Ahmadianfar, X. Chu, and Z. M. Yaseen, "Prediction of surface water total dissolved solids using hybridized wavelet-multigene genetic programming: new approach," *Journal of Hydrology*, vol. 589, Article ID 125335, 2020.

[28] D. Nalley, J. Adamowski, B. Khalil, and A. Biswas, "A comparison of conventional and wavelet transform based methods for streamflow record extension," *Journal of Hydrology*, vol. 582, Article ID 124503, 2020.

[29] L. Ni, D. Wang, V. P. Singh et al., "Streamflow and rainfall forecasting by two long short-term memory-based models," *Journal of Hydrology*, vol. 583, Article ID 124296, 2020.

[30] V. Nourani, A. Hosseini Baghanam, J. Adamowski, and O. Kisi, "Applications of hybrid wavelet-Artificial Intelligence models in hydrology: a review," *Journal of Hydrology*, vol. 514, pp. 358–377, 2014.

[31] B. Cannas, A. Fanni, L. See, and G. Sias, "Data preprocessing for river flow forecasting using neural networks: wavelet transforms and data partitioning," *Physics and Chemistry of the Earth, Parts A/B/C*, vol. 31, no. 18, pp. 1164–1171, 2006.

[32] C.-C. Kuo, T. Y. Gan, and P.-S. Yu, "Wavelet analysis on the variability, teleconnectivity, and predictability of the seasonal rainfall of taiwan," *Monthly Weather Review*, vol. 138, no. 1, pp. 162–175, 2010.

[33] L. L. Wehmeyer, F. H. Weirich, and T. F. Cuffney, "Effect of land cover change on runoff curve number estimation in Iowa, 1832-2001," *Ecohydrology*, vol. 4, no. 2, pp. 315–321, 2011.

[34] P. S. Addison, *The Illustrated Wavelet Transform Hanbook: Introductory Theory and Applications in Science, Engineering, Medicine and Finance*, CRC Press, Boca Raton, FL, USA, 2016.

[35] G. E. P. Box, G. M. Jenkins, G. C. Reinsel, and G. M. Ljung, *Time Series Analysis: Forecasting & Control*, Wiley, Hoboken, NJ, USA, 2016.

[36] ASCE, "Artificial neural networks in hydrology. II: hydrologic applications," *Journal of Hydrologic Engineering*, vol. 5, no. 2, pp. 124–137, 2000.

[37] E. Sharghi, V. Nourani, H. Najafi, and A. Molajou, "Emotional ANN (EANN) and Wavelet-ANN (WANN) approaches for markovian and seasonal based modeling of rainfall-runoff process," *Water Resources Management*, vol. 32, no. 10, pp. 3441–3456, 2018.

[38] R. Weron, *Modeling and Forecasting Electricity Loads*, John Wiley & Sons, Hoboken, NJ, USA, 2006.

[39] R. Hyndman and Y. Khandakar, "Automatic time series forecasting: the forecast package for R," *Journal Of Statistical Software*, vol. 27, no. 3, pp. 1–22, 2008.

[40] E. Stellwagen, "Exponential smoothing: the workhorse of business forecasting," *Foresight*, vol. 27, no. 27, pp. 23–28, 2012.

[41] M. Natrella, *NIST/SEMATECH E-Handbook of Statistical Methods*, NIST/SEMATECH, Austin, TX, USA, 2002.

[42] E. Sharghi, V. Nourani, A. Molajou, and H. Najafi, "Conjunction of emotional ANN (EANN) and wavelet transform for rainfall-runoff modeling," *Journal of Hydroinformatics*, vol. 21, no. 1, pp. 136–152, 2019.

[43] D. R. Legates and G. J. McCabe, "Evaluating the use of "goodness-of-fit" Measures in hydrologic and hydroclimatic model validation," *Water Resources Research*, vol. 35, no. 1, pp. 233–241, 1999.

[44] V. Nourani, T. R. Khanghah, and A. H. Baghanam, "Application of entropy concept for input selection of wavelet-ANN based rainfall-runoff modeling," *Journal of Environmental Informatics*, vol. 26, no. 1, pp. 52–70, 2015.

[45] K. E. Taylor, "Summarizing multiple aspects of model performance in a single diagram," *Journal of Geophysical Research: Atmospheres*, vol. 106, no. D7, pp. 7183–7192, 2001.

[46] Y.-M. Zhu, X. X. Lu, and Y. Zhou, "Suspended sediment flux modeling with artificial neural network: an example of the Longchuanjiang River in the Upper Yangtze Catchment, China," *Geomorphology*, vol. 84, no. 1-2, pp. 111–125, 2007.

[47] Y. Sun, J. Niu, and B. Sivakumar, "A comparative study of models for short-term streamflow forecasting with emphasis on wavelet-based approach," *Stochastic Environmental Research and Risk Assessment*, vol. 33, no. 10, pp. 1875–1891, 2019.

Hindawi
Complexity
Volume 2021, Article ID 6631564, 14 pages
https://doi.org/10.1155/2021/6631564

Research Article

Bayesian Regularized Neural Network Model Development for Predicting Daily Rainfall from Sea Level Pressure Data: Investigation on Solving Complex Hydrology Problem

Lu Ye,[1] Saadya Fahad Jabbar,[2] Musaddak M. Abdul Zahra,[3,4] and Mou Leong Tan[5]

[1]*School of Computer Science, Baoji University of Arts and Sciences, Baoji 721007, China*
[2]*College of Education for Human Science-ibn Rushed, University of Baghdad, Baghdad, Iraq*
[3]*Computer Techniques Engineering Department, Al-Mustaqbal University College, 51001 Hillah, Babil, Iraq*
[4]*Electrical Engineering Department, College of Engineering, University of Babylon, Hilla, Babil, Iraq*
[5]*Geoinformatic Unit, Geography Section, School of Humanities, Universiti Sains Malaysia, 11800 USM, Pulau Pinang, Malaysia*

Correspondence should be addressed to Mou Leong Tan; mouleong@usm.my

Received 9 November 2020; Revised 18 December 2020; Accepted 18 March 2021; Published 1 April 2021

Academic Editor: Zaher Mundher Yaseen

Prediction of daily rainfall is important for flood forecasting, reservoir operation, and many other hydrological applications. The artificial intelligence (AI) algorithm is generally used for stochastic forecasting rainfall which is not capable to simulate unseen extreme rainfall events which become common due to climate change. A new model is developed in this study for prediction of daily rainfall for different lead times based on sea level pressure (SLP) which is physically related to rainfall on land and thus able to predict unseen rainfall events. Daily rainfall of east coast of Peninsular Malaysia (PM) was predicted using SLP data over the climate domain. Five advanced AI algorithms such as extreme learning machine (ELM), Bayesian regularized neural networks (BRNNs), Bayesian additive regression trees (BART), extreme gradient boosting (xgBoost), and hybrid neural fuzzy inference system (HNFIS) were used considering the complex relationship of rainfall with sea level pressure. Principle components of SLP domain correlated with daily rainfall were used as predictors. The results revealed that the efficacy of AI models is predicting daily rainfall one day before. The relative performance of the models revealed the higher performance of BRNN with normalized root mean square error (NRMSE) of 0.678 compared with HNFIS (NRMSE = 0.708), BART (NRMSE = 0.784), xgBoost (NRMSE = 0.803), and ELM (NRMSE = 0.915). Visual inspection of predicted rainfall during model validation using density-scatter plot and other novel ways of visual comparison revealed the ability of BRNN to predict daily rainfall one day before reliably.

1. Introduction

Rainfall decides agricultural activities, ecology, and environment of a region. Therefore, it is considered as the key factor of social and economic development of any region [1]. At the same time, rainfall is the most influencing factor for different kinds of natural hazards [2]. Excess rainfall and floods are the most common natural hazards all over the earth [3]. Rainfall deficit and droughts are the most devastating disasters in terms of economic damages [4]. Rainfall is also the defining factor of many other kinds of natural hazards like landslides, soil erosion, and river bank subsidence [5, 6]. Therefore, the forecasting of rainfall is the major topic of interest to hydrologists and disaster management scientists for many decades [7, 8].

Numerous attempts have been made for forecasting rainfall using various physical, empirical, and physio-empirical models. Such models have been used for forecasting rainfall at annual, seasonal, monthly, and daily scale in different regions of the world [9, 10]. Physical models are developed considering the synoptic climate and physical mechanism of interactions of different climatic variables causing rainfall in a region [11]. Mathematical models are developed to represent those physical processes to forecast rainfall in physical models. Such models are generally complex and need data and information about many land-

ocean-atmospheric variables. Still, the physical models are often not very successful in reliable forecasting of rainfall as it often makes the simple approximation of complex physical phenomena for model development [12]. Empirical models based on statistical methods have been employed as an alternative to physical models [13]. Such models are generally developed focusing a certain climate variable only like forecasting rainfall based on the statistical relationship of rainfall with its antecedent values or with other atmospheric variables related to it. The statistical model is always region-specific which means the model developed based on the statistical relationship of the regional rainfall with other atmospheric variables is only applicable for the region [14]. Therefore, such models are also known as empirical models. The advantages of empirical models are easy development and implementation and better accuracy compared with physical models in most of the cases. However, the major drawback of the empirical model is their complete dependency on historical data used for their development. Therefore, they cannot simulate rainfall for an unknown situation [15, 16]. For example, the rapid changes in rainfall that earth experienced in recent years and projected for the future cannot be forecasted by empirical models accurately as the models were not developed with such large variability in data [17]. Physical models are the option for forecasting in such situation. To tradeoff the disadvantages of both types of the modeling approach, recent focus is to develop physical-empirical models where empirical models are developed based on the variables physically responsible for the climate of the region. Therefore, more emphasis has been given on the development of the physical-empirical model for forecasting rainfall [18, 19]. Yim et al. [20] developed a physical-empirical model for the prediction of summer rainfall in southern China using several ocean-atmospheric variables. Yim et al. [9] used sea surface temperature in a regression model for the development of a physical-empirical model for the prediction of rainfall in Taiwan. Chen and Sun [21] used the physical-empirical model for performance improvement of a dynamical model in seasonal rainfall forecasting using sea level pressure (SLP) data. Pour et al. [22] employed SLP in development of physical-empirical models for the development of seasonal rainfall in Peninsular Malaysia.

Generally, statistical models are developed using different forms of regressions ranging from linear to higher-order polynomial (nonlinear) regressions. However, the relationship of rainfall with atmospheric variables responsible for rainfall is often highly intriguing and cannot be represented using generally used statistical methods. Machine learning (ML) algorithms are often used for developing complex regression analysis [23–25]. Therefore, the development of ML-based physical-empirical forecasting models has grown very fast in recent years.

Forecasting daily rainfall in tropical region is much different compared with other regions due to the presence of highly extreme values and year-round rainfall. Use of more efficient ML algorithms is required for forecasting daily rainfall in such region. Some of the ML models have shown their superiority over others in solving environmental prediction problems. Though there is no single method that shows consistent excellence in solving all kinds of environmental problems in many regions, overall it has been noticed that some models often perform better in solving complex prediction problems which include extreme learning machine (ELM), Bayesian regularized neural networks (BRNNs), Bayesian additive regression trees (BART), extreme gradient boosting (xgBoost), and hybrid neural fuzzy inference system (HNFIS) [26–31]. Therefore, the comparative performance of these efficient algorithms in forecasting daily rainfall can provide the best forecasting model.

The main research objective is to develop a robust machine learning model for forecasting daily rainfall of East Coast of Peninsular Malaysia (ECPM). The ECPM is considered as the most vulnerable region of the peninsula to different kinds of rainfall-driven hazards [32]. Hence, a reliable rainfall pattern forecasting is highly essential for climate sustainable development of the region. Across large number of studies have been conducted for rainfall forecasting in Peninsular Malaysia, only one attempt was made for forecasting rainfall in Peninsular Malaysia (PM) using physical-empirical models [22]. However, the previous study of Pour et al. [1] was limited to the seasonal forecasting only. To the best knowledge of the current study, this is the first attempt to use an array of sophistical ML algorithms for the development of physical-empirical models for forecasting daily rainfall of PM.

2. East Coast of Peninsular Malaysia (ECPM)

The ECPM (Figure 1) is the most interesting region of PM in terms of rainfall and rainfall-driven hydrological hazards [33]. The area has an undulating topography which varies from 4.0 m in the coastline to 2270.0 m in the interior mountainous region. A considerable part of the interior of the ECPM is mountainous, which influences the climate of the region. The region is characterized by high uniform temperature, high humidity, and copious rainfall [34]. The area receives a significant amount of rainfall even in the driest month. The study area experiences two monsoon seasons, namely, the northeast (NE) monsoon from the mid of October to end of February and the southwest (SW) monsoon from April to September [35]. The months of March and October are intermonsoonal transitional periods. The eastern coastal region is wetter compared with other parts of PM. It receives an annual average rainfall of 2800 mm. Monthly variations in rainfall in ECPM are shown in Figure 2. Heavy rainfall in the region occurs during NE monsoon. Maximum rainfall in a year is usually recorded in November or December. Some parts of the study area suffer flooding at this time of year [36]. On the other hand, the longest dry spell in a year is observed during SW monsoon, particularly in June and July.

The mean temperature in ECPM is found more or less uniform throughout the year. Seasonal variation of mean temperature (27.0°C) is always less than 2.0°C. The daily maximum temperature in the study area varies from 29.0°C in January to 33.0°C in April. The minimum temperature varies from 23.0°C in January-February to 25°C in May [37].

Several rivers originate in the mountainous interior region of ECPM. Due to high variation in topography and a high amount of rainfall, the region has a dense river network.

3. Description of the Data Used

The APHRODITE gridded dataset was used as a proxy to observed data. APHRODITE rainfall was developed using gauge precipitation data obtained from the Global Telecommunication System (GTS) network and other hydrometeorological in situ records [38]. It has been developed based on a new interpolation technique with accurate long-term gridded orographic precipitation for Asia [38]. The data are available at http://aphrodite.st.hirosakiu.ac.jp/product/APHRO_V1101EX_R1/APHRO_MA/025deg_nc/.

The recently released NCEP/NCAR ERA2 reanalysis data of SLP with a resolution of $0.25^{\circ} \times 0.25^{\circ}$ were used as predictors for the prediction of rainfall. The NCEP/NCAR reanalysis provides datasets of various atmospheric variables at 17 different pressure levels [39]. The NCEP dataset has been utilized for the development of prediction models [40]. Rainfall in ECPM mostly occurs due to moist air from the ocean. The wind circulation in the region depends on SLP. Therefore, it was considered in the present study for the development of the rainfall prediction model. The climate domain consisted of 2730 grid points for the extraction of probable predictors. The climate domain and the grid points from where SLP data were collected are shown in Figure 3. The NCEP SLP data are available at https://www.ncdc.noaa.gov/data-access/model-data/model-datasets/reanalysis-1-reanalysis-2.

APHRODITE rainfall data are available for the period 1951–2015 while the NCEP ERA2 reanalysis SLP data are available for the period 1948 to present. Therefore, a common period of 1951–2015 was considered in the present study for model development and validation. APHRODITE daily rainfall and NCEP ERA daily SLP data for the period 1951–2015 were collected from the corresponding websites.

4. Description of Employed Machine Learning Algorithms

Five advanced AI algorithms such as ELM, BRNN, BART, EGB, and HNFIS were used considering the complex relationship of rainfall with SLP. The SLPs over the climate domain having a significant correlation with daily rainfall of ECPM were used to compute their principal components and selection of inputs. The APHRODITE rainfall of all the grid points over the ECPM was average to prepare the daily rainfall of the area. The ML models were used for the prediction of areal averaged daily rainfall of the region. The description of the ML models used in this study is given in the following subsections.

4.1. Extreme Learning Machine (ELM). The ELM model was developed following the structure of a feedforward neural network (FNN) [41]. Basic difference of ELM and FFN is that ELM uses the Moore–Penrose generalized inverse algorithm to calculate the weights of hidden neurons in contrast to gradient algorithms of FFN [42]. A general structure of ELM is shown in Figure 4.

The algorithm of ELM is very simple. It takes the predictors as inputs (x) and multiplies them with the estimated weights (w), adds bias (b), applies activation function (g), and repeats the steps for a time equal to the number of layers used to get the output as follows:

$$f_L(x) = \sum_{i=1}^{L} \beta_i g(w_i * x_i + b_i), \quad j = 1, 2, \ldots, N, \tag{1}$$

in which L represents the number of hidden layers, N is training data size, and β is the weight multiplied with the output of hidden layer to get the output, which is calculated as the ratio of hidden layer output matrix H and target matrix T. The H and T can be expressed as follows:

$$T = \begin{bmatrix} t_1^T \\ \vdots \\ t_N^T \end{bmatrix}_{N\times 1}, \qquad H = \begin{bmatrix} g(w_1 * x_1 + b_1) & \ldots & g(w_L * x_i + b_L) \\ \vdots & \cdots & \vdots \\ g(w_1 * x_N + b_i) & \cdots & g(w_L * x_N + b_L) \end{bmatrix}_{N\times L}. \tag{2}$$

The obtained output using equation (1) is back-propagated to the network to repeat the process until the desired level of error in prediction achieved. ELM has a good nonlinear adaptive capability to overcome the limitations of many other ML algorithms [43].

4.2. Bayesian Regularized Neural Network (BRNN). BRNN is a version of an artificial neural network (ANN), which is much robust compared with conventional ANN [44]. The robustness in BRNN is achieved due to Bayesian regularization of ANN parameters. A common error function (E_D) of ANN using early stopping can be expressed as follows:

$$E_D(D \mid w, M) = \sum_{i=1}^{n} (t_i - \hat{t}_i)^2, \tag{3}$$

where w is the weight, M is the ANN structure, n is the training data size, and t_i is i-th target while $\hat{t}_i$ is the output.

Immature convergence of ANN causes overfitting of the model. A regularization of ANN using the Bayesian method helps optimization of ANN parameters using prior values of ANN parameters. For this purpose, an additional term (E_w) is included in objective function in BRNN as follows:

$$E_D(D \mid w, M) = \sum_{i=1}^{n} (t_i - \hat{t}_i)^2 + E_w, \tag{4}$$

where E_w is used to penalize the unrealistic weights to have a better generalization and gradual conversion. A gradient-based optimization method is used to minimize the function:

$$F = \beta E_D(D \mid w, M) + \alpha E_w(w \mid M), \quad (5)$$

in which $E_w(w \mid M)$ is the sum of the square of ANN architecture and α and β represent the hyperparameters to be optimized.

BRNN can reveal theoretically complex input-output relationship and thus considered as an efficient predictive model [28, 29].

4.3. Bayesian Additive Regression Trees (BART). BART is an ensemble of easily adjustable regression models [26]. It uses the basic structure of random forest (RF) [45], but the outcomes of the trees are estimated using a Bayesian inferential system. This allows estimation of uncertainty and regularization of model parameters to enhance the capability of the conventional tree-based regression method.

The procedure used by BART to improve the performance of RF is like the gradient boosting (GB) where many weak models are used to learn the problem [46]. In RF, the outcomes of all trees are averaged whereas in GB, the outcomes are adjusted using constants [47]. The novelty of BART is the use of Bayesian framing. In BART, priors are used to achieve the posterior of the outcomes of the trees. This provides a higher performance of the model. Besides, a sophisticated penalty system is used which helps in parameter regularization efficiently [26].

4.4. Extreme Gradient Boosting (xgBoost). Gradient boosting (GB) integrates the outcomes of many weak models for prediction [27]. This improves or boosts the prediction capability of weak models, and thus it is called GB. The xgBoost is an advanced version of GB where model parameters are regularized properly to enhance its performance [48]. The major advantage of xgBoost is the combination of both high speed and good efficiency. It is generally found to outperform many conventional models when the prediction is done using large datasets [49].

The basic structure of xgBoost is like a random forest where multiple decision trees are generated using data samples following either bagging or boosting method [50]. However, the main difference is in the learning process. In xgBoost, the model tries to learn from the mistake in the previous step. It means, in each step, it focuses on the part which is hard to learn or the model failed to predict properly. It tries to correct the mistake in the previous step by an attempt to solve the hard part of problem. A simple diagram of xgBoost is shown in Figure 5. An ensemble of models is used in this process where different models are used to solve different parts. The more error by a model indicates that the model is weak or the problem is hard enough to solve by this model. The xgBoost tried to improve this weak model to improve the total prediction capability of the model. In each step, it estimates the error and focuses on the part which generates a higher error and try to solve the problem until the desired level of error is achieved [51].

4.5. Hybrid Neuro Fuzzy Inference System (HNFIS). The HNFIS is developed by hybridization of the fuzzy inference system (FIS) with artificial neural network (ANN) [30], where the parameters of FIS were optimized using ANN which enables the system to learn the problem systematically and helps to enhance the predictive performance of the model. ANN has a good capacity to learn automatically. However, it cannot acquire outcomes efficiently. The FIS cannot learn automatically like ANN, but it can acquire the outcomes efficiently through fuzzy logic. Therefore, the hybridization of ANN with FIS can improve the learning capability of the nonlinear problem [52].

A typical HNFIS system is presented using the diagram in Figure 6. It is very similar to the adaptive neuro fuzzy inference system (ANFIS) where a multilayer feedforward ANN is the core [53]. The AND operation is employed first, followed by product, normalization, and sum operations, and finally centroid to get the output. However, the weights connecting the nodes are defined using fuzzy sets. The least-squares approach is used to decide the set of weights. The weights are adjusted using fuzzy rules to reduce model error [54].

4.6. Generation of Model Inputs. The SLP of all the NCEP grid points over the selected climate domain was correlated with the areal averaged daily APHRODITE rainfall over the ECPM. Spearman rank correlation (Spearman, 1904) was used considering high skewness in daily rainfall data [55]. The significance of the correlation was estimated at a significance level of 0.5 ($p < 0.05$). The SLP data which found significantly correlated with the areal average rainfall of ECPM were used to estimate their principal components (PCs). The principal component analysis (PCA) allows reduction of dimensionality in data [56]. The PCs which are found to represent the maximum variability in SLP data were used as input. In this study, the above procedure was conducted for SLPs for 1- to 3-day lags and the PCs of each lag were used as model input. The PCA has been found as an efficient method for the selection of inputs from a large dataset in previous studies [57, 58].

4.7. Development of Models and Assessment of Model Performance. APHRODITE daily rainfall and PCs of daily SLP data for the period 1951–2015 were used for the development of the model. There is no universal rule of using the proportion of data for training and validation. However, conventionally 70% of available data are used for model training. Following the generally adopted division rule, 70% of time series data (01 January 1951 to 30 June 1995) were used to train the models while the data for the period July 1995 to December 2015 were used for model validation.

The performance of the ML model depends on optimum values of model parameters. In this study, a k-fold validation was used for the optimization of ML model parameters, where k was considered as 10. Data were shuffled in each

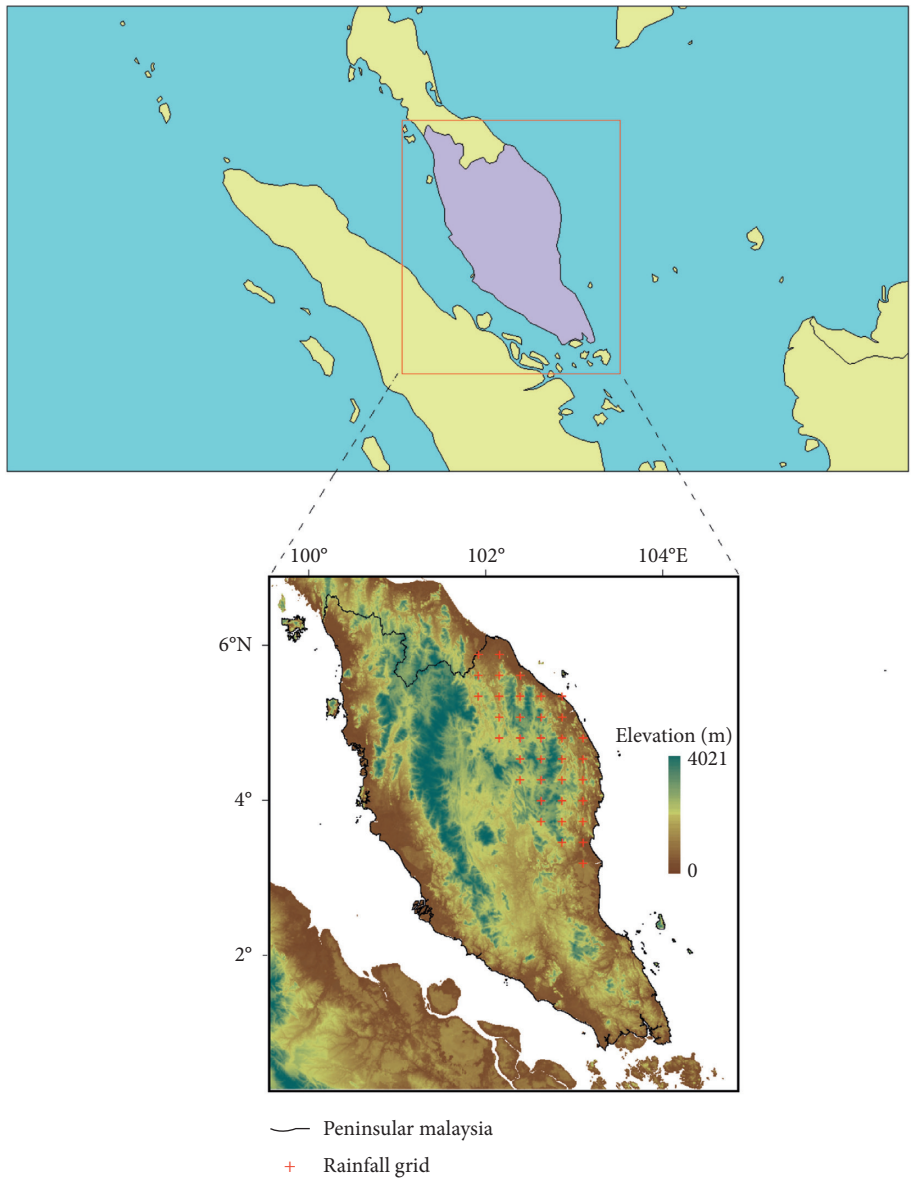

Figure 1: Location of Peninsular Malaysia in Southeast Asia. The elevation and location of grid points from where rainfall data were extracted.

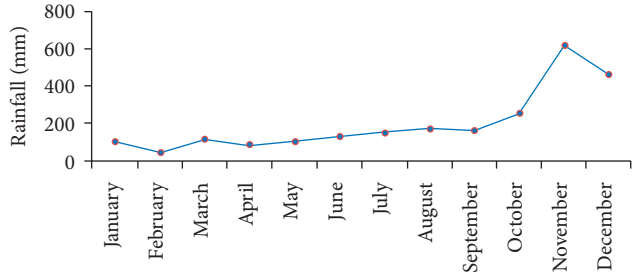

Figure 2: Mean monthly rainfall in the study area (1961–2000).

iteration so that all the data are used for model validation. The parameter values estimated in each iteration were averaged to get the optimum parameters. In this study, two parameters for ELM (number of hidden units and activation function), three parameters for BRNN (α, β, and the number of neurons), five parameters for BART (number of trees, prior boundary, base terminal not, power terminal node, and degrees of freedom), four parameters for xgBoost (number

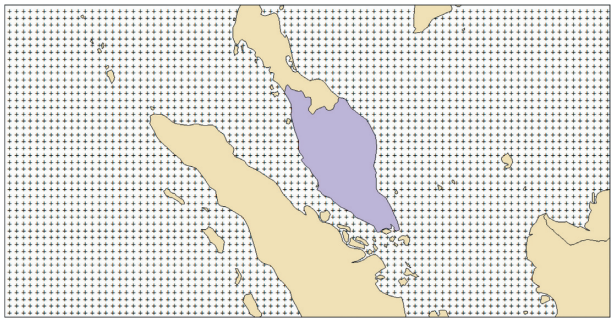

Figure 3: Climate domain considered for extraction of sea level pressure data for the prediction of rainfall in Peninsular Malaysia.

of boosting iterations, two regularization parameters, and learning rate), and two HNFIS parameters (number of fuzzy terms and maximum iterations) were optimized.

The *caret* package of statistical software *R* was used for this purpose. All the models were also developed using different packages available in *R*.

Two error metrics, namely, mean absolute error (MAE) and normalized root mean square error (NRMSE) and two association metrics such as Wilmott's modified index of agreement (WI) and Kling–Gupta efficiency (KGE) were used to assess the performance of the models statistically [59, 60]. The model performance was evaluated during the validation period to show the relative performance of the models in predicting an areal average of daily rainfall in ECPM with a lag time of one day. The mathematical formulas are as follows:

$$\begin{aligned} \mathrm{MAE} &= 1/N \sum_{i=1}^{N} \left| y_f - y_o \right|, \\ \mathrm{NRMSE} &= \frac{\sqrt{1/N \sum_{i=1}^{N} \left(y_f - y_o \right)^2}}{\overline{y_o}}, \\ \mathrm{WI} &= 1 - \frac{\sum_{i=1}^{N} \left| y_f - y_o \right|}{\sum_{i=1}^{N} \left| y_f - \overline{y_o} \right| + \left| y_o - \overline{y_o} \right|}, \\ \mathrm{KGE} &= 1 - \sqrt{(r-1)^2 + (\gamma - 1)^2 + (\beta - 1)^2}, \end{aligned} \tag{6}$$

where N is the number of observations, y_f is the forecasted values, y_o is the observed values, $\overline{y_f}$ and $\overline{y_o}$ are the mean values of the forecasted and observed, β is the bias, γ is the fraction of the coefficient of variation, and r is the linear correlation.

5. Results and Discussion

5.1. Analysis of SLP Data for Generation of Inputs. The areal average rainfall of ECPM was first correlated with different lags of the SLP data at different NCEP grid points over the climate domain. Obtained results are presented in Figure 7. The correlation of rainfall with 1- to 3-lag days is presented in three maps in the figure. The colour ramp in the maps is used to show the positive (negative) correlation. The significant correlation ($p < 0.05$) is presented with dots. The figure shows that rainfall in ECPM is positively correlated with SLP in the north and negatively correlated with SLP in the south. The differences in SLP cause movement of air over the region. The moist air from the sea when enters the land causes rainfall. Therefore, SLP data can be used for prediction of rainfall in ECPM. The SLP data of nearly 2321 to 2486 are found to correlate with rainfall for different lags. Such a big number of variables cannot be used for the development of the model. Therefore, PCA was used to reduce the dimensionality of data.

The significantly correlated SLP data were used to estimate their PCs using PCA. Obtained PCs for one-day lag SLP are shown in Figure 8. The scree plot of the first 10 PCs for one-day lag SLP is shown in Figure 8(a). The figure shows that the first PC explains most of the variance compared with other PCs. The eigenvalue at 1 is shown using a red dashed horizontal line in the figure. It can be seen from the figure that the first 5 PCs are above the red line. The cumulative variance plot of the first 10 PCs is shown in Figure 8(b). The vertical blue dashed line represents the cutoff line for PC-5. The results showed that the first 5 PCs represent 99% of the variance in the SLP data over the climate domain. The first PC covered 91.7% of variability, the first 2 PCs covered 95.4% of variability, the first 3 PCs covered 98.3% of the variability, and so on. The results indicated increasing of PCs after the first PC does not increase the explained variability by the PCs significantly. Similar results were obtained for SLP with 2- and 3-day lags. The first PC along was able to explain more than 91% of the variability in data for all the three lags. The higher number of PCs as inputs increases the complexity of the model. Therefore, to make a parsimonious model, only the first PC of each lag was selected. These three PCs were finally used as input to train the models.

5.2. Comparison of Model Performance Using Statistical Metrics. The performance of the models was first evaluated using statistical metrics. Obtained results are given in Table 1. Only two error and association metrics were used as they can assess the capability of the models in replicating all the aspects including bias in mean and variability and association in rainfall amount and volume. For a better comparison of the relative performance of the model based on all the metrics together, the results are also presented using a radar chart in Figure 9.

The results showed that none of the models was able to attain very high metric values such as KGE or WI above 0.8.

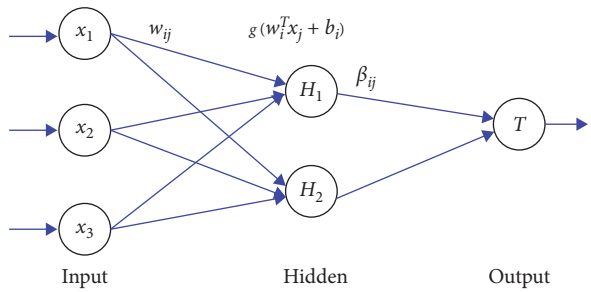

Figure 4: Schematic diagram showing the basic structure of an extreme learning machine.

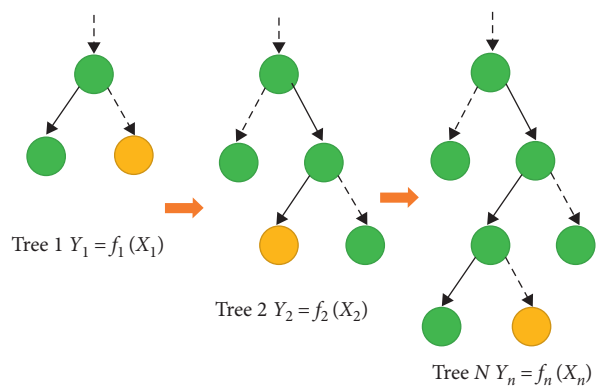

Figure 5: Schematic diagram explaining the gradient boosting algorithm.

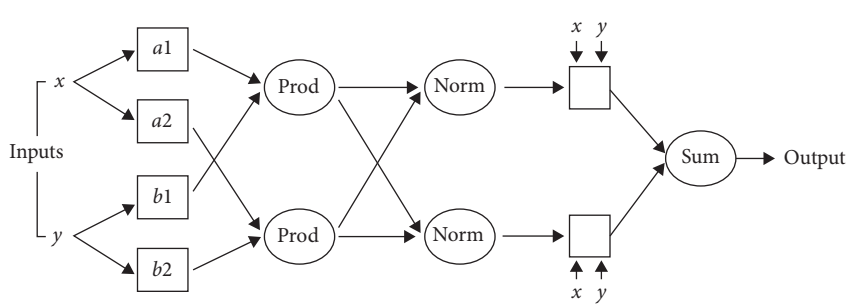

Figure 6: The basic structure of a hybrid neuro fuzzy inference system.

However, metric values obtained by the models should be judged considering the amount of sample size of data. The obtained statistics were estimated for the validation period July 1995 to December 2015 which means the sample size of 7120. Computation of any statistical metrics depends on sample size (n), where metric value decreases with the increase in n, even when the model behave the same. Therefore, the KGE or WI values more than 0.5 should be considered very good for this high amount of data size. This can be justified with a small amount of error in terms of MAE and NRMSE.

Overall, all the models were found to perform similarly with a slightly better or less performance in terms of different indices. However, BRNN was found to perform best in term of all metrics. Figure 9 shows lower values of BRNN in terms of error metrics and high values in terms of association-based metrics. The HNFIS can be considered as the second-best model followed by BART and xgBoost, while ELM showed the least performance.

It is a well-established fact that the performance of ML models depends on the data used. There is no universal ML model which shows good performance for all kinds of data. It is not possible to justify the better performance of BRNN and the least performance of ELM. Only it can be remarked that the present study revealed that BRNN is more suitable for prediction of rainfall in ECPM using SLP data over the climate domain of PM.

5.3. Comparison of Model Performance through Graphical Presentations. The performance of the five ML models used in this study was evaluated using graphical presentation of

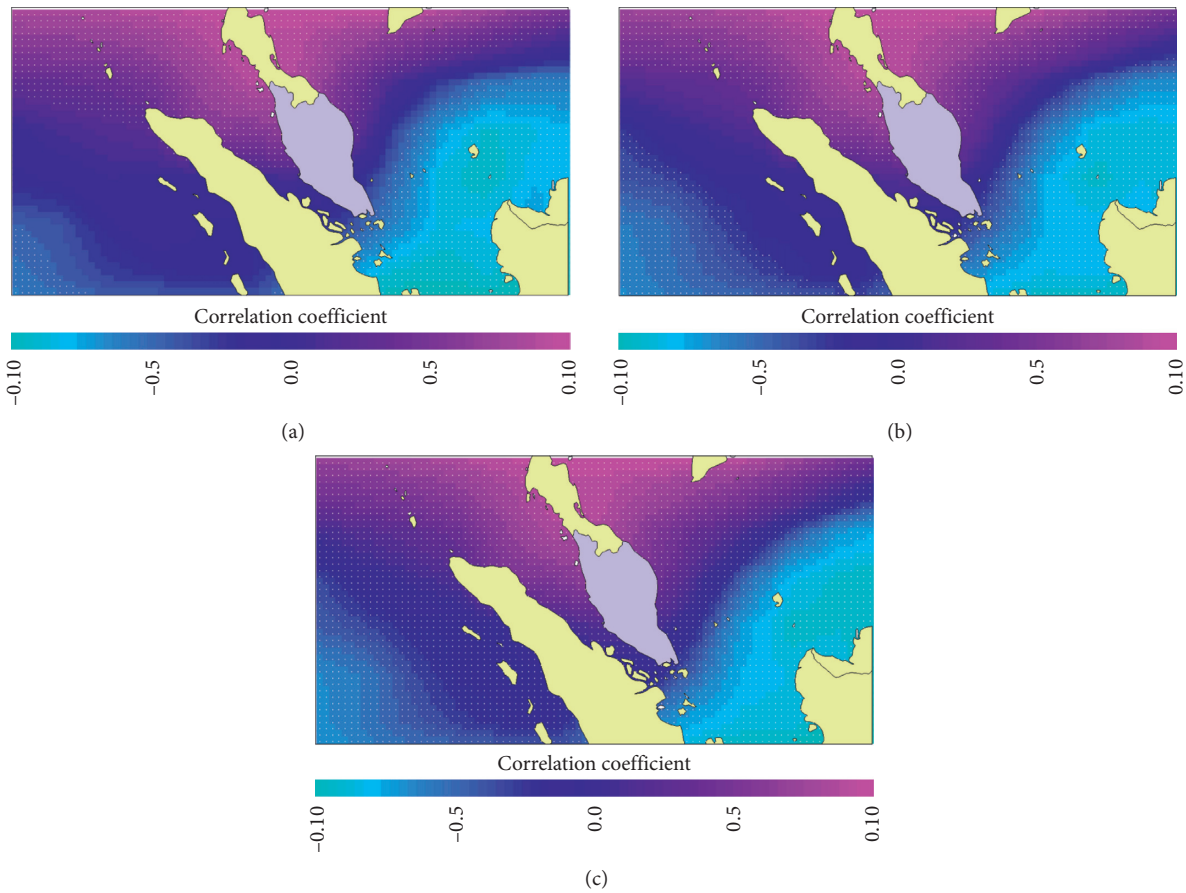

Figure 7: Correlation of areal average rainfall in the East Coast of Peninsular Malaysia with sea level pressure at different locations for (a) 1-day; (b) 2-day, and (c) 3-day lags. The colour ramp is used to show the positive (negative) correlation. The significant correlation ($p < 0.05$) is presented using white dots.

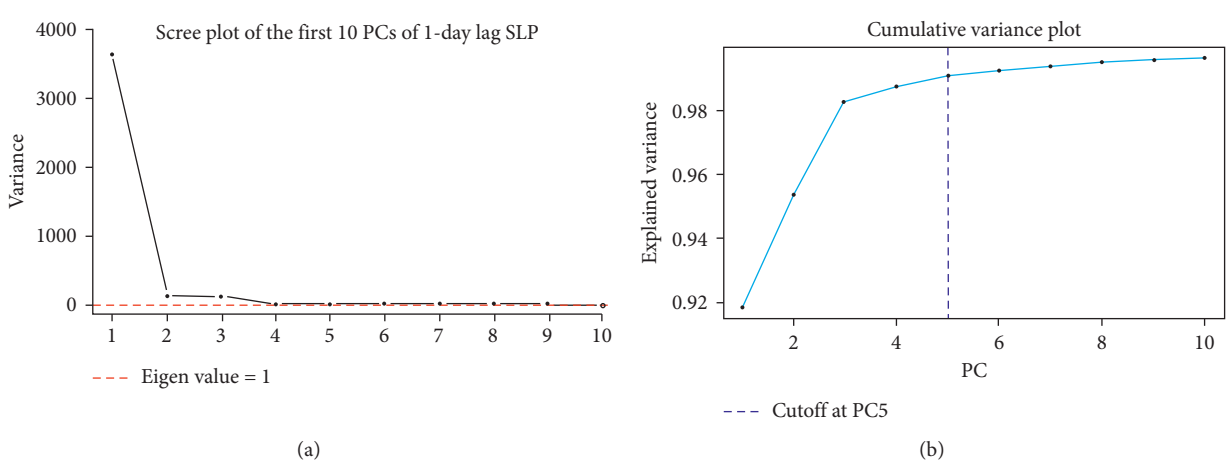

Figure 8: (a) The scree plot and (b) cumulative variance plot of the first ten principal components of one-day lag sea level pressure data over the climate domain of Peninsular Malaysia.

observed and model data in three different ways. Considering the large volume of data, different innovative approaches were employed for the presentation of data.

First, the density-scatter plots were prepared. This type of plot is suitable for comparison of a large amount of data. As the data size was 7120, it was not possible to compare effectively using a simple scatter plot. Therefore, density-scatter plots are used in this study. Obtained results are presented in Figure 10. The red colour in the plot represents a higher density of data, while the blue represents a lower

Table 1: Performance of the ML models in terms of two error and two association-based statistical metrics. The bold number indicates the best performance.

Model	MAE	NRMSE	WI	KGE
ELM	0.045	0.915	0.53	0.53
BRNN	**0.035**	**0.678**	**0.62**	**0.69**
BART	0.039	0.784	0.58	0.64
xgBoost	0.039	0.803	0.58	0.63
HNFIS	0.036	0.708	0.61	0.68

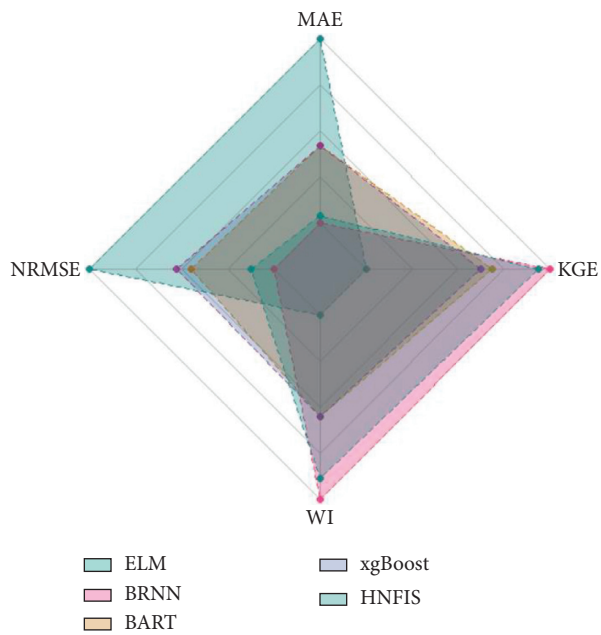

Figure 9: Radar chart showing the relative performance of five ML models considered in the present study based on four statistical metrics.

density of data. As the days with zero or low rainfall is very high compared with days with higher rainfall, the red zones (high density of data) were noticed only for the lower rainfall. If the diagonal line of the plot bisects the red and other higher rainfall zones symmetrically, the model is considered better. The results presented in Figure 10 reveal that high-density data were more above the bisecting line for all the models which indicates over prediction of low rainfall values by all the models. However, the BRNN was most perfect followed by HNFIS and BART in symmetrically bisecting the high-density rainfall data. The results also showed that none of the models was capable to simulate the high rainfall of values. All the model underpredicted the high rainfall amount. Overall, the underprediction was less for BRNN followed by BART. Daily rainfall data are highly skewed. It follows a gamma distribution. The number of no rainfall days is very high compared with days having different amounts of rainfall. Again, the days with low rainfall values are always very high compared with the days having high rainfall values. Another major problem is the outliers in rainfall data. Among thousands of rainfall data, only a few are very high and exceed the range of three standard deviations from the mean. Prediction of such outliers by training a model with all rainfall data is still a challenge. Overprediction of low rainfall values and underprediction of high rainfall values in modeling daily or hourly rainfall are still a subject of investigation for both physical and empirical modelers.

The capability of the models in estimating rainfall of all the months and the seasonal variability was evaluated using side-by-side bar plots. Obtained results for the five models are presented in Figure 11. The results revealed that all the models were able to replicate the seasonal variability in rainfall (high rainfall during November-December and low rainfall during June–August). However, it was also noticed that all the models overpredicted rainfall during low rainfall months and underpredicted rainfall during high rainfall months. Almost no difference among the models was noticed based on the monthly presentation of data. However, close observation of results revealed a bit less underprediction and overprediction by BRNN.

Finally, the performance of the models was visually compared by plotting the first two PCs of the data. For this purpose, the PCs of observed and model outputs were estimated. The PCs were then plotted (first PC in the x-axis and the second PC in the y-axis). This provides a visualization of how the data are related to each other in PCs. It gives an assessment of which samples are similar and which are not. Obtained results are presented in Figure 12. The results showed similarity in results of BRNN, xgBoost, and

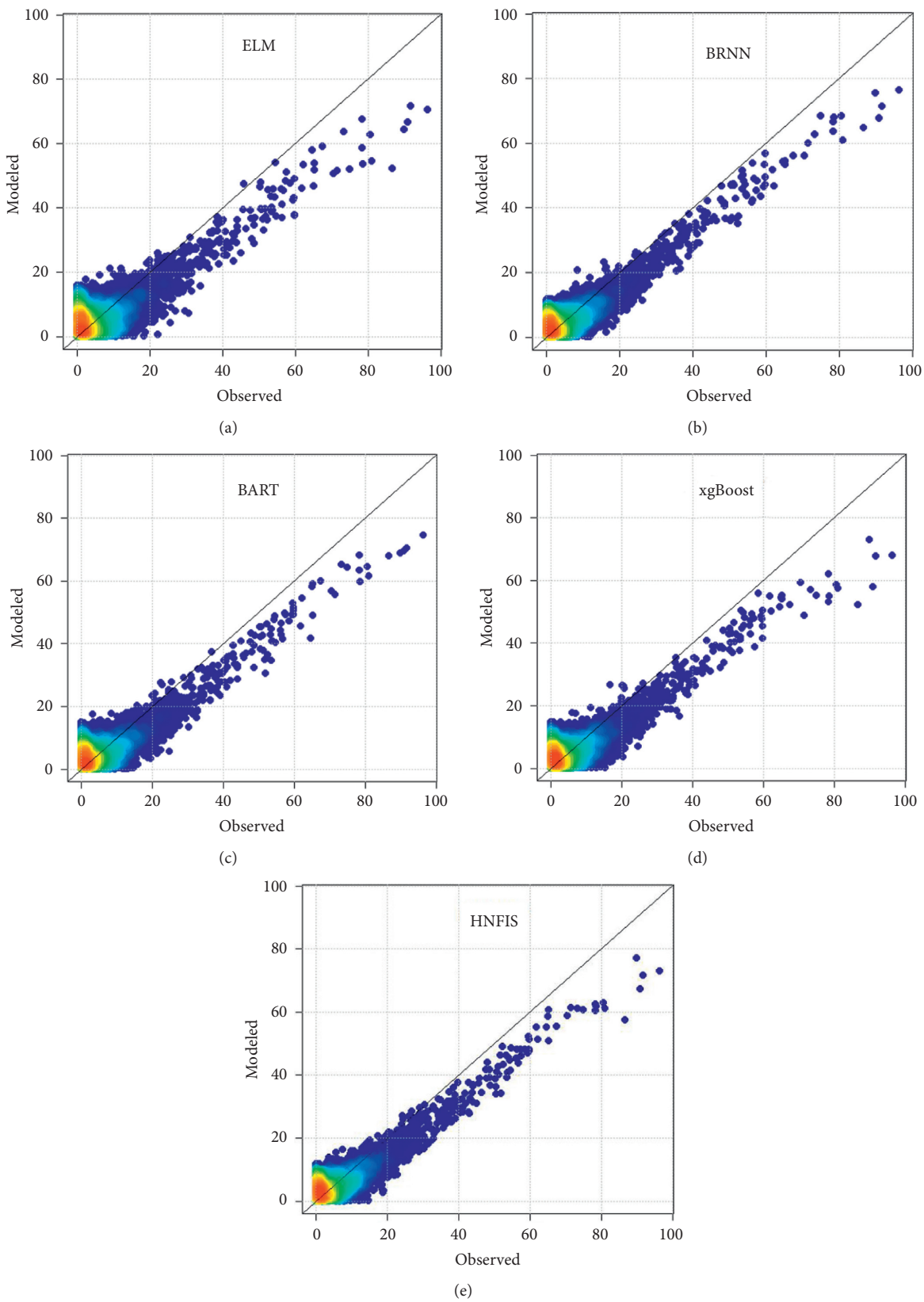

Figure 10: Comparison of observed and model simulated rainfall using density-scatter plot.

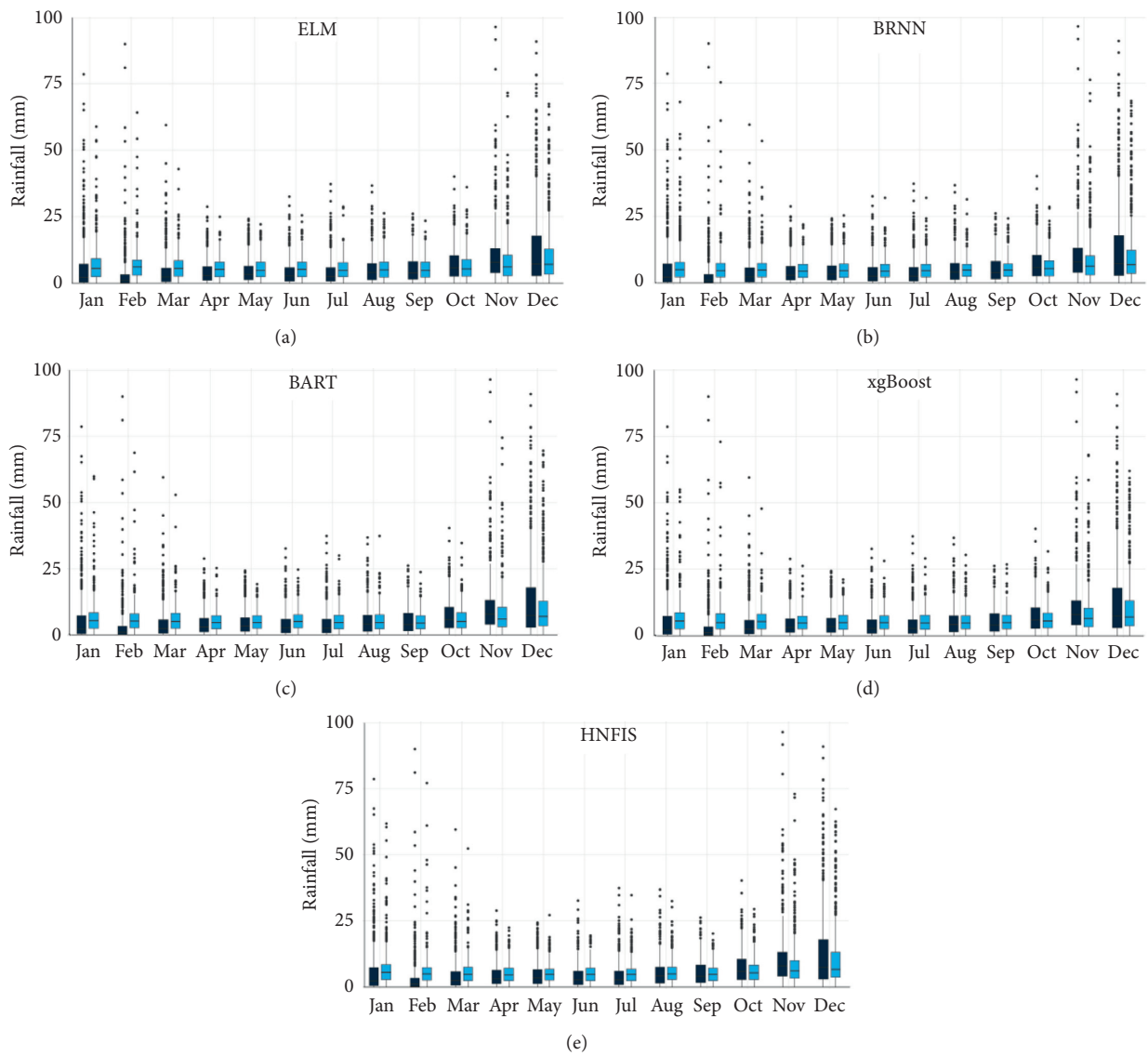

Figure 11: Side-by-side presentation of whisker-box plot of observed and simulated rainfall by the model showing the capability of the models in simulating rainfall for each month and replicate the seasonal variability of rainfall in the study area.

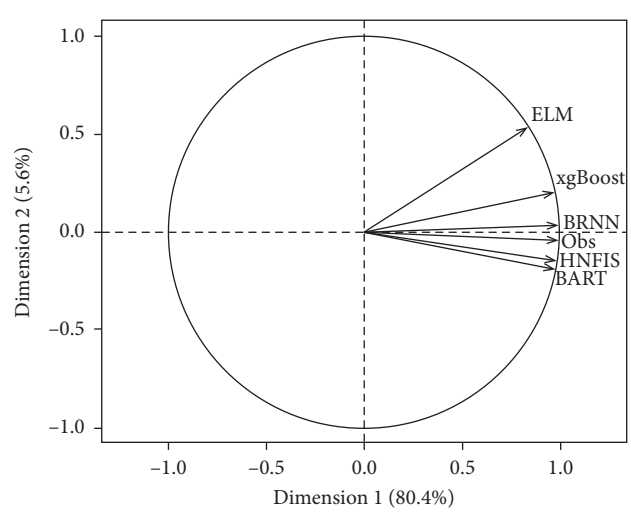

Figure 12: Assessment of similarity of model outputs with the observed rainfall-based variability plots of principal components of observed and simulated rainfall.

ELM while the results of HNFIS and BART were different from the other three model outputs. However, when compared with the observed data, the BRNN was found closer to the observed line in the plot followed by HNFIS and BART. The ELM is found to locate most apart from the observed line and also from the other models. The results indicate the best performance of BRNN in replicating observed rainfall followed by HNFIS and BART.

6. Conclusion

Five advanced AI algorithms, namely, ELM, BRNN, BART, xgBoost, and HNFIS were employed for the developed of the physical-empirical models for the prediction of rainfall in the eastern coastal region of PM from SLP data collected from the climate domain of PM. The parameters of the models were optimized using a *k*-fold validation approach. The performance of the models was evaluated using various innovative visuals presented along with statistical metrics. The results showed better performance of BRNN compared with other models in predicting daily rainfall one-day ahead. Prediction of daily rainfall is an extremely challenging task for the tropical region where daily rainfall data can be compared with a high fluctuating extremely noisy data without any exportable temporal pattern. The capability of the physical-empirical model of incorporation of physical mechanism and use of advanced ML algorithms has made the models developed in this study efficient in rainfall prediction. The Bayesian regularization of neural network parameters makes it more capable to reveal theoretically complex input-output relationship. It might be concluded that the complexity due to a very chaotic relationship of SLP and rainfall in the ECPM was able to capture through Bayesian regularization of the ANN model. The results revealed the potential of the model to be employed for the development of early warning of rainfall. However, it should be noted that the model was not capable to replicate very high rainfall which means it cannot be employed for prediction of extreme rainfall and probable flash flood. Besides, the model overpredicted low rainfall and thus more rainfall days which restricted this applicability in predicting dry spells. In the future, more attention should be given to improve the performance of the models in simulating extreme rainfall for expanding their applicability in prediction of extreme rainfall.

Data Availability

The data used to support the findings of this study are available from the corresponding author upon request.

Conflicts of Interest

The authors declare that they have no conflicts of interest.

Acknowledgments

This research was funded by the Ministry of Higher Education Malaysia under the Fundamental Research Grant Scheme, (203.PHUMANITI.6711695) and the USM Publication Fund. The first author would like to acknowledge the support from the Science and Technology Plan Project of Shaanxi Province grant no. 2020GY-041 and Doctoral Research Initiation Project grant no. 209040080.

References

[1] S. H. Pour, A. K. A. Wahab, and S. Shahid, "Spatiotemporal changes in aridity and the shift of drylands in Iran," *Atmospheric Research*, vol. 233, 2020.

[2] D. B. Wright, R. Mantilla, and C. D. Peters-Lidard, "A remote sensing-based tool for assessing rainfall-driven hazards," *Environmental Modelling & Software*, vol. 90, 2017.

[3] I. Belachsen, F. Marra, N. Peleg, and E. Morin, "Convective rainfall in a dry climate: relations with synoptic systems and flash-flood generation in the Dead Sea region," *Hydrology and Earth System Sciences*, vol. 21, 2017.

[4] S. S. B. Brito, A. P. M. A. Cunha, C. C. Cunningham, R. C. Alvalá, J. A. Marengo, and M. A. Carvalho, "Frequency, duration and severity of drought in the Semiarid Northeast Brazil region," *International Journal of Climatology*, vol. 38, 2018.

[5] V. Joshi and K. Kumar, "Extreme rainfall events and associated natural hazards in Alaknanda valley, Indian Himalayan region," *Journal of Mountain Science*, vol. 3, 2006.

[6] H. R. Pourghasemi, A. Gayen, M. Edalat, M. Zarafshar, and J. P. Tiefenbacher, "Is multi-hazard mapping effective in assessing natural hazards and integrated watershed management?" *Geoscience Frontiers*, vol. 11, 2020.

[7] B. Praveen, S. Talukdar, Shahfahad et al., "Analyzing trend and forecasting of rainfall changes in India using non-parametrical and machine learning approaches," *Scientific Reports*, vol. 10, 2020.

[8] M. Zeynoddin, H. Bonakdari, A. Azari, I. Ebtehaj, B. Gharabaghi, and H. Riahi Madavar, "Novel hybrid linear stochastic with non-linear extreme learning machine methods for forecasting monthly rainfall a tropical climate," *Journal of Environmental Management*, vol. 222, 2018.

[9] S. Y. Yim, B. Wang, W. Xing, and M. M. Lu, "Prediction of Meiyu rainfall in Taiwan by multi-lead physical–empirical models," *Climate Dynamics*, vol. 44, 2015.

[10] Y. Luo, J. Sun, Y. Li et al., "Science and prediction of heavy rainfall over China: research progress since the reform and opening-up of new China," *Journal of Meteorological Research*, vol. 34, 2020.

[11] X. Yang, R. He, J. Ye et al., "Integrating an hourly weather generator with an hourly rainfall SWAT model for climate change impact assessment in the Ru River Basin, China," *Atmospheric Research*, vol. 244, p. 105062, 2020.

[12] E. Toth, A. Brath, and A. Montanari, "Comparison of short-term rainfall prediction models for real-time flood forecasting," *Journal of Hydrology*, vol. 239, no. 1–4, pp. 132–147, 2000.

[13] C. L. Wu and K. W. Chau, "Prediction of rainfall time series using modular soft computingmethods," *Engineering Applications of Artificial Intelligence*, vol. 26, no. 3, pp. 997–1007, 2013.

[14] P. Satyanarayana and V. V. Srinivas, "Regional frequency analysis of precipitation using large-scale atmospheric variables," *Journal of Geophysical Research*, vol. 113, 2008.

[15] S. Q. Salih, A. Sharafati, I. Ebtehaj et al., "Integrative stochastic model standardization with genetic algorithm for rainfall pattern forecasting in tropical and semi-arid environments," *Hydrological Sciences Journal*, vol. 65, no. 1–13, 2020.

[16] P. Deb, A. S. Kiem, and G. Willgoose, "A linked surface water-groundwater modelling approach to more realistically simulate rainfall-runoff non-stationarity in semi-arid regions," *Journal of Hydrology*, vol. 575, 2019.

[17] A. Banerjee, R. Chen, M. E. Meadows, R. B. Singh, S. Mal, and D. Sengupta, "An analysis of long-term rainfall trends and variability in the uttarakhand himalaya using google earth engine," *Remote Sensing*, vol. 12, 2020.

[18] S. K. Jain, P. Mani, S. K. Jain et al., "A Brief review of flood forecasting techniques and their applications," *International Journal of River Basin Management*, vol. 16, no. 3, pp. 329–344, 2018.

[19] S. Segoni, L. Piciullo, and S. L. Gariano, "A review of the recent literature on rainfall thresholds for landslide occurrence," *Landslides*, vol. 15, 2018.

[20] S. Y. Yim, B. Wang, and W. Xing, "Prediction of early summer rainfall over south China by a physical-empirical model," *Climate Dynamics*, vol. 47, 2014.

[21] P. Chen and B. Sun, "Improving the dynamical seasonal prediction of western Pacific warm pool sea surface temperatures using a physical–empirical model," *International Journal of Climatology*, vol. 40, 2020.

[22] S. H. Pour, A. K. A. Wahab, and S. Shahid, "Physical-empirical models for prediction of seasonal rainfall extremes of Peninsular Malaysia," *Atmospheric Research*, vol. 233, p. 104720, 2020.

[23] T. Hai, A. Sharafati, A. Mohammed et al., "Global solar radiation estimation and climatic variability analysis using extreme learning machine based predictive model," *IEEE Access*, vol. 8, pp. 12026–12042, 2020.

[24] J. Yuval and P. A. O'Gorman, "Stable machine-learning parameterization of subgrid processes for climate modeling at a range of resolutions," *Nature Communications*, vol. 11, 2020.

[25] X. Chen, J. Parajka, B. Széles, P. Strauss, and G. Blöschl, "Spatial and temporal variability of event runoff characteristics in a small agricultural catchment," *Hydrological Sciences Journal=Journal des Sciences Hydrologiques*, vol. 65, no. 13, 2020.

[26] H. A. Chipman, E. I. George, and R. E. McCulloch, "BART: Bayesian additive regression trees," *The Annals of Applied Statistics*, vol. 4, no. 1, pp. 266–298, 2010.

[27] R. Bekkerman, M. Bilenko, and J. Langford, *Scaling Up Machine Learning: Introduction*, pp. 1–20, Cambridge University Press, Cambridge, UK, 2012.

[28] H. Okut, "Bayesian regularized neural networks for small n big p data," *Artificial Neural Networks-Models and Applications*, InTech, London, UK, 2016.

[29] M. Kayri, "Predictive abilities of bayesian regularization and levenberg–marquardt algorithms in artificial neural networks: a comparative empirical study on social data," *Mathematical and Computational Applications*, vol. 21, no. 2, p. 20, 2016.

[30] S. Supatmi, R. Hou, and I. D. Sumitra, "Study of hybrid neurofuzzy inference system for forecasting flood event vulnerability in Indonesia," *Computational Intelligence and Neuroscience*, vol. 2019, Article ID 6203510, 13 pages, 2019.

[31] A. Dormishi, M. Ataei, R. Khaloo Kakaie, R. Mikaeil, and S. Shaffiee Haghshenas, "Performance evaluation of gang saw using hybrid ANFIS-DE and hybrid ANFIS-PSO algorithms," *Journal of Mining and Environment*, vol. 10, 2018.

[32] L. Juneng, F. T. Tangang, and C. J. C. Reason, "Numerical case study of an extreme rainfall event during 9–11 December 2004 over the east coast of Peninsular Malaysia," *Meteorology and Atmospheric Physics*, vol. 98, 2007.

[33] O. O. Mayowa, S. H. Pour, S. Shahid et al., "Trends in rainfall and rainfall-related extremes in the east coast of peninsular Malaysia," *Journal of Earth System Science*, vol. 124, no. 8, pp. 1609–1622, 2015.

[34] N. Khan, S. H. Pour, S. Shahid et al., "Spatial distribution of secular trends in rainfall indices of peninsular Malaysia in the presence of long-term persistence," *Meteorological Applications*, vol. 26, 2019.

[35] M. F. Mohd Akhir, N. Z. Zakaria, and F. Tangang, "Intermonsoon variation of physical characteristics and current circulation along the east coast of peninsular Malaysia," *International Journal of Oceanography*, vol. 2014, Article ID 527587, 9 pages, 2014.

[36] H. Brammer, "Floods in Bangladesh: II. Flood mitigation and environmental aspects," *The Geographical Journal*, vol. 156, 1990.

[37] C. L. Wong, R. Venneker, S. Uhlenbrook, A. B. M. Jamil, and Y. Zhou, "Variability of rainfall in peninsular Malaysia," *Hydrology and Earth System Sciences*, vol. 183, 2009.

[38] A. Yatagai, O. Arakawa, K. Kamiguchi, H. Kawamoto, M. I. Nodzu, and A. Hamada, "A 44-year daily gridded precipitation dataset for Asia based on a dense network of rain gauges," *SOLA*, vol. 5, pp. 137–140, 2009.

[39] E. Kalnay, M. Kanamitsu, R. Kistler et al., "The NCEP/NCAR 40-year reanalysis Project," *Bulletin of the American Meteorological Society*, vol. 77, no. 3, pp. 437–471, 1996.

[40] C. Folberth, A. Baklanov, J. Balkovič, R. Skalský, N. Khabarov, and M. Obersteiner, "Spatio-temporal downscaling of gridded crop model yield estimates based on machine learning," *Agricultural and Forest Meteorology*, vol. 264, pp. 1–15, 2019.

[41] G.-B. Huang, Q.-Y. Zhu, and C.-K. Siew, "Extreme learning machine: theory and applications," *Neurocomputing*, vol. 70, no. 1–3, pp. 489–501, 2006.

[42] G.-B. Huang and C.-K. Siew, "Extreme learning machine: RBF network case," in *Proceedings of the ICARCV 2004 8th Control, Automation, Robotics and Vision Conference*, vol. 2, pp. 1029–1036, Kunming, China, December 2004.

[43] J.-M. Park and J.-H. Kim, "Online recurrent extreme learning machine and its application to time-series prediction," in *Proceedings of the 2017 International Joint Conference On Neural Networks (IJCNN)*, IEEE, Anchorage, AK, USA, May 2017.

[44] F. Burden and D. Winkler, "Bayesian regularization of neural networks," *Methods In Molecular Biology™*, pp. 23–42, Humana Press, Totowa, NJ, USA, 2008.

[45] L. Breiman, "Random forests," *Machine Learning*, vol. 45, no. 1, pp. 5–32, 2001.

[46] S. Abu-Nimeh, D. Nappa, X. Wang, and S. Nair, "A distributed architecture for phishing detection using Bayesian additive regression trees," in *Proceedings of the 2008 eCrime Researchers Summit*, IEEE, Atlanta, GA, USA, October 2008.

[47] S. Zhang, Y.-C. T. Shih, and P. Müller, "A spatially-adjusted Bayesian additive regression tree model to merge two datasets," *Bayesian Analysis*, vol. 2, no. 3, pp. 611–633, 2007.

[48] H. Zhang, D. Qiu, R. Wu, Y. Deng, D. Ji, and T. Li, "Novel framework for image attribute annotation with gene selection XGBoost algorithm and relative attribute model," *Applied Soft Computing*, vol. 80, 2019.

[49] T. Chen, H. Li, Q. Yang, and Y. Yu, "General functional matrix factorization using gradient boosting," in *Proceedings of the 30th International Conference On Machine Learning, ICML 2013*, Atlanta, GA, USA, June 2013.

[50] L. Breiman, "Random forrests," *Machine Learning*, vol. 45, pp. 5–32, 2001.

[51] A. Asuncion and D. Newman, *UCI Machine Learning Repository*, UCI, Irvine, CA, USA, 2007.
[52] M. Rezakazemi, A. Dashti, M. Asghari, and S. Shirazian, "H2-selective mixed matrix membranes modeling using ANFIS, PSO-ANFIS, GA-ANFIS," *International Journal of Hydrogen Energy*, vol. 42, no. 22, pp. 15211–15225, 2017.
[53] K. Li, H. Su, and J. Chu, "Forecasting building energy consumption using neural networks and hybrid neuro-fuzzy system: a comparative study," *Energy and Buildings*, vol. 43, 2011.
[54] E. Kim, M. Park, S. Ji, and M. Park, "A new approach to fuzzy modeling," *IEEE Transactions on Fuzzy Systems*, vol. 5, no. 3, pp. 328–337, 1997.
[55] J. H. Zar, "Spearman rank correlation: overview," in *Wiley StatsRef: Statistics Reference Online*John Wiley & Sons, Hoboken, NJ, USA, 2014.
[56] I. Jolliffe, "Principal component analysis," *International Encyclopedia Of Statistical Science*, pp. 1094–1096, Springer, Berlin, Germany, 2011.
[57] U. Demšar, P. Harris, C. Brunsdon, A. S. Fotheringham, and S. McLoone, "Principal component analysis on spatial data: an overview," *Annals of the Association of American Geographers*, vol. 103, 2013.
[58] Y. Liu, A. Singleton, and D. Arribas-Bel, "A Principal Component Analysis (PCA)-based framework for automated variable selection in geodemographic classification," *Geospatial Information Science*, vol. 22, no. 4, pp. 251–264, 2019.
[59] B. Choubin, H. Darabi, O. Rahmati, F. Sajedi-Hosseini, and B. Kløve, "River suspended sediment modelling using the CART model: a comparative study of machine learning techniques," *Science of The Total Environment*, vol. 615, pp. 272–281, 2018.
[60] M. S. Al-Musaylh, R. C. Deo, J. F. Adamowski, and Y. Li, "Short-term electricity demand forecasting with MARS, SVR and ARIMA models using aggregated demand data in Queensland, Australia," *Advanced Engineering Informatics*, vol. 35, 2018.

Hindawi
Complexity
Volume 2021, Article ID 6643472, 16 pages
https://doi.org/10.1155/2021/6643472

Research Article

Improvement in Explicit Prediction of Water Quality Using Wavelet-Based LSSVR and M5pRT

Rashmi Bhardwaj [1] **and Aashima Bangia** [2]

[1] *University School of Basic and Applied Sciences (USBAS), Head, Non-Linear Dynamics Research Lab, GGS Indraprastha University, Delhi, India*
[2] *USBAS, GGS Indraprastha University, Delhi, India*

Correspondence should be addressed to Rashmi Bhardwaj; rashmib@ipu.ac.in

Received 3 November 2020; Revised 29 January 2021; Accepted 1 March 2021; Published 20 March 2021

Academic Editor: Zaher Mundher Yaseen

Imbalance in the pH of water reduces this precious resource as an extremely dangerous liquid for human health and plants' growth. Change in the pH levels of the drinkable water has majorly raised concern towards diverse health issues like heart problems, infant mortality rates, pigmentation of skin, and cholera outbreaks. Therefore, it is necessary to keep a check on essential water quality components that include acidic/basic nature of water. As per the US Environmental Protection Agency (USEPA), the drinkable water should have a pH level ranging from 6.5 to 8.5. Two sample situates have been identified wherever highly reported pollutants levels were found and have been analyzed through artificial intelligence (AI) techniques. It can be observed that wavelet denoised signals fed into the least squares support vector regression (LSSVR) and M5 prime regression tree (M5pRT) predicted more accurately on the basis of the performance errors that are as follows: (a) root mean squared error (RMSE); (b) mean squared error (MSE); (c) mean absolute error (MAE). On the basis of these errors, the coefficient of determination/goodness of fit (R^2) simulated for the prototypes is developed in this study. RMSE outcomes diminish on the whole on applying the training and forecasting data-division via WLSSVR and WM5pRT as compared with fitting the normalized data through LSSVR and M5pRT. These performance measures are essential to analyze the concentration levels of pH in the river streams at the identified sites of study. Thus, the observed pattern from this study may help for future estimation of the quality of water at their sources so that it prohibits the further increase in either acidic or basic salts which prove to be lethal for the environment. Thus, these predictors would be helpful towards formulation of strategies for protection of ecosystem and human health.

1. Introduction

Water sustains life. It is referred to be the most precious resource for all the living creatures on Earth. Each and every natural water source that is counted upon as fresh contains salts in varying concentrations. This results in increase in pH levels as the water flows through oceans, rivers, and waterways and finally gets consumed by either mammals or plants and trees in the ecological system. A stream/river evolving through the mountain watershed could contain as less as 50 parts per million (i.e., ppm) in total dissolved solutes. Ocean water averages about 35,000 ppm which is about 3.5% of the dissolved solutes. Gradually, this has risen the health and ecological concerns universally [1]. Mostly consumed for drinking by humans and animals alike plus plants' growth makes water an integral part of ecosystem.

Consuming water with unfair pH levels has developed devastating replications on human health. The WHO a standard health monitoring unit has laid clear instructions for maintaining the balanced pH levels of water used for human intake [2, 3]. This is because people consuming inappropriate quality of water are unaware to health effects caused by inappropriate levels of water. Thus, it had to be

clearly stated and identified that water pH should not be compromised as it is affecting numerous households on yearly basis. Drinking of such waters has led to cardiovascular, hypertension, epidermal, and other serious diseases.

In general, it has been observed that the health hazards, spread of waterborne diseases, and treatment costs have worsened due to imbalanced potential of hydrogen (pH) level. People consuming acidic/basic water have increased manifold and are unaware of its substantial negative impacts on their wellbeing in the longer run. It has over the time transformed into an added dimension in view of the health insecurities that possibly lead to increased financial liabilities. While, some prescribed limit of salts are essential for the human body to avoid iodine deficiency. Still, increased intake of salt on a regular basis is intolerable by the body as it is difficult to be absorbed by the body fluids present. The abrupt amount of iodine is undesirable and thus turns the body prone to hypertension, increased levels of blood pressure, heart stroke, and various other ailments. Therefore, universal authorities such as USEPA and WHO believe salt should be consumed by the body within limits considering health as a topmost priority.

Simulations through moving average combined with the wavelet model are carried out on rainfall data for forecasting noise [4]. The adaptive neuro-fuzzy system is applied to study the BOD of River Surma [5]. Prediction of dynamic indicators is applied on atmospheric pollutants [6]. AI techniques have been integrated with the wavelet decomposition for restructuring the data to predict the river water quality [7]. Large-scale info-data applications are explained with LSSVR [8]. Control and prediction of time series are done [9]. Simulated and forecasted surface flows via self-tuned ANN model are studied [10]. SVR with the kernel estimated short-term loading is studied [1]. The algorithm of GWO-ANFIS for prediction of hydropower generator is developed [11]. River-flow in Plata-basin attribution is studied [12]. Transboundary rivers from Romania were discussed regarding the water pollution and quality being affected [13]. Discharge of pollutants in a vegetated compound meandering river is studied [14]. DWT with ANN analyzed the short-term stream-flows [15]. Detailed development and analysis through neural networks are provided [16]. ANN technique is applied in various real-life applications such as biological and environmental phenomena [17]. Precipitations on monthly basis info using the neuro-fuzzy method are predicted [18]. Deep learning networks are designed to assess water quality of mariculture with accuracy [19]. Water quality of Karoun River via regression and ANFIS is forecasted [20]. Various neural network-based models such as ANN, BNN, and ANFIS modeling are discussed for groundwater level predictions [21]. Variations, i.e., seasonal along with spatial ones are studied for the quality of river Yamuna [2]. Hybrid of SSMD-whale optimization is devised for prediction of longitudinal dispersion coefficients [22]. The SVR algorithm for predicting river water quality is improved [23]. ANN-ANFIS carried out uncertainty analysis for assessment of gravel transport [24]. Optimal multigene programming simulated the dispersion coefficients [25]. Analysis is carried out through wavelet transform, genetics algo, and neural networks of monsoon floods [26]. WQI prediction is simulated through AI for studying groundwater systems [27]. Hourly records of ozone concentrations with the help of wavelet and ARIMA are forecasted [28]. Different machine learning-based hybrid models are carried out for estimating evapotranspiration in Iran [29]. Artificial intelligence methodologies on survey of long-term data from 2000–2020 for water quality are explored [3]. Decomposition mode ensemble modeling is analyzed for LSTM for streamflow forecasts [30].

This research article consists of case study and its dataset assessment in Section 2. Discussion of the mathematical model designing of LSSVR and M5pRT and further WD conjuncted to LSSVR and M5pRT procedure are given in Section 3. Performance measures for prediction are computed in Section 4 with algorithms for building models such as LSSVR, M5pRT, WLSSVR, and WM5pRT. Section 5 includes results observed from these hybrid models plus the errors are numerically simulated.

As per the literature survey carried out, none of the articles simulated the acidic or basic salts' presence in Yamuna waters through decomposition of wavelet (WD) with LSSVR and M5pRT for the sample sites considered in this study.

2. Case Study and Dataset Assessment for River Yamuna

The data consist of values from 2000 to 2019 of pH level at two major monitoring stations Nizamuddin Bridge in Old Delhi and Palla on the outskirts of Delhi as recorded by *Central Pollution Control Board* (*CPCB*). A total of 19 years' monthly values, i.e., from the year 2000 to 2019 have been trained and then simulated via intelligent learning regressive models LSSVR, M5pRT, WLSSVR, and WM5pRT in the study. For the conjuncted models WLSSVR and WM5pRT, first ten input data values are fed as the responses for the training and validation of the each of the datasets. It was detected that these proposed models give enriched efficiency and diminish error extreme sharply in contrast to existent classical models. Two stations have been numbered according to the flow of the river crossing stations in Table 1.

Starting at Yamunotri flowing till Allahabad, total extent of river Yamuna measures up to 1,376 kilometer with a total basin area as 3,66,223 km^2. The river tends to be practically dried-up in the region ranging from Hathnikund towards Delhi. The only source adding up waters is from the groundwater and small tributaries. From Hathnikund, the river reaches Delhi at Palla which has a spread of 224 km. Delhi itself dumps more than 58% of its unwanted garbage into these waters. Thus, the level of contamination is highest around *Delhi-NCR* geologically. The *Central Pollution Control Board (CPCB)* reported that adulterated expanse of Yamuna augmented from 500 to 600 km. Acidic or basic levels of water that have been highly reported into the river waters have been studied via pH turning greater than or lesser than 7 lying in the range 6.5–8 or outside, at the above listed stations. The location of Old Delhi Bridge and Palla can be spotted in the geological map given in Figure 1.

Table 1: Data sets for simulation of five hybrid models.

Cross validation	Data sets	Time period (monthwise recorded)	
		From	Up to
Data type 1	Old Delhi (Nizzamuddin Bridge)	Jan, 2000	Jan, 2019
Data type 2	Palla (outskirts of Delhi)	Jan, 2000	Jan, 2019

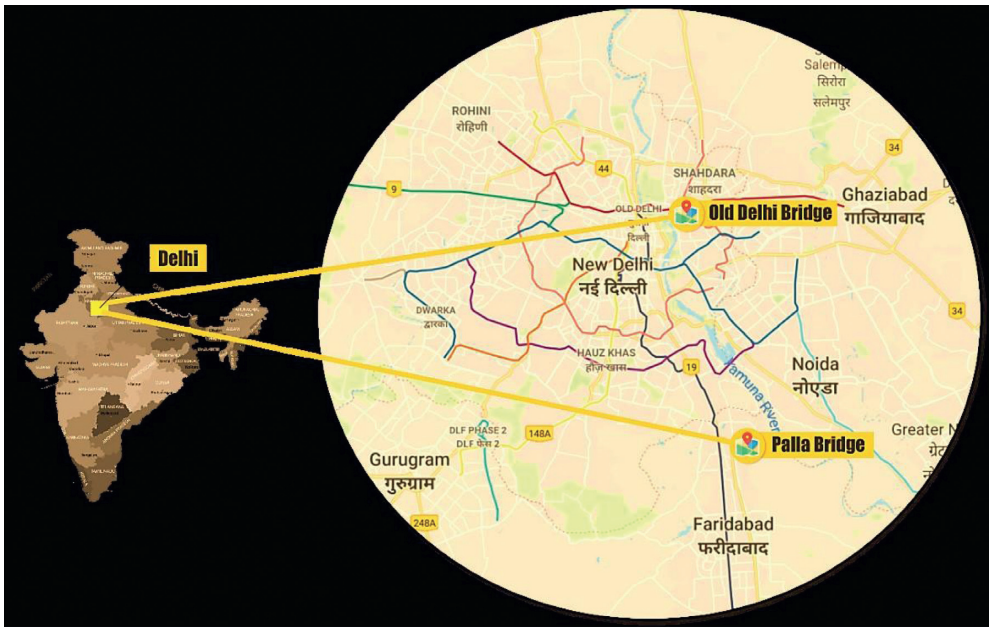

Figure 1: Map showing the two monitoring stations of river Yamuna.

This article studies at each location 229 data sets have been observed. This article studies 2 data types each having 229 data values.

3. Methodology

3.1. Least Square Support Vector Regression (LSSVR). Consider in general a function approximation problem that would be represented as follows:

$$f = g(x) = <\omega, x> + h = \sum_{j=1}^{K} w_j x_j + h, \quad f, h \in \mathbb{R}, x, \omega \in \mathbb{R}^K,$$
$$f(x) = \begin{bmatrix} \omega \\ h \end{bmatrix}^T \begin{bmatrix} x \\ 1 \end{bmatrix} = \omega^T x + h, \quad x, \omega \in \mathbb{R}^{K+1}. \tag{1}$$

This problem can be solved efficiently by transforming into an optimization problem which is carried out through support vector regression (SVR) as follows:

$$\min_{\omega} \frac{1}{2} \|\omega\|^2, \tag{2}$$

where $\|\omega\|$ is themagnitude of normal to the surface to be estimated.

The measure of weights can be computed through:

$$g(x, \omega) = \sum_{j=1}^{K} \omega_j \cdot x^j, \quad x \in \mathbb{R}, \omega \in \mathbb{R}^K, \tag{3}$$

where K is the order of the polynomial.

Mainly, the constraint aims towards minimizing the performance measures that prevails in the predictors of the provided inputs and actual ones. Also, espouses ε-based loss function would penalize predictions farther than ε from anticipated output. Then, ε-value governs tube-width; a, that is, smaller the value, tolerance reduces towards simulation error and also affects number of support vectors that subsequently leads to sparsity of the solutions. If ε decreases, it leads to boundary to shift inwards. Thus, a greater number of target points around the boundary clearly indicate the increase in the number of support vectors. Similarly, the case of increasing ε fewer points around the boundary follows from the result.

Evolving on this technique, the least squares extension applied to the SVR modifies the minimization problem as follows:

$$\min \phi_2(\omega, h, \epsilon) = \frac{\gamma}{2} \omega^T \omega + \frac{\zeta}{2} \sum_{i=1}^{N} \epsilon_i^2, \tag{4}$$

and subjects to following constraints:

$$y_i \left[\omega^T \sigma(x_i) + h \right] = 1 - \epsilon_i, \quad i = 1, \ldots, K. \tag{5}$$

LSSVR representation involves explanation via the binary points as $y_i = \pm 1$

Now, with $y_i^2 = 1$,

$$\sum_{i=1}^{N} \epsilon_i^2 = \sum_{i=1}^{K} (y_i \epsilon_i)^2 = \sum_{i=1}^{K} \epsilon_i^2 = \sum_{i=1}^{K} \left(y_i - \left(\omega^T \sigma(x_i) + h\right)\right)^2, \tag{6}$$

where $\epsilon_i = y_i - (\omega^T \sigma(x_i) + h)$

LSSVRs have been designed to tackle higher complicacies than SVR as put forward by Suykens. Objective function does not change much as compared with that of the existing SVR. Difference arises when ε-based loss function replaces the classical squared-loss function, and explaining every b_i coefficient becomes nonzero. Alongside, model proficiency increases on creating Lagrange multiplier that is obtained via resolving the Karush–Kuhn–Tucker (KKT) scheme. Solution of this system is carried out with the help of most standard approaches to solve sets-of linear equalities. SVR has three fine-tuning components defined whereas execution of LSSVR involves two such components. The prediction errors simulated are found to be least through LSSVR. It is said this prototype eradicates noises and moderates computational labor.

Remark 1. Thus, this LSSVR formulation modifies into the following:

$$\phi_2(\omega, h, \epsilon) = \gamma A_W + \zeta A_D,$$

with,

$$A_W = \frac{1}{2}\omega^T \omega \text{ and } A_D = \frac{1}{2}\sum_{i=1}^{K} \epsilon_i^2 = \frac{1}{2}\sum_{i=1}^{K} \left(y_i - \left(\omega^T \sigma(x_i) + h\right)\right)^2, \tag{7}$$

where γ and ζ are hyperparameters tuning amount of regularization w.r.t sum squared error (SSE).

Now, further LSSVR regressor solution can be obtained by the following Lagrangian function:

$$\left\{ L_m(\omega, h, \epsilon, \alpha) = \phi_2(\omega, \epsilon) - \sum_{i=1}^{K} \alpha_i \left\{\left[\omega^T \sigma(x_i) + h\right] + \epsilon_i - y_i\right\} = \frac{1}{2}\omega^T \omega + \frac{\mu}{2}\sum_{i=1}^{K} \epsilon_i^2 - \sum_{i=1}^{K} \psi_i \left\{\left[\omega^T \sigma(x_i) + h\right] + \epsilon_i - y_i\right\} \right\}. \tag{8}$$

Representing $\psi_i \in \mathbb{R}$ as Lagrange multipliers, minimality conditions can be counted in as follows:

$$\begin{aligned} &\left\{ \frac{\partial L_m}{\partial \omega} = 0 \quad \longrightarrow \omega = \sum_{i=1}^{N} \psi_i \sigma(x_i), \frac{\partial L_m}{\partial h} = 0 \longrightarrow \sum_{i=1}^{K} \psi_i = 0, \frac{\partial L_m}{\partial \epsilon_i} = 0 \longrightarrow \psi_i \right. \\ &\quad = \mu \epsilon_i, i = 1, \ldots, K, \frac{\partial L_m}{\partial \psi_i} = 0 \longrightarrow y_i = \omega^T \sigma(x_i) + h + \epsilon_i, i = 1, \ldots, K. \end{aligned} \tag{9}$$

Now, it is imperative to eliminate ω and ϵ for the creation of the linear system as follows:

$$\begin{bmatrix} 0 & 1_K^T \\ 1_N & \Lambda + \mu^{-1} I_K \end{bmatrix} \begin{bmatrix} h \\ \psi \end{bmatrix} = \begin{bmatrix} 0 \\ Y \end{bmatrix}. \tag{10}$$

Having $Y = [y_1, \ldots, y_N]^T, 1_N = [1, \ldots, 1]^T$ and $\psi = [\psi_1, \ldots, \psi_N]^T$;

I_N is the N dimensional identity matrix and $\Lambda_{ij} = \sigma(x_i)^T \sigma(x_j) = K_n(x_i, x_j)$ where $\Lambda \in \mathbb{R}^{N \times N}$ is the kernel matrix which can be linear kernel, polynomial kernel, multilayer kernel, or radial-basis function-based kernel. Thus, RBF kernel is defined as follows:

$$K_n(x_i, x_j) = \exp\left(-\frac{\left\|x_i - x_j\right\|^2}{\phi^2}\right), \tag{11}$$

with $\phi \in R^+$ is the constant value.

The choice of kernel essentially determines the resultant regressor obtained from LSSVR as it normalizes data under study [14].

3.2. M5 Prime Regression Tree (M5pRT). Introduced by Quinlan in 1992, M5 model tree was established keeping in mind binary decision-tree that consisted of linear regression functions at terminal nodes referred to as leaf. The leaf stores relationship between independent and dependent variables. Such tree forming methodologies are based on the split and rule strategy that constructs a connection between independent and dependent variables. Tree models are also implemented on qualitative/quantitative corpora.

Theorem. The dividing criterion is basically standard deviation of the values of the subset formed on reaching the node to be taken as scale of error of that node plus computing estimated reduction error arising due to the process of testing carried out for each attribute at that particular node. Thus, standard deviation reduction (SDR) can be simulated from the following:

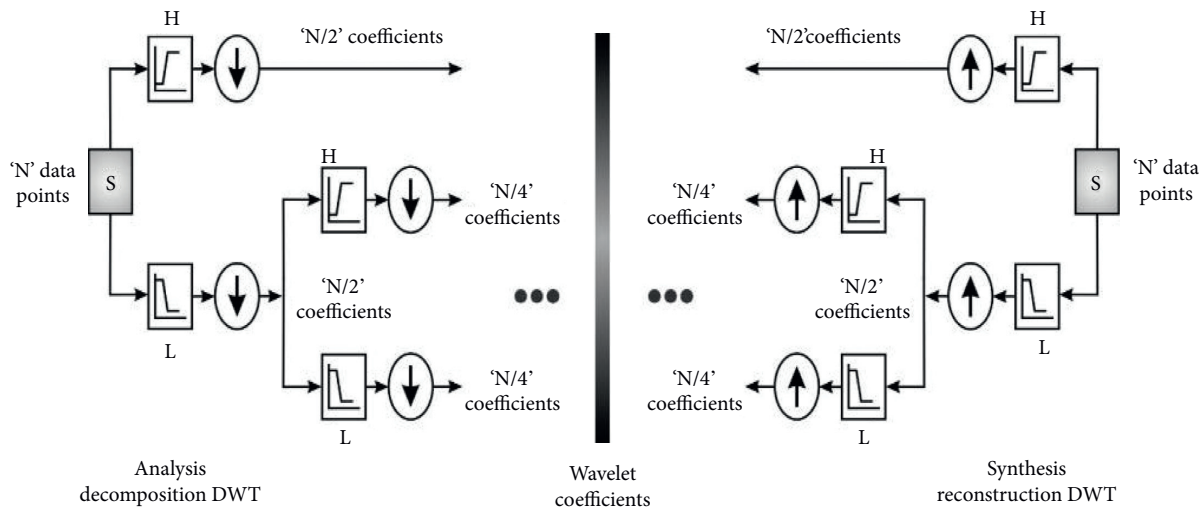

Figure 2: Wavelet study carried upon decomposition/synthesis and reconstruction through coefficients.

$$S\ DR = s\ d(T) - \sum_i \frac{|T_i|}{|T|} \times s\ d(T_i), \tag{12}$$

where *sd* is the standard deviation; T– is the set of instances that touch the node; and T_i is the sets obtained through node splitting w.r.t. the particular characteristic having value assigned to split.

Remark 2. Splitting process dismisses as and when outcomes for every instance which touch the node vary only slightly else if some instance remain.

The M5 algorithm over a period of time got extended into M5'. It was designed to substitute conventional regression structured by existing trees as M5' based on their splitting through *if-then* rules. Thus, this prototype is designed for dividing response realm into multiple subdomains plus linear regressive model to be fitted at every subdomain. M5' constructs regressors' tree on recursively splitting rule on the standard deviation calculated for class values that would influence nodes and error measures at each particular one. Attributes which maximize predictable inaccuracy that decrease get opted for splitting at the node. As branching process, data in child nodes (subtree or smaller nodes) have fewer SD than parent nodes (greater nodes). Reasonably eliminating all possible tree-forms, one that would have the maximum estimated error reduction is finalized.

3.3. Multiresolution-Based Discrete Wavelet Denoising

Theorem 1. *Wavelet is an apt balance of sine-cosine waves comprehending characteristics that would vary around zero and also lies within an interval domain. Wavelet-function is developed into father wavelet (ϕ) and mother wavelet (ψ) holding properties as follows:*

$$\int_{-\infty}^{\infty} \phi(x)dx = 1 \text{ and } \int_{-\infty}^{\infty} \psi(x)dx = 0. \tag{13}$$

Remark 3. By integration of amplified dyadic along with integral transformations, mother-father wavelets are transformed into the wavelet family as follows:

$$\phi_{j,k}(x) = 2^{j/2}\phi\left(2^j x - k\right) \text{ and } \psi_{j,k}(x) = 2^{j/2}\psi\left(2^j x - k\right) \tag{14}$$

3.3.1. Wavelet Decomposition Algorithm. It can be demarcated as follows: $c_{j-1,k} = \sum_l a_{j-1,l-2k} c_{j,l}$ and $d_{j-1,k} = \sum_l b_{j-1,l-2k} c_{j,l}$ that embrace high-low pass filters accordingly.

3.3.2. Wavelet-Reconstruction Algorithm. Representation of $c_{j,l} = \sum_k p_{j,l-2k} c_{j-1,k} + \sum_k q_{j,l-2k} d_{j-1,k}$ with filters is as follows.

Both Wavelet decomposition and reconstruction processes can be together observed in Figure 2 as it clearly shows the analysis through decomposition and synthesis through reconstruction in DWTs.

3.4. Wavelet Least Squares Support Vector Regression (WLSSVR). The following flowchart in Figure 3 clearly puts forward every step involved in the simulation of the responses obtained after training through WD into

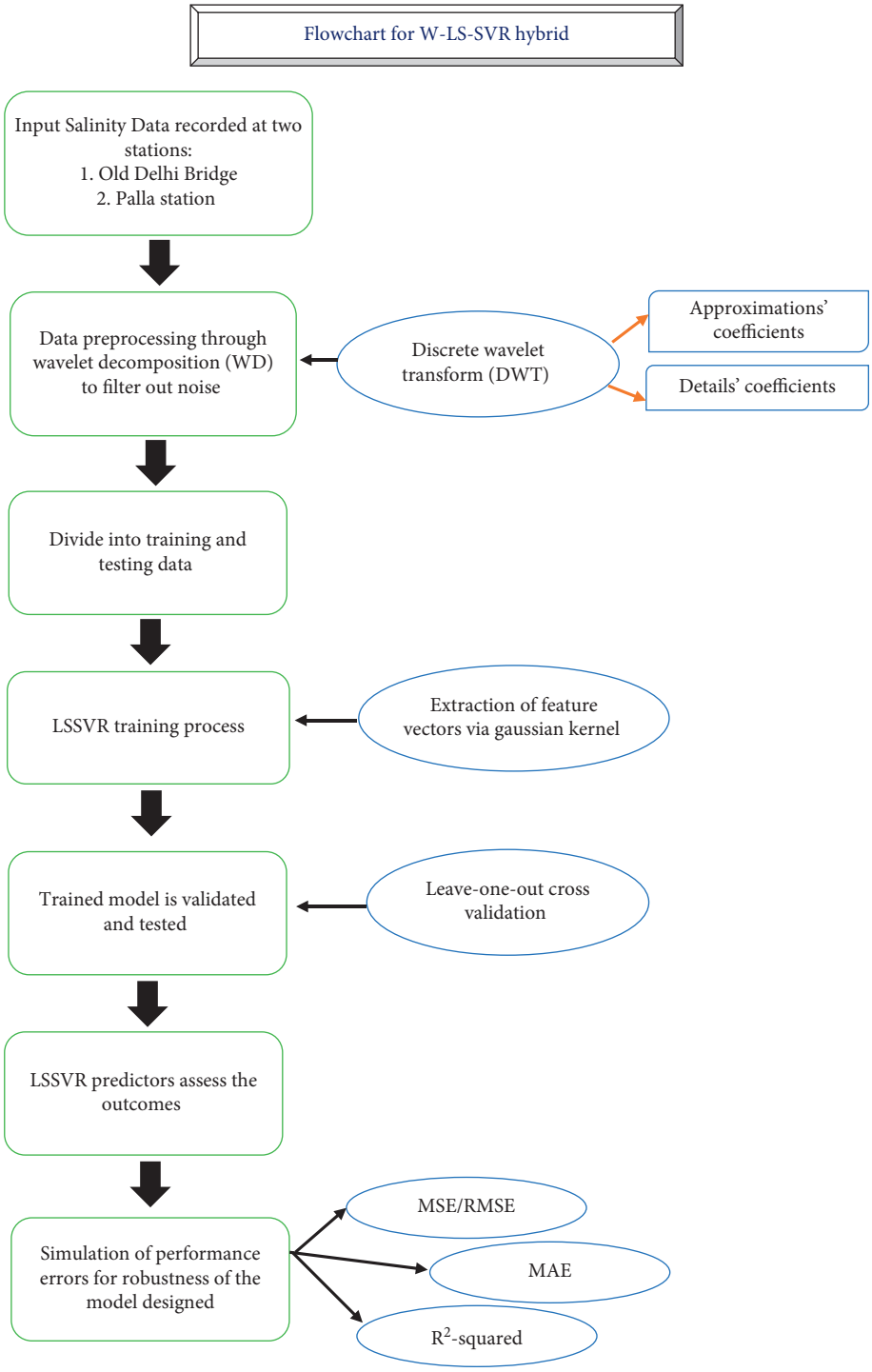

Figure 3: Flowchart of wavelet LSSVR prototype.

approximations and details and then fed into the least squares support vector regressors' setup where Gaussian kernel is an integral part of solving the so formed optimization formulation. WD filters out noise which can be also understood as outliers so as to compute results with better accuracy.

3.5. Wavelet M5 Prime Regression Tree (WM5pRT). Following flowchart in Figure 4 clearly puts forward every step involved in the simulation of the responses obtained after training through WD into approximations and details and then fed into the M5 prime regressors' tree setup where

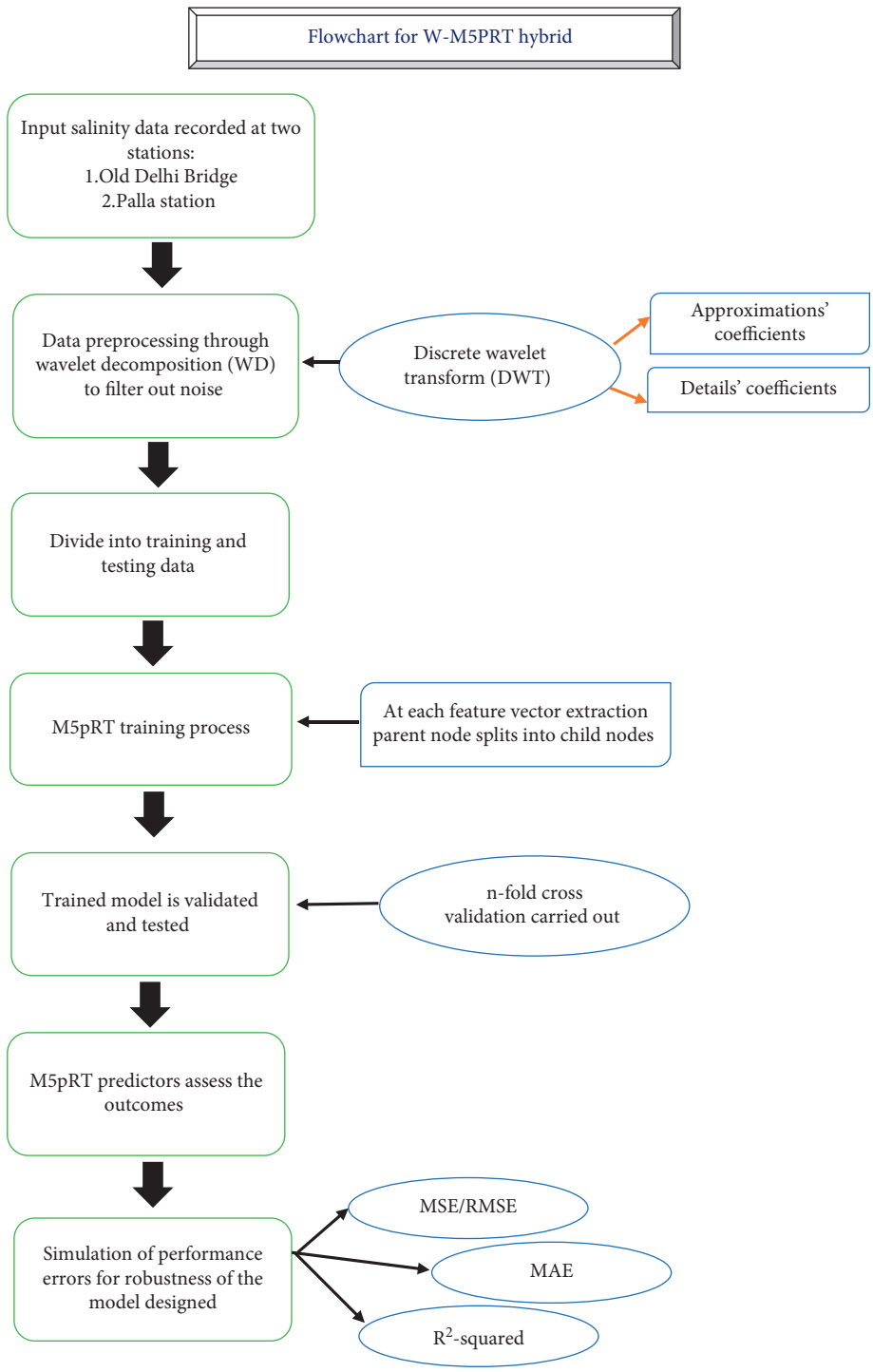

Figure 4: Flowchart of wavelet M5pRT prototype.

at every feature, f extracted the parent node splits into the child nodes and thus a tree formation takes place.

4. Performance Measures

For estimation of performance, each of the hybrid models' forecasting errors is computed for a comparison to understand which of the hybrids best suits the info under study. So, with regard to this, model responses recorded are used to simulate statistical measures referred to as the computational errors represented through root mean squared error (RMSE), mean absolute error (MAE), and also coefficient of determination (R^2) [14].

$$\mathrm{MSE} = \frac{\sum_{i=1}^{n} \left(y_i - \hat{y}_i\right)^2}{n}, \tag{15}$$

where y_i denotes the actual quantity; $\hat{y}_i$ denotes the predicted assessment; and n is the no. of days in prediction.

Table 2: Comparison of prediction errors for data recorded two stations.

Learning methods	Stations	Performance measures			Goodness of fit statistic
		RMSE	MSE	MAE	R^2
LSSVR	Palla (outer Delhi)	7.7988	60.8711	7.7934	0.7260
	Old Delhi bridge	7.5796	57.4510	7.557	0.8420
M5pRT	Palla (outer Delhi)	77.740	6.1284e03	63.5206	0.4814
	Old Delhi bridge	42.464	1.8566e03	35.9128	0.4225
WLSSVR	Palla (outer Delhi)	7.7980	60.8208	7.7919	0.8640
	Old Delhi bridge	7.5714	57.4779	7.5765	0.8759
WM5pRT	Palla (outer Delhi)	101.1626	1.001e04	68.7353	0.6800
	Old Delhi bridge	49.5543	2.5661e03	42.0013	0.6079

The root mean squared error is square root for MSE.

$$\text{RMSE} = \sqrt{\text{MSE}},$$
$$R^2 = 1 - \frac{\text{SSE}}{\text{SST}}. \tag{16}$$

Having sum squared errors of regression fitting, $SSE = \sum_{i=1}^{n} (y_i - \hat{y}_i)^2$, and sum squared errors of the actual data fitting, $SST = \sum_{i=1}^{n} (y_i - \overline{y}_i)^2$,

$$MAE = \frac{1}{N}\left(\sum_{i=1}^{N} |y_i - \hat{y}_i|\right), \tag{17}$$

where y_i denotes the actual quantity, $\hat{y}_i$ denotes the predicted assessment, and n is the no. of days in prediction in all the performance errors above.

5. Results and Discussion

Intelligent learning algorithms, namely, WLSSVR and WM5pRT are computed from the monthly basis data provided via Central Pollution Control Board, CPCB, for the pH recorded and noted at two discussed sample sites. This study helps in understanding through comparison of three neuronal models which one could improve the performance of the model-based structures and with time and would be cost effective. Table 2 represents the errors: MSE, RMSE, and MAE along with the fitness measure, i.e., R^2 for the explained for four models for the two stations: Old Bridge and Palla. At the station Palla, following graphs analyze the data and forecast with the help of responses. Figure 5 shows the decomposition of the wavelet-form signals according to Db8 into approximations (A_3) and details (D_1, D_2, and D_3) to filter out the noise which takes care of all kinds of nonlinearities for the extensive analysis. Wavelet filtered neuronal fuzzified inferences' data are divided into training and testing data for better predictions. Figure 6 graphs the linear fit on daily basis at Palla. It can be observed that pH values range from 6.8 to 8.8 and mostly data lie above the pH level of 7. Figures 7(a) and 7(b) clearly demonstrate the regression fitting through LSSVR and linear fit of LSSVR trained values separately. Here, LSSVR trains in the pH level range of 7.4 to 8.4 which is in the drinkable range as prescribed. Figures 8(a) and 8(b) clearly validate regression fitting through M5pRT and linear fit of M5pRT trained values separately. Values are concentrated from pH levels 7 to 8. Figures 9(a) and 9(b) demonstrate the regression fitting through WLSSVR and linear fit of WLSSVR trained values separately. WLSSVR captures most of the values concentrated around pH range 7.5 to 8.5 even though outliers can be seen around 6.5–7 and 9–9.5. Figures 10(a) and 10(b) clearly demonstrate regression fitting through WM5pRT and linear fit of WM5pRT trained values separately. Trains data and concentration lie from pH range 7 to 8.5 as for every feature extracted, and the parent node divides into child nodes and thus tree gets created.

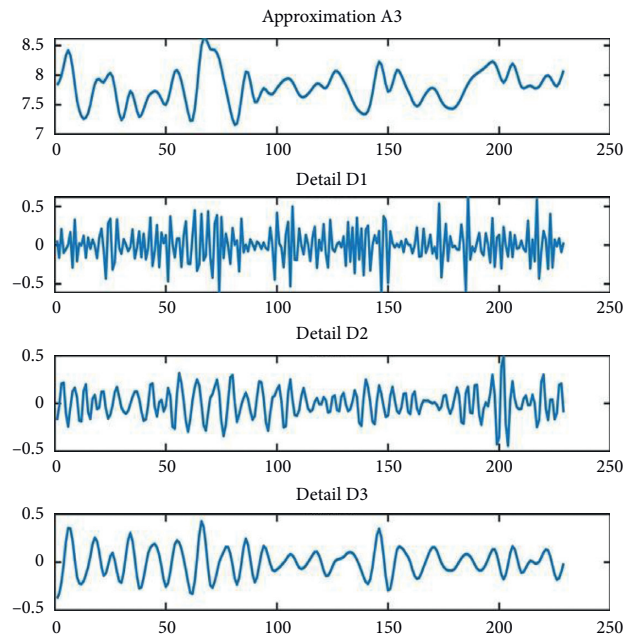

Figure 5: Wavelet decomposition of pH values at Palla.

Now, at the station Bridge with the help of daily data of values of pH levels, it can be observed whether the pH changes at this point due to various external factors and the effect of pH on the adjoining areas. Figure 11 shows the decomposition of the wavelet-form signals according to Db8 into approximations (A_3) and details (D_1, D_2, and D_3) to filter out the noise which takes care of all kinds of nonlinearities for the extensive analysis. Wavelet filtered neuronal fuzzified inferences' data are divided into training and testing data for better predictions. Figure 12 graphs the linear fit on daily basis at Old Delhi Bridge. It can be observed that linear fit line has pH values 7.4 to a little over 7.8.

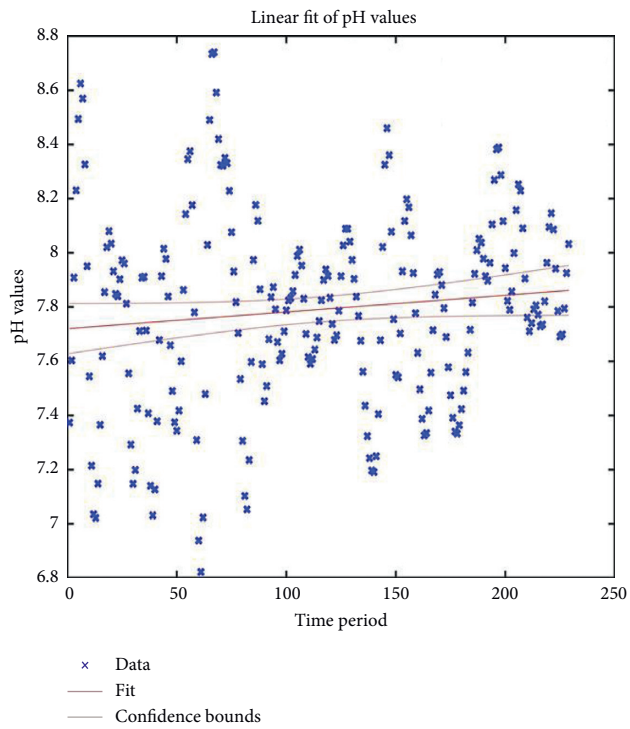

Figure 6: Linear regression fit of pH values at Palla.

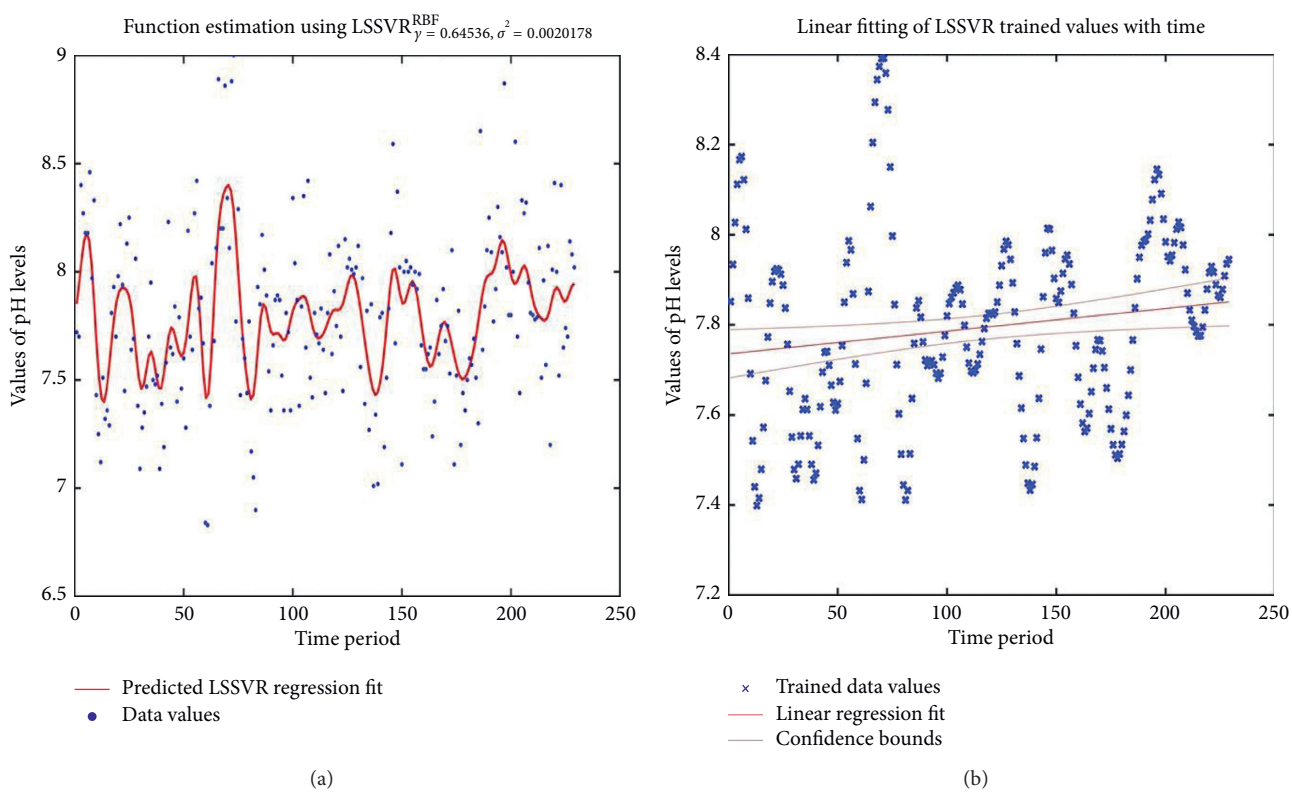

Figure 7: (a) LSSVR regression fit of pH data at Palla. (b) Linear regression fit of LSSVR trained pH values at Palla.

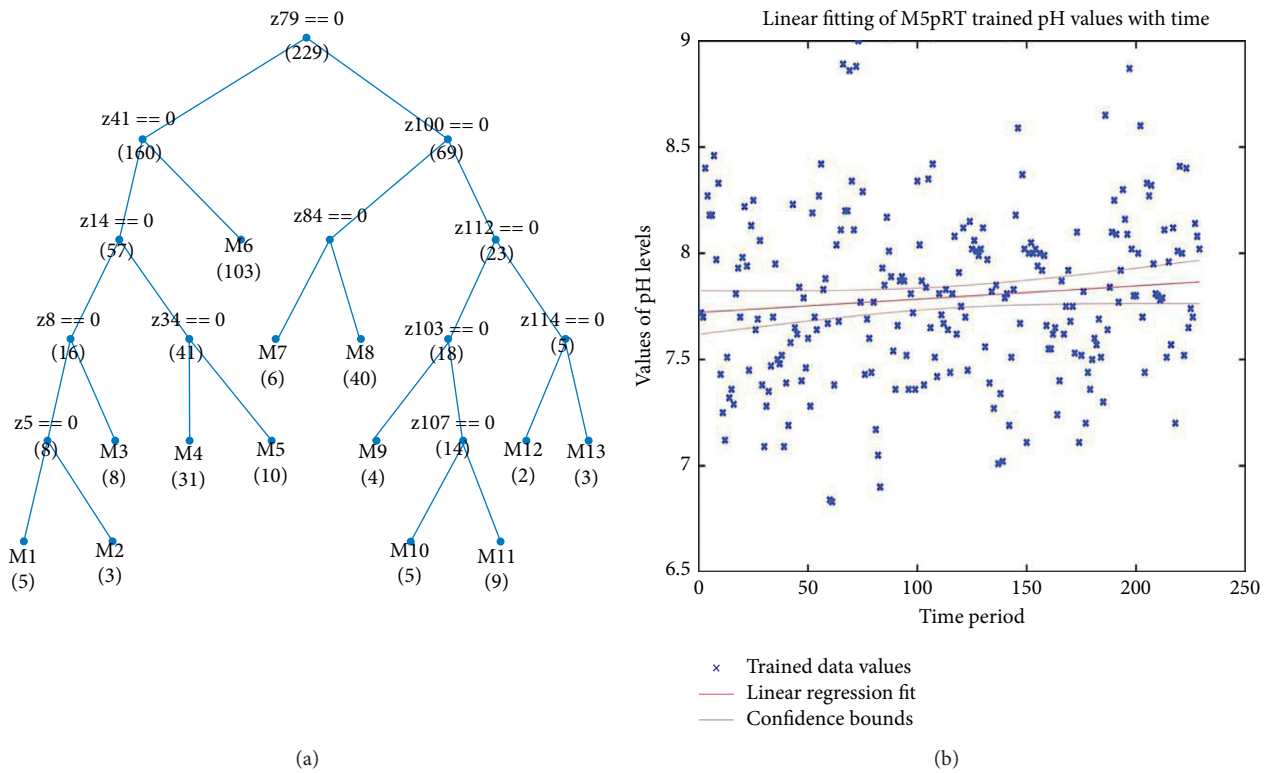

Figure 8: (a) Regression tree simulated via M5pRT at Palla. (b) Linear regression fit of M5pRT trained pH data at Palla.

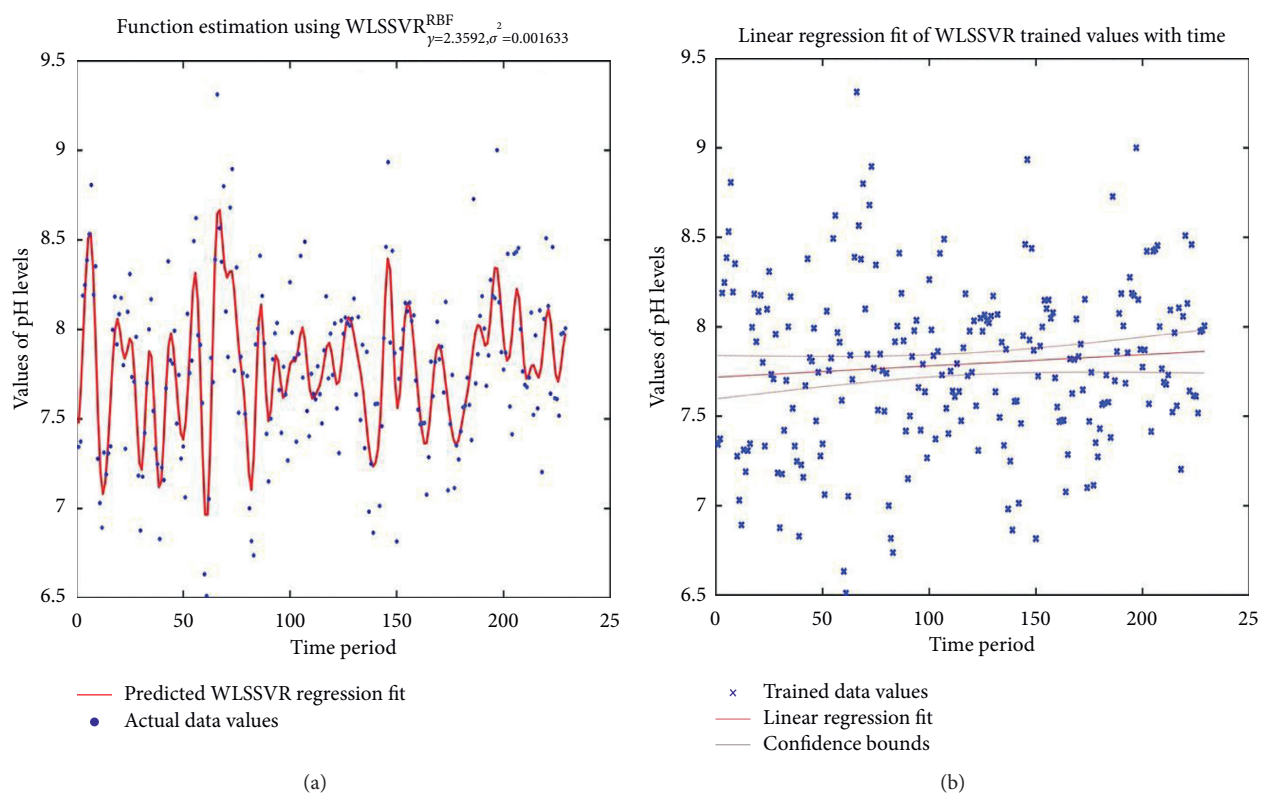

Figure 9: (a) WLSSVR regression fit of pH values at Palla. (b) Linear regression fit of WLSSVR trained pH values at Palla.

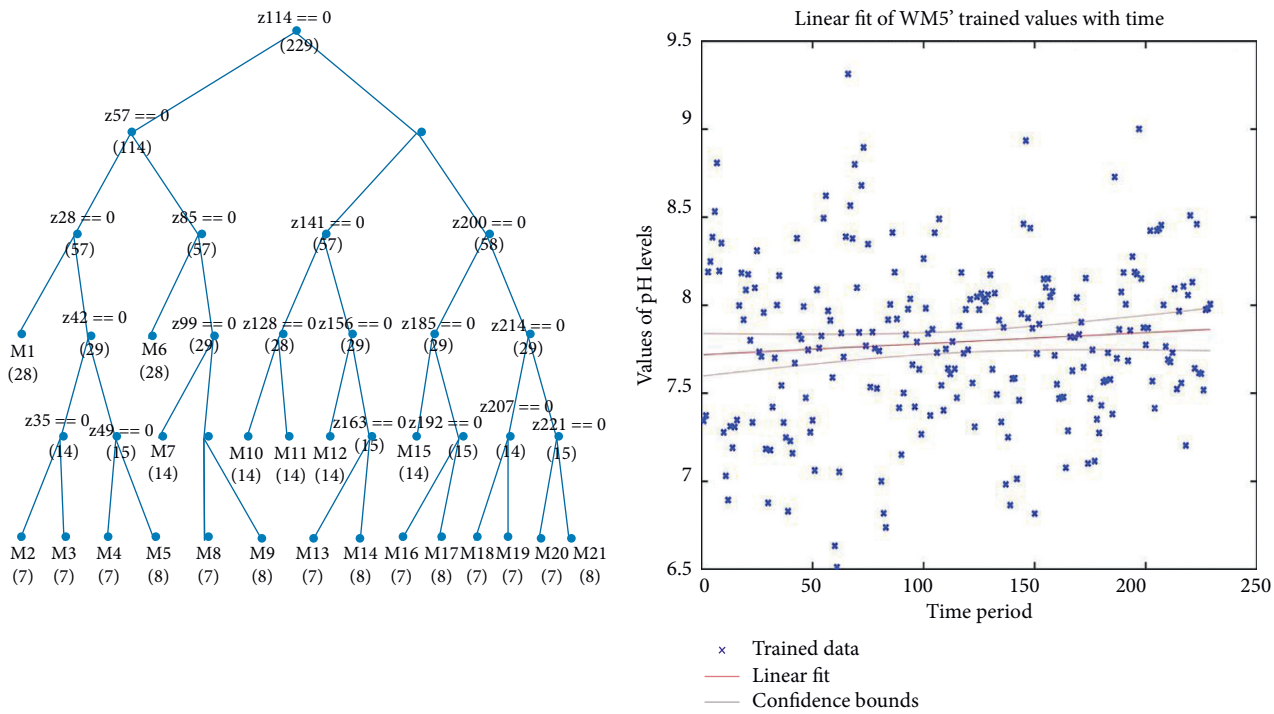

Figure 10: (a) WM5pRT regression tree of pH values at Palla. (b) Linear regression fit of WM5pRT trained pH values at Palla.

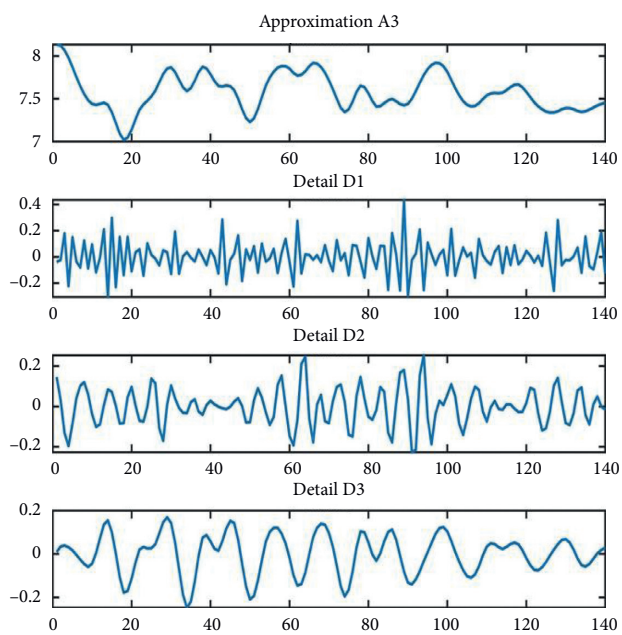

Figure 11: Wavelet decomposition for pH values at Bridge.

Figures 13(a) and 13(b) clearly demonstrate the regression fitting through LSSVR and linear fit of LSSVR trained values separately. Here, LSSVR trains in the pH level range of 7.2 to above 8 upto 8.4. Figures 14(a) and 14(b) clearly validate regression fitting through M5pRT and linear fit of M5pRT trained values separately. Values concentrated for pH levels 7.6 to 7.8. Figures 15(a) and 15(b) demonstrate the regression fitting through WLSSVR and linear fit of WLSSVR trained values separately. WLSSVR captures most of the values concentrated around pH levels 7 to 8 even though outliers can be seen around 6.5–7 and 8–8.2 and decreases with time. Figures 16(a) and 16(b) clearly demonstrate regression fitting through WM5pRT and linear fit of WM5pRT trained values separately. Trains data and

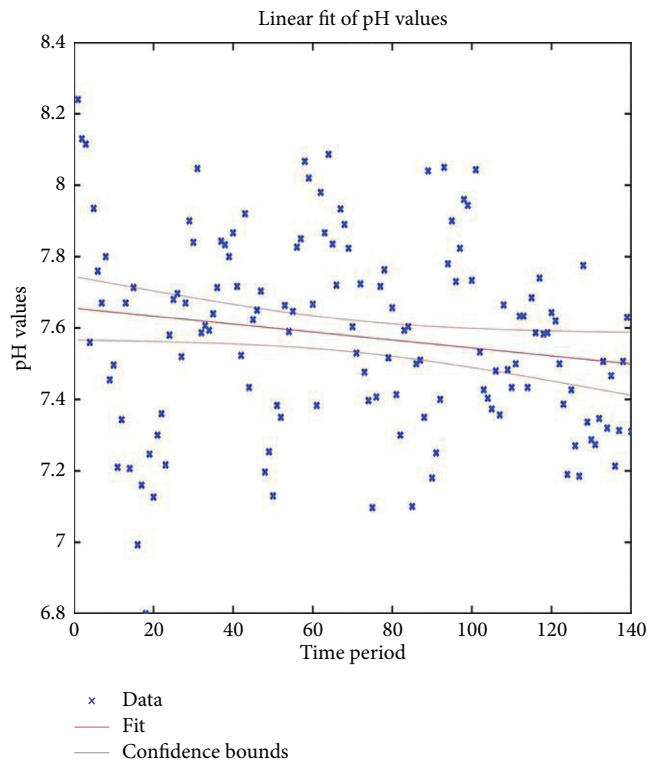

Figure 12: Linear regression fit of pH values at Bridge.

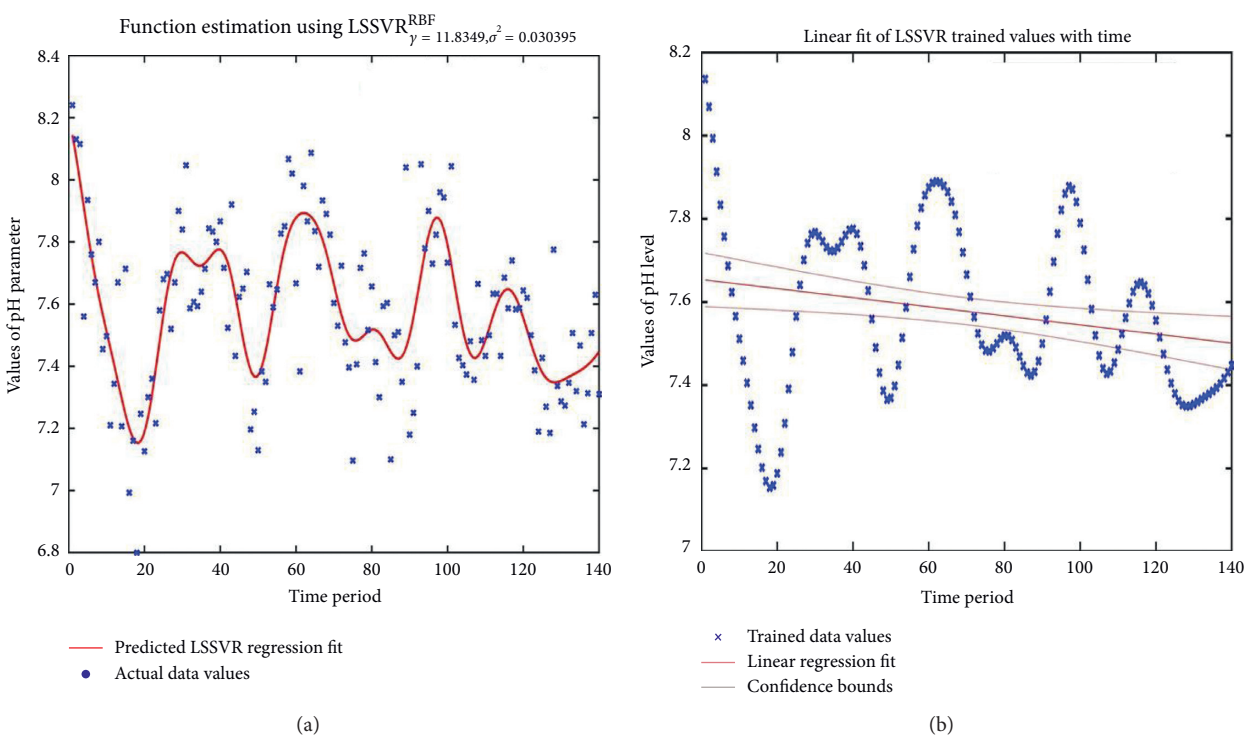

Figure 13: (a) LSSVR regression fit of pH data at Bridge. (b) Linear regression fit of LSSVR trained pH values at Bridge.

concentration can be observed from pH 7.2 to 8 as for every feature extracted, the parent node divides into child nodes, and thus tree gets created. Table 2 compares prediction errors RMSE, MSE, and MAE and also records goodness of fit (R^2) statistic for data recorded at two stations through different learning methods.

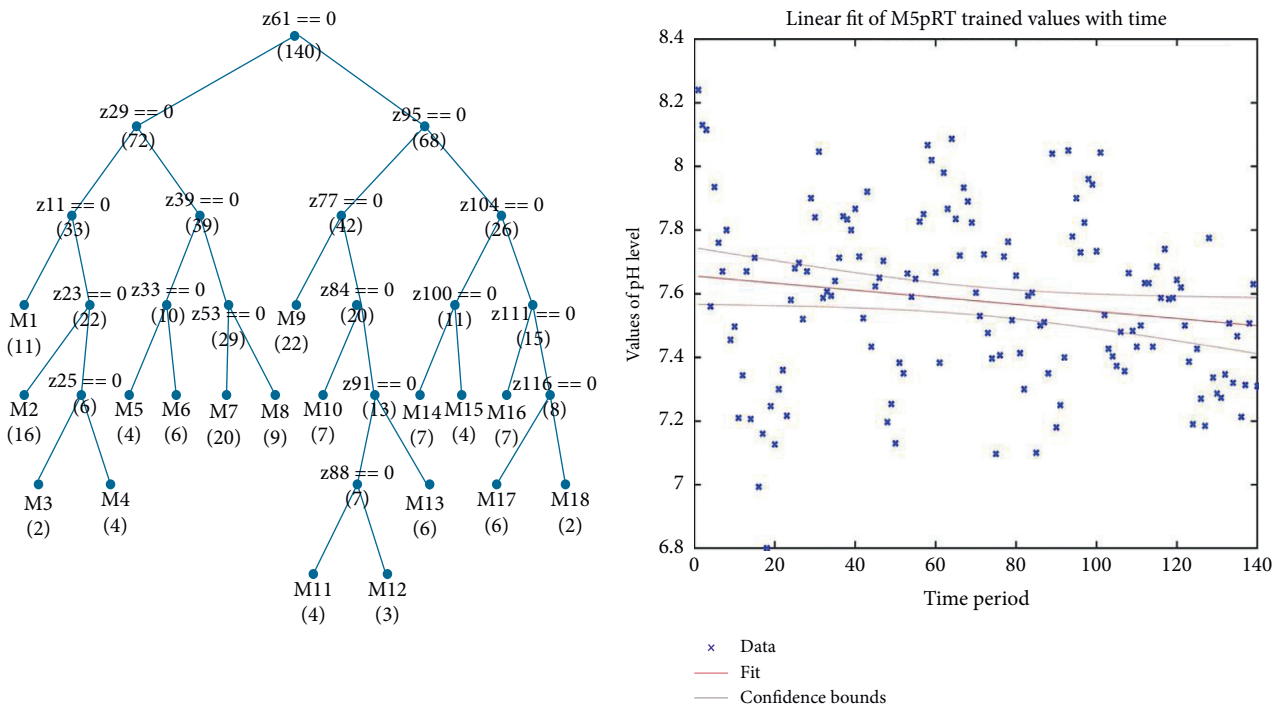

Figure 14: (a) Regression tree simulated via M5pRT at Bridge. (b) Linear regression fit of M5pRT trained data at Bridge.

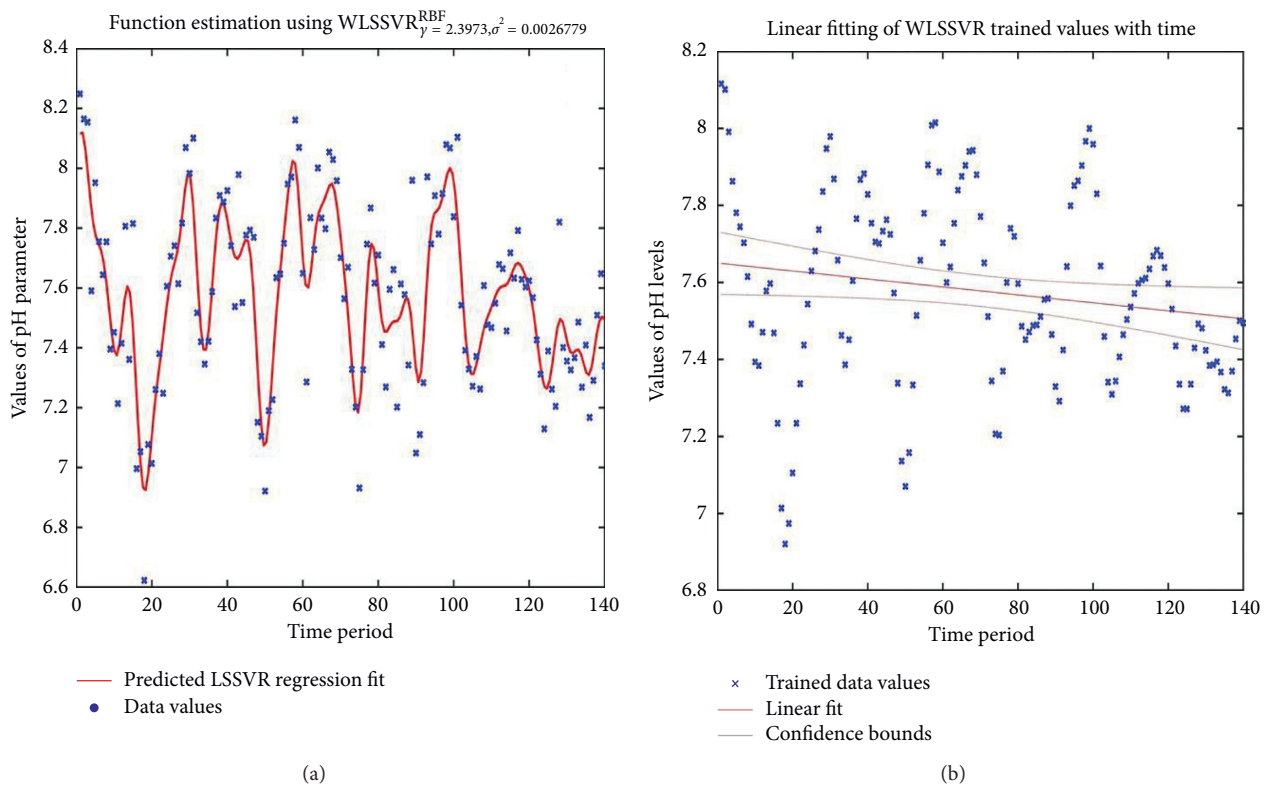

Figure 15: (a) WLSSVR regression fit of pH values at Bridge. (b) Linear regression fit of WLSSVR trained pH values at Bridge.

For LSSVR, RMSEs of Palla and Old Bridge are 7.7988 and 7.5796, respectively, which depict lesser error in simulation for Old Delhi Bridge. Similarly, MSE values are 60.8711 and 57.4510; MAEs are computed to be 7.7934 and 7.557 which shows lesser error in prediction for Old Delhi Bridge. Now, R-squared values are more accurate for Old

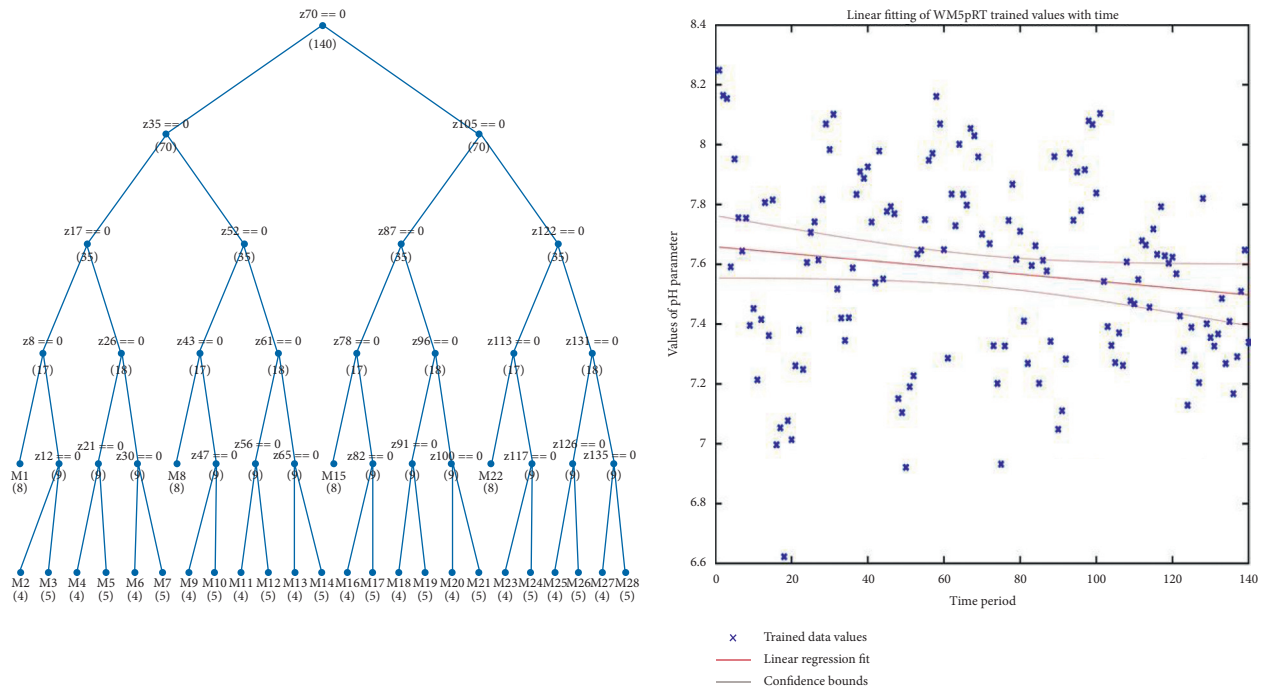

(a) (b)

Figure 16: (a) WM5p regression tree of pH values at Bridge. (b) Linear regression fit of WM5pRT trained pH values at Bridge.

Table 3: Various studies using different intelligent models.

Year	Author	Description	Parameters simulated	Results limited to
2014	Akrami SA. et al.	Rainfall data analyzing using moving average (MA) model and wavelet multiresolution intelligent model for noise evaluation to improve the forecasting accuracy	Wavelet transform (WT), moving average (MA)	RMSE and R^2 computed for MA at various levels of WT.
2018	Mahmoodabadi M. and Rezaei Arshad R.	Evaluated water quality parameters of the Karoun River using a regression approach and adaptive neuro-fuzzy inference system	Mann–Kendall regression, ANFIS	RMSE, MAE, and R^2 computed for the ANFIS model.
2019	Salazar L. et al.	Hourly ozone concentrations predicted using wavelets and ARIMA models	Haar discrete wavelet transform (HDWT), ARIMA	MSE and MSPE computed for ARIMA, HDWT, and combine model. The combined model performed better.
2019	Dehghani M. et al.	Predicted hydropower generation using the grey wolf optimization adaptive neuro-fuzzy inference system	ANFIS and GWO-ANFIS	RMSE, MAE, R^2, relative error, and confidence index computed for ANFIS and GWO-ANFIS. GWO-ANFIS was observed to be better.
2020	Seifi A. and Riahi H.	Estimated daily reference evapotranspiration using hybrid gamma test-least square support vector machine, gamma test-ANN, and gamma test-ANFIS models in an arid area of Iran	LSSVM, ANN, and ANFIS (all with gamma parameter)	RMSE, MAE, and R^2 computed for LSSVR, ANN, and ANFIS. LSSVR performed well overall.
2020	Present study Bhardwaj R., Bangia A.	Improved explicit prediction of river water quality using wavelet- based LSSVR and M5pRT	LSSVR, M5pRT, WLSSVR, WM5pRT	MSE, RMSE, MAE, and R^2 computed for LSSVR, M5pRT, WLSSVR, and WM5pRT. Wavelet conjuncted LSSVR and M5pRT observed to be better prediction models in our study.

Bridge as it would have detected lesser pollutants than at Palla while for WLSSVR, RMSEs of Palla and Bridge are 7.2990 and 7.5714, respectively; similarly, for MSEs; MAE values are 7.7919 and 7.5765. R^2 value at Old Bridge is 0.8759 more close to 1, i.e., WLSSVR predicts better responses for Old Bridge. Considering the M5pRT and WM5pRT model, all performance statistics have outcomes in favour of Palla station on the basis of performance as the data are training and validating through WM5pRT in comparison to M5PRT. It can be detected that MAE outcomes demonstrate lesser reduction compared with RMSE. Overall, MAE has lesser variation for the delta-error outputs through WLSSVR and WM5pRT. Thus, the proposed model, WM5pRT is good for estimation and simulation of the pH at Palla station whereas WLSSVR works better for Old Delhi Bridge station. Error tolerance set for all the learning prototypes is equivalent to $10^{(-4)}$ and 500 epochs of training. The forward and backward phase training depends on the termination condition which is when R^2 (goodness of fit) improvement converges below threshold. Table 3 tabulates findings of various authors that were referred in designing the algorithms for this study.

6. Conclusion

In this proposed study, forecasting pH level of Yamuna River provides improved accurateness on appointing decompositions of wavelets into approximations and details. Evaluation clarifies that the novel algorithm provides precise predictors for estimation. Nonlinearity of data is incompetent for training without the help of LSSVR and M5pRT. Thus, the decomposition of wavelet-form signals into details (D_1, D_2, and D_3) along with approximations' coefficients (A_1, A_2, and A_3) simulation has dynamic role in computation of the concentration of acidic/basic salt levels for river waters. It is observed that the anticipated prototype applying WLSSVR and WM5pRT is better than applying tools such as LSSVR and M5pRT, respectively, as the exactness grows. It can be determined that these additional wavelet layer in models filter-out disturbances while moderating computational-labour. Also, it is believed that the motivation to balance the pH level in the river basins is because there is high consumption of water for various chores and environmental natural processes. It can be better understood if the hydrological background having complexities is studied. These hybrid models with appropriate modifications can be used for training and predicting that would help estimating other water quality parameters such as BOD, DO, and COD at various other monitoring stations allocated by the designated authorities. It can be observed that it is best if water dependency on river basin can be reduced by shifting to rainwater harvestings and also to manage fresh surface-water, ground-water resources, and expansion of the concept of rainwater harvesting as a sustainable solution for future generations. For water quality changes that may happen due to unforeseen naturally occurring events or some man-made hazards, these models will have to be redesigned. Some modifications in the artificial networks will accommodate those factors in the layers of the hybrid models in the best possible manner to achieve optimal quality of the river water. This will help in consumption of clean and healthy drinking water and other purposes to humans and the vast ecosystem dependent on water.

Data Availability

Data were sourced from the Central Pollution Control Board (CPCB).

Conflicts of Interest

The authors declare that they have no conflicts of interest regarding the publication of this paper.

Acknowledgments

The authors thank G.G.S. Indraprastha University for providing financial support and research facilities for this work.

References

[1] K. Chansaengkrachang, A. Luadsong, and N. Aschariyaphotha, "A study of the time lags of the Indian ocean dipole and rainfall over Thailand by using the cross wavelet analysis," *Arabian Journal for Science and Engineering*, vol. 40, no. 1, pp. 215–225, 2015.

[2] P. Mandal, R. Upadhyay, and A. Hasan, "Seasonal and spatial variation of Yamuna River water quality in Delhi, India," *Environmental Modeling & Assessment*, vol. 170, no. 1-4, pp. 661–670, 2010.

[3] Tiyasha, T. M. Tung, and Z. M. Yaseen, "A survey on river water quality modelling using artificial intelligence models: 2000-2020," *Journal of Hydrology*, vol. 585, Article ID 124670, 2020.

[4] S. A. Akrami, A. El-Shafie, M. Naseri, and C. A. G. Santos, "Rainfall data analyzing using moving average (MA) model and wavelet multi-resolution intelligent model for noise evaluation to improve the forecasting accuracy," *Neural Computing and Applications*, vol. 25, no. 7-8, pp. 1853–1861, 2014.

[5] A. A. M. Ahmed and S. M. A. Shah, "Application of adaptive neuro-fuzzy inference system (ANFIS) to estimate the biochemical oxygen demand (BOD) of Surma River," *Journal of King Saud University—Engineering Sciences*, vol. 29, no. 3, pp. 237–243, 2017.

[6] R. Bhardwaj and A. Bangia, "Dynamic indicator for the prediction of atmospheric pollutants," *Asian Journal of Water, Environment and Pollution*, vol. 16, no. 4, pp. 39–50, 2019.

[7] A. Bangia, R. Bhardwaj, and K. V. Jayakumar, "River water quality estimation through artificial intelligence conjuncted with wavelet decomposition," in *Advances in Intelligent Systems and Computing (AISC) Volume 979. Numerical Optimization in Engineering and Sciences*, J. Kacprzyk, D. Dutta, and B. Mahanty, Eds., pp. 159–166, Springer, Berlin, Germany, 2020.

[8] K. D. Brabanter, *Least Square Support Vector Regression with Applications to Large-Scale Data: A Statistical Approach*, Katholieke Universiteit Leuven, Belgium, Europe, 2011.

[9] G. E. P. Box and G. M. Jenkins, *Time Series Analysis, Forecasting and Control*, Holden Day, San Fran-Cisco, CA, USA, 1976.

[10] O. Bozorg-Haddad, M. Zarezadeh-Mehrizi, M. Abdi-Dehkordi, H. A. Loáiciga, and M. A. Mariño, "A self-tuning ANN model for simulation and forecasting of surface flows," *Water Resources Management*, vol. 30, no. 9, pp. 2907–2929, 2016.

[11] M. Dehghani, H. Riahi-Madvar, F. Hooshyaripor et al., "Prediction of hydropower generation using grey wolf optimization adaptive neuro-fuzzy inference system," *Energies*, vol. 12, no. 2, p. 289, 2019.

[12] M. E. Doyle and V. R. Barros, "Attribution of the river flow growth in the Plata basin," *International Journal of Climatology*, vol. 31, no. 15, pp. 2234–2248, 2011.

[13] A.-M. Dunca, "Water pollution and water quality assessment of major transboundary rivers from banat (Romania)," *Journal of Chemistry*, vol. 2018, Article ID 9073763, , 2018.

[14] M. Farzadkhoo, A. Keshavarzi, H. Hamidifar, and M. Javan, "Sudden pollutant discharge in vegetated compound meandering rivers," *Catena*, vol. 182, Article ID 104155, 2019.

[15] P. K. d. M. M. Freire, C. A. G. Santos, and G. B. L. d. Silva, "Analysis of the use of discrete wavelet transforms coupled with ANN for short-term streamflow forecasting," *Applied Soft Computing*, vol. 80, pp. 494–505, 2019.

[16] M. T. Hagan, H. B. Demuth, and M. H. Beale, *Neural Network Design*, PWS Publishing Company, Boston, MA, USA, 1996.

[17] G. Hanrahan, *Artificial Neural Network in Biological and Environmental Analysis*, Taylor and Francis Group, New York, NY, USA, 2011.

[18] C. Jeong, J.-Y. Shin, T. Kim, and J.-H. Heo, "Monthly precipitation forecasting with a neuro-fuzzy model," *Water Resources Management*, vol. 26, no. 15, pp. 4467–4483, 2012.

[19] J. Liu, C. Yu, Z. Hu et al., "Accurate prediction scheme of water quality in smart mariculture with deep Bi-S-SRU learning network," *IEEE Access*, vol. 8, pp. 24784–24798, 2020.

[20] R. Mahmoodabadi and R. Rezaei Arshad, "Long-term evaluation of water quality parameters of the Karoun River using a regression approach and the adaptive neuro-fuzzy inference system," *Marine Pollution Bulletin*, vol. 126, pp. 372–380, 2018.

[21] S. Maiti and R. K. Tiwari, "A comparative study of artificial neural networks, Bayesian neural networks and adaptive neuro-fuzzy inference system in groundwater level prediction," *Environmental Earth Sciences*, vol. 71, no. 7, pp. 3147–3160, 2014.

[22] R. Memarzadeh, H. Ghayoumi Zadeh, M. Dehghani, H. Riahi-Madvar, A. Seifi, and S. M. Mortazavi, "A novel equation for longitudinal dispersion coefficient prediction based on the hybrid of SSMD and whale optimization algorithm," *Science of The Total Environment*, vol. 716, p. 137007, 2020.

[23] C. Min, "An improved recurrent support vector regression algorithm for water quality prediction," *Journal of Computational Information*, vol. 12, pp. 4455–4462, 2011.

[24] H. Riahi-Madvar and A. Seifi, "Uncertainty analysis in bed load transport prediction of gravel bed rivers by ANN and ANFIS," *Arabian Journal of Geosciences*, vol. 11, no. 21, p. 688, 2018.

[25] H. Riahi-Madvar, M. Dehghani, A. Seifi, and V. P. Singh, "Pareto optimal multigene genetic programming for prediction of longitudinal dispersion coefficient," *Water Resources Management*, vol. 33, no. 3, pp. 905–921, 2019.

[26] R. R. Sahay and A. Srivastava, "Predicting monsoon floods in rivers embedding wavelet transform, genetic algorithm and neural network," *Water Resources Management*, vol. 28, no. 2, pp. 301–317, 2014.

[27] M. Sakizadeh, "Artificial intelligence for the prediction of water quality index in groundwater systems," *Modeling Earth Systems and Environment*, vol. 2, no. 1, p. 8, 2016.

[28] L. Salazar, O. Nicolis, F. Ruggeri, J. Kisel'ák, and M. Stehlík, "Predicting hourly ozone concentrations using wavelets and ARIMA models," *Neural Computing and Applications*, vol. 31, no. 8, pp. 4331–4340, 2019.

[29] H. Riahi and H. Riahi-Madvar, "Estimating daily reference evapotranspiration using hybrid gamma test-least square support vector machine, gamma test-ANN, and gamma test-ANFIS models in an arid area of Iran," *Journal of Water and Climate Change*, vol. 11, no. 1, pp. 217–240, 2020.

[30] G. Zuo, J. Luo, N. Wang, Y. Lian, and X. He, "Decomposition ensemble model based on variational mode decomposition and long short-term memory for streamflow forecasting," *Journal of Hydrology*, vol. 585, Article ID 124776, 2020.

Hindawi
Complexity
Volume 2021, Article ID 6627011, 21 pages
https://doi.org/10.1155/2021/6627011

Research Article

Assessment of Artificial Intelligence Models for Developing Single-Value and Loop Rating Curves

Majid Niazkar [1] **and Mohammad Zakwan** [2,3]

[1] *Department of Civil and Environmental Engineering, Shiraz University, Shiraz, Iran*
[2] *Civil Engineering Department, IIT Roorkee, Roorkee, India*
[3] *Civil Engineering Department, MANUU, Hyderabad, India*

Correspondence should be addressed to Majid Niazkar; mniazkar@shirazu.ac.ir

Received 26 November 2020; Revised 11 January 2021; Accepted 13 February 2021; Published 23 February 2021

Academic Editor: Zaher Mundher Yaseen

Estimation of discharge flowing through rivers is an important aspect of water resource planning and management. The most common way to address this concern is to develop stage-discharge relationships at various river sections. Various computational techniques have been applied to develop discharge ratings and improve the accuracy of estimated discharges. In this regard, the present study explores the application of the novel hybrid multigene genetic programming-generalized reduced gradient (MGGP-GRG) technique for estimating river discharges for steady as well as unsteady flows. It also compares the MGGP-GRG performance with those of the commonly used optimization techniques. As a result, the rating curves of eight different rivers were developed using the conventional method, evolutionary algorithm (EA), the modified honey bee mating optimization (MHBMO) algorithm, artificial neural network (ANN), MGGP, and the hybrid MGGP-GRG technique. The comparison was conducted on the basis of several widely used performance evaluation criteria. It was observed that no model outperformed others for all datasets and metrics considered, which demonstrates that the best method may be different from one case to another one. Nevertheless, the ranking analysis indicates that the hybrid MGGP-GRG model overall performs the best in developing stage-discharge relationships for both single-value and loop rating curves. For instance, the hybrid MGGP-GRG technique improved sum of square of errors obtained by the conventional method between 4.5% and 99% for six out of eight datasets. Furthermore, EA, the MHBMO algorithm, and artificial intelligence (AI) models (ANN and MGGP) performed satisfactorily in some of the cases, while the idea of combining MGGP with GRG reveals that this hybrid method improved the performance of MGGP in this specific application. Unlike the black box nature of ANN, MGGP offers explicit equations for stream rating curves, which may be counted as one of the advantages of this AI model.

1. Introduction

For quantification of discharge in open channels, hydraulic engineers often restore to the application of rating curves to avoid the need for in situ discharge measurements conducted either continuously or at particular time intervals [1]. These curves are developed by analysing the relationship between the water level and discharge at a specific river section under steady and unsteady circumstances. In the former, the rating curve is single-valued because of the one-to-one relationship between water depth and discharge. However, corresponding to the same water level, higher discharges are observed when the water level is rising during floods than in receding stages resulting in a hysteresis relationship and loop ratings [2]. Finally, once a discharge rating curve is obtained, it can be deliberately used to estimate discharges by measuring water depth exclusively.

Realizing the importance and wide applications of rating curves, the topic has been studied remarkably. Different issues investigated on the topic include [3] (1) developing discharge rating curves using various data-driven techniques under both steady and unsteady flows [4, 5], (2) physical interpretations of different parts of rating curves, (3) uncertainties associated with stage-discharge relationships

[6, 7], (4) introducing a rating curve applicable beyond the range of discharge measurements [8, 9], and (5) applying rating curves to practical problems in water resources [10, 11]. Among these issues, the majority of the efforts in the literature may be allocated to the first category, which indicates that the inevitable need to develop more rigorous rating curves is the main problem investigated in many previous studies. Likewise, the problem statement in this study focuses on the assessment of different models for defining single-value and loop rating curves.

According to the literature, available approaches for deriving a stage-discharge relationship may be categorized into two main groups named hard computing and soft computing models. The former exploited either numerical models [12–14] or empirical models [15–17] to determine discharge rating equations, whereas the latter utilized artificial intelligence (AI) models for the same purpose [18–23]. Starting from the simple regression-based ratings, hydraulic engineers gradually have turned towards complex computer programming and machine learning approaches not only to develop discharge rating curves but also to estimate discharges more accurately. Moreover, several studies have reported the superiority of AI models over general regressive techniques [24]. Despite all conducted efforts, the quest not only for new approaches but also for assessing different models available for estimating the stage-discharge relation more precisely is still ongoing due to the importance and wide applications of discharge rating curves.

This study aims not only to explore the applicability of AI models in developing rating curves for steady as well as unsteady flow conditions but also to assess their performances in comparison with some other approaches available in the current literature. Therefore, the performances of the MHBMO algorithm, multigene genetic programming (MGGP), and the hybrid MGGP-GRG, which has been recommended for this specific purpose for the first time in the literature, were compared with the performances of the conventional method, the Excel Solver or evolutionary algorithm (EA), rise and fall (RF) method, and ANN. The comparison is conducted for eight datasets with single-value and loop rating curves using several metrics.

2. Materials and Methods

2.1. Datasets. In the present study, eight datasets (four under the steady and four under the unsteady flow conditions) were used in this study. These data, which have already been published in the literature [16, 17, 24–28], are depicted in Figure 1. As shown, the first four datasets have single-value stage-discharge relations, whereas the next four ones display a loop relationship.

Each dataset used in this study was randomly divided into two parts: (1) train data (75% of each dataset) and (2) test data (25% of each dataset). The former was utilized for calibrating and training different methods, while the latter was exploited for comparing the estimated and observed discharges. The ranges of the train and test data of the eight datasets are summarized in Table 1. As shown, in each dataset, the minimum and maximum values of each parameter in the train data are lower and higher than the minimum and maximum of the same parameter in the test data, respectively. This characteristic in the data division enables to calibrate or train different methods for a wider range of values so that they can predict the test data better.

2.2. Models Used for Developing Rating Curves. In the subsequent section, the seven models including the conventional method, EA, RF, the MHBMO algorithm, ANN, MGGP, and the hybrid MGGP-GRG model, which were used to develop rating curves, are presented.

2.2.1. Conventional Method. The general form of a discharge rating curve is based on Manning's equation. This stage-discharge relationship is generally expressed in the following equation [24]:

$$Q = K(G - a)^n, \tag{1}$$

where Q is a stream discharge, G is a river stage, a is a constant representing the gauge reading corresponding to zero discharge, and $K$and $n$are the rating curve parameters.

In the conventional method, the value of a is determined by the straight line fitted to the curve of $\log Q$ versus $\log(G - a)$. This curve is commonly plotted by adopting a trial-and-error process by playing with the value of a. In this regard, the transformed logarithmic form of equation (1) is given in the following equation:

$$\log Q = n \log(G - a) + \log K. \tag{2}$$

By defining $Y = \log Q$, $A = n$, $X = \log(G - a)$, and $B = \log K$, equation (2) provides a straight relation between Y and Xas is $Y = AX + B$. The values of A and B can be calculated by using the conventional regression analysis (the least square method).

2.2.2. Evolutionary Algorithm. EA is a population-based probabilistic method with a bioinspired principle of survival of the fittest. This algorithm can be used to solve highly nonlinear problems with less than 200 decision variables [29]. In essence, EA is a combination of evolutionary algorithms, GA, and classical optimization methods. In this zero-order algorithm embedded within Microsoft Excel, a population is initialized randomly. Thereafter, it is subjected to the selection, recombination, and mutation iteratively until it finds a better fit solution in the given time regarding a set of constraints specified.

In the present study, the Excel Solver has been used to optimize the parameters of the rating curve relation shown in equation (1). To obtain the optimal values of the decision variables (K, a, and n), minimization of sum of square of errors (SSE) was set as the objective function. A constraint was put on the variable a so that its optimal value is less than or equal to the stage corresponding to the minimum

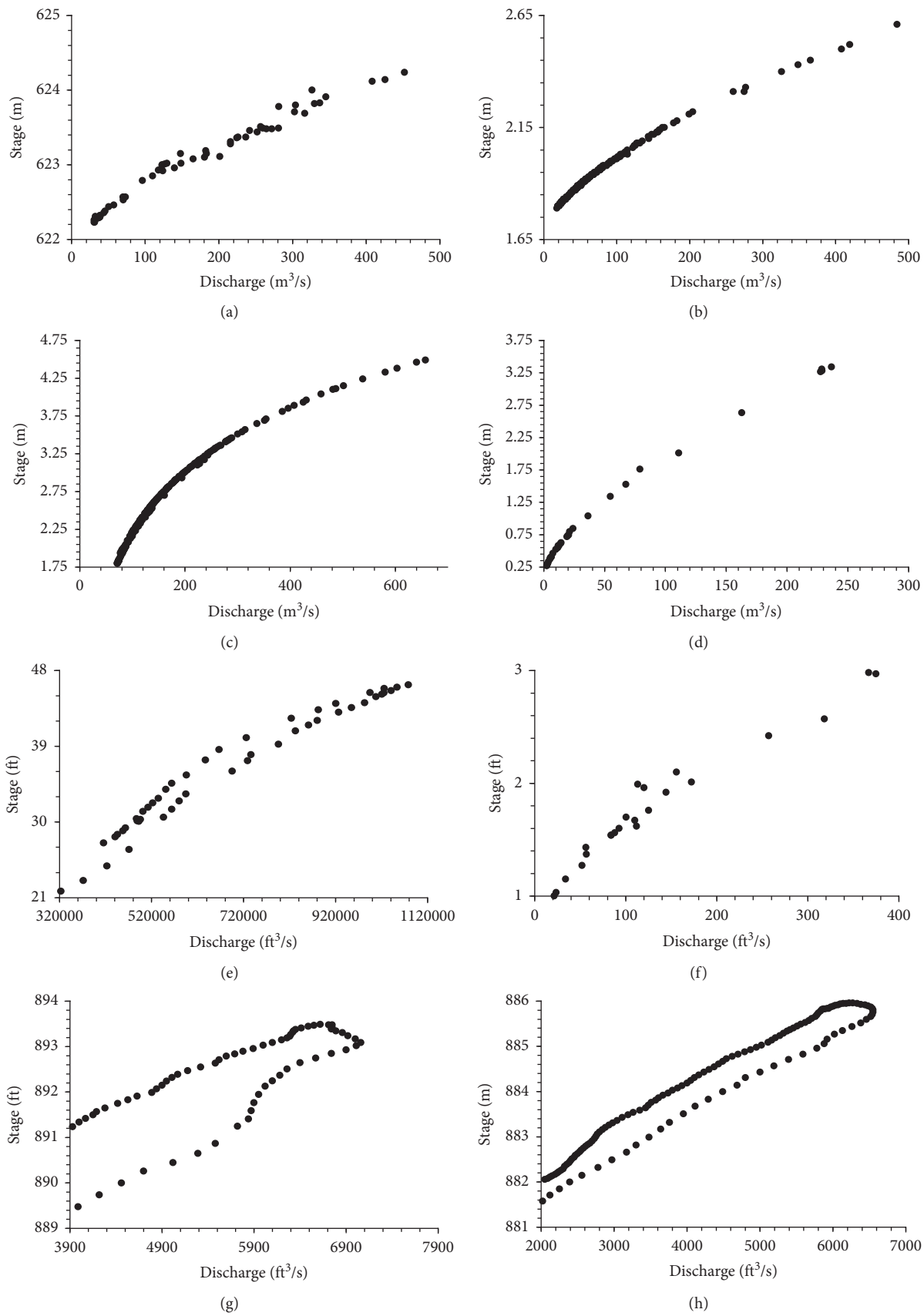

Figure 1: Observed rating curves of the eight datasets. (a) Dataset 1. (b) Dataset 2. (c) Dataset 3. (d) Dataset 4. (e) Dataset 5. (f) Dataset 6. (g) Dataset 7. (h) Dataset 8.

Table 1: Range of calibration and validation data.

Data	Reference of data	Parameter	Training data			Test data		
			Minimum	Maximum	Mean	Minimum	Maximum	Mean
Dataset 1	[25]	G (m)	622.23	624.24	623.06	622.24	624.14	623.08
Dataset 2	[16]	G (m)	1.79	2.61	1.94	1.8	2.5	1.93
Dataset 3	[24]	G (m)	1.8	4.49	2.14	1.8	4.46	2.39
Dataset 4	[26]	G (m)	0.27	3.34	1.12	0.3	3.306	0.98
Dataset 5	[27]	G (ft)	21.78	46.29	36.15	22.08	46.23	36.62
Dataset 6	[28]	G (ft)	1.00	2.98	1.79	1.04	2.51	1.65
Dataset 7	[17]	G (ft)	885.99	981.10	892.69	886.11	893.48	891.28
Dataset 8	[17]	G (ft)	881.01	885.96	883.98	881.01	885.96	883.89
Dataset 1	[25]	Q (m^3/s)	30.56	451.87	170.79	31.48	425.71	171.19
Dataset 2	[16]	Q (m^3/s)	17.7	484.22	73.63	19.11	407.76	71.65
Dataset 3	[24]	Q (m^3/s)	71.08	656.95	173.71	71.08	639.96	174.43
Dataset 4	[26]	Q (m^3/s)	2.33	236.6	54.37	2.923	228.5	44.39
Dataset 5	[27]	Q (ft^3/s)	323237	1078225	690475	337255	1058347	709212
Dataset 6	[28]	Q (ft^3/s)	21.38	374.74	133.02	23.65	236.93	99.97
Dataset 7	[17]	Q (ft^3/s)	1110.00	7060.00	4973.71	1380.00	6920.00	4886.75
Dataset 8	[17]	Q (ft^3/s)	1490.00	6550.00	4122.27	1490.00	6520.00	4047.19

observed discharge. The mutation rate was set as 0.05, while the population size and convergence criterion were fixed as 50 and 0.00001, respectively.

2.2.3. Rise and Fall (RF) Method. Several attempts have also been made by various researchers to address the issues related to the measurement of unsteady flow. During floods, higher discharges are observed when flood waves propagate through the gauging site, while lower discharges are observed for the same stage when the flood wave recedes. This subsequently leads to different relationships between stages and discharges during the rising and falling limbs of flood hydrographs. Since the failure probability of hydraulic structures increases during high discharges, it is vital to distinguish different behaviours of water levels in different limbs of a flood hydrograph. In this regard, separate rating curve equations are fitted to the rising and falling limbs of stage-discharge flood hydrographs, commonly known as the rise and fall (RF) method. Therefore, separate rating curves will be required to be developed to comply with changes in the stage-discharge relationship.

2.2.4. The MHBMO Algorithm. The MHBMO algorithm is a zero-order optimization algorithm that simulates the mating process of honey bees between a queen and drones of a generation. This simulation process mainly searches for the best honey bee (queen) by producing successive generations, which are improved in the light of the fitness criterion through the mating process. Similar to other metaheuristic algorithms, the MHBMO algorithm has several controlling parameters, which have been set in accordance with that of previous studies in the literature [30]. Based on the literature, it is the first time that the MHBMO algorithm has been used for developing rating curves.

2.2.5. Artificial Neural Network. Artificial neural network (ANN) serves as an estimation tool in various fields of research. In essence, it comprises an organized network, which contains three main layers named as input layer, hidden layer, and output layer. Each layer consists of a specific number of neurons, which are permitted to have connections exclusively with other neurons placed in different layers [31]. This principle dictates that the input data, like the output data, should be independent variables. The former and latter data are commonly placed in the input and output layers, respectively. On the other hand, the neurons of the hidden layers play the role of transferring the input data to the output data. Finally, the data flow in the ANN architecture continues until an adequate relationship, which satisfies a desirable accuracy, is obtained [32].

In this study, the input and output data for each dataset consist of normalized stages and normalized discharges, respectively. For the training process of ANN, normalized variables were utilized instead of dimensional variables to capture the relationship between the input and output data more accurately, while normalized variables were turned into ones with dimensions for comparison purposes. Additionally, a feed-forward backpropagation ANN with the Levenberg–Marquardt optimization algorithm was used, while the ANN controlling parameters, except the minimum gradient parameter, were assumed the same as those adopted in the literature [33]. The best value for the minimum gradient parameter was determined by a trial-and-error procedure as it was found that the value of this parameter may have a major impact on the results. Finally, ANN used in this study has a three-layer network, which contains one, ten, and one neurons in the input, hidden, and output layers, respectively.

2.2.6. Multigene Genetic Programming. Genetic programming (GP) is categorized as one of the AI models and as a modified variant of GA. In the latter context, GA works as the search engine of GP to strive for finding a relationship between two sets of variables. To be more precise, GP not only benefits from the random-based searching

characteristics of GA but also overcomes one of its limitations, which is known to be the incapability of determining a relation between input and output data associated with a problem with a high order of complexity. The latter advantage of GP over GA is provided with the use of a tree-like configuration [33].

Among various versions of GP, MGGP contains a user-defined number of genes, which enables the implementation of various types of functions and mathematical operators in the quest for a suitable relation between the data under consideration. MGGP exploits GA as an optimization engine to minimize a defined objective function [34]. In the process of solving an optimization problem using MGGP, the main steps of GA, which includes initialization, selection, reproduction, and termination, are successively repeated [35]. To be more specific, it commences with the creation of an initial population. This randomly generated population basically includes different functions and terminals, which are subjected to GA operators, such as crossover and mutation. This process is repeated until one of the termination criteria, which are the maximum number of generation and fitness termination value, is met [36]. Finally, MGGP assigns a weight to each member of the GP population containing a number of trees or genes, while the MGGP output is a linear combination of these trees.

In this study, a MATLAB version code of MGGP, which was adopted from the literature [34, 37], was used. The objective function of this code is minimizing the root mean square of errors between the estimated and observed sets of normalized discharges, while normalized stages were utilized as the input data. Furthermore, the same data division considered for ANN was applied to MGGP. Also, Table 2 summarizes the MGGP parameters used in this study. Since MGGP attempts to solve a defined optimization problem, each run of MGGP may lead to a different equation. Hence, many (more than 50) runs of MGGP were conducted for each dataset, and the relation with the best fitness value was selected as the final MGGP result.

2.2.7. Hybrid MGGP-GRG Method. The hybrid MGGP-GRG refers to the combination of multigene genetic programming and generalized reduced gradient technique. The latter is a first-order optimization algorithm, which has been combined with other models in the literature [30]. Figure 2 illustrates the detailed flowchart of the hybrid MGGP-GRG method used for developing rating curves. As shown, the best-fit MGGP model is selected in the first stage. Then, the coefficients of the model developed by MGGP are obtained by GRG optimization technique with target cell as minimization of SSE. In this way, the equation obtained by MGGP can be further improved by applying GRG optimization technique. Based on the current literature, it is the first time that the hybrid MGGP-GRG has been proposed.

2.3. Performance Evaluation Criteria. The developed ratings obtained by different models were compared on the basis of several performance evaluation criteria including (1) SSE (equation (3)), (2) Nash–Sutcliffe efficiency (NE) (equation (4)), (3) relative error (RE) (equation (5)), (4) mean absolute relative error (MARE) (equation (6)), and (5) maximum absolute relative error (MXARE) (equation (7)). In this regard, the model with the highest efficiency and lowest error will be the best-fit model:

$$\mathrm{SSE} = \sum_{i=1}^{N} \left(Q_{o_i} - Q_{e_i}\right)^2. \tag{3}$$

$$\mathrm{NE} = 1 - \frac{\sum_{i=1}^{N} \left(Q_{o_i} - Q_{e_i}\right)^2}{\sum_{i=1}^{N} \left(Q_{o_i} - \left(\sum_{i=1}^{N} Q_{o_i}/N\right)\right)^2}, \tag{4}$$

$$\mathrm{RE}_i = \frac{Q_{e_i} - Q_{o_i}}{Q_{o_i}}, \quad \text{for } i = 1, \ldots, N, \tag{5}$$

$$\mathrm{MARE} = \frac{1}{N} \sum_{i=1}^{N} \left| \frac{Q_{e_i} - Q_{o_i}}{Q_{o_i}} \right|, \tag{6}$$

$$\mathrm{MXARE} = \max\left(\left| \frac{Q_{e_i} - Q_{o_i}}{Q_{o_i}} \right|, \quad \text{for } i = 1, \ldots, N \right), \tag{7}$$

where Q_{o_i} and Q_{e_i} are the ith observed and estimated discharges for each dataset, respectively.

3. Results

The seven methods described in the previous section were used to develop rating curves for all datasets separately. For this purpose, the training part of each dataset was used for (1) calibrating equation (1) using the conventional method, EA, RF, and the MHBMO algorithm and (2) training the AI and hybrid models. The rest of the data in each dataset (test data) were utilized for quantifying the performances of different methods. The results achieved by different methods are presented as follows.

3.1. Results of the Conventional Method, EA, and the MHBMO Algorithm. The rating curve parameters of equation (1), which were obtained by the conventional method, EA, and the MHBMO algorithm, are reported in Table 3. As shown, although these three models applied to the same relation for discharge rating curves (equation (1)), they yielded completely different values of rating curve parameters for Dataset 3, Dataset 5, and Dataset 7. Furthermore, applying EA and the MHBMO algorithm to Dataset 1, Dataset 2, Dataset 4, and Dataset 6 resulted in almost similar optimal parameters of equation (1), while the parameters calibrated by the three methods (the conventional method, EA, and the MHBMO algorithm) are quite close for Dataset 8. The discrepancy in this parameter estimation mainly arises because the parameter a in the conventional method is obtained from the best fit of a straight line through a trial-and-error procedure, and the estimates of the other two parameters ($K$and n) are dependent on the value of the

Table 2: Values of MGGP controlling parameters.

Parameter	Values
Function set	Arithmetic (trigonometric, plog, psqroot, and exponential functions) and operations
Number of generations	120
Maximum number of genes allowed in individual	5
Maximum tree depth	4
Tournament size	4
Elitism	0.05 of population
Crossover events	0.85
High-level crossover	0.2
Low-level crossover	0.8
Standard deviation of perturbation applied in mutation Gaussian perturbation of a randomly selected constant	0.1
Subtree mutation	0.9
Replacing input terminal with another random terminal	0.05
Gaussian perturbation of randomly selected constant	0.05
Direct reproduction	0.05
Ephemeral random constants	[−10, 10]

parameter a. On the other hand, all the rating curve parameters calibrated by EA and the MHBMO algorithm are optimized simultaneously to obtain the global optima. Evidently, the datasets whose parameters gained different values in the calibration process may provide a better perspective when the performances of the conventional method, EA, and the MHBMO algorithm are compared.

3.2. Results of ANN. ANN, as an AI model, leads to a calibrated network for estimating discharges for the train and test data. By conducting many attempts for running ANN, it was found that the minimum gradient parameter in the training process of ANN has a major impact on the discharges estimated by ANN. Therefore, a trial-and-error procedure was adopted to find appropriate values of this controlling parameter.

3.3. Results of MGGP. MGGP provides explicit equations in terms of stage so that discharges can be directly estimated. In the proposed equations, the stage and discharge values were normalized before applying MGGP to achieve better results. For instance, the observed discharges of the ith dataset (Q_0) were normalized by $Q_i = (Q_o - Q_{\min}/Q_{\max} - Q_{\min})$, where Q_i, $Q_{\min}$, and $Q_{\max}$ are the normalized, minimum, and maximum discharges of the ith dataset. The explicit equation obtained by MGGP for estimating normalized discharges of the ith dataset is a function of the normalized water depth (y_i). After the dimensionless discharges predicted by the MGGP-based models were transformed back to the dimensional variable (the estimated discharge), they were compared with the corresponding observed values. The equations developed by MGGP are presented in the following for the eight datasets:

(1) For Dataset 1:

$$\begin{aligned} Q_1 = {} & 0.4503y_1 + 0.3962\sin(177.2y_1) - 0.3955\sin(177.3y_1) + 0.4503y_1^2 \\ & - 0.02175\sin(88.6y_1 - 750.3) - 0.04285\cos[18.84\cos(y_1)] + 0.04287. \end{aligned} \tag{8}$$

(2) For Dataset 2:

$$\begin{aligned} Q_2 = {} & 0.05899\cos(11.78y_2) - 0.07737\cos[-9.779y_2 - \cos(y_2)] \\ & + 7.196\sin(0.8161y_2) - 0.01603\sin(15.46y_2) + \frac{36.2\cos(y_2)}{5.937y_2 + 6.1} - 5.953, \end{aligned} \tag{9}$$

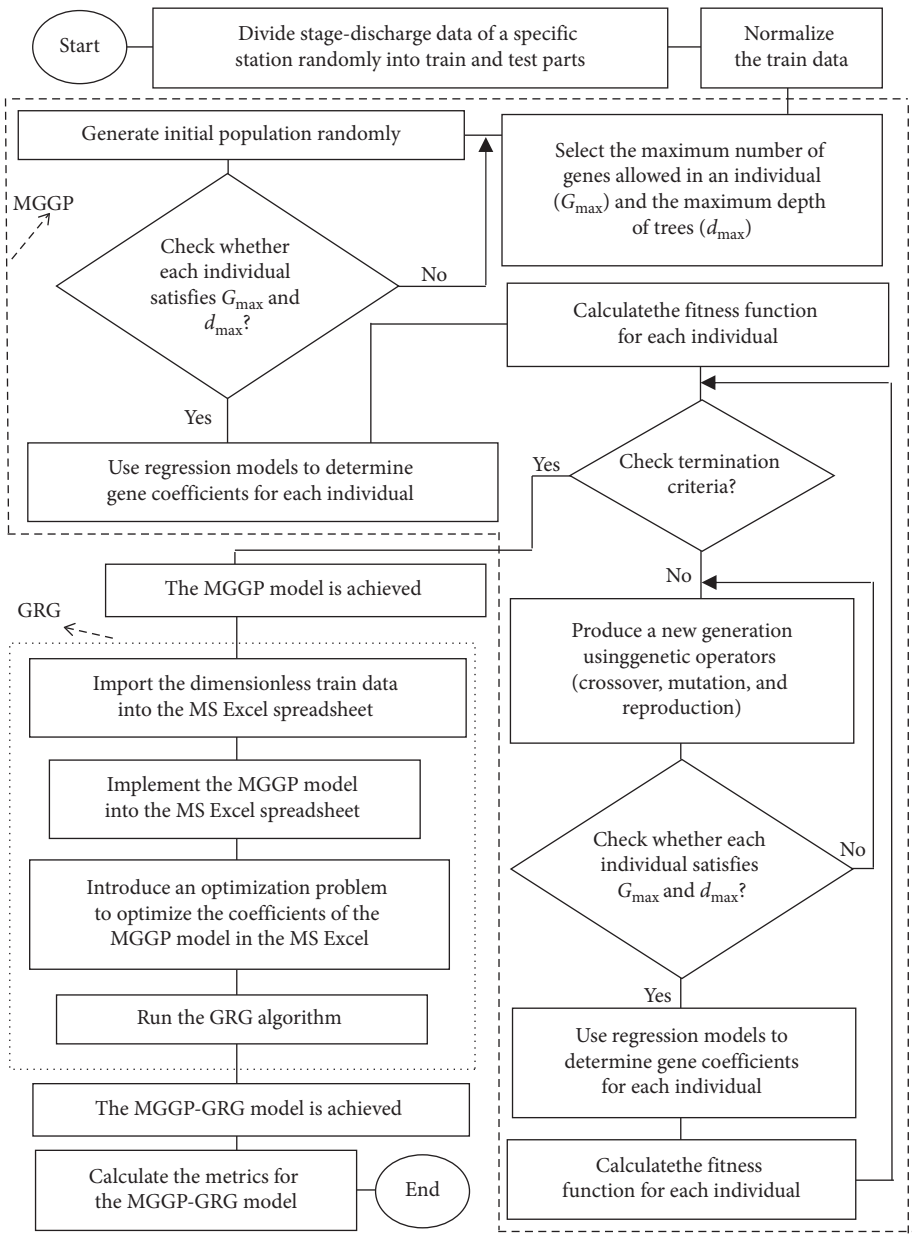

Figure 2: Flowchart of the hybrid MGGP-GRG model for developing rating curves.

Table 3: Coefficients of equation (1) calibrated by the conventional method, EA, and the MHBMO algorithm.

Method	Coefficients	Dataset 1	Dataset 2	Dataset 3	Dataset 4	Dataset 5	Dataset 6	Dataset 7	Dataset 8
Conventional	K	38.38	578.07	23.74	42.80	1351.46	63.76	779.64	19.85
	a	621.30	1.61	0.21	0.15	0.10	0.40	881.00	875.00
	n	2.37	1.98	2.10	1.43	1.73	1.89	0.76	2.41
EA	K	126.16	543.41	11.02	40.75	1322.00	80.38	3415.67	19.30
	a	621.88	1.68	0.00	0.13	0.00	0.54	885.98	875.00
	n	1.42	1.57	2.67	1.51	1.74	1.74	0.23	2.42
MHBMO	K	126.16	543.44	1.00×10^{-15}	40.74	2.43×10^{-13}	80.40	3403.68	24.66
	a	621.88	1.68	−13.87	0.13	−136.28	0.53	885.90	875.28
	n	1.42	1.57	14.10	1.51	8.24	1.74	0.23	2.35

where $p\log(y_2) = \begin{cases} \log(y_2) & \text{for} \quad y_2 > 0 \\ 0 & \text{for} \quad y_2 \le 0 \end{cases}$ and

$\text{psqroot}(y_2) = \begin{cases} \sqrt{y_2} & \text{for} \quad y_2 > 0 \\ 0 & \text{for} \quad y_2 \le 0 \end{cases}$.

(3) For Dataset 3:

$$\begin{aligned} Q_3 = {} & 0.328y_3 - 0.006875\sin[\sin(7.901y_3)] + 0.328\cos[\cos(y_3)] \\ & - 0.0009848\sin(2y_3) - 0.0009848\sin(22.75y_3) + 3.208\cos(y_3) \\ & - 3.418\cos[2y_3 - \sin(y_3)] + 0.03491. \end{aligned} \tag{10}$$

(4) For Dataset 4:

$$\begin{aligned} Q_4 = {} & 0.216y_4 + 1.133\left(2y_4 - y_4^2\right)^2 - \frac{0.093\left(2y_4 - y_4^2\right)}{6.031y_4 - 3.498} - 2.812y_4^2 \\ & + 2.38y_4^3 + \frac{0.3006y_4^2}{5.978y_4 - 3.498} - 0.0008927. \end{aligned} \tag{11}$$

(5) For Dataset 5:

$$\begin{aligned} Q_5 = {} & 0.0172\sin\left(63.21y_5^2\right) + 0.01468\sin(319.7y_5) + 0.02307\sin(163.2y_5) \\ & + 0.02196\sin(480.3y_5) - 0.5722y_5^2 + 0.5722y_5\exp(y_5) + 0.01377. \end{aligned} \tag{12}$$

(6) For Dataset 6:

$$\begin{aligned} Q_6 = {} & 0.0253\sin\left[(8.549y_6)^2\right] - 109.7\exp\left(y_6^2 - \frac{6.604}{y_6}\right) - 0.03472\sin\left[(y_6 + 6.604)^2\right] \\ & + 0.1227\tanh(6.528y_6) - 7.162\tanh\{\tanh[\cos(y_6)]\} + 4.585, \end{aligned} \tag{13}$$

where the second term in the right-hand side of equation (13) is zero when $y_6 = 0$.

(7) For Dataset 7:

$$\begin{aligned} Q_7 = {} & \frac{1155}{\exp(0.4073/y_7)} - \frac{64.57y_7^3}{y_7^2 + 0.0002876} - \frac{10700y_7^3}{8.076y_7 - \exp(y_7)} \\ & + \frac{6140y_7^2}{4.836y_7 + \exp(y_7)} - \frac{y_7^2(355.4y_7 - 2866)}{7.944y_7 - \exp(y_7)} + 0.03322, \end{aligned} \tag{14}$$

where the first term in the right-hand side of equation (14) is zero when $y_7 = 0$.

(8) For Dataset 8:

$$Q_8 = \frac{0.0007984(y_8 - 0.366)}{y_8^2 - 0.2897} - \frac{0.004208[y_8 - \sin(y_8)]}{y_8 - 0.366} + \frac{0.445y_8}{2y_8 + 0.2737} - 0.03444\exp(y_8)\exp[\exp(y_8)] + 1.062\exp[\cos(y_8)]\exp(y_8^2) - 2.795. \tag{15}$$

3.4. Results of the Hybrid MGGP-GRG Model. The hybrid MGGP-GRG model modified the coefficients of the equations obtained by MGGP. These equations are given in the following for the eight datasets:

(1) For Dataset 1:

$$Q_1 = 0.4480y_1 + 0.3976\sin(176.967y_1) - 0.393\sin(177.09y_1) + 0.4587y_1^2 - 0.0266\sin(90.107y_1 - 751.049) - 0.0445\cos[18.8143\cos(y_1)] + 0.0404. \tag{16}$$

(2) For Dataset 2:

$$Q_2 = 0.05899\cos(11.7924y_2) - 0.07737\cos[-9.7849y_2 - \cos(y_2)] + 7.1919\sin(0.8159y_2) - 0.01603\sin(15.459y_2) + \frac{36.1584\cos(y_2)}{5.9348y_2 + 6.0984} - 5.9479. \tag{17}$$

(3) For Dataset 3:

$$Q_3 = 0.328y_3 - 0.006875\sin[\sin(7.91y_3)] + 0.328\cos[\cos(y_3)] - 0.0009848\sin(2y_3) - 0.0009848\sin(22.75y_3) + 3.2075\cos(y_3) - 3.4185\cos[1.9998y_3 - \sin(y_3)] + 0.03491. \tag{18}$$

(4) For Dataset 4:

$$Q_4 = 0.2751y_4 + 0.9121(1.8105y_4 - y_4^2)^2 - \frac{0.0316(0.084y_4 - y_4^2)}{6.9433y_4 - 4.3146} - 1.375y_4^2 + 1.4796y_4^3 + \frac{0.0409y_4^2}{8.629y_4 - 4.62} - 0.00025. \tag{19}$$

(5) For Dataset 5:

$$Q_5 = 0.0145\sin(63.45y_5^2) + 0.01635\sin(319.37y_5) + 0.02336\sin(163.475y_5) + 0.02248\sin(480.07y_5) - 0.6305y_5^2 + 0.595y_5\exp(y_5) + 0.01005. \tag{20}$$

(6) For Dataset 6:

$$Q_6 = 0.0257\ \sin\left[\left(8.559y_6\right)^2\right] - 111.73\ \exp\left(y_6^2 - \frac{6.649}{y_6}\right) - 0.031696\ \sin\left[\left(y_6 + 6.616\right)^2\right] + 0.1195\ \tanh\left(5.343y_6\right) - 7.091\ \tanh\{\tanh\left[\cos\left(y_6\right)\right]\} + 4.5475, \tag{21}$$

where the second term in the right-hand side of equation (21) is zero when $y_6 = 0$.

(7) For Dataset 7:

$$Q_7 = -\frac{64.53y_7^3}{y_7^2 + 0.0002879} - \frac{10700y_7^3}{8.0768y_7 - \exp\left(y_7\right)} + \frac{6140y_7^2}{4.8346y_7 + \exp\left(y_7\right)} - \frac{y_7^2\left(355.4y_7 - 2866\right)}{7.9436y_7 - \exp\left(y_7\right)} + 0.03332. \tag{22}$$

(8) For Dataset 8:

$$Q_8 = \frac{0.000528\left(y_8 - 0.4779\right)}{y_8^2 - 0.2907} - \frac{0.003506\left[y_8 - \sin\left(y_8\right)\right]}{y_8 - 0.3659} + \frac{0.4689y_8}{2.162y_8 + 0.2685} - 0.03478\ \exp\left(y_8\right)\exp\left[\exp\left(y_8\right)\right] + 1.0707\ \exp\left[\cos\left(y_8\right)\right]\exp\left(y_8^2\right) - 2.8195. \tag{23}$$

3.5. Comparison of Different Methods for Single-Value Rating Curves. The discharges estimated by the conventional method, AE, the MHBMO algorithm, ANN, MGGP, and the hybrid MGGP-GRG method are compared with the observed ones using four performance criteria for the single-value rating curves. The results of this comparative analysis are reported in Table 4 and Figure 3 for both train and test data. According to Table 4 and Figure 3, the results obtained by the conventional method are the most inferior for the first four datasets. Since the coefficients determined by EA and the MHBMO algorithm are the same for Dataset 1 and Dataset 2, the performances of these methods are the same for these data. Furthermore, the application of the MHBMO algorithm to Dataset 3 and Dataset 4 slightly improves discharge ratings estimated by EA because it relatively resulted in lower SSE, MARE, and MXARE and higher NE. According to Table 4, ANN improved SSE of the test part of Dataset 1 and SSE of the train parts of Dataset 3 and Dataset 4 comparing to the MHBMO algorithm, whereas the MHBMO algorithm achieved better SSE for the test part of Dataset 3. Based on Figure 3, the MXARE value calculated by ANN is better than that of the MHBMO algorithm for the test part of Dataset 1, whereas the latter has better MXARE and MARE for Dataset 4. The discrepancy between MARE and MXARE obtained by the MHBMO algorithm and ANN is not considerable for Dataset 2 and Dataset 3. Based on the SSE values shown in Table 4, the discharges of the train part of all four datasets estimated by MGGP are much closer to the observed ones in comparison with those of ANN and the MHBMO algorithm, while the hybrid MGGP-GRG improved the SSE values of MGGP for the train part of all single-value rating curves. Furthermore, the MGGP-based model obtained the best SSE for the test part of Dataset 2 compared with ANN and the MHBMO algorithm. Also, the hybrid MGGP-GRG model achieved the best SSE in Table 4 for the test parts of Dataset 2 and Dataset 3, while the best SSE values in this table were computed by ANN and EA for the test parts of Dataset 1 and Dataset 4, respectively. Finally, the lowest MXARE values for the test parts of Dataset 1 and Dataset 3 (shown in Figure 3) were achieved by ANN and the MHBMO algorithm, respectively, while several methods reach the best MXARE values for the test parts of Dataset 2 and Dataset 4.

For better clarification, Dataset 2 was selected to be focused for further investigations. In this regard, Figure 4 depicts the comparison analysis conducted between different models in terms of relative errors for the test part of Dataset 2. As shown, the conventional method yielded the widest range of relative errors for developing single-value rating curves, whereas the maximum and minimum of relative errors are quite the same in other methods. Also, Figure 4 shows that the patterns of relative errors are quite similar for the applied methods. The similarity of these patterns may reveal that the data belong to a single-value rating curve, whose each stage is designated with a unique discharge.

3.6. Loop Rating Curves. The performances of different models for the hysteresis-affected data are presented in Table 5 and Figure 5. As shown in Table 5, the highest SSE values were obtained by the conventional method and EA for the training part and the conventional method, EA, and

Table 4: Comparing SSE of different methods for developing single-value rating curves.

Method	Data part	Dataset 1	Dataset 2	Dataset 3	Dataset 4
Conventional	Training	27905.48	19621.30	85158.32	426.12
	Testing	4978.88	3741.23	31583.23	47.00
EA	Training	15005.11	511.32	21602.35	691.18
	Testing	5752.12	183.24	7365.09	16.39
MHBMO	Training	15005.11	511.32	573.11	69.18
	Testing	5752.13	183.60	220.34	16.40
ANN	Training	15513.37	4321.46	593.16	386.15
	Testing	4706.09	184.38	311.06	16.55
MGGP	Training	7670.02	398.97	530.02	4.16
	Testing	6120.16	113.60	229.25	18.16
Hybrid MGGP-GRG	Training	7136.91	398.18	474.26	2.15
	Testing	6028.23	110.80	214.63	16.71

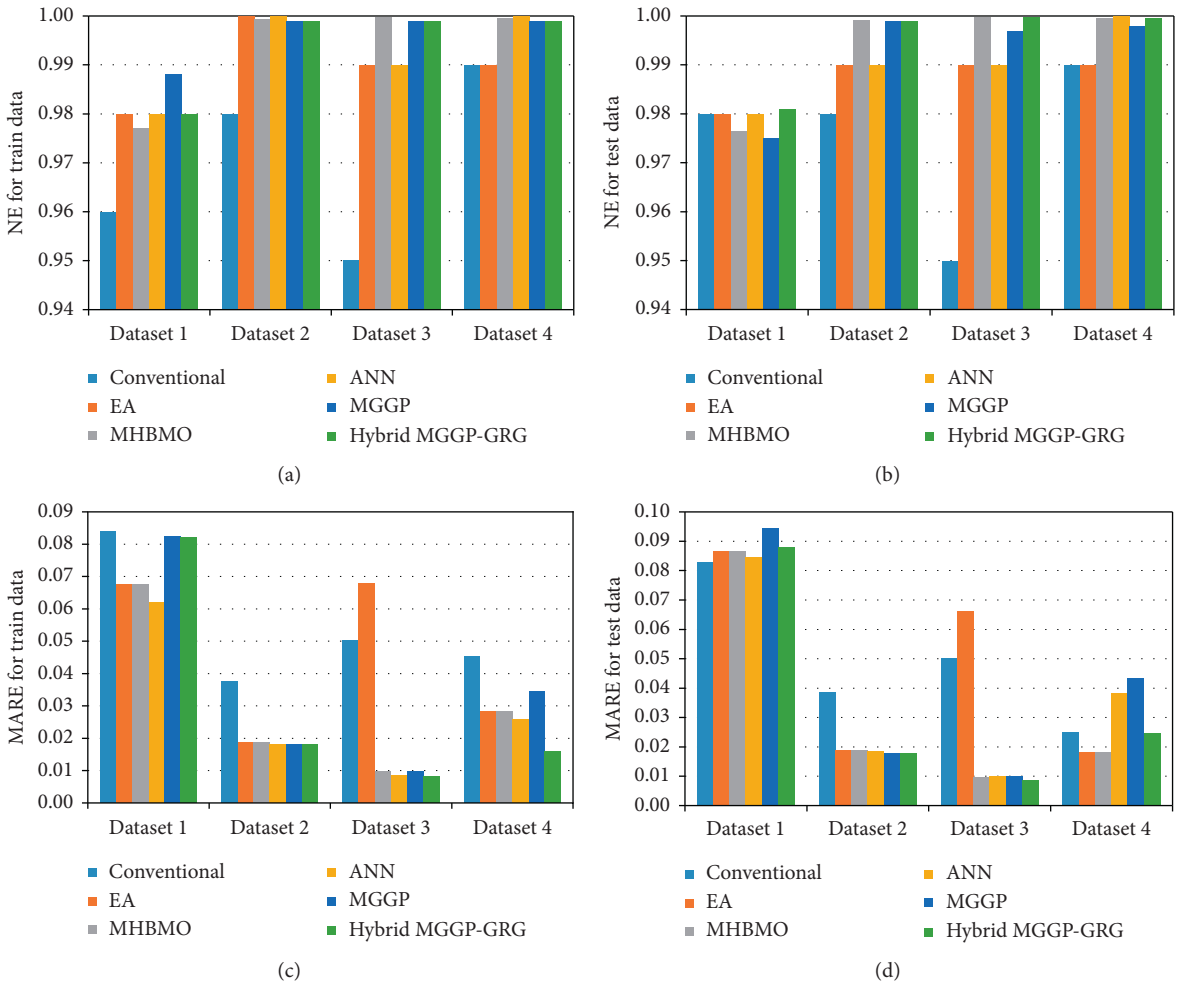

Figure 3: Continued.

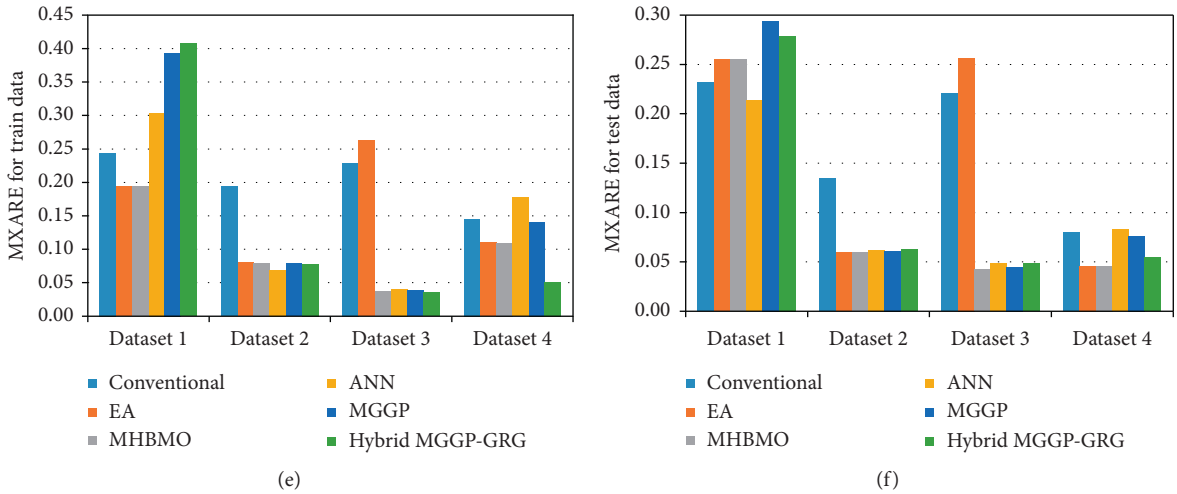

Figure 3: Comparison of the performances of different methods for the data with single-value rating curves based on NE, MARE, and MXARE.

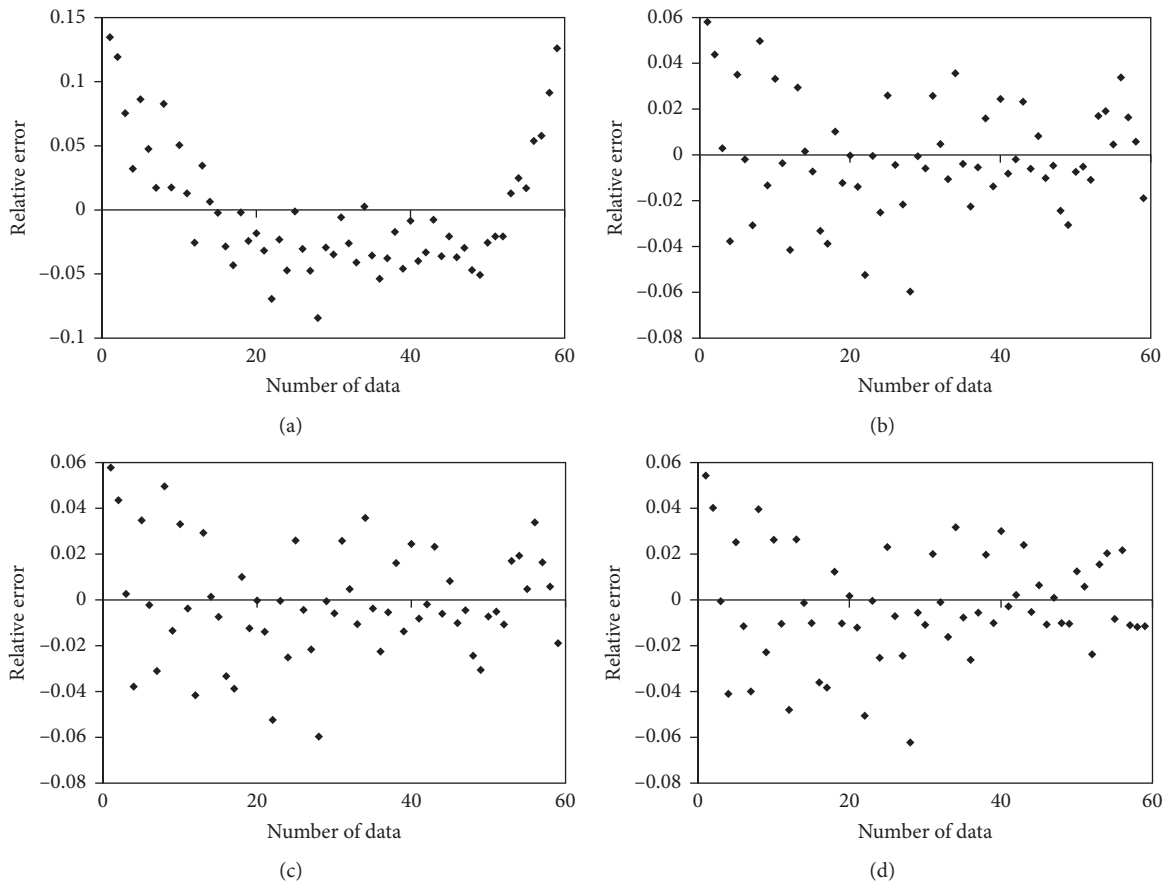

Figure 4: Continued.

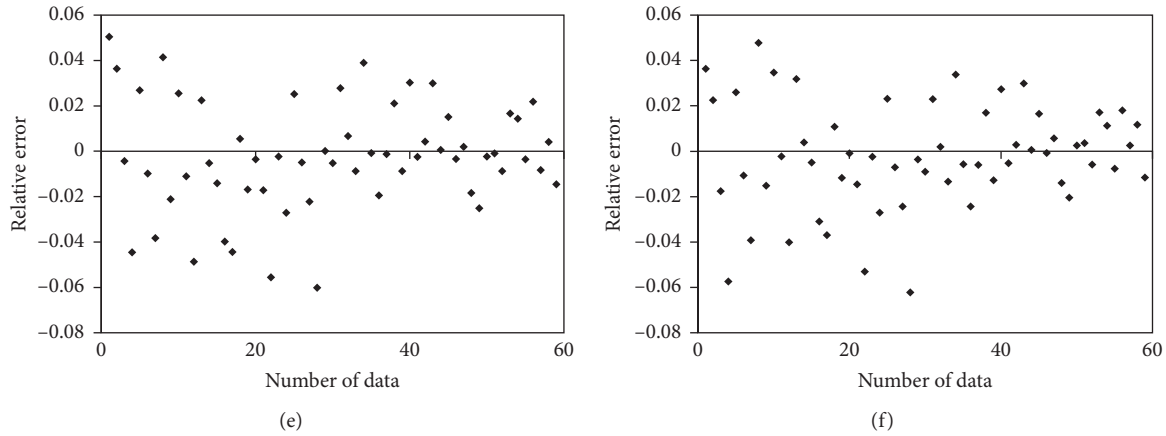

Figure 4: Comparison of relative errors of discharges predicted by different methods for Dataset 2. (a) Conventional method. (b) EA. (c) MHBMO. (d) ANN. (e) MGGP. (f) MGGP-GRG.

Table 5: Comparing SSE of different methods for developing loop rating curves.

Method	Data part	Dataset 5	Dataset 6	Dataset 7	Dataset 8
Conventional	Training	68050636919	6057	476798368	10082970
	Testing	21822676000	1814	24906002	3018398
EA	Training	67935976928	6006	87692181	10047888
	Testing	21780067017	1916	24133003	2992628
RF	Training	26498285944	2462	61379579	1172853
	Testing	12548719606	3574	15944107	8379269
MHBMO	Training	46177882487	6006	89711266	10047482
	Testing	13839023896	1916	24907408	2988805
ANN	Training	35089435935	1681.726874	17520075.67	9352598.961
	Testing	22189984412	2651.39974	6499608.451	3376646.962
MGGP	Training	19204199283	2107	30070788	8838013
	Testing	11708806606	2500	6572739	2889826
Hybrid MGGP-GRG	Training	18655186649	2082	17645820	8822776
	Testing	11337677713	2496	6492404	2881054

ANN for the test part of Dataset 5. On the other hand, the hybrid MGGP-GRG model achieved the lowest SSE values for both parts of Dataset 5. According to Table 5, the worst SSE for the train part and the best SSE for the test part of Dataset 6 belong to the conventional method, whereas ANN and RF reach the best and the worst SSE values for the train and test parts of Dataset 6, respectively. For the train part of Dataset 7, the conventional method resulted in an SSE value, which is 4.5 times higher than SSE values obtained by other methods. Furthermore, ANN and the hybrid MGGP-GRG method achieved the best SSE value for Dataset 7. Table 5 shows that the conventional method, EA, and the MHBMO algorithm yielded the highest SSE for the test part of Dataset 7, whereas the AI models (ANN and MGGP) and the hybrid MGGP-GRG model significantly improved the SSE of other methods for the corresponding data. Additionally, the best SSE values for the train and test parts of Dataset 8 were achieved by RF and the hybrid MGGP-GRG model, respectively. Moreover, the conventional method achieved the lowest NE for most train and test parts of loop rating curves, whereas the AI models and the hybrid MGGP-GRG method overall performed acceptably and even the best in some cases as shown in Figure 5. Comparing the MARE and MXARE values reported in Figure 5, it is obviously seen that the AI models and the hybrid MGGP-GRG model yielded the lowest values for the train parts of Dataset 5, Dataset 6, and Dataset 7. These methods also resulted in better MARE for the test parts of Dataset 5, Dataset 7, and Dataset 8 and better MXARE for the test parts of Dataset 6 and Dataset 7 than other methods compared in Figure 5. Additionally, the hybrid MGGP-GRG model significantly reduced MXARE for the test part of Dataset 5.

Figure 6 compares relative errors computed by seven methods for the test part of Dataset 7, whose rating curve is affected by the hysteresis phenomenon. Unlike Figure 4, Figure 6 show that the AI models and the hybrid MGGP-GRG method resulted in relatively smaller ranges of relative errors compared to other methods. Moreover, the patterns

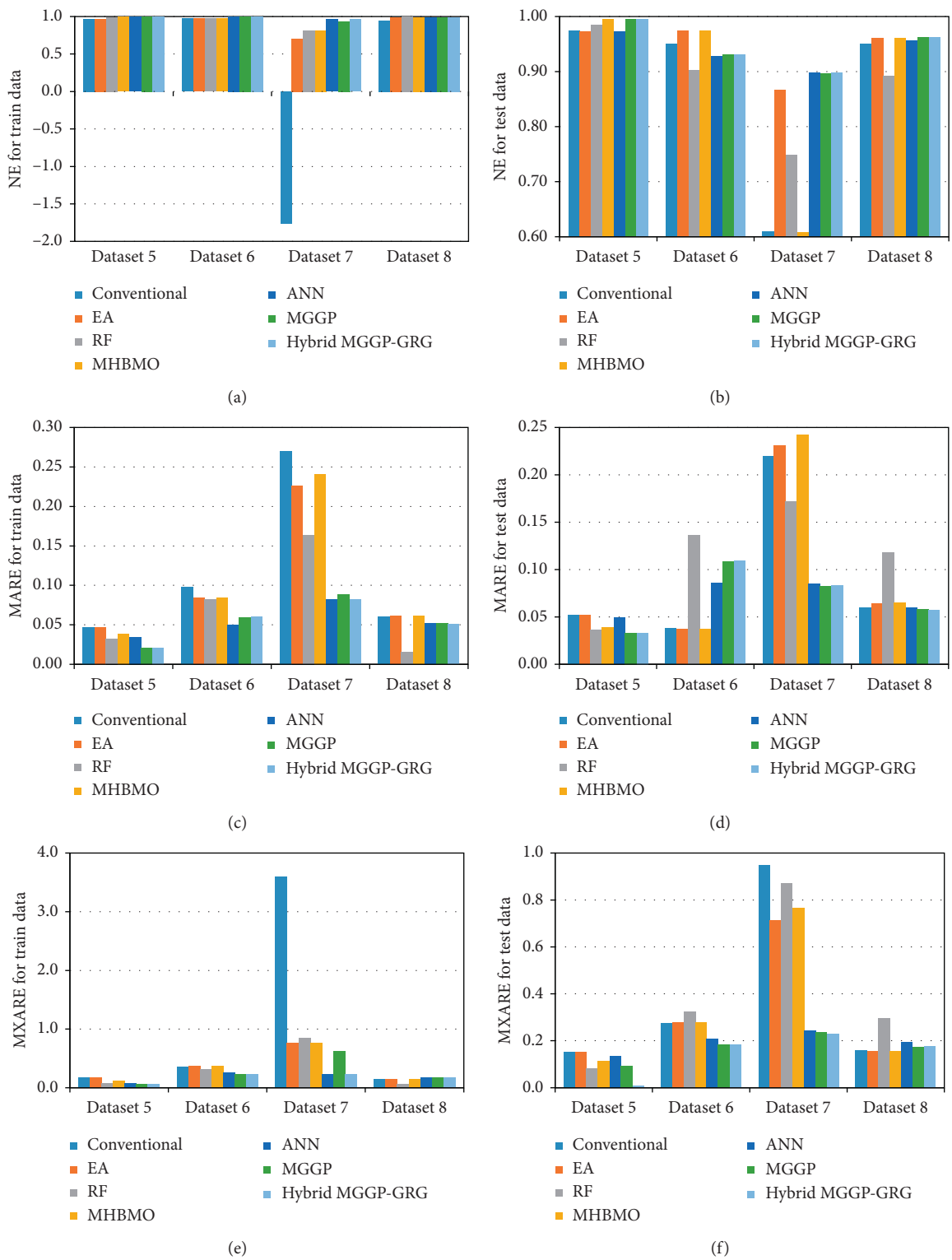

Figure 5: Comparison of the performances of different methods for the data with loop rating curves based on NE, MARE, and MXARE.

of relative errors presented by the former methods are completely different from those achieved by the latter ones. This clearly indicates that equation (1) yielded the same pattern of relative errors for loop rating curves, while the methods used for calibrating equation (1) may have an impact on the maximum and minimum relative errors and not on the corresponding patterns. On the other hand, the AI models and the hybrid MGGP-GRG technique achieved

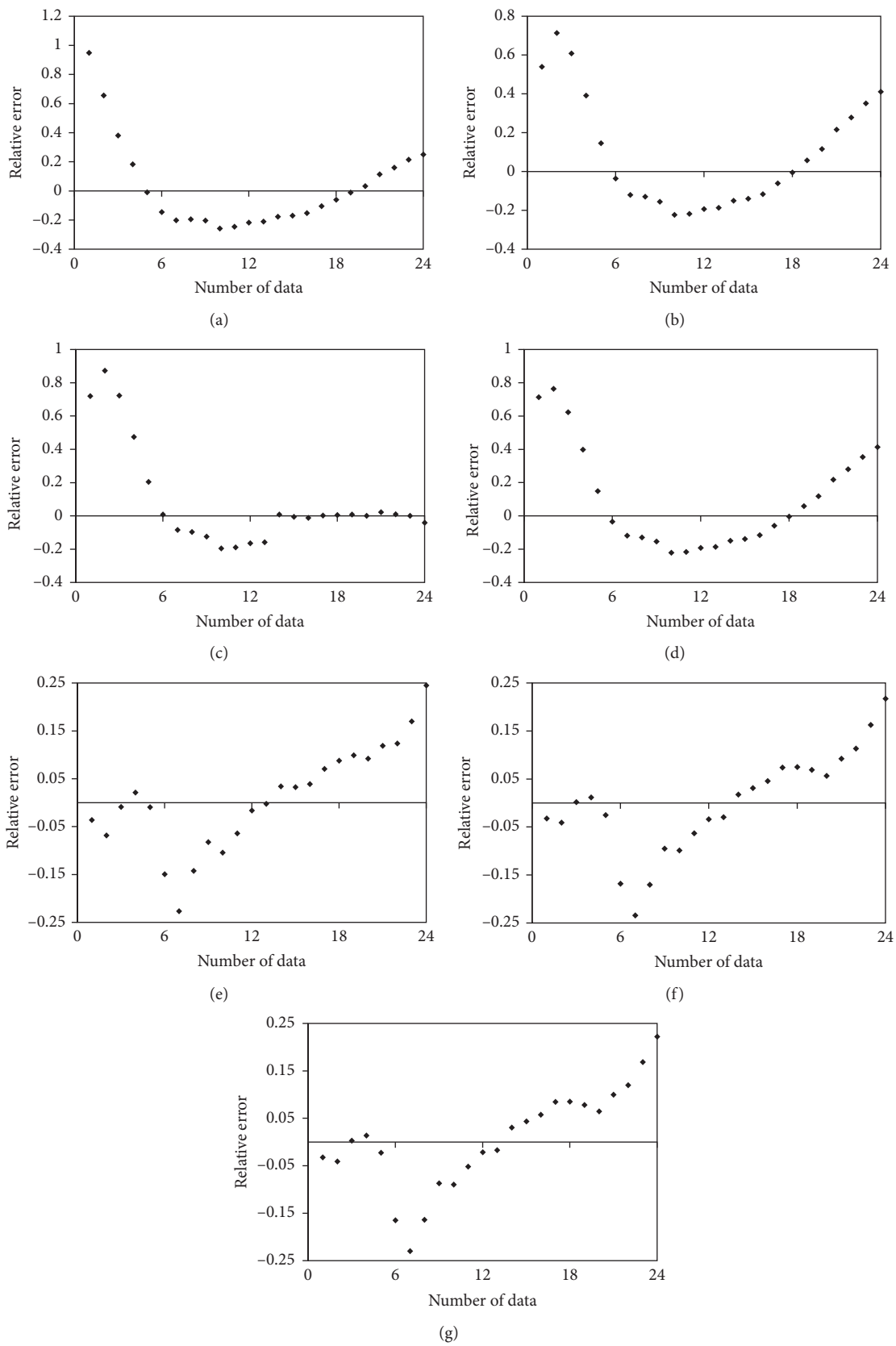

Figure 6: Comparison of relative errors of discharges predicted by different methods for Dataset 7. (a) Conventional method. (b) EA. (c) RF. (d) MHBMO. (e) ANN. (f) MGGP. (g) MGGP-GRG.

quite the same patterns of relative errors, while the maximum and minimum relative errors are different. Therefore, Figure 6 demonstrates that equation (1), regardless of which method is adopted for the calibration, has limited potential to capture the relation between stages and discharges in loop rating curves, whereas the AI models and the hybrid MGGP-GRG model were found to have more capabilities when it comes to develop hysteresis-affected rating curves.

Figure 7 compares the confidence limits of different models for the test data of the eight datasets. First of all, the datasets used in this study have a wide range of discharge values as shown in both Figure 7 and Table 1. Based on Figure 7, the most considerable discrepancy is between the confidence limits of Dataset 6, Dataset 7, and Dataset 8. By comparing the confidence limits presented in Figure 7, it can be observed that the confidence limits obtained by the AI models and the hybrid MGGP-GRG model are closer to the observed values compared to other methods. Based on the comparison carried out in Tables 4 and 5 and Figures 3–5, it can be concluded that MGGP and the hybrid MGGP-GRG method not only provided explicit equations between the stage and discharge for each dataset but also significantly improved discharge estimations by developing precise stage-discharge relations, particularly for the loop rating curves.

4. Discussion

Characterization of the stage-discharge relationship at different river sections has remained an important aspect of hydraulic as well hydrologic studies. Initially, Tawfik et al. [18] employed ANN to simulate hysteresis-affected discharge rating curves. Since Tawfik et al.'s [18] contribution, ANN has remained a preferred choice to address the stage-discharge curves. Ghimire and Reddy [38] suggested that GA is more efficient than model tree and the conventional method for developing rating curves. Azamathulla et al. [23] proposed the application of gene expression programming (GEP) and the classical GP, which are both modified versions of GA, for developing discharge rating curves. They concluded that the efficiency of GEP is higher than that of GP for this purpose. Recently, Zakwan et al. [4] asserted that EA is as efficient as GA for determining stage-discharge relationships. Progressing in a similar direction, the present study has explored the capability of MGGP and the hybrid MGGP-GRG model as compared to the conventional method, EA, RF, the MHBMO algorithm, and ANN to develop stage-discharge curves. Unlike most of the earlier studies, this study examined the proposed models for their efficiency in case of steady as well as unsteady flow conditions by considering four datasets for steady and four datasets for unsteady flow conditions.

The application of MGGP to problems in water resource field is limited to very recent investigations. MGGP and hybrid models incorporating MGGP have been already used for several applications like estimating sediment transport [39], forecasting monthly streamflow [40], developing a rainfall-runoff model to predict streamflow [41], river flow forecasting [42], and predicting longitudinal dispersion coefficients [43]. In almost all of these applications, MGGP has been found to be an accurate estimation tool, particularly when the problem under investigation is complicated. According to the conducted literature review, it is the first time that MGGP has been utilized for developing rating curves, while the hybrid MGGP-GRG method has been introduced for the first time in this study.

When machine learning techniques are used as estimation models, one of the challenges is to take care of the overfitting. In this study, a considerable number of runs of the AI models were conducted. Afterwards, the achieved results were checked and the ones that performed well for the test data alone (and not well for the train data) were excluded because they did not generalize well from the train data to the test data. According to Tables 4 and 5, the results of the AI models are acceptable for both train and test parts of the data for each dataset considered.

As previously mentioned, various functions were considered in applying MGGP to develop stage-discharge relations for each dataset considered in this study. The opportunity to implement a desirable series of functions is indeed one of the main characteristics of MGGP, which makes it a powerful estimation tool. Because of the availability of various built-in functions in MGGP, several combinations of functions were considered to determine the best-fitted rating curves. As a result, MGGP may result in different equations comprising of different types of functions, which yield different numbers of accurate equations for different databases as shown in equations (8)–(15). This feature can be beneficial particularly when the user is not sure about which types of equation are suitable for a specific set of data. The entire process of the application of MGGP and the hybrid MGGP-GRG technique can be found in Figure 2.

Tables 4 and 5 and Figures 3 and 5 present quantitative and qualitative comparative analysis of the performances of different techniques used in the present study. Although much variation is not seen in NE values presented in Figures 3 and 5, there have been significant discrepancies between SSE values obtained by different methods in Tables 4 and 5. To be more specific, the hybrid MGGP-GRG model improved SSE values obtained by the conventional method from 4.5% (for the test part of Dataset 8) to 99% (for the test part of Dataset 3), while the conventional method achieved the second best and the best SSE values for the test parts of Dataset 1 and Dataset 5, respectively. Also, Tables 4 and 5 indicate that the reduction of SSE as a result of combining MGGP with GRG varies between 0.16% (for the test part of Dataset 6) and 7.9% (for the test part of Dataset 4). This improvement reveals that the hybrid MGGP-GRG method performed better than MGGP in terms of SSE for all datasets considered in this study.

By comparing the results shown in Tables 4 and 5 and Figures 3 and 5, it is not evident that which technique outperformed others in all cases. In order to determine which model performs the best, a ranking system was

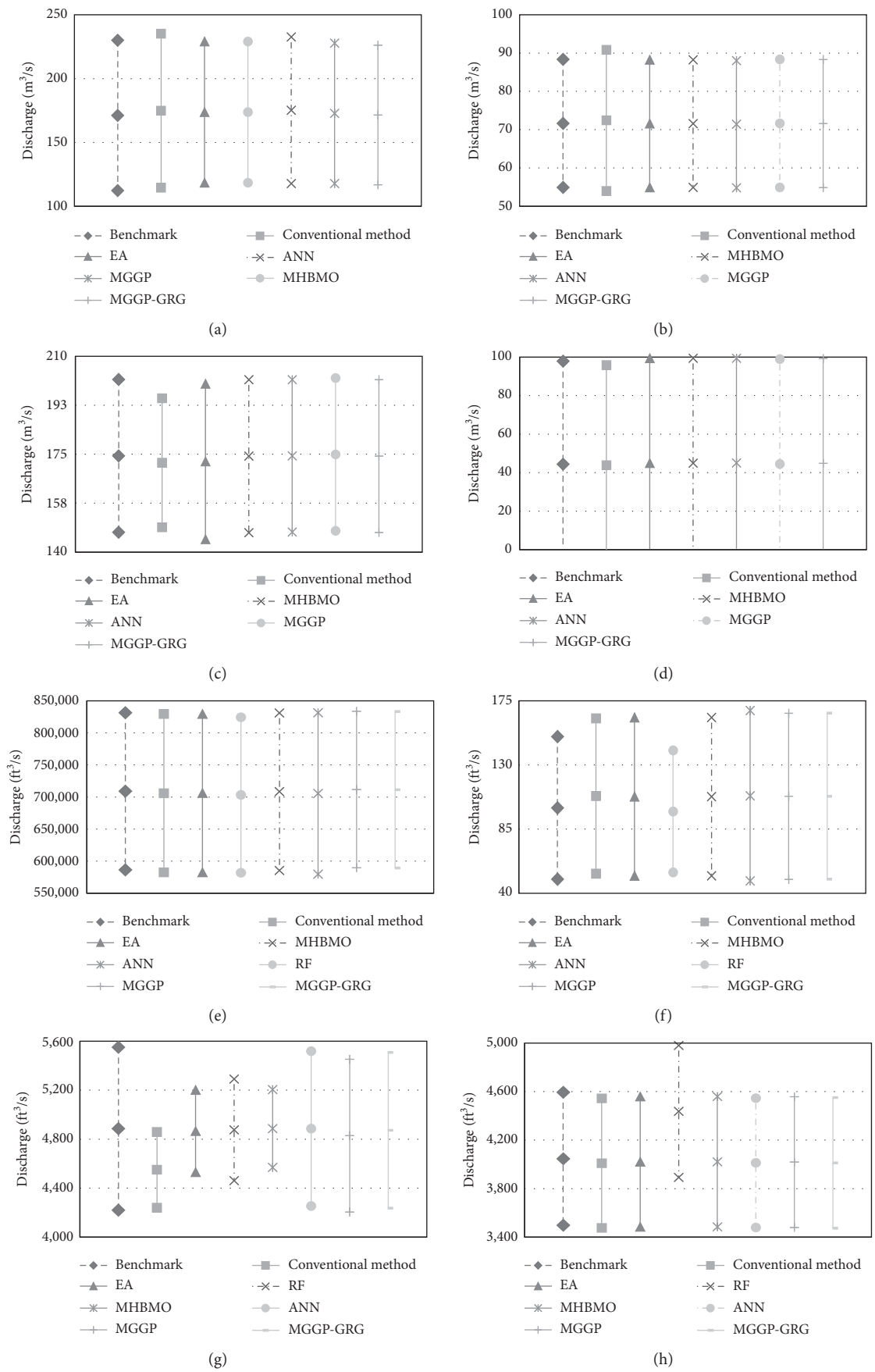

Figure 7: Confidence limits of the observed and estimated discharges for the test parts of all eight datasets. (a) Dataset 1. (b) Dataset 2. (c) Dataset 3. (d) Dataset 4. (e) Dataset 5. (f) Dataset 6. (g) Dataset 7. (h) Dataset 8.

adopted from the literature [32] to evaluate different methods based on the criteria and datasets considered. In essence, this ranking system assumes an equal weight for each criterion. For the test part of each dataset, an integer value from one (the best performance) to seven (the worst performance) was designated to each model based on its performance in terms of each criterion (SSE, NE, MARE, and MXARE). As a result, each model has four ranking values for each dataset. The algebraic summation of these four ranking values is basically used to assign a ranking number to each model for each dataset. The detailed process of this ranking system is presented in Supplementary Materials for each and every dataset considered in this study. The ranking numbers achieved for each model applied to the data with single-value rating curves are given in Table 6. The summation of the ranking numbers of each model is also computed in Table 6, which is called summation of ranks. It was utilized to determine the total rank, which delineates the overall performance of each method for all data and criteria considered. According to Table 6, the hybrid MGGP-GRG model obtained the best summation of ranks and the best ranking numbers for data whose rating curves indicate a one-to-one relation between stage and discharge values. This implies that it has the best performance among different methods for single-value rating curves. Moreover, the MHBMO algorithm takes the second place in Table 6. Furthermore, the summation of ranks calculated for EA and ANN is the same, which shows that their performances for developing the stage-discharge relations for single-value rating curves were overall close to one another, while they took the third total ranks. On the other hand, the conventional method yielded a relatively high summation of ranks, and consequently, it was identified as the fourth (worst) method for developing single-value rating curves. Comparing the total ranks of MGGP and the hybrid MGGP-GRG method indicates that the idea of combining MGGP with GRG significantly improved the performances of MGGP in estimating discharges under steady conditions.

The results of the ranking analysis conducted for the hysteresis-affected data are presented in Table 7. As shown, it indicates that the first two best performances for data with loop rating curves are the hybrid MGGP-GRG model and MGGP. Although ANN was identified as the third best method in Table 6, it performs as the worst model in Table 7. By considering the results of Tables 6 and 7, it can be concluded that no method can be found that performs the best for all eight datasets based on the metrics considered. In other words, ANN or MGGP or even the hybrid MGGP-GRG technique is not the best model for all datasets and metrics considered, while the best method may be different from one case to another one. Nevertheless, Tables 6 and 7, which show the ranking results for the datasets and metrics considered, demonstrate that the hybrid MGGP-GRG method overall performs the best in developing rating curves considered in this study.

GP and its variants (like MGGP) can be used as a sensitivity analysis tool because they have the ability to formulate and structure the equation used for forecasting [40]. For the case of this study, the discharge (output) is exclusively a function of stage (input). Hence, the sensitivity analysis does not give any perspective on which independent variable has the highest impact and which one has the lowest impact on the dependent variable based on the proposed MGGP-based models.

When MGGP is applied to develop stream rating curves, functions, parameters, and the structure of the stage-discharge relation do not need to be known in advance, whereas the conventional method, EA, RF, and the MHBMO algorithm require assuming a specific formula for the stage-discharge relationship. In other words, MGGP requires to know neither the equation form nor functions comprising the relation between the input and output data, while it exploits a set of built-in functions to construct an adequate relation. This is one of the advantages of MGGP, which enables developing a stage-discharge relationship without shape limitation. It also allows the user to decide about the inclusion of each built-in function in the estimation process, while it does not provide the chance to add new functions to the list. This may be counted as one of the major drawbacks of the version of MGGP used in this study. Since MGGP benefits from a search-based optimization algorithm, it may yield a different result in each run. Therefore, it requires running a considerable number of times to make sure that the best results have been obtained. This may be accounted as one of the shortcomings of MGGP. In this regard, several studies suggested coupling MGGP with another program or optimization algorithm not only to improve its efficiency but also to tailor it to their specific problem [40]. In this regard, the hybrid MGGP-GRG model has been proposed for the first time in this study, while it improved the performance of MGGP in this particular application.

MGGP provides the opportunity to choose between the precision and complexity of the stage-discharge relation. This trade-off can be addressed by tuning the several controlling parameters playing the key roles in MGGP. The two controlling parameters, which have a major impact on the accuracy and simplicity of the final results, are the maximum genes allowed in each individual and the depth of trees [35]. These parameters should be set based on either previous studies or a sensitivity analysis because the poor evaluation of these parameters may have a significant influence on the final results.

MGGP is basically a flexible estimation tool that seeks the best relation between any given input and output data regardless of the physical meaning or theoretical background of the data. This feature enables us to apply MGGP to various applications. Combining MGGP with other optimization algorithms can improve the performance of this artificial intelligence technique. Thus, application of different hybrid MGGP-based models can be explored in various sectors of engineering and allied sciences.

Table 6: Ranking the performances of different methods for developing single-value rating curves.

Method	Ranking results for each data set				Summation of ranks	Total rank
	Dataset 1	Dataset 2	Dataset 3	Dataset 4		
Conventional	2	6	6	6	20	6
EA	3	4	5	2	14	3
MHBMO	5	3	2	1	11	2
ANN	1	5	4	4	14	3
MGGP	6	1	3	5	15	5
Hybrid MGGP-GRG	4	2	1	3	10	1

Table 7: Ranking the performances of different methods for developing loop rating curves.

Method	Ranking results for each data set				Summation of ranks	Total rank
	Dataset 5	Dataset 6	Dataset 7	Dataset 8		
Conventional	5	3	6	5	19	5
EA	5	1	4	3	13	3
RF	3	7	4	7	21	6
MHBMO	4	1	7	3	15	4
ANN	7	6	3	6	22	7
MGGP	2	4	2	2	10	2
Hybrid MGGP-GRG	1	5	1	1	8	1

5. Conclusions

Rating curves have wide applications in water resource engineering. Numerous studies have been carried out to improve the accuracy of stream rating curves using optimization algorithms as well as AI models. In the present study, an attempt was made to develop ratings considering four datasets under steady (single rating curve) and four datasets under unsteady (loop rating curve) conditions based on the conventional method, EA, the MHBMO algorithm, ANN, MGGP, and the hybrid MGGP-GRG method. Rating curves for the four sites affected by hysteresis (loop rating curves) were also developed by the RF method. The performances of these techniques were compared based on the commonly used performance indicators and error indices. Comparing the performances of different methods applied to the eight datasets indicated that none of the methods outperformed in each and every case. For instance, the conventional method achieved the second best SSE for the first dataset and the best SSE for the sixth dataset, whereas the hybrid MGGP-GRG model improved SSE obtained by the conventional method between 4.5% and 99% for the rest of the datasets. To assess the overall performances of these techniques, a ranking system with equal weight designated to each metric was adopted from the literature. It was observed that the discharges estimated by the hybrid MGGP-GRG model were in good agreement with the observed data for both single and loop rating curves as it achieved the first ranking place for both scenarios. Based on the comparative analysis, the conventional method provided the worst estimates of discharge, whereas the MGGP-based models yielded the most precise discharge values based on SSE, MARE, and MXARE in most of the cases. However, this significant improvement was obtained by the compensation of relatively more complex equations, which can be directly used to predict discharges. The MHBMO algorithm and ANN also performed satisfactorily in most of the cases. Additionally, ANN performed satisfactorily during training, but failed to produce reliable discharge estimations during testing of several cases, which is probably due to overfitting during the training phase. Comparing the confidence limits of different methods with the observed data showed that the discrepancies between estimated and observed discharges are much evident for the hysteresis-affected rating curves than those of single ones. Moreover, MGGP provides several explicit equations between the stage and discharge that can be selected depending on the requirements of accuracy and simplicity. Also, one of the advantages of MGGP is that there is no need to assume both functions and parameters of the stage-discharge relation, while tuning of its parameters requires a bit of trial-and-error process, like any other AI models. However, application of MGGP not only requires a number of trials before the best results could be obtained but also may involve relatively more complex equations than that used by the conventional method in this study. Application of MGGP and hybrid MGGP-based techniques can be explored in the field of water resource engineering, especially in the field of sediment transport, as it involves highly nonlinear and complex equations. Finally, the results of this study demonstrated that a combination of MGGP with another optimization algorithm like GRG can improve the performance of this AI model in water resource applications.

Data Availability

Data may be obtained upon request to authors as authors are not entitled to provide the data openly.

Conflicts of Interest

The authors declare that they have no conflicts of interest.

Supplementary Materials

This appendix presents the detailed calculation process of the ranking system applied to different methods for developing stage-discharge rating curves. (*Supplementary Materials*)

References

[1] K. Roushangar and F. Alizadeh, "Scenario-based prediction of short-term river stage–discharge process using wavelet-EEMD-based relevance vector machine," *Journal of Hydroinformatics*, vol. 21, no. 1, pp. 56–76, 2019.

[2] V. Travaš, N. Krvavica, and I. Radman, "Numerical analysis of hysteresis in rating curves for open channel flow," *International Journal for Engineering Modelling*, vol. 25, no. 1–4, pp. 1–6, 2012.

[3] G. Braca, *Stage-discharge Relationships in Open Channels: Practices and Problems*, Univ. degli Studi di Trento, Dipartimento di Ingegneria Civile e Ambientale, London, UK, 2008.

[4] M. Zakwan, M. Muzzammil, and J. Alam, "Application of data driven techniques in discharge rating curve - an overview," *Aquademia: Water, Environment and Technology*, vol. 1, no. 1, 2 pages, 2017.

[5] J. D. Fenton, "On the generation of stream rating curves," *Journal of Hydrology*, vol. 564, pp. 748–757, 2018.

[6] A. Paris, R. Dias de Paiva, J. Santos da Silva et al., ""Stage-discharge rating curves based on satellite altimetry and modeled discharge in the Amazon basin," *Water Resources Research*, vol. 52, no. 5, pp. 3787–3814, 2016.

[7] S. Alvisi and M. Franchini, "A grey-based method for evaluating the effects of rating curve uncertainty on frequency analysis of annual maxima," *Journal of Hydroinformatics*, vol. 15, no. 1, pp. 194–210, 2013.

[8] M. Lang, K. Pobanz, B. Renard, E. Renouf, and E. Sauquet, "Extrapolation of rating curves by hydraulic modelling, with application to flood frequency analysis," *Hydrological Sciences Journal*, vol. 55, no. 6, pp. 883–898, 2010.

[9] G. Di Baldassarre and P. Claps, "A hydraulic study on the applicability of flood rating curves," *Hydrology Research*, vol. 42, no. 1, pp. 10–19, 2011.

[10] S. Barbetta, T. Moramarco, and M. Perumal, "A Muskingum-based methodology for river discharge estimation and rating curve development under significant lateral inflow conditions," *Journal of Hydrology*, vol. 554, pp. 216–232, 2017.

[11] M. Niazkar, N. Talebbeydokhti, and S. H. Afzali, "One dimensional hydraulic flow routing incorporating a variable grain roughness coefficient," *Water Resources Management*, vol. 33, no. 13, pp. 4599–4620, 2019.

[12] A. R. Schmidt and B. C. Yen, "Theoretical development of stage-discharge ratings for subcritical open-channel flows," *Journal of Hydraulic Engineering*, vol. 134, no. 9, pp. 1245–1256, 2008.

[13] G. A. Lindner and A. J. Miller, "Numerical modeling of stage-discharge relationships in urban streams," *Journal of Hydrologic Engineering*, vol. 17, no. 4, pp. 590–596, 2012.

[14] A. Kavousizadeh, M. F. Maghrebi, and A. Ahmadi, "Stage-discharge estimation in compound open channels with composite roughness," *Hydrology Research*, vol. 50, no. 3, pp. 809–824, 2019.

[15] A. Petersen-øverleir, "Modelling stage-discharge relationships affected by hysteresis using the Jones formula and nonlinear regression," *Hydrological Sciences Journal*, vol. 51, no. 3, pp. 365–388, 2006.

[16] M. Zakwan, M. Muzzammil, and J. Alam, "Modelling of stage-discharge relationship," *NDCWWC Journal (A Half Yearly Journal of New Delhi Centre of WWC)*, vol. 7, no. 1, pp. 10–12, 2018.

[17] M. Zakwan, "Spreadsheet-based modelling of hysteresis-affected curves," *Applied Water Science*, vol. 8, no. 4, pp. 101–105, 2018.

[18] M. Tawfik, A. Ibrahim, and H. Fahmy, "Hysteresis sensitive neural network for modeling rating curves," *Journal of Computing in Civil Engineering*, vol. 11, no. 3, pp. 206–211, 1997.

[19] K. P. Sudheer and S. K. Jain, "Radial basis function neural network for modeling rating curves," *Journal of Hydrologic Engineering*, vol. 8, no. 3, pp. 161–164, 2003.

[20] P. Deka and V. Chandramouli, "A fuzzy neural network model for deriving the river stage-discharge relationship," *Hydrological Sciences Journal*, vol. 48, no. 2, pp. 197–209, 2003.

[21] C. Sivapragasam and N. Muttil, "Discharge rating curve extension-a new Approach," *Water Resources Management*, vol. 19, no. 5, pp. 505–520, 2005.

[22] A. Goel and M. Pal, "Stage-discharge modelling using support vector machine," *International Journal of Engineering*, vol. 25, no. 1, pp. 1–9, 2011.

[23] H. M. Azamathulla, A. A. Ghani, C. S. Leow, C. K. Chang, and N. A. Zakaria, "Gene-expression programming for the development of a stage-discharge curve of the Pahang River," *Water Resources Management*, vol. 25, no. 11, pp. 2901–2916, 2011.

[24] M. Zakwan, M. Muzzammil, and J. Alam, "Application of data driven techniques in discharge rating curve-an overview," *Aquademia: Water, Environment and Technology*, vol. 1, 2020.

[25] M. Muzzammil, J. Alam, and M. Zakwan, "An optimization technique for estimation of rating curve parameters," *National Symposium on Hydrology*, vol. 2015, 2015.

[26] R. W. Herschy, *Streamflow Measurement*, E & FN Spon, London, UK, 3rd edition, 2008.

[27] D. L. Fread, "A dynamic model of stage-discharge relations affected by changing discharge," 1973.

[28] C. A. Ramírez, Y. Carvajal, R. A. Bocanegra, and M. C. Sandoval, "Determination of simple and complex water level-discharge relationship in a river," *Case of the Cauca River. Ingeniería Y Competitividad*, vol. 20, no. 2, pp. 45–56, 2018.

[29] M. D. De los Ríos and E. H. Ramos, "Determination of the Hansen solubility parameters and the Hansen sphere radius with the aid of the solver add-in of Microsoft Excel," *SN Applied Sciences*, vol. 2, no. 4, pp. 1–7, 2020.

[30] M. Niazkar and S. H. Afzali, "Parameter estimation of an improved nonlinear Muskingum model using a new hybrid method," *Hydrology Research*, vol. 48, no. 5, pp. 1253–1267, 2017.

[31] M. Niazkar, N. Talebbeydokhti, and S. H. Afzali, "Novel grain and form roughness estimator scheme incorporating artificial intelligence models," *Water Resources Management*, vol. 33, no. 2, pp. 757–773, 2019.

[32] H. R. Niazkar and M. Niazkar, "Application of artificial neural networks to predict the COVID-19 outbreak," *Global Health Research and Policy*, vol. 5, no. 1, 2020.

[33] M. Niazkar, "Assessment of artificial intelligence models for calculating optimum properties of lined channels," *Journal of Hydroinformatics*, vol. 22, no. 5, pp. 1410–1423, 2020.

[34] D. P. Searson, D. E. Leahy, and M. J. Willis, "GPTIPS: an open source genetic programming toolbox for multigene symbolic regression," 2010.
[35] H. R. Niazkar and M. Niazkar, "COVID-19 outbreak: application of multi-gene genetic programming to country-based prediction models," *Electronic Journal of General Medicine*, vol. 17, no. 5, 2020.
[36] M. Niazkar, "Revisiting the estimation of colebrook friction factor: a comparison between artificial intelligence models and C-W based explicit equations," *KSCE Journal of Civil Engineering*, vol. 23, no. 10, pp. 4311–4326, 2019.
[37] D. Searson, "GPTIPS: Genetic Programming and Symbolic Regression for MATLAB," 2009.
[38] B. N. Ghimire and M. J. Reddy, "Development of stage-discharge rating curve in river using genetic algorithms and model tree," 2010.
[39] B. Kumar, A. Jha, V. Deshpande, and G. Sreenivasulu, "Regression model for sediment transport problems using multi-gene symbolic genetic programming," *Computers and Electronics in Agriculture*, vol. 103, pp. 82–90, 2014.
[40] S. J. Hadi and M. Tombul, "Monthly streamflow forecasting using continuous wavelet and multi-gene genetic programming combination," *Journal of Hydrology*, vol. 561, pp. 674–687, 2018.
[41] A. D. Mehr and V. Nourani, "Season algorithm-multigene genetic programming: a new approach for rainfall-runoff modelling," *Water Resources Management*, vol. 32, no. 8, pp. 2665–2679, 2018.
[42] M. A. Ghorbani, R. Khatibi., A. Danandeh Mehr, and H. Asadi, "Chaos-based multigene genetic programming: a new hybrid strategy for river flow forecasting," *Journal of Hydrology*, vol. 562, pp. 455–467, 2018.
[43] H. Riahi-Madvar, M. Dehghani, A. Seifi, and V. P. Singh, "Pareto optimal multigene genetic programming for prediction of longitudinal dispersion coefficient," *Water Resources Management*, vol. 33, no. 3, p. 905, 2019.

Hindawi
Complexity
Volume 2021, Article ID 6610228, 16 pages
https://doi.org/10.1155/2021/6610228

Research Article

Forecasting Different Types of Droughts Simultaneously Using Multivariate Standardized Precipitation Index (MSPI), MLP Neural Network, and Imperialistic Competitive Algorithm (ICA)

Pouya Aghelpour and Vahid Varshavian

Agricultural Meteorology, Department of Water Engineering, Faculty of Agriculture, Bu-Ali Sina University, Hamedan, Iran

Correspondence should be addressed to Vahid Varshavian; v.varshavian@basu.ac.ir

Received 11 October 2020; Revised 8 November 2020; Accepted 29 December 2020; Published 19 January 2021

Academic Editor: Shamsuddin Shahid

Precipitation deficit causes meteorological drought, and its continuation appears as other different types of droughts including hydrological, agricultural, economic, and social droughts. Multivariate Standardized Precipitation Index (MSPI) can show the drought status from the perspective of different drought types simultaneously. Forecasting multivariate droughts can provide good information about the future status of a region and will be applicable for the planners of different water divisions. In this study, the MLP model and its hybrid form with the Imperialistic Competitive Algorithm (MLP-ICA) have been investigated for the first time in multivariate drought studies. For this purpose, two semi-arid stations of western Iran were selected, and their precipitation data were provided from the Iranian Meteorological Organization (IRIMO), during the period of 1988–2017. MSPI was calculated in 5-time windows of the multivariate drought, including $MSPI_{3-6}$ (drought in perspectives of soil moisture and surface hydrology simultaneously), $MSPI_{6-12}$ (hydrological and agricultural droughts simultaneously), $MSPI_{3-12}$ (soil moisture, surface hydrology, and agricultural droughts simultaneously), $MSPI_{12-24}$ (drought in perspectives of agriculture and groundwater simultaneously), and $MSPI_{24-48}$ (socio-economical droughts). The results showed acceptable performances in forecasting multivariate droughts. In both stations, the larger time windows ($MSPI_{12-24}$ and $MSPI_{24-48}$) had better predictions than the smaller ones ($MSPI_{3-6}$, $MSPI_{6-12}$, and $MSPI_{3-12}$). Generally, it can be reported that, by decreasing the size of the time window, the gradual changes of the index give way to sudden jumps. This causes weaker autocorrelation and consequently weaker predictions, e.g., forecasting droughts from the perspective of soil moisture and surface hydrology simultaneously ($MSPI_{3-6}$). The hybrid MLP-ICA shows stronger prediction results than the simple MLP model in all comparisons. The ICA optimizer could averagely improve MLP's accuracy by 28.5%, which is a significant improvement. According to the evaluations (RMSE = 0.20; MAE = 0.15; $R = 0.95$), the results are hopeful for simultaneous forecasting of different drought types and can be tested for other similar areas.

1. Introduction

Drought, one of the most complex environmental catastrophes, continuously has an effect on the rest of the world [1]. It occurs naturally in all climatic areas, such as pluvial and arid areas, and causes many economic, environmental, and social costs around the world [1–4]. In recent decades, drought has been one of the costliest natural disasters that has created major challenges in Iranian water resource management. The arid and semiarid climate of Iran has made it highly vulnerable to droughts [5]. During 1998–2000, Iran experienced one of the worst and most damaging drought periods in the last 50 years [6]. During this 3-year period, water shortage in more than 270 cities fell down to below the critical point, and as a result, thousands of villages lost their drinking water, surface water flow decreased to 55%, and Iran's dams and tanks were forced to act with minimal capacity for water transfer because of low input flow and high temperature [6, 7]. So, during this period, the country faced different types of droughts, such as

meteorological, hydrological, agricultural, social, and economic droughts simultaneously.

Drought prediction is a major concern for water managers, farmers, and other final users because it limits their decisions. Since droughts have slowly begun, it is possible to present temporal forecasts in order to take measures and develop policies to reduce the effects of droughts [8–10]. A wide range of artificial intelligence (AI) models and modified standalone and hybrid versions have been used for the forecasting of different drought indices. The studies revealed the higher performance of AI models in forecasting drought indices [11–17]. In fact, the AI models can predict the drought events that do not have a good and straightforward mathematical solution and were proven to have the ability to capture the white noise, nonstationary, and nonlinearity in the time series [18]. Multilayer Perceptron (MLP) neural network is the most famous type of AIs which has been widely used in hydrological and meteorological modeling studies [19–30]. Malik and Kumar [31] used the MLP model for meteorological drought prediction based on Effective Drought Index (EDI) in the Uttarakhand state of India and reported the acceptable performance of this model. MLP is also used for predicting the Standardized Precipitation Index (SPI) in Iran as a meteorological drought indicator and was superior compared to the other models such as Adaptive Neuro-Fuzzy Inference System (ANFIS), Radial Basis Function Neural Network (RBFNN), and Support Vector Machine (SVM) [32]. In forecasting agricultural drought based on the Standardized Precipitation-Evapotranspiration Index (SPEI), the MLP model was reported as an acceptable predictor model in Pakistan [33]. This model has been well evaluated for predicting SPI as a meteorological drought index in Awash river basin in Ethiopia [34], Selangor river basin in Malaysia [35], and Santa Ysabel Creek and Leaf rivers in America [36]. The study of Borji et al. [37] based on the Streamflow Drought Index (SDI) confirms the ability of the MLP model for drought forecasting from the perspective of surface hydrology too.

In the abovementioned studies, the referred indices can monitor the different drought types separately, for example, SPI individually for meteorological droughts, SDI individually for hydrological droughts [38], and SPEI for agricultural droughts. Among the drought indices, SPI is a different index that can indicate different types of droughts in its different time windows [39]. For example, the 1-month SPI (SPI1) shows the meteorological drought condition. Also, 3-month, 6-month, 12-month, or 24-month SPI (SPI3, SPI6, SPI12, or SPI24) talk about droughts in perspectives of soil moisture, surface hydrology, agriculture, and groundwater, respectively [12, 40]. According to the literature, no model has been evaluated in forecasting different drought types simultaneously. Multivariate drought indices can theoretically monitor different types of droughts simultaneously. So, forecasting a multivariate drought index can theoretically present a perspective about the status of different drought types in the future. Multivariate Standardized Precipitation Index (MSPI) is one of the newest introduced multivariate drought indices. This index was developed by Bazrafshan et al. [1] based on SPI by merging SPI's different time windows. Also, MSPI was superior in comparison with the Joint Deficit Index (JDI) [41] to monitor multivariate drought in all of the Iranian climates [6]. Up to now, MSPI was used in agricultural drought studies. Bateni et al. [42] used MSPI to develop an agrometeorological drought index. Aghelpour et al. [12] evaluated MSPI in monitoring and forecasting agricultural drought for Iranian climates and found the index acceptable for the issue.

According to the literature, no investigation was carried out on MSPI for different types of droughts simultaneously (multivariate drought forecasting). Due to MLP's high capability in drought forecasting and, generally, hydrological modeling studies, this model is used in the current study for forecasting MSPI for multivariate drought forecasting. Two semiarid climate stations located in western Iran have been selected for this issue. Also, in numerical modeling issues of hydrology, the optimization algorithms such as Genetic Algorithm (GA), Particle Swarm Optimization (PSO), and Firefly Algorithm (FA) have been well used recently to optimize the prediction/estimation accuracies of the MLP model. The imperialistic Competitive Algorithm (ICA) is another powerful optimization algorithm developed by Atashpaz-Gargari and Lucas [43], which has been used less in hydrological modeling cases, especially in drought forecasting cases. Therefore, as another innovation in drought studies, in this study, the ICA is merged with MLP to improve its forecasting accuracy.

2. Materials and Methods

2.1. Study Area. According to the extended De-Martonne climatic classification, about 22.91% of the total area of Iran located in a semiarid climatic condition is equal to 377533.4 km^2 [44]. These semiarid regions receiving appropriate solar radiation are important areas for agricultural production, but they are highly dependent on available water and affected by incoming rainfall and consequent drought events, which directly and indirectly affect various aspects of human life. In fact, precipitation deficit and consequent drought events can be more effective in semiarid regions than humid areas. Therefore, the current study aims to investigate and predict the multivariate drought condition for two ground station about Iran's semiarid climate. Hamedan and Kermanshah are located in western Iran. Hamedan and Kermanshah having urban area of 19368 and 24998 square kilometers are elevated with 1820 meters and 1400 meters, respectively (Figure 1).

Calculating MSPI needs total monthly precipitation data. The precipitation data was provided from the Iranian Meteorological Organization (IRIMO) for these synoptic stations and were used for MSPI calculation. The stations' geographical coordinates and statistical characteristics of their monthly precipitation data are shown in Table 1.

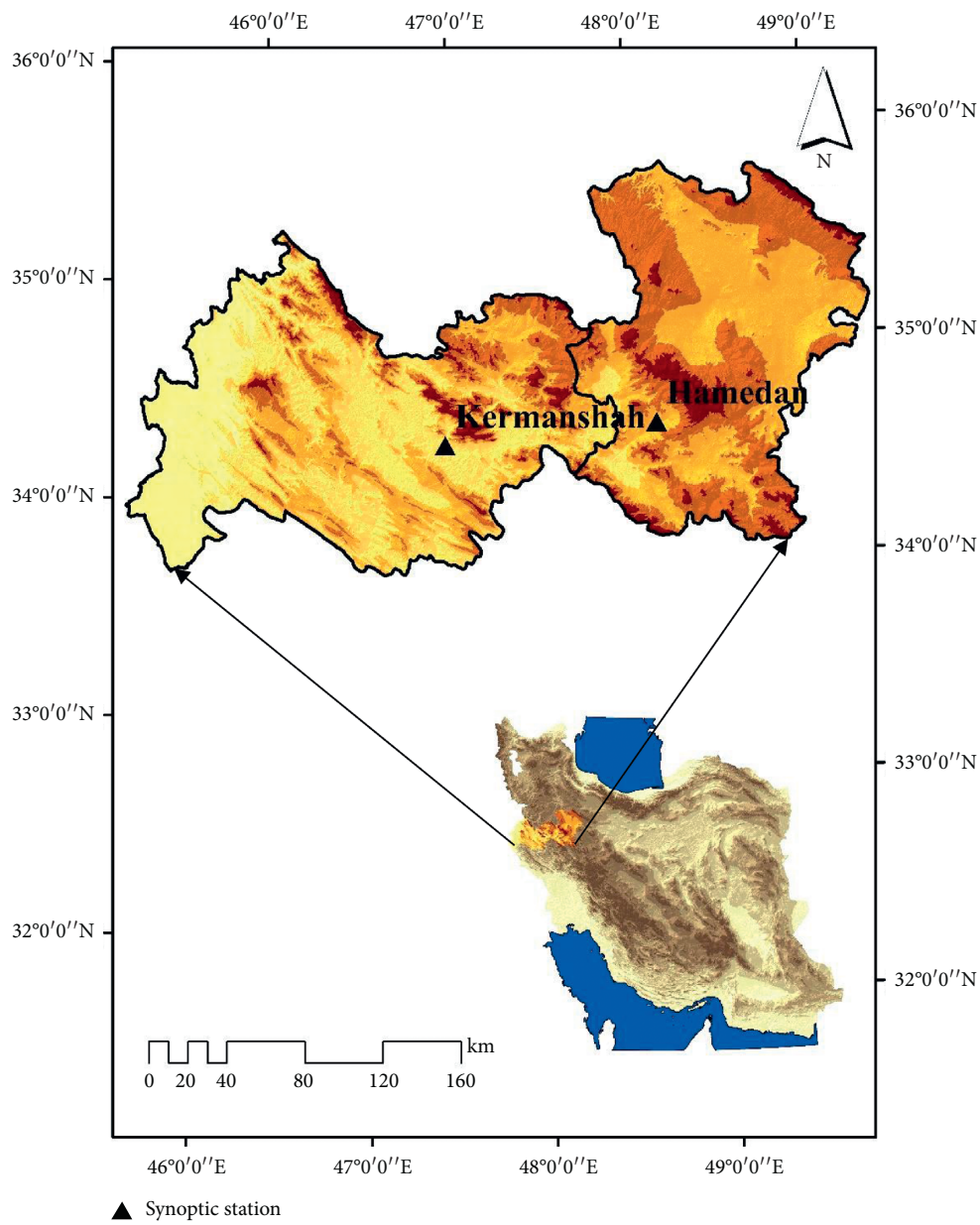

Figure 1: The geographical location of Hamedan and Kermanshah provinces.

Table 1: Coordinates of the stations; descriptive statistics of the monthly precipitation time series; climate type based on the extended De-Martonne classification method [44].

Station	Latitude (°)	Longitude (°)	Elevation (m)	Mean (mm)	St. Dev (mm)	Min (mm)	Max (mm)	Skew.	Period	Climate
Hamedan	+30.87	+48.53	+1741.5	25.07	26.62	0.00	186.10	1.43	1988–2017	Semiarid very cold
Kermanshah	+34.35	+47.15	+1318.6	34.21	40.05	0.00	295.40	1.63	1988–2017	Semiarid cold

2.2. Multivariate Standardized Precipitation Index. Multivariate standardized precipitation index (MSPI) is derived by applying Principal Components Analysis (PCA) on the K time series of SPI (where K is corresponding to the time window K). The first major component (PC_1) of the PCA analysis is used to describe the percentage changeability in K of the initial variable. Due to the PC_1 character, unlike the SPI, which has a mean 0 and standard deviation 1, its values are not comparable between months. Therefore, it is necessary to standardize the PC_1 time series using the average and standard deviation of the different months of the year using [1]

$$Z_{1ym} = \frac{PC_{1ym} - \overline{PC_{1m}}}{SD_{1m}} \approx \frac{PC_{1ym}}{SD_{1m}}, \quad (1)$$

where Z_{1ym} is the standardized value of PC1 in year (y) and month (m), PC_{1ym} is the value of PC1 in year (y) and month (m), $\overline{PC_{1m}}$ is the average PC1 in the month (m), SD_{1m} is the standard deviation of PC1 in month (m), and Z_{1ym} is taken as the multivariate Standard Precipitation index (MSPI). The value of PC_{1m} is statistically very small and close to zero; hence, in the case of the fraction of the above equation, it can be neglected [1, 45]. In order to determine the drought severity classes of the MSPI, the time series is arranged in ascending order, and its probability distribution is plotted on a diagram (for example, Figure 2).

Then, the values corresponding to the probability thresholds of different classes of SPI (Table 2) are extracted from the above diagram. The extracted values are taken as the MSPI thresholds, which can be used in the MSPI time series classification for drought severity [1].

According to the main literature of MSPI [1], MSPI can simultaneously monitor different droughts by its five time windows; so, these time windows are getting calculated in the current study. The time windows included are 3–6 months ($MSPI_{3-6}$), 6–12 months ($MSPI_{6-12}$), 3–12 months ($MSPI_{3-12}$), 12–24 months ($MSPI_{12-24}$), and 24–48 months ($MSPI_{24-48}$). The mentioned time windows of MSPI are its multivariate drought time windows and theoretically related to more than one type of droughts. SPI's time windows show the different drought types' severity and weakness. Extensionally, the time windows SPI_3, SPI_6, SPI_{12}, and SPI_{24} relate to droughts in perspectives of soil moisture, surface hydrology, agriculture, and groundwater level, respectively, and the larger time windows can be related to the economic and social effects of drought [1, 12, 40]. Therefore, the merged form of these time windows of MSPI can theoretically monitor the different perspectives of droughts simultaneously. For example, the $MSPI_{3-6}$ time window can theoretically monitor drought in perspectives of soil moisture and surface hydrology or $MSPI_{6-12}$ can monitor both hydrological and agricultural droughts, simultaneously. $MSPI_{3-12}$ relates to 3 perspectives of droughts simultaneously, including soil moisture, hydrological, and agricultural droughts. Among the larger time windows, $MSPI_{12-24}$ can simultaneously indicate drought in perspectives of agriculture and groundwater, and $MSPI_{24-48}$ is theoretically related to the socio-economic effects of droughts [1, 6, 12, 39, 47].

2.3. Artificial Neural Networks. An artificial neural network is a parallel information processing system that has a distinct function inspired by the biological structure of the human brain [48]. These systems are able to determine the complexity and nonlinear relationship between the inputs and outputs of a physical system by a network of nodes that are interconnected. In these systems, the activity of each of these connections is set by historical information (learning process).

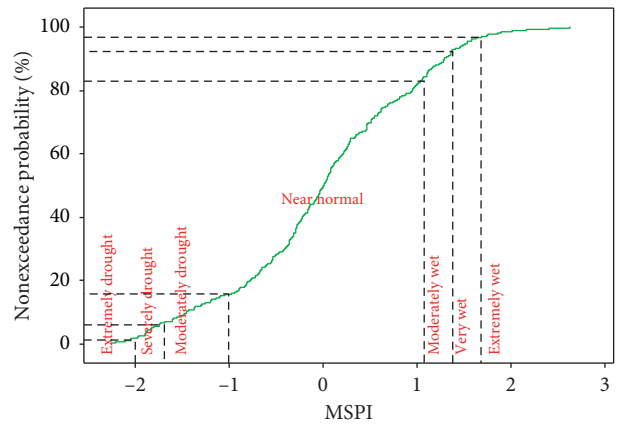

Figure 2: Percentiles of 6 to 12 months' time window of MSPI for Hamedan synoptic station.

Table 2: Classification of the SPI's values and corresponding probability limits [1, 46].

SPI classes	Probability limits	Description
SPI ≥ 2	≥97%	Extremely wet
2 > SPI ≥ 1.5	93.3–97.7%	Severely wet
1.5 > SPI ≥ 1	84.1–93.3%	Moderately wet
1 > SPI > −1	15.9–84.1%	Normal
−1 ≥ SPI > −1.5	6.7–15.9%	Moderately dry
−1.5 ≥ SPI > −2	2.3–6.7%	Severely dry
−2 ≥ SPI	2.3%≥	Extremely dry

2.3.1. MLP Neural Network. MLP network is one of the most important structures of artificial neural networks. These networks consist of the layers of sensory units (neurons), the input layer made of one or more hidden layers, and the output layer. The input signal is transmitted through the network in the forward direction to the hidden layer and then to the output layer [48]. The output of each neuron is multiplied by weight coefficients and given as input to a nonlinear excitation function. In the training phase, the training data is given to the perceptron, and then, the grid weights are adjusted to minimize the error between the target and output of the model or to reach the number of training times to the default value. Then, like all modeling processes, different inputs (not present in the training phase) are used for model validation. The training of neural networks is generally very complex and can be stated to be an optimization problem with a large number of variables [49].

2.3.2. Imperialistic Competitive Algorithm (ICA). The imperialistic competitive algorithm was first proposed by Atashpaz-Gargari and Lucas in 2007 [43]. This algorithm, in the first place, with a completely new perspective on optimization, establishes a new link between the humanities and social sciences on the one hand and the technical and mathematical sciences on the other. In particular, this algorithm views the process of colonization as a stage of human socio-political evolution and uses mathematical

modeling as the source of inspiration for a powerful optimization algorithm. With the formation of the early empires, the imperialist rivalry between them began. Any empire that fails to compete for colonial power and increase its power (or at least prevent it from losing its influence) will be removed from the arena of imperialistic competition. Thus, the survival of an empire will depend on its power to attract and control the colonies of rival empires. As a result, during the imperialists' competitions, the power of the larger empires gradually increased, and the weaker empires were eliminated. To increase their power, empires will have to develop their colonies as well. Over time, the colonies will become closer to the empires in terms of power, and we will see a kind of convergence. The final limit of imperialistic competition is when there is a single empire in the world with colonies that are very close to the imperialist country in terms of position. In the following sections, different parts of the algorithm are presented [43].

Like other evolutionary algorithms, this algorithm starts with several random primary populations, in which each of them is called a "country." A number of the best elements of the population (equivalent to elitism in genetic algorithm or particle in particle swarm optimization) are selected as imperialists. The rest of the population is also considered a colony. Depending on their power, the colonizers will specially colonize these colonies; they pull towards themselves. The total power of an empire depends on both its constituent parts and the imperialist country (as the central nucleus) and its colonies. In mathematical terms, this dependence is modeled by defining the power of the empire as the total power of the imperial state, plus a percentage of the average power of its colonies. For supplementary information about this algorithm and its mathematical equations, the references are suggested [43, 50, 51]. The learning processes of the ICA algorithm is presented step by step in the form of a flowchart (Figure 3).

2.3.3. Combining MLP with Imperialist Competitive Algorithm (MLP-ICA). As a metainnovative neural network, the ICA can be merged with MLP to improve MLP's modeling accuracy. This approach gets done by optimizing the parameters of MLP by ICA. The makeup of MLP depends on the hidden layers, neurons, and transfer functions, which are found by the trial and error method. The optimizable parameters are the weights and biases of the MLP neural network that these two subjects are optimized by ICA optimization. The schematic form of merging MLP with ICA (MLP-ICA) is shown in Figure 4.

2.4. Evaluation Measures. To ensure the accuracy of modeling and predicting, the outputs of the model should be compared with their actual values. For this purpose, the model performance evaluation criteria are used. The criteria used in this study are the Root Mean Square Error (RMSE), Mean Absolute Error (MAE), and Pearson correlation coefficient (R), whose equations (2)–(4) have been described below:

$$\mathrm{RMSE} = \sqrt{\frac{1}{n}\sum_{i=1}^{n}\left(y_i - f_i\right)^2}, \tag{2}$$

$$\mathrm{MAE} = \frac{1}{n}\sum_{i-1}^{n}\left|\left(y_i - f_i\right)\right|, \tag{3}$$

$$\mathrm{R} = \frac{\sum_{i=1}^{N}\left(y_i - \overline{y}\right)\left(f_i - \overline{f}\right)}{\sqrt{\sum_{i=1}^{N}\left(y_i - \overline{y}\right)^2} * \sqrt{\sum_{i=1}^{N}\left(f_i - \overline{f}\right)^2}}. \tag{4}$$

In the above equations, y_i and $\overline{y}$ are the observational data and their mean and f_i and $\overline{f}$ are the models' predictions and their mean, respectively, and n is the number of data, respectively. The values closer to zero for RMSE and MSE criteria and the values close to 1 for the Pearson correlation coefficient represent the optimal performance of the model. In this research, coding in MATLAB software has been used to run the MLP and MLP-ICA models.

3. Results

3.1. Input Selection. According to the main reference [1], the MSPI was calculated in five time windows including MSPI_{3-6}, MSPI_{6-12}, MSPI_{3-12}, MSPI_{12-24}, and MSPI_{24-48}, which resulted 5 time series for each station. For predicting the index, the model's input must be the previous amounts of the index (time lags of MSPI). For this, the Autocorrelation Function (ACF) plot was used to determine the correlation signification of the time lags (Figure 5).

ACF plots (Figure 5) can show the significance of the variable's correlation with its time lags, and due to this, the significantly correlated time lags can be used as the models' inputs for prediction. Figure 5 shows the ACF plots of Hamedan station, drawn for the 5 mentioned time windows of MSPI. As it is observable in the ACF plot of MSPI_{3-6}, the time lags of 1, 2, and 3 have significant correlations, and so, they are selected as the predictor inputs. In both MSPI_{6-12} and MSPI_{3-12} time windows, the 1, 2, 3, 4, and 5 time lags are significantly correlated. For MSPI_{12-24}, the significant time lags are 1, 2, . . ., 12, and for MSPI_{24-48} time window, the significant correlations belong to the 1, 2, . . ., 17 time lags. This method was similarly implemented for Kermanshah station, and the total results are shown in Table 3.

3.2. Predicting Multivariate Drought and Assessment. After selecting the input variables for each of the time windows, the input-target samples were divided into two phases: 75% for the training phase and 25% for the testing phase. Data with specified inputs were entered into the two artificial intelligence models for modeling and evaluation. The parameters of the MLP neural network model includes the number of hidden layers, number of neurons in hidden layers, and type of transfer functions within the neurons, which were selected by the trial and error method. Consequently, the best suitable number of hidden layers was up to 3 hidden layers (1, 2, and 3 hidden layers), best number of neurons was from 6 neurons to 18 neurons in each hidden

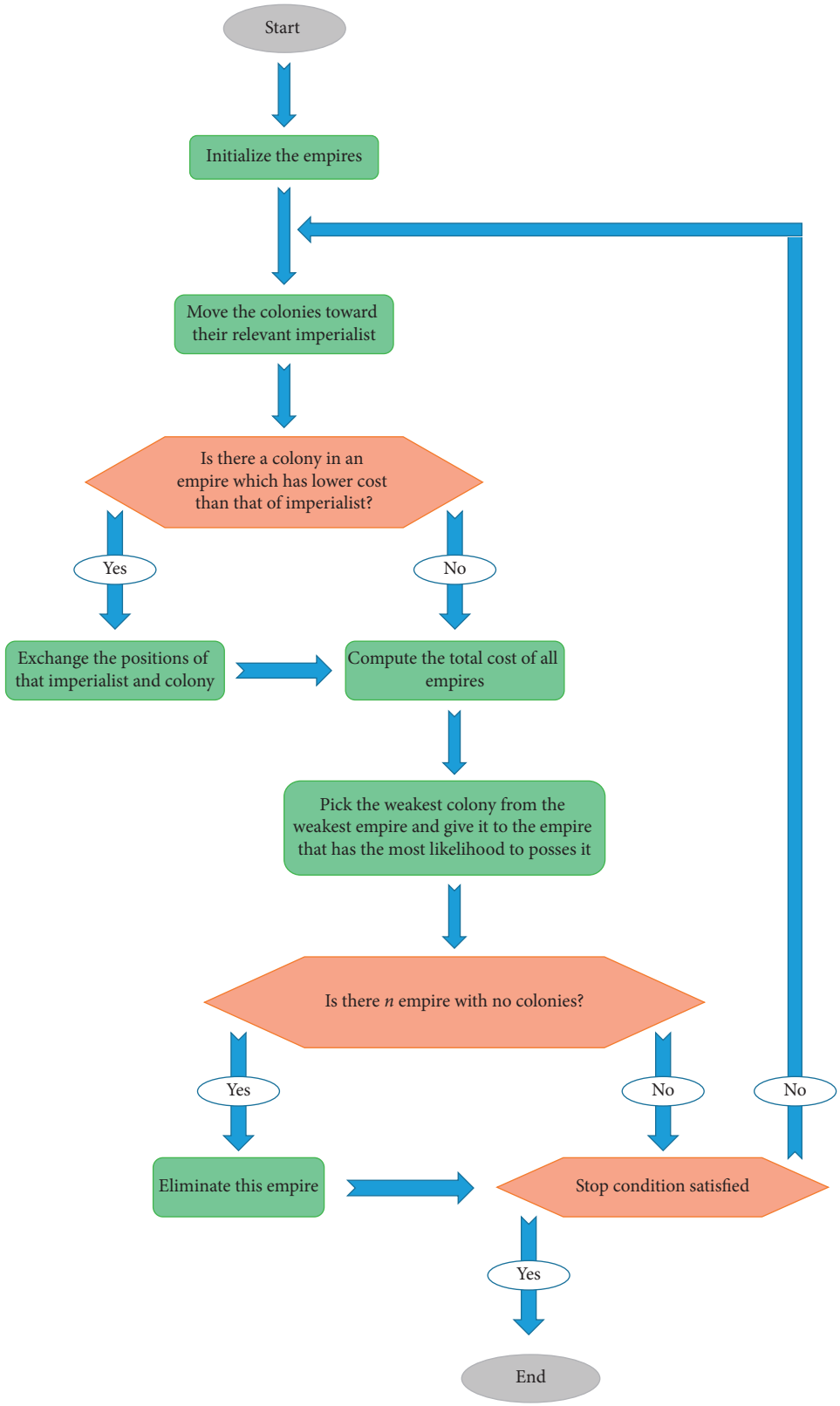

Figure 3: Flowchart of the ICA optimization.

layer, and best-fitted transfer function was the saturating linear transfer function (satlin). In the MLP-ICA model, the weights and biases of MLP (with similar makeup) were optimized by the ICA algorithm. The evaluation is carried out by the evaluation criteria of RMSE, MAE, and R, and the results are shown in Table 4.

In Table 4, the models are evaluated separately for stations and time windows. The predictive section is actually

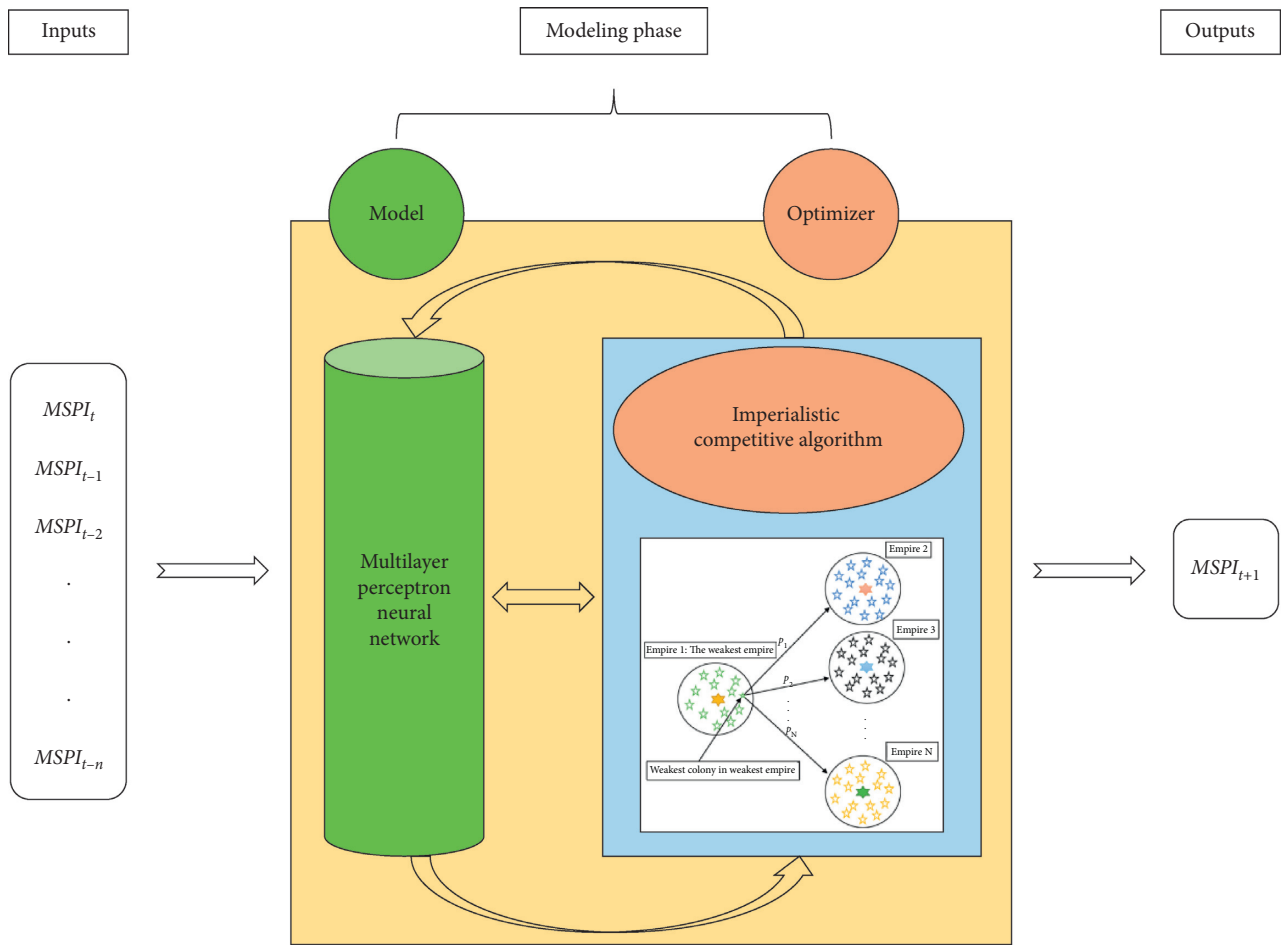

Figure 4: The interaction of the MLP model with Imperialist Competitive Algorithm in a schematic structure.

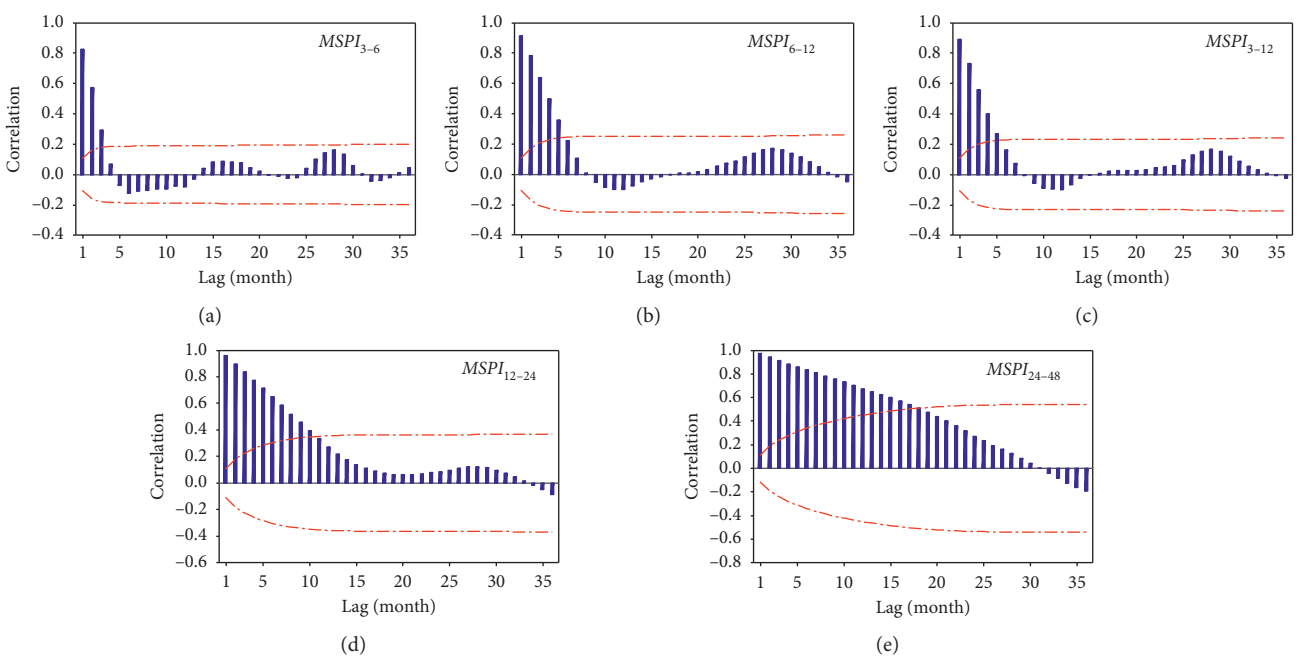

Figure 5: ACF plots of the five time windows of MSPI for Hamedan station.

Table 3: Time lags of MSPI as inputs selected by ACF.

Time window	Station	Time significant correlated time lags (month)
$MSPI_{3-6}$	Hamedan	1, 2, 3
	Kermanshah	1, 2, 3
$MSPI_{6-12}$	Hamedan	1, 2, 3, 4, 5
	Kermanshah	1, 2, 3, 4, 5
$MSPI_{3-12}$	Hamedan	1, 2, 3, 4, 5
	Kermanshah	1, 2, 3, 4, 5
$MSPI_{12-24}$	Hamedan	1, 2, 3, 4, 5, 6, 7, 8, 9, 10
	Kermanshah	1, 2, 3, 4, 5, 6, 7, 8, 9, 10, 11, 12
$MSPI_{24-48}$	Hamedan	1, 2, 3, 4, 5, 6, 7, 8, 9, 10, 11, 12, 13, 14, 15, 16, 17
	Kermanshah	1, 2, 3, 4, 5, 6, 7, 8, 9, 10, 11, 12, 13, 14, 15, 16, 17, 18, 19, 20

Table 4: Evaluating the predictions of the models MLP and MLP-ICA.

Station	Time window	Model	RMSE		MAE		R	
			Train	Test	Train	Test	Train	Test
Hamedan	$MSPI_{3-6}$	MLP	0.42	0.63	0.31	0.46	0.91	0.78
		MLP-ICA	0.40	0.60	0.29	0.46	0.92	0.81
	$MSPI_{6-12}$	MLP	0.31	0.50	0.22	0.38	0.95	0.87
		MLP-ICA	0.29	0.40	0.21	0.28	0.95	0.92
	$MSPI_{3-12}$	MLP	0.30	0.54	0.21	0.38	0.95	0.84
		MLP-ICA	0.30	0.53	0.22	0.38	0.95	0.86
	$MSPI_{12-24}$	MLP	0.23	0.36	0.17	0.26	0.98	0.89
		MLP-ICA	0.20	0.27	0.14	0.20	0.98	0.94
	$MSPI_{24-48}$	MLP	0.19	0.32	0.15	0.26	0.98	0.91
		MLP-ICA	**0.14**	**0.20**	**0.10**	**0.15**	**0.99**	**0.95**
Kermanshah	$MSPI_{3-6}$	MLP	0.42	0.73	0.29	0.57	0.91	0.73
		MLP-ICA	0.42	0.64	0.31	0.47	0.90	0.80
	$MSPI_{6-12}$	MLP	0.42	0.71	0.29	0.53	0.92	0.67
		MLP-ICA	0.32	0.59	0.23	0.41	0.95	0.79
	$MSPI_{3-12}$	MLP	0.40	0.80	0.30	0.60	0.92	0.60
		MLP-ICA	0.40	0.63	0.28	0.44	0.92	0.79
	$MSPI_{12-24}$	MLP	0.24	0.47	0.18	0.37	0.98	0.79
		MLP-ICA	0.16	0.31	0.12	0.24	0.99	0.92
	$MSPI_{24-48}$	MLP	0.18	0.30	0.14	0.25	0.99	0.78
		MLP-ICA	**0.12**	**0.20**	**0.09**	**0.15**	**0.99**	**0.92**

The bold numbers are the best predictions of each station.

the test section discussed here. At first glance, it is clear that, in both stations, as the time windows get bigger, the accuracy of the models also increases. In both stations, the accuracy of the models from low to high is reported in the time windows $MSPI_{3-6}$, $MSPI_{3-12}$, $MSPI_{6-12}$, $MSPI_{12-24}$, and $MSPI_{24-48}$, respectively. In all cases, the comparison between the two models, which includes 10 series (5 time windows for each of the stations), and the MLP-ICA hybrid model has higher accuracy in predicting MSPI. This shows that ICA is effective in optimizing the MLP model and is able to improve its performance. The lowest percentage of MLP performance improvement by ICA at Hamedan station belongs to the $MSPI_{3-12}$ time window (about 1.9%) and the highest, which is about 60%, was reported for the $MSPI_{24-48}$ time window (where the model error is reduced from 0.32 to 0.20). At Kermanshah station, the MLP-ICA hybrid model has performed much better compared to the simple MLP model. In $MSPI_{12-24}$ and $MSPI_{24-48}$ time windows, it was able to improve MLP forecasting accuracy by more than 50% (in $MSPI_{12-24}$, the model error was reduced from 0.47 to 0.31, and in $MSPI_{24-48}$, the model error was reduced from 0.30 to 0.20). The lowest performance improvement from ICA merging with MLP at Kermanshah station belonged to the $MSPI_{3-6}$ time window, where the model error was reduced from RMSE = 0.73 to RMSE = 0.64 (about 14.1% improvement in prediction accuracy). It can be said that, on average, the ICA algorithm in Hamedan and Kermanshah stations caused 25% and 32% increase in accuracy for the MLP model, respectively. The strongest and weakest performance in Hamedan station was reported in $MSPI_{24-48}$ window by the MLP-ICA model (with RMSE = 0.20, MAE = 0.15, and $R = 0.95$) and $MSPI_{3-6}$ time window by the MLP model, respectively. In Kermanshah station, the best forecast was reported by the MLP-ICA model and $MSPI_{24-48}$ time window (RMSE = 0.20, MAE = 0.15, and $R = 0.92$) and the weakest was obtained by the simple MLP model in the $MSPI_{3-12}$ time window (RMSE = 0.80, MAE = 0.60, and $R = 0.60$). These overlays of the models' predictions and their observations are shown in time series plots (Figure 6).

In the $MSPI_{6-12}$ time window of Hamedan station, the models have relatively close estimates of the actual value so

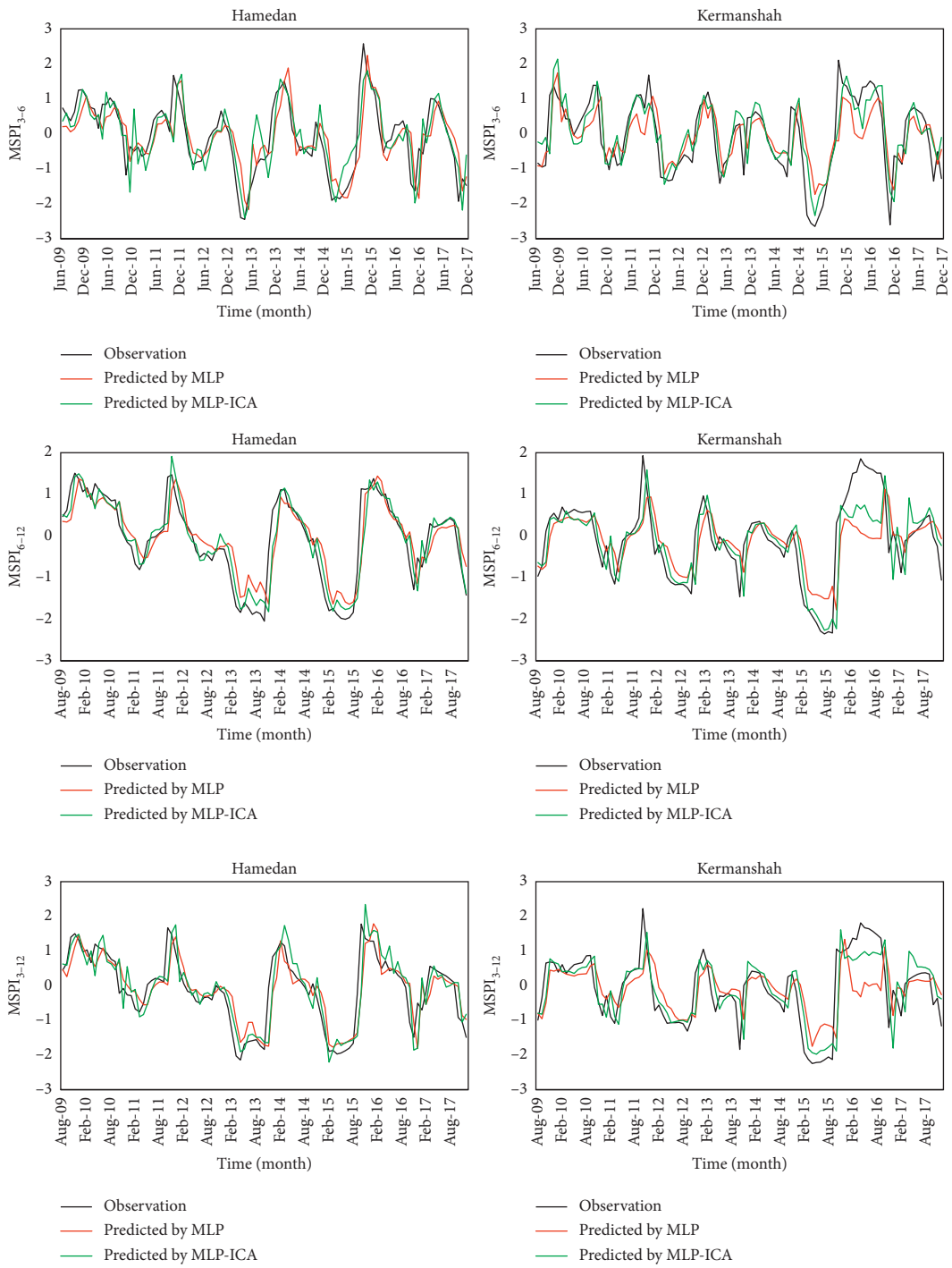

(a)

Figure 6: Continued.

(b)

Figure 6: Time series plots of the observed and predicted values of MSPI in the test period.

that, in most of the months, there are overlaps. During the severe drought from May–October 2013 and March–July 2015, both of the models were overestimated but the MLP-ICA's overestimation is milder so that this model could present an acceptable prediction for the classes of these severe drought months. In the same time window ($MSPI_{6-12}$) at Kermanshah Station, the forecasts are also suitable, but compared to Hamedan Station, the overlap is somewhat weaker. The error was enormous during the months of January through October 2016. The months are in wet conditions, so this underestimation in forecasting does not cause problems. Another remarkable point in $MSPI_{6-12}$ of Kermanshah is the severe and extreme drought status during April–November 2015. In this case, MLP was weak and overestimated, but MLP-ICA could have a highly accurate prediction for these important months.

The prediction of models for the $MSPI_{24-48}$ time window of the two stations was very accurate in most of the months, especially in the diagnosis of the drought classes. At the Hamedan station (Figure 6), the MLP model in all months of 2013 (unlike the MLP-ICA) had a large difference with actual values. However, in the course of May–July 2015 (with a little difference), it could have forecast a long-term severe drought class as well as the MLP-ICA. In this diagram ($MSPI_{24-48}$ of Hamedan), the proximity of the MLP-ICA prediction curve is clearly visible with the actual value curve compared to the MLP. This comparison between the two models at Kermanshah station, due to the significant difference in the forecast of two more convenient models, shows the superiority of the MLP-ICA hybrid model. The MLP's error in forecasting the $MSPI_{24-48}$ time window is more than MLP-ICA in most of the months. However, in March–December 2012, February–September 2016, and April–Nov 2017, it is too clear that MLP-ICA is more accurate than MLP, with a large difference. The ability of the models in predicting drought severity classes of MSPI has been evaluated in Table 5. In this table, the number of months of the test period that predicted drought severity correctly was divided by the total number of test periods. This method is done for both models in each of the time windows of both stations, and the resulted likelihood is shown by percentage.

Observing all of the comparison cases (a specific time window in a station) between the two models shows the superiority of MLP-ICA's likelihood against the MLP simple form. The error decreasing by increasing the time window size is reported here (evaluation of the class prediction) too. The least likelihood percentage is reported for $MSPI_{3-6}$ of Kermanshah station, which is 65.05%, and resulted in the

Table 5: The models' likelihood in determining MSPI drought classes.

Time window	Likelihood percentage of the drought severity classes (%)			
	Hamedan		Kermanshah	
	MLP	MLP-ICA	MLP	MLP-ICA
$MSPI_{3-6}$	69.90	73.79	65.05	68.93
$MSPI_{6-12}$	68.32	77.23	70.30	75.25
$MSPI_{3-12}$	72.28	75.25	67.33	69.31
$MSPI_{12-24}$	80.00	90.00	86.67	88.89
$MSPI_{24-48}$	79.52	86.75	95.78	96.39

MLP model. The largest likelihood percentage is 96.39%, which is reported for the MLP-ICA model in predicting $MSPI_{24-48}$ of Kermanshah station. This can show the good capability of AI methods in forecasting the severity classes of different types of droughts simultaneously. The improvement of drought class prediction by the new hybrid model (MLP-ICA) is clearer in Hamedan station compared to Kermanshah station. The biggest improvement reached by combining ICA with MLP is 10%, which is reported for the $MSPI_{12-24}$ time window of Hamedan station. This case can make another confirmation on the ability of the new hybrid model, MLP-ICA. In Figure 7 (regression diagrams), the correlation of the output of the two models with actual values is investigated. It is clear that the distribution of points around the axis of the regression line is greater in smaller time windows, and in larger time windows, the points are closer and more concentrated to the models' regression lines.

This indicates a higher correlation and therefore a more accurate prediction in larger time windows, which is consistent with the results in Table 4. At Hamedan station, $MSPI_{24-48}$ forecasts have the highest concentration around their fitted regression lines and as a result, have the highest correlation between the time windows. The R^2 coefficients in these series for the MLP and MLP-ICA models are 0.827 and 0.928, respectively, which shows a very good correlation in predicting socio-economic droughts. The $MSPI_{3-6}$ time window, which represents drought from the perspectives of soil moisture and surface hydrology simultaneously, had the weakest forecasts in Hamedan (R^2 is equal to 0.605 and 0.654 for MLP and MLP-ICA, respectively). The reason for this difference in accuracy can be the sudden jumps in the time series of the index. Sudden jumps occur more frequently among smaller time windows, but in larger time windows that reflect the long-term effects of lack of precipitation, monthly changes are gradual (see Figure 6 for a better understanding). The index with gradual changes will always have a more accurate prediction, while the presence of sudden jumps in the time series naturally increases the prediction error. Among the time windows smaller than 12 months ($MSPI_{3-6}$, $MSPI_{6-12}$, and $MSPI_{3-12}$), the $MSPI_{6-12}$ time window, which is associated with both hydrological and agricultural droughts, had the strongest predictions at both stations. From the theoretical point of view, the $MSPI_{3-12}$ time window simultaneously represents 3 types of drought perspectives (drought from soil moisture perspective, hydrological drought, and agricultural drought), while $MSPI_{6-12}$ simultaneously represents two types of droughts (hydrological drought and agricultural drought). Therefore, it is logical that the simultaneous forecasting of two types of droughts will be more accurate than three types of droughts. At Kermanshah station, the best forecasts for the $MSPI_{12-24}$ time window (which could theoretically be a simultaneous indicator of drought from agricultural and groundwater perspectives) and $MSPI_{24-48}$ time window were presented. The R^2 value of the MLP-ICA output for the $MSPI_{12-24}$ and $MSPI_{24-48}$ time windows of Kermanshah are 0.849 and 0.841, respectively. In predicting all cases (all 10 series investigated), the slope of the MLP-ICA regression line is closer to the 1 : 1 line, and the R^2 value is higher than the simple MLP model. This demonstrates the reliable performance of the ICA algorithm in optimizing the MLP model, which results in a more accurate prediction of simultaneous droughts. The highest increased correlation by the MLP-ICA hybrid model is observed in the $MSPI_{3-12}$ time window of Kermanshah station, where the R^2 value has increased from 0.355 to 0.601. Distribution and concentration of the model error around zero can be another measure of predictability. In this section, the violin plot (Figure 8) is used to examine the distribution of prediction errors.

This diagram was drawn separately for each station, and the power of the two models was compared in each time window. The results of this plot also confirm the strength of the MLP-ICA model compared to the simple MLP model. For example, in Kermanshah's $MSPI_{3-6}$ time window, the curvature of the MLP-ICA violin around the error = 0 axis is greater than that of the MLP (the so-called wider violin). This indicates a higher percentage of zero errors in MLP-ICA, which shows its superiority against the simple MLP model. This is true of all time windows and is more noticeable in larger time windows. In the $MSPI_{24-48}$ time window, the width of the MLP-ICA violin is about twice that of the MLP. Therefore, in predicting larger MSPI time windows, the use of the MLP-ICA hybrid model is highly recommended. The situation is similar at Hamedan station, and MLP-ICA violins are wider than MLP, at error = 0 axis. Also, as the size of the time window increases, the width of the violins increases, the distance between the first and third quartiles (IQR) decreases, and the upper and lower tails of the frequency distributions gradually disappear. This indicates that the prediction error is centered on zero, which is minimized in the largest time window ($MSPI_{24-48}$).

4. Discussion

MSPI forecasts were so far only reported in the Aghelpour et al. [12] study, which used the ANFIS model and its hybrid models. In this study, 31 stations from different climates of Iran have been studied, and MSPI has been monitored and predicted from the perspective of agricultural drought (the time window of $MSPI_{9-12}$). In Aghelpour et al. [12] study, the Kermanshah station was also examined, which in its most accurate forecast was RMSE equal to 0.356. While in the present study, the RMSE rate for Kermanshah varies between 0.2 and 0.6. This difference is due to the different dimensions

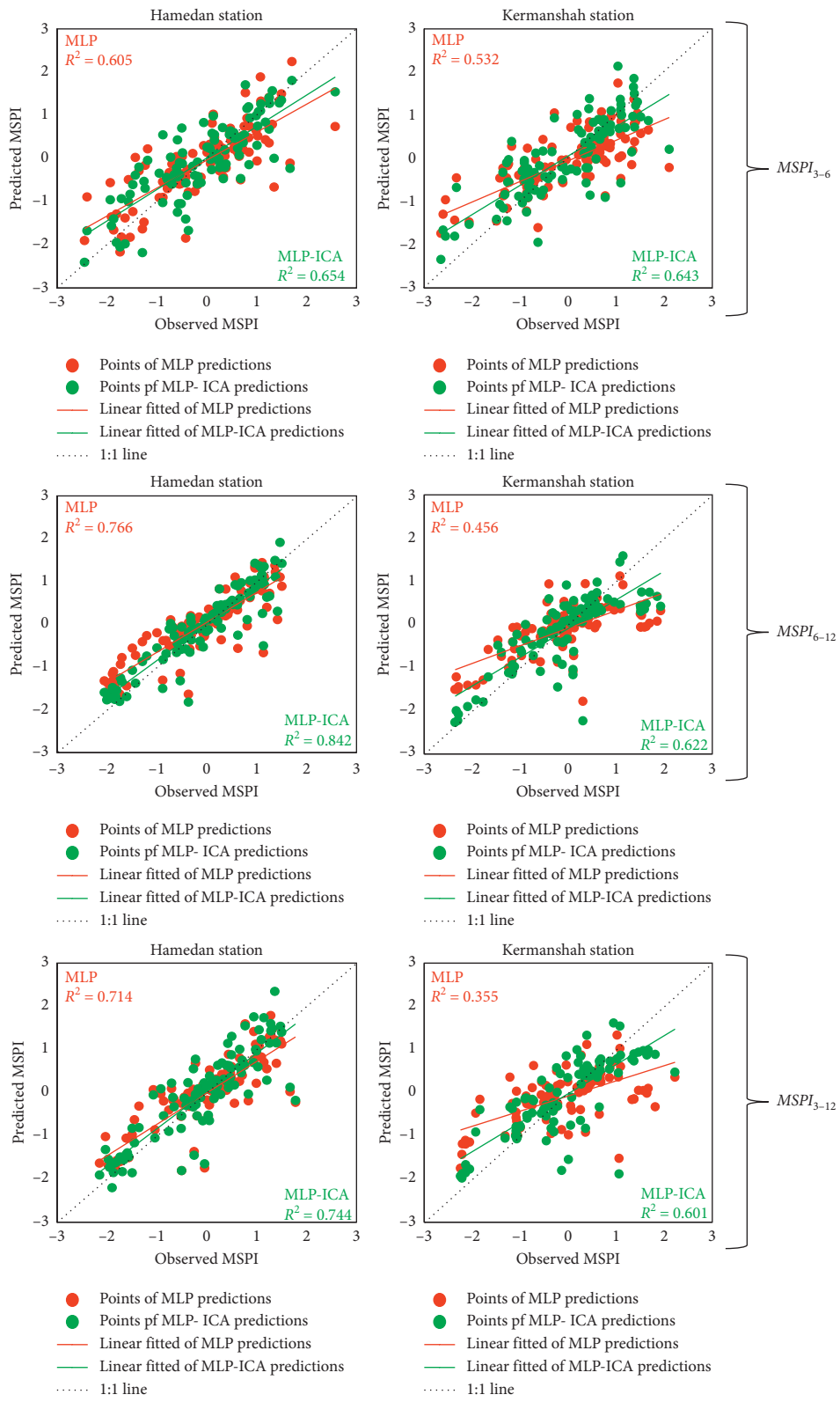

(a)

Figure 7: Continued.

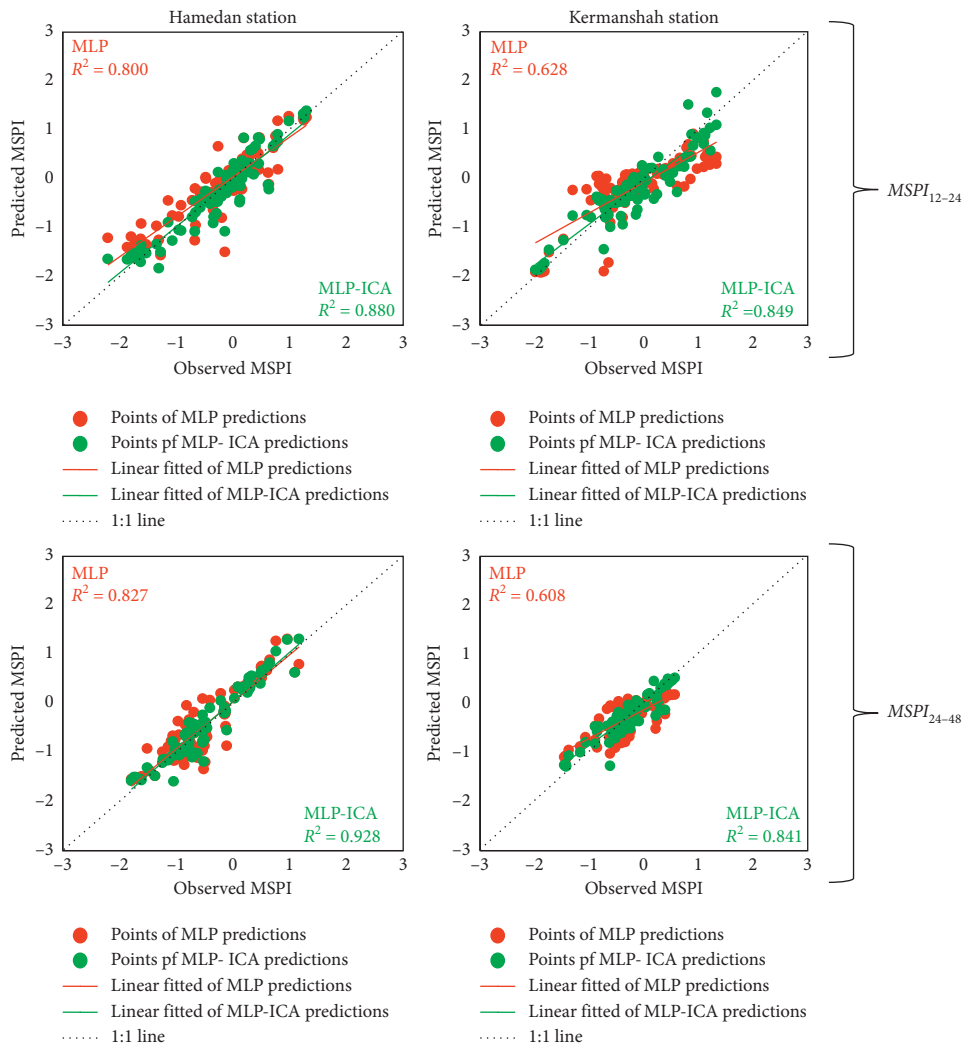

(b)

Figure 7: Scatter plots to evaluate the correlations between the models' outputs and their observations in the test period.

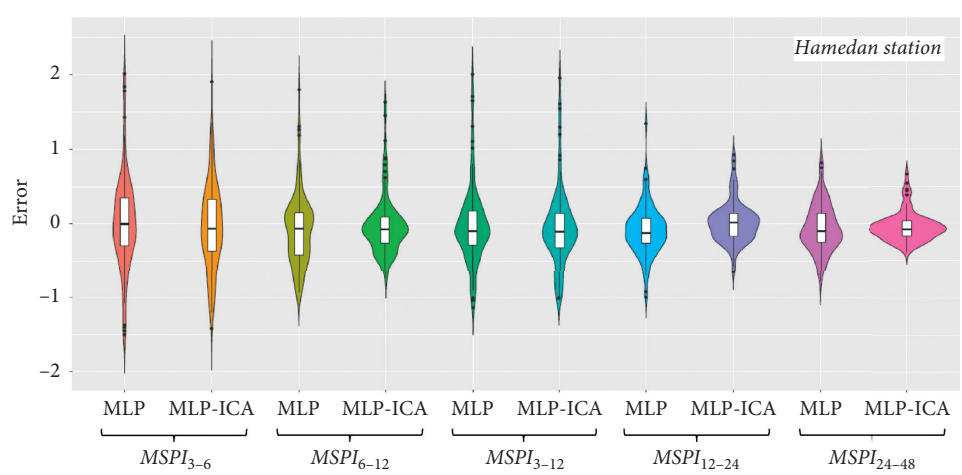

(a)

Figure 8: Continued.

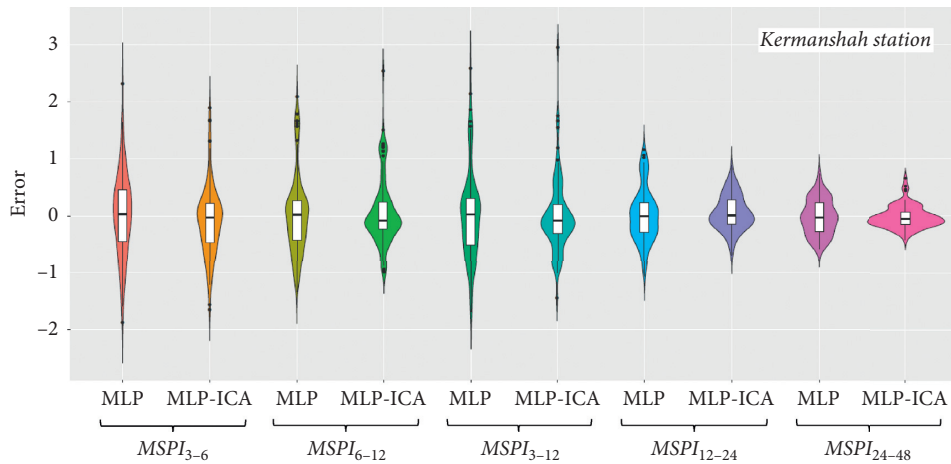

(b)

Figure 8: Violin plots of the error distributions in the test period.

of the time windows of the present study ($MSPI_{3-6}$, $MSPI_{6-12}$, $MSPI_{3-12}$, $MSPI_{12-24}$, and $MSPI_{24-48}$). This difference also conceptually creates a different perspective for MSPI. In other words, the $MSPI_{9-12}$ time window can only comment on one type of drought (agricultural drought), while the time windows examined in the current study are multivariate. These current time windows of MSPI can discuss several different types of droughts simultaneously. The ICA algorithm has been used in drought studies in only one study of Hosseini-Moghari et al. [50] to predict SPI, which has not studied drought in the multivariate type. Also, the MLP-ICA hybrid model has not been compared to its simple form to evaluate the improvement of the hybrid model.

The reason for the discrepancy between the results obtained in the two stations studied in the current study could be due to their microclimatic and topographic differences. Also, the difference in the type and number of atmospheric systems that affect these areas could be another reason for the difference in the accuracy of forecasts [52]. The Mediterranean low-pressure system approaches Iran from the northwest and the Sudanese low-pressure system approaches from the southwest. Due to having the Zagros Mountains in the west, Iran has favorable conditions for intensifying and expanding rainfall and sometimes flooding. Also, the role of the Red Sea is to provide more precipitation moisture to Kermanshah compared to Hamedan. In fact, the existence and role of higher mountains in the Hamedan region can be the main controlling factor of atmospheric systems and fronts. This orographic factor decreases the effects of the systems and consequently decreases the irregularity in precipitation time series in Hamedan compared to Kermanshah. So, while the MSPI is originated from the precipitation regime, this can cause weaker autocorrelation and finally weaker predictions in Kermanshah compared to Hamedan.

5. Conclusion

The results show that the simultaneous forecasting of different drought types can have acceptable accuracies for semiarid climates of western Iran. The best performance will be resulted in predicting the $MSPI_{24-48}$ time window, which is related to socio-economic drought. Also, the weakest accuracy belongs to the predictions of the short-term effects of precipitation deficit, such as soil moisture and surface hydrological droughts simultaneously ($MSPI_{3-6}$). Evaluating the models shows the significant capability of an imperialistic competitive optimization algorithm in improving MLP's prediction accuracy, which is reported 28.5% on average for the current study. As the first use of the MLP models and its hybrid form MLP-ICA in multivariate drought forecasting, it has been reported to be promising and is suggested for other similar climatic areas. Also, using the other previous well-used optimizers of MLP-like genetic algorithm, particle swarm, and firefly are suggested for future researchers to be compared with the imperialistic competitive algorithm and to choose the best optimizer of MLP in multivariate drought forecasting. One of the most important points in this area is that the current results are theoretically acceptable, and to have an actual or applicable investigation, it would be better to consider some more points. For example, in the simultaneous investigation and consequent prediction of agricultural and hydrological droughts, it is better suggested to investigate the relation of the index with the natural events, such as dam reservoir water content's variations (to validate the index in hydrological drought monitoring) or vegetation cover variations (to validate the index in agricultural drought monitoring). This subject can be another suggestion for future studies. Consequently, according to the acceptable results of the current investigated climate (semiarid and cold climate type), the work has research value for other different climates around the world.

Data Availability

The data used to support the findings of this study are available from the corresponding author upon request.

Conflicts of Interest

The authors declare that they have no conflicts of interest.

Acknowledgments

The work was supported by the Bu-Ali Sina University Deputy of Research and Technology (Grant no. 98-941).

References

[1] J. Bazrafshan, S. Hejabi, and J. Rahimi, "Drought monitoring using the multivariate standardized precipitation index (MSPI)," *Water Resources Management*, vol. 28, no. 4, 2014.

[2] D. A. Wilhite, "Planning for drought: a methodology," in *Drought assessment, Management, and Planning: Theory and Case Studies*, pp. 87–108, Springer, Berlin, Germany, 1993.

[3] A. K. Mishra and V. P. Singh, "A review of drought concepts," *Journal of Hydrology*, vol. 391, no. 1-2, pp. 202–216, 2010.

[4] A. H. Ahmed, T. A. Awchi, M. Al-mola, and S. Shahid, "Evaluation of remotely sensed precipitation sources for drought assessment in Semi-Arid Iraq," *Atmospheric Research*, vol. 242, Article ID 105007, 2020.

[5] S. Nabaei, A. Sharafati, Z. M. Yaseen, and S. Shahid, "Copula based assessment of meteorological drought characteristics: regional investigation of Iran," *Agricultural and Forest Meteorology*, vol. 276-277, Article ID 107611, 2019.

[6] J. Bazrafshan, M. Nadi, and K. Ghorbani, "Comparison of empirical copula-based joint deficit index (JDI) and multivariate standardized precipitation index (MSPI) for drought monitoring in Iran," *Water Resources Management*, vol. 29, no. 6, pp. 2027–2044,, 2015.

[7] M. Abbaspour and A. Sabetraftar, "Review of cycles and indices of drought and their effect on water resources, ecological, biological, agricultural, social and economical issues in Iran," *International Journal of Environmental Studies*, vol. 62, no. 6, pp. 709–724, 2005.

[8] W. Pozzi, J. Sheffield, R. Stefanski et al., "Toward global drought early warning capability: expanding international cooperation for the development of a framework for monitoring and forecasting," *Bulletin of the American Meteorological Society*, vol. 94, no. 6, pp. 776–785, 2013.

[9] R. S. Pulwarty and M. V. K. Sivakumar, "Information systems in a changing climate: early warnings and drought risk management," *Weather and Climate Extremes*, vol. 3, pp. 14–21, 2014.

[10] E. E. Moreira, C. L. Pires, and L. S. Pereira, "SPI drought class predictions driven by the North Atlantic Oscillation index using log-linear modeling," *Water (Switzerland)*, vol. 8, no. 2, 2016.

[11] Z. M. Yaseen and S. Shahid, "Drought index prediction using data intelligent analytic models: a review," *Intelligent Data Analytics for Decision-Support Systems in Hazard Mitigation*, Springer, Berlin, Germany, 2020.

[12] P. Aghelpour, H. Bahrami-Pichaghchi, and O. Kisi, "Comparison of three different bio-inspired algorithms to improve ability of neuro fuzzy approach in prediction of agricultural drought, based on three different indexes," *Computers and Electronics in Agriculture*, vol. 170, 2020.

[13] O. Kisi, A. Docheshmeh Gorgij, M. Zounemat-Kermani, A. Mahdavi-Meymand, and S. Kim, "Drought forecasting using novel heuristic methods in a semi-arid environment," *Journal of Hydrology*, vol. 578, Article ID 124053, 2019.

[14] A. Abbasi, K. Khalili, J. Behmanesh, and A. Shirzad, "Drought monitoring and prediction using SPEI index and gene expression programming model in the west of Urmia Lake," *Theoretical and Applied Climatology*, vol. 138, pp. 553–567, 2019.

[15] M. Masinde, "Artificial neural networks models for predicting effective drought index: factoring effects of rainfall variability," *Mitigation and Adaptation Strategies for Global Change*, vol. 19, no. 8, pp. 1139–1162, 2014.

[16] A. Belayneh, J. Adamowski, and B. Khalil, "Short-term SPI drought forecasting in the Awash River Basin in Ethiopia using wavelet transforms and machine learning methods," *Sustainable Water Resources Management*, vol. 2, no. 1, pp. 87–101, 2016.

[17] M. Ozger, A. K. Mishra, and V. P. Singh, "Estimating Palmer Drought Severity Index using a wavelet fuzzy logic model based on meteorological variables," *International Journal of Climatology*, vol. 31, no. 13, pp. 2021–2032, 2011.

[18] K. F. Fung, Y. F. Huang, C. H. Koo, and Y. W. Soh, "Drought forecasting: a review of modelling approaches 2007-2017," *Journal of Water and Climate Change*, vol. 11, no. 3, pp. 771–799, 2020.

[19] P. Aghelpour, Y. Guan, H. Bahrami-Pichaghchi, B. Mohammadi, O. Kisi, and D. Zhang, "Using the MODIS sensor for snow cover modeling and the assessment of drought effects on snow cover in a mountainous area," *Remote Sensing*, vol. 12, no. 20, p. 3437, 2020.

[20] B. Mohammadi and S. Mehdizadeh, "Modeling daily reference evapotranspiration via a novel approach based on support vector regression coupled with whale optimization algorithm," *Agricultural Water Management*, vol. 237, 2020.

[21] S. Mehdizadeh, B. Mohammadi, Q. Bao Pham, D. Nguyen Khoi, and N. Thi Thuy Linh, "Implementing novel hybrid models to improve indirect measurement of the daily soil temperature: elman neural network coupled with gravitational search algorithm and ant colony optimization," *Measurement*, vol. 165, Article ID 108127, 2020.

[22] A. Ashrafzadeh, O. Kişi, P. Aghelpour, S. M. Biazar, and M. A. Masouleh, "Comparative study of time series models, support vector machines, and GMDH in forecasting long-term evapotranspiration rates in northern Iran," *Journal of Irrigation and Drainage Engineering*, vol. 146, no. 6, 2020.

[23] P. Aghelpour and V. Varshavian, "Evaluation of stochastic and artificial intelligence models in modeling and predicting of river daily flow time series," *Stochastic Environmental Research and Risk Assessment*, vol. 34, no. 1, pp. 33–50, 2020.

[24] P. Aghelpour, B. Mohammadi, and S. M. Biazar, "Long-term monthly average temperature forecasting in some climate types of Iran, using the models SARIMA, SVR, and SVR-FA," *Theoretical and Applied Climatology*, vol. 138, no. 3-4, pp. 1471–1480, 2019.

[25] R. C. Deo, M. A. Ghorbani, S. Samadianfard, T. Maraseni, M. Bilgili, and M. Biazar, "Multi-layer perceptron hybrid model integrated with the firefly optimizer algorithm for windspeed prediction of target site using a limited set of neighboring reference station data," *Renewable Energy*, vol. 116, pp. 309–323, 2018.

[26] S. M. Biazar, V. Rahmani, M. Isazadeh, O. Kisi, and Y. Dinpashoh, "New input selection procedure for machine learning methods in estimating daily global solar radiation," *Arabian Journal of Geosciences*, vol. 13, p. 431, 2020.

[27] A. Ashrafzadeh, M. A. Ghorbani, S. M. Biazar, and Z. M. Yaseen, "Evaporation process modelling over northern Iran: application of an integrative data-intelligence model with the krill herd optimization algorithm," *Hydrological Sciences Journal*, vol. 64, no. 15, pp. 1843–1856, 2019.

[28] S. M. Biazar, A. F. Fard, V. P. Singh, Y. Dinpashoh, and A. Majnooni-Heris, "Estimation of evaporation from saline-

water with more efficient input variables," *Pure and Applied Geophysics*, vol. 177, pp. 5599–5619, 2020.

[29] A. Ashrafzadeh, A. Malik, V. Jothiprakash, M. A. Ghorbani, and S. M. Biazar, "Estimation of daily pan evaporation using neural networks and meta-heuristic approaches," *ISH Journal of Hydraulic Engineering*, vol. 26, no. 4, pp. 421–429, 2020.

[30] M. R. Khaledian, M. Isazadeh, S. M. Biazar, and Q. B. Pham, "Simulating Caspian Sea surface water level by artificial neural network and support vector machine models," *Acta Geophysica*, vol. 68, pp. 553–563, 2020.

[31] A. Malik and A. Kumar, "Meteorological drought prediction using heuristic approaches based on effective drought index : a case study in Uttarakhand," *Arabian Journal of Geosciences*, vol. 13, 2020.

[32] S. Mohamadi, S. Sh, and S. Fatemeh, *Zoning Map for Drought Prediction Using Integrated Machine Learning Models with a Nomadic People Optimization Algorithm*, Springer, Dordrecht, Netherlands, 2020.

[33] N. Khan, D. A. Sachindra, S. Shahid, K. Ahmed, M. Sanusi, and N. Nawaz, "Advances in water resources prediction of droughts over Pakistan using machine learning algorithms," *Advances in Water Resources*, vol. 139, 2020.

[34] A. Belayneh and J. Adamowski, "Standard precipitation index drought forecasting using neural networks, wavelet neural networks, and support vector regression," *Applied Computational Intelligence and Soft Computing*, vol. 2012, Article ID 794061, , 2012.

[35] D. Hong and K. A. Hong, "Drought forecasting using MLP neural networks," in *Proceedings of the 2015 8th International Conference on U-And E-Service, Science and Technology (UNESST)*, pp. 62–65, IEEE, Jeju, South Korea, November 2015.

[36] P. Maca and P. Pech, "Forecasting SPEI and SPI drought indices using the integrated artificial neural networks," *Computational Intelligence and Neuroscience*, vol. 2016, Article ID 3868519, 17 pages, 2016.

[37] M. Borji, A. Malekian, A. Salajegheh, and M. Ghadimi, "Multi-time-scale analysis of hydrological drought forecasting using support vector regression (SVR) and artificial neural networks (ANN)," *Arabian Journal of Geosciences*, vol. 9, no. 19, p. 725, 2016.

[38] P. Aghelpour, H. Bahrami-Pichaghchi, and V. Varshavian, "Hydrological drought forecasting using multi-scalar streamflow drought index, stochastic models and machine learning approaches, in northern Iran," *Stochastic Environmental Research and Risk Assessment*, pp. 1–21.

[39] P. Aghelpour, B. Mohammadi, S. M. Biazar, O. Kisi, and Z. Sourmirinezhad, "A theoretical approach for forecasting different types of drought simultaneously, using entropy theory and machine-learning methods," *ISPRS Int. J. Geo-Information*, vol. 9, no. 12, p. 701, 2020.

[40] M. Svoboda, M. Hayes, and D. Wood, *Standardized Precipitation Index User Guide*, World Meteorological Organization, Geneva, Switzerland, 2012.

[41] S.-C. Kao and R. S. Govindaraju, "A copula-based joint deficit index for droughts," *Journal of Hydrology*, vol. 380, no. 1-2, pp. 121–134, 2010.

[42] M. M. Bateni, J. Behmanesh, C. De Michele, J. Bazrafshan, and H. Rezaie, "Composite agrometeorological drought index accounting for seasonality and autocorrelation," *Journal of Hydrologic Engineering*, vol. 23, no. 6, 2018.

[43] E. Atashpaz-Gargari and C. Lucas, "Imperialist competitive algorithm: an algorithm for optimization inspired by imperialistic competition," in *Proceedings of the 2007 IEEE Congress on Evolutionary Computation*, pp. 4661–4667, Singapore, September 2017.

[44] J. Rahimi, M. Ebrahimpour, and A. Khalili, "Spatial changes of Extended De Martonne climatic zones affected by climate change in Iran," *Theoretical and Applied Climatology*, vol. 112, no. 3–4, 2013.

[45] J. A. Keyantash and J. A. Dracup, "An aggregate drought index: assessing drought severity based on fluctuations in the hydrologic cycle and surface water storage," *Water Resources Research*, vol. 40, no. 9, 2004.

[46] T. B. McKee, N. J. Doesken, and J. Kleist, "The relationship of drought frequency and duration to time scales," *Applied Climatology*, vol. 17, no. 22, pp. 179–183, 1993.

[47] M. Svoboda and B. Fuchs, *Handbook of Drought Indicators and Indices*, World Meteorological Organization, Geneva, Switzerland, 2016.

[48] S. Haykin, *Neural Networks: A Comprehensive Foundation*, Prentice-Hall, Inc., Upper Saddle River, NY, USA, 2007.

[49] D. E. Rumelhart, G. E. Hinton, and R. J. Williams, *Learning Internal Representations by Error Propagation*, University of California, San Diego, CA, USA, 1985.

[50] S.-M. Hosseini-Moghari, S. Araghinejad, and A. Azarnivand, "Drought forecasting using data-driven methods and an evolutionary algorithm," *Modeling Earth Systems and Environment*, vol. 3, no. 4, pp. 1675–1689, 2017.

[51] Z. Beheshti, M. Firouzi, S. M. Shamsuddin, M. Zibarzani, and Z. Yusop, "A new rainfall forecasting model using the CAPSO algorithm and an artificial neural network," *Neural Computing and Applications*, vol. 27, no. 8, pp. 2551–2565, 2016.

[52] M. Ahmadi, S. Salimi, S. A. Hosseini, H. Poorantiyosh, and A. Bayat, "Iran's precipitation analysis using synoptic modeling of major teleconnection forces (MTF)," *Dynamics of Atmospheres and Oceans*, vol. 85, pp. 41–56, 2019.

Hindawi
Complexity
Volume 2020, Article ID 8844367, 22 pages
https://doi.org/10.1155/2020/8844367

Research Article

Training and Testing Data Division Influence on Hybrid Machine Learning Model Process: Application of River Flow Forecasting

Hai Tao,[1] **Ali Omran Al-Sulttani**,[2] **Ameen Mohammed Salih Ameen**,[2] **Zainab Hasan Ali**,[3] **Nadhir Al-Ansari**,[4] **Sinan Q. Salih**,[5] **and Reham R. Mostafa**[6]

[1]*Computer Science Department, Baoji University of Arts and Sciences, Baoji, Shaanxi, China*
[2]*Department of Water Resources Engineering, College of Engineering, University of Baghdad, Baghdad, Iraq*
[3]*Civil Engineering Department, College of Engineering, University of Diyala, Baquba, Iraq*
[4]*Civil, Environmental and Natural Resources Engineering, Lulea University of Technology, 97187 Lulea, Sweden*
[5]*Institute of Research and Development, Duy Tan University, Da Nang 550000, Vietnam*
[6]*Information Systems Department, Faculty of Computers and Information Sciences, Mansoura University, Mansoura 35516, Egypt*

Correspondence should be addressed to Sinan Q. Salih; sinanq.salih@duytan.edu.vn

Received 17 August 2020; Revised 18 September 2020; Accepted 1 October 2020; Published 30 October 2020

Academic Editor: Shamsuddin Shahid

The hydrological process has a dynamic nature characterised by randomness and complex phenomena. The application of machine learning (ML) models in forecasting river flow has grown rapidly. This is owing to their capacity to simulate the complex phenomena associated with hydrological and environmental processes. Four different ML models were developed for river flow forecasting located in semiarid region, Iraq. The effectiveness of data division influence on the ML models process was investigated. Three data division modeling scenarios were inspected including 70%–30%, 80%–20, and 90%–10%. Several statistical indicators are computed to verify the performance of the models. The results revealed the potential of the hybridized support vector regression model with a genetic algorithm (SVR-GA) over the other ML forecasting models for monthly river flow forecasting using 90%–10% data division. In addition, it was found to improve the accuracy in forecasting high flow events. The unique architecture of developed SVR-GA due to the ability of the GA optimizer to tune the internal parameters of the SVR model provides a robust learning process. This has made it more efficient in forecasting stochastic river flow behaviour compared to the other developed hybrid models.

1. Introduction

The hydrological, environmental, and climatological processes related to different components of the hydrologic cycle such as rainfall, evaporation, infiltration, groundwater, and river flow are embedded with high nonlinearity, nonstationery, and redundancy [1, 2]. Mathematical models are generally used to address the different forms of nonlinearity and model different hydrological processes [3, 4]. A large number of hydrological models have been developed and successfully applied for forecasting different components of hydrological cycles [5]. Among them, the hydrological model for forecasting river flow has received the highest attention due to its enormous importance [6]. Being that river flow pattern is difficult to be fully understood due to the temporal and spatial changes in basin characteristics and variabilities in the rainfall-runoff process, univariate river flow simulation has become a trending topic in the field of hydrology [7]. River flow modeling in a particular climate environment (e.g., semiarid) is highly complicated as it is associated with regional climate and human interventions. Significant changes in climate have been witnessed across the globe in recent years. Streamflow time series is dynamic, complex, and presenting nonlinear and randomness phenomena. These characteristics make the forecasting process challenging for most of the hydrological researchers [8, 9].

Accurate long-term forecasting of river flow at monthly and yearly scale is very important for the planning and operation of water reservoir, agricultural and irrigation water management, estimation of catchment water balance, estimating minimum instream environmental flow, and other purposes [10, 11]. The accurate short-term (real-time) forecasting of river flow such as hourly or daily time step is important for flood and/or water scarcity forecasting in order to minimize and mitigate their effects on infrastructure and public health [12]. In addition, this river flow forecast makes it possible to predict the minimum instream environmental flow that is primarily used to sustain organisms' reproduction and growth and provide optimum habitat area [13].

Several developments have been recorded over the years in the application of machine learning (ML) models, artificial intelligence (AI) models, and big data mining technology for the solution of related hydrological engineering problems [14–18]. Being that these models do not depend on a physical meaning, they are suitable for solving problems, which are influenced by several complex factors, such as nonlinear natural processes and forecasting problems [19]. These models have also been found suitable for the solution of hydrological problems [20]. The ML models, unlike the physically based models, can mimic the actual trend of hydrological time series data by autonomously learning the various hydrological processes. However, ML models need a low level of expertise for the implementation and they can provide a fast solution compared to physically based models.

Despite the suitability of the ML models in hydrological studies, they are still prone to several drawbacks, such as prolonged computation time and insufficient feature extraction capability [21]. The recent interest in the ML models has exposed many other drawbacks of the classical ML models like artificial neural network (ANN), support vector regression (SVR), adaptive neurofuzzy inference (ANFIS), and random forest (RF) [22], which include trapping at local optima and gradient disappearance. Therefore, exploration of new robust and reliable versions of ML models for the modeling of various hydrological phenomena is always the motivation of hydrologists and soft computing scientists [20]. Recently, the new era of ML models is configured in the form of hybridized models where in integral of tuning parameter algorithms, it is conducted for solving the internal parameters using some bio-inspired or mathematical optimizers. The hybrid ML model has been emerged as the sought-after model due to its capability to overcome the drawbacks of standalone ML models [23]. It has been successfully applied in recent years for complex hydrological problems [24, 25].

The traditional ML models can build their learning processes using trial and error procedure that is associated with the possibility of the limited learning process. Hence, introducing the new optimization approaches can solve this problem and provide a reliable and robust learning mechanism. Risks associated with flooding can be reduced via accurate modeling of river flow time series dynamics. This can also enhance the capability of proper management of reservoirs during droughts [26]. The accurate forecasting of river flow time series should preferably be based on the existing long data with memory networks. Hybrid ML models as a robust methodology provide an excellent learning memory that could better model river flow patterns and provide better forecasting. During training the predictive model, the data is divided into the training and testing phase. A low ratio of training data may decrease the performance of the model, whereas the high ratio leads to overfitting. In both cases, the models get bad performance and unacceptable results. So, choosing the best ratio of data division is considered a challenging task in developing a machine learning model [27].

The main objective of the present study is to investigate the impact of training and testing data divisions on the process of several hybrid ML models including hybridized ANN and SVR with genetic algorithm (GA) and hybridized SVR and RF with the grid search algorithm. The development of the introduced models is investigated for river flow forecasting using historical data, which belongs to the Tigris River in semiarid climate of Iraq. The capacity of the developed model is examined to solve the complexity of river flow by using statistical metrics and graphical presentation.

The modeling procedure is structured based on different antecedent values of river flow and is defined as the matrix attributes for univariate modeling. Three data division scenarios for the training and testing dataset were inspected. The obtained results are discussed comprehensively and analysed comparatively to reveal the forecasting ability of different models. Thereafter, the forecasted river flow was used to estimate minimum instream environmental flow that is primarily used to sustain organisms' reproduction and growth and provide optimum habitat area.

2. Description of Study Areas and Data

The Tigris River is one of the largest rivers in Middle East. The total length of the river is about 1718 km which is shared by Turkey, Syria, and Iraq. About 85% of the total basin of Tigris River (253,000 km) lies in Iraq. The Tigris River along with the Euphrates River supplies the major share of total water required for irrigation, human use, and industrial purposes for several cities in Iraq, Turkey, and Iran counties. The climate of the basin is predominantly arid; however, semiaridity is the main characteristic of the river. The average rainfall in the basin is 216 mm with most of the rainfall occurring during winter (December to February) [28]. However, the rainfall concentration is varied from the north, middle, and south of Iraq [29]. The temperature varies from maximum 45°C during summer to minimum 10°C in winter [29]. The monthly river flow data of Tigris River for the period January 1991 to November 2010 was obtained from the USGS Data Series 540 for the present study [30]. The mean monthly discharge and the standard deviation of Tigris River flow at Baghdad Station are 411.35 m^3/s and 234.52 m^3/s, respectively [31]. The location of Tigris River in the map of Iraq is presented in Figure 1.

3. Data Division Scenarios and Input Combinations

In order to utilize the machine learning methods for forecasting, the observed river flow data was split into two sets

Figure 1: The location of the case study on Tigris River, Iraq.

(training and testing). Three data divisions were inspected in this research including 70%–30%, 80%–20, and 90%–10%. This is owing to the fact that ML models can behave differently based on the supplied dataset span for the learning process and testing phases [32].

The identification of the input parameters for the ML model's development is an essential step prior to the models' learning process. In this study, as the intended is the river flow forecasting, lead times were determined using the statistical approaches including the autocorrelation function (ACF) and the partial autocorrelation function (PACF). The suitable input parameters were decided based on the highly influential lead times toward the one-step-ahead forecasting. Valuable temporal pattern may exist in observed data which can be used as an input pattern for the development of the forecasting model. ACF can be used to capture information on the temporal patterns existing in time series. ACF provides information about the correlation between two separate points on the time series at different time leads and provides information about the repeating patterns in the time series. Thus, it tells how the past river flow influences the future river flow.

The ACF value ranges between 1 and −1; the value near to 1 indicates near-perfect correlation and the value near to

−1 indicates complete anticorrelation. However, the time series data for the river flow is time-independent, and therefore, the correlation between the pair of values depends only on the time differences between the two points without considering their position in the series. In order to distinguish the most appropriate lead times of the time series that notably or substantially might influence the forecasting, the reference value of ACF should be identified. In this study, the ACF values equal to or more than 0.5 were considered for the selection of the time-lag pattern [33, 34]. Figure 2 illustrates the ACF values for different lead times up to 20 time differences. Figure 2 shows that the ACF values for Tigris River for the lead times Q_{t-1} to Q_{t-5} are more than 0.2. In other words, five input combinations were constructed (Model I, Model II, . . . , Model V).

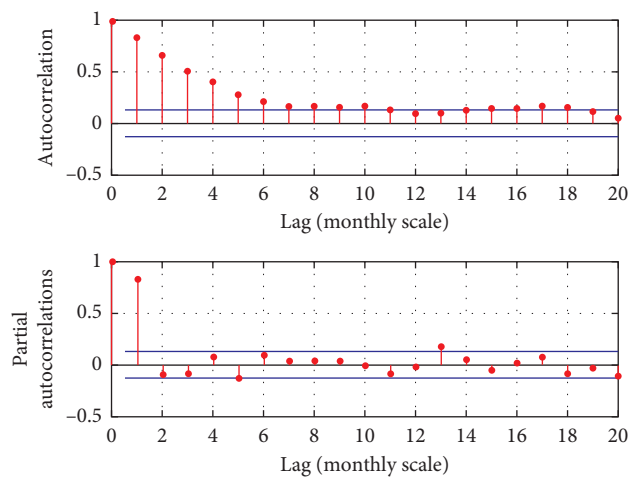

Figure 2: The statistics of the autocorrelation function (ACF) and the partial autocorrelation function (PACF) for the studied time series river flow.

4. Machine Learning Models Overview

In this study, four different hybrid machine learning models were developed including ANN-GA, SVR-GA, Grid-SVR, and Grid-RF for monthly river flow forecasting located in semiarid region, Iraq. RapidMiner software was used to develop machine learning models. RapidMiner is an open-source, free, and flexible software implemented by Java language. The program has been used in data analysis, application design, and developing complex models [35]. The development of predictive models using the above hybrid ML models is described in the following sections.

4.1. ANN-GA. Inspired by the human neural network, ANN was proposed and developed to simulate the human brain during learning. With high computing power, ANN can outperform the performance of the human in some cases. ANN was applied for solving many regression, clustering, and classification tasks.

ANN, as shown in Figure 3, consists of three types of layers: input layer, hidden layer, and output layer [36]. Each layer consists of a set of nodes called artificial neurons that perform elementary calculations [37]. Weighted connections connect neurons in the successive layers. During the training procedure of ANN, weights are defined and updated with the aim of minimizing the error between the actual output and the computed output. ANN has the ability to produce output with reasonable accuracy [38], if it has gone through an effective learning phase.

The backpropagation neural network (BPNN) proposed by Rumelhart et al. [39] is one of the most popular learning algorithms. BP aims to optimize the network parameters by minimizing the least square error between actual and computed output.

Inspired by Darwin's theory of biological evolution, GA was developed as a heuristic method for finding the function's optimal value [40, 41]. It represents one of the most popular forms of an evolutionary algorithm used to solve different optimization problems [42, 43]. GA is initialized by generating a random population of individuals (solutions) and tries to optimize these individuals by applying three successive operations:

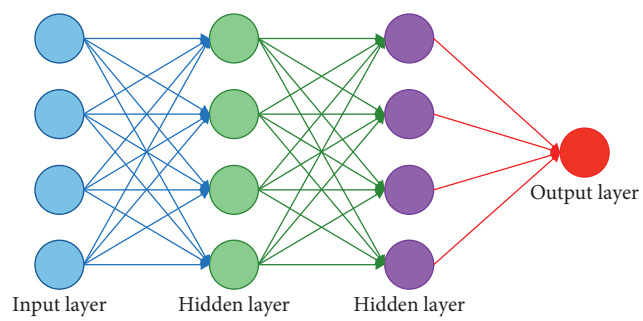

Figure 3: ANN architecture.

(i) Selection of the best individuals with high fitness values.

(ii) The crossover between two individuals to generate a new population.

(iii) The mutation performed by introducing random changes in individuals.

This procedure is repeated a certain number of times until the optimum values are obtained. In this section, the performance of BP was optimized using GA for tuning the parameters that affect the NN's performance. The training procedure for BP starts by using GA to perform a global search for network weight values. It refines an initially random set of weights to get a better estimate, and it is likely to be close to the global optimum [44, 45]. After that comes the role of BP in training in order to refine the solution provided by the GA to bring it to the optimum solution.

The general steps of ANN-GA can be summarized as follows. The flowchart of the GA-ANN method is illustrated in Figure 4. Initially, a feasible NN's topology was predefined through determining the number of neurons in the hidden layer [46, 47]. After that, steps to improve the performance of neural networks through GA algorithms begin as follows:

Step 1: initialize the random values for weight and bias (w_{ij} and b_i) according to initial network topology.

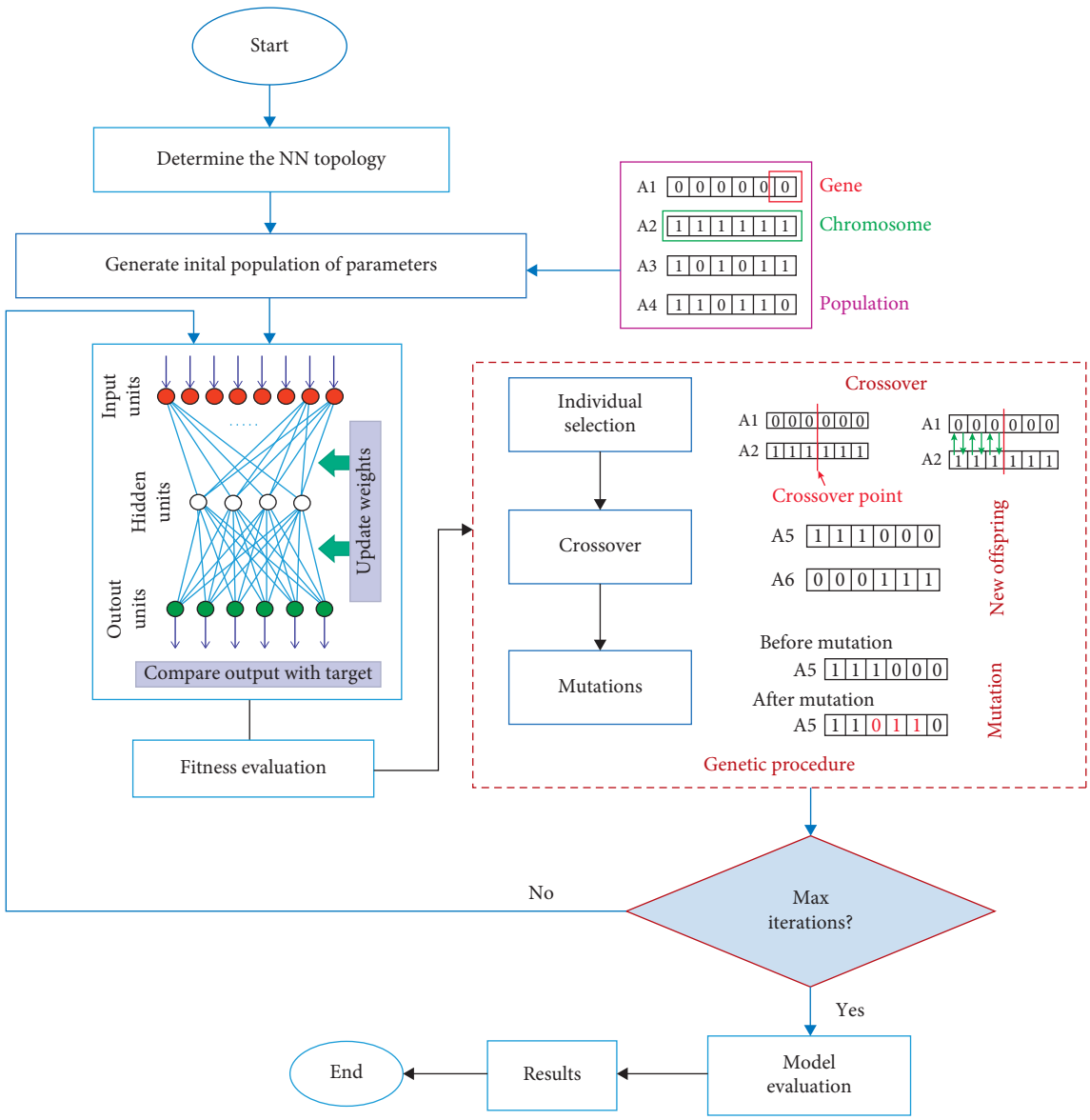

Figure 4: Flow diagram of ANN-GA model.

Step 2: generate an initial random population of parameters. Then perform the following steps until reaching the maximum number of iterations:

Step 2.1: calculate the fitness value by applying the fitness function on each individual in the population.
Step 2.2: update the network parameters (w_{ij} and b_i) based on the lowest error E.
Step 2.3: generate a new population through performing GA operations: selection, crossover, and mutation.

Step 3: obtain the optimal value of parameters from the last population

Step 4: train NN by PB training procedure (updating final weight and bias).

Step 5: evaluate the performance of NN using testing data. If the error is acceptable, stop and return the optimal model; otherwise, change the network topology (number of hidden layer's neurons) and return to step 1.

4.2. RF-Grid. Grid search is a traditional way for performing hyperparameters optimization for ML models. It is simply an exhaustive search method that sets up a grid of the possible values of the hyperparameters (Figure 5) and trains a model for each of the combinations [48]. In this method, all the possible combinations of the data are tried and tested using k-fold cross-validation technique.

Random forest (RF) is one of the most potent ensemble learning techniques developed by Breiman in 2001 [49] to solve different regression, classification, and clustering problem, and it exhibited excellent performance in many fields [50–52].

Despite the advantages of decision trees of its simplicity, ease of use, and interpretability [53, 54], it has many

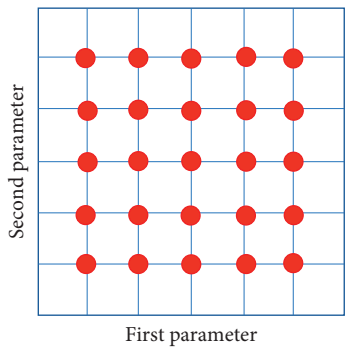

Figure 5: Grid search method.

limitations, such as their suboptimal performance and lack of robustness. Therefore, RF can overcome the limitations of traditional decision trees by combining the performance of many randomized, decorrelated decision trees to predict or classify the variable to a specific class. RF is a boosting technique in which it boosted the performance of a number of decision trees via a voting scheme. An example of RF is shown in Figure 6 in which the forest consists of n trees and a voter.

Regarding the main advantages of RF in regression tasks, it includes (i) bootstrap resampling, (ii) random features selection, and (iii) out-of-bag error estimation.

Suppose there are n trees $T_1(X), T_2(X), \ldots, T_n(X)$, where $X = x_1, x_2, \ldots, x_m$ is a m-dimension vector of inputs. The prediction value of each decision tree is $\widehat{Y}_i = T_i(x)$. While the final prediction output Y results from aggregating the outputs of all randomly generated trees. The aggregation process is accomplished in the classification task by taking the majority votes, while in regression task, it is accomplished by taking the average:

$$Y = \sum_{i=1}^{n} \widehat{Y}_i(x) = \frac{1}{n} \sum_{i=1}^{n} T_i(x). \tag{1}$$

The RF algorithm can be summarized as follows [55, 56]:

(i) Generate n number of trees by selecting randomly different bootstrap samples from the training data. The out-of-bag samples are the samples that are not selected.

(ii) For each bootstrap sample, grow a full decision tree to the maximum size without pruning. In splitting the nodes of the tree, a specific number of features were selected randomly instead of choosing all features (this refers to a random feature selection).

(iii) Repeat step 2 until forming a randomly generated forest consisting of n decision trees.

(iv) Predict the new data by applying the n trees and aggregate the results.

In this section, the grid search algorithm was used to optimize the RF algorithm by tuning the hyperparameters of it. The primary hyperparameters of RF that affect its performance are (1) the number of trees in the forest that must be generated before taking the maximum voting or average of predictions and (2) the maximum number of features to split in each node of the tree. The hybrid structure of RF and grid search was considered in the following steps (Figure 7):

(i) Step 1: define RF searching parameters range: maximum value, minimum value, and step size.

(ii) Step 2: build the grid search space on the coordinate system.

(iii) Step 3: build the RF models using all possible combinations of parameters and evaluate the performance of RF.

(iv) Step 4: return the multiple set of optimal parameters.

(v) Step 5: if the accuracy is satisfied, stop and return the optimal parameters; otherwise go to step 6.

(vi) Step 6: redefine the range of searching near the optimal parameters and reduce step size. Then, go to step 2.

(vii) Step 7: repeat steps 2–6 until the optimal hyperparameters values satisfying the accuracy were found.

(viii) Step 8: build RF forest model with the optimal parameters.

(ix) Step 9: predict the output value of data in testing set by RF model.

4.3. SVR-GA. Support vector regression (SVR) is introduced by Vapnik [57] as an extension of SVM for solving the regression problem. SVR is a very useful tool for prediction because of its ability to map nonlinear data space into a higher dimensional feature space [58].

Consider a learning dataset defined as $\{x_i, y_i\}$ $(i = 1, \ldots, n)$, where $x_i \in R^n$ is the input vector and $y_i \in R$ is its corresponding output vector. The main objective of SVR is to deduce the regression function $f(x)$ that describes the relationship between the input data x and the target output y with an error value that is less than epsilon ε deviation for all training data.

The SVR function can be written as follows [59]:

$$f(x) = w^T \varphi(x) + b, \tag{2}$$

where $f(x)$ is the computed output of x, $\varphi(x)$ is the nonlinear feature mapping function of inputs, and w and b are adjustable coefficients that represent the weight vector and intercept vector, respectively. The training of SVR is to find w and b values by minimizing the upper bound of the regression error.

Therefore, SVR is considered as an optimization problem that tries to make the regression function $f(x)$ as flat as possible by minimizing the value of w, which necessitates the minimization of Euclidean norm, that is, $\|w\|^2$.

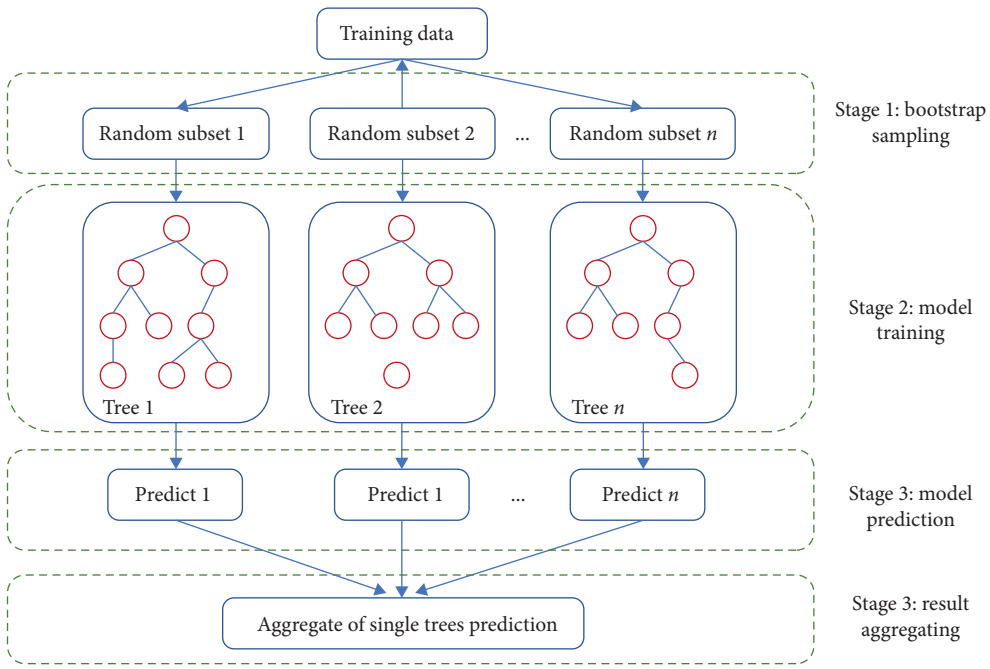

Figure 6: Example of random forest (RF) algorithm.

The optimization problem that is used to identify the regression problem is given as follows:

$$\begin{aligned} &\text{minimize} \quad \frac{1}{2}\|w\|^2 \\ &\text{subject to} \quad \begin{aligned} &y_i - w^T\varphi(x) - b \le \varepsilon \\ &-y_i + w^T\varphi(x) + b \le \varepsilon. \end{aligned} \end{aligned} \tag{3}$$

The preceding equation applies if there is function $f(x)$ which approximates all pairs of (x_i, y_i) with an accuracy of ε. Besides, some mistakes that violate the conditions above are introduced. The inaccessible limitations of the optimization problem are addressed by the slack variables ξ_i and ξ_i^*. Equation (2) can, therefore, be rewritten as explained as follows:

$$\begin{aligned} &\text{minimize} \quad \frac{1}{2}\|w\|^2 + C\sum_{i=1}^{l}(\xi_i + \xi_i^*) \\ &\text{subject to} \quad \begin{aligned} &y_i - w^T\varphi(x) - b \le \varepsilon + \xi_i \\ &-y_i + w^T\varphi(x) + b \le \varepsilon + \xi_i^*, \\ &\xi_i, \xi_i^* \ge 0, \quad i = 1, 2, \ldots, n, \end{aligned} \end{aligned} \tag{4}$$

where C is defined as a nonnegative constant which expresses the box constraint that is responsible for monitoring data points above the ε-insensitive error range and which is also helpful when avoiding overfitting problems [58]. There are several commonly used kernel types in SVR that convert the nonlinear function in equation (1) into higher dimensional space. The radial basis function (RBF) has been widely used in previous studies [5, 60]:

$$\begin{aligned} f(x) &= w^T K(x, x_i) + b, \\ K(x, x_i) &= \exp\left(-\frac{|x - x_i|^2}{2\gamma^2}\right), \end{aligned} \tag{5}$$

where $K(x, x_i)$ is the kernel function and γ is the width parameter.

The performance of the SVR model depends on the hyperparameter tuning of the model: the regularization parameter (C), the epsilon (ε), and the kernel parameter (γ). These parameter values affect the performance of the model incredibly, in which the influence of these parameter values is presented as follows. The value of the first parameter (i.e., regularization parameter, also called box constraints) is used to decide the penalty of the approximation function. It must not be very small or large. If it is too small (large), it will cause underfitting (overfitting). In contrast, the decision boundary's maximum margin is controlled by the insensitivity loss function (ε). Finally, the kernel function controls the ability to make the model for dealing with nonlinear function responsible for transforming the nonlinear function into a more suitable function [61, 62].

Many researches were conducted to tune the hyperparameters of SVR using manual or grid search [63, 64]. However, this approach's complexity is increased incredibly when the width of the search space is increased. Also, this approach does not always get the best hyperparameter values for the model. Other approaches have been inspired to overcome these limitations, that is, the genetic algorithm (GA). GA is considered one of the power optimization algorithms proposed by Holland in 1975 and inspired by Darwin's theory. In this section, GA is inspired and used to find the hyperparameter of SVR. The proceeding procedure

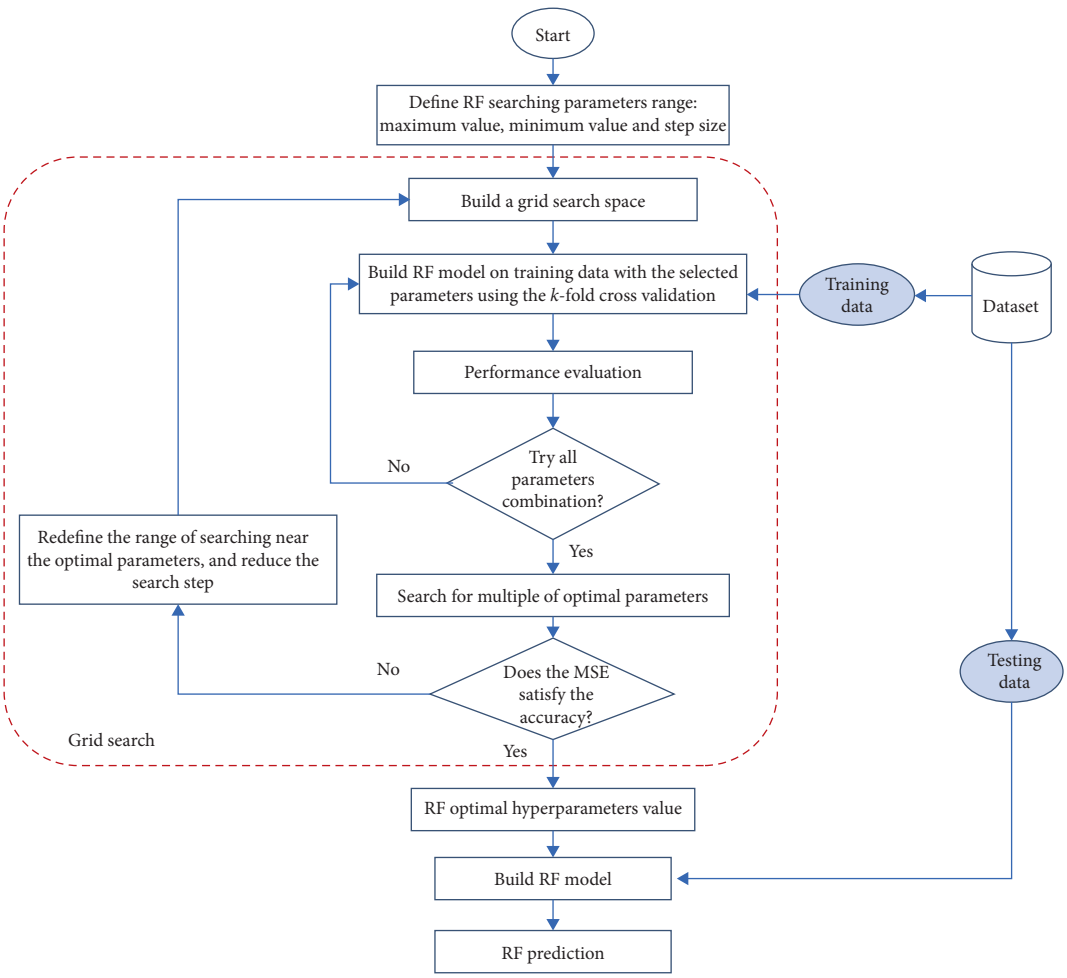

Figure 7: Flowchart of RF-grid model.

of optimizing SVR hyperparameters using GA was illustrated in Figure 8, and the steps involved are summarized as follows:

Step 1: initialize the SVR parameters (ε, C) and the kernel parameters γ. Code these parameters to create a chromosome directly.

Step 2: initialize the GA parameters randomly: population size, number of generations, mutation rate, and crossover rate.

Step 3: perform SVR model on training data using the k-fold cross validation.

Step 4: calculate the fitness value of each individual in the population according to the mean square error (MSE).

Step 5: generate new offspring parameters population through selection, crossover, and mutation.

Step 6: repeat steps 4-5 until ε, C, γ are satisfied with minimal error; otherwise, continue to optimize.

Step 7: output the optimal parameters found at the end of the generation. Train SVR model with these parameters

Step 8: predict the out of data in the testing dataset part by SVR model.

4.4. SVR-Grid. In this section, the grid search algorithm is used to obtain the optimal values of the SVR parameters (ε, C, and g). The grid search algorithm is based on trying all possible values of the parameters in a given space with a specified step distance. The cross-validation technique [65] derives the SVR model's parameters that improve its performance with the best accuracy.

The hybrid structure of SVR optimized by grid search is illustrated through a flowchart, as shown in Figure 9, and consists of the following steps:

Step 1: define the range of SVR searching parameters.

Step 2: initialize the values of the parameters and step distance.

Step 3: split dataset into two sets (training and testing sets)

Step 4: train SVR model using k-fold cross validation on the training dataset.

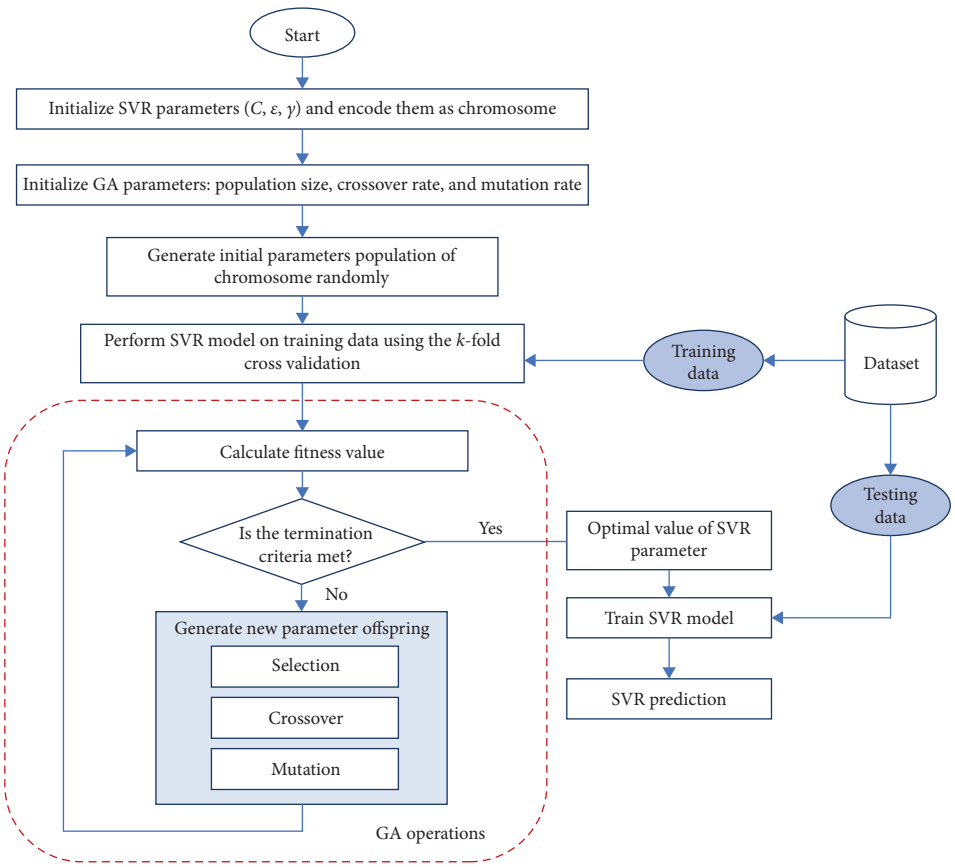

Figure 8: The flowchart of SVR-GA model.

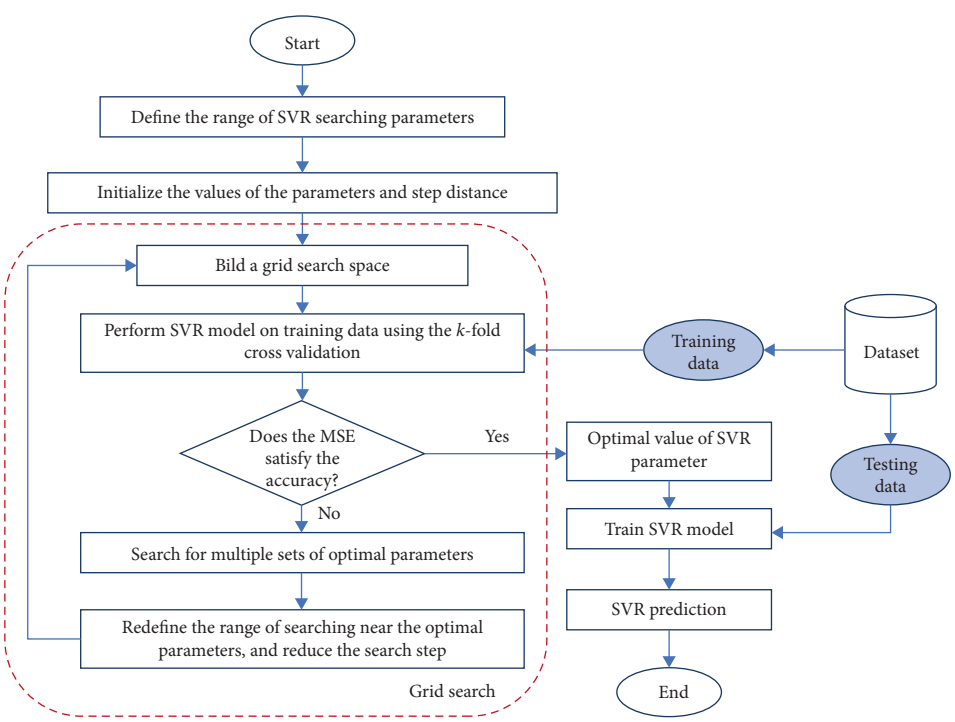

Figure 9: The flowchart of SVR-grid model.

Step 5: if the MSE satisfies the accuracy, then select the sets of parameters with the minimum MSE; otherwise, continue the optimize and go to step 5.

Step 6: search for multiple sets of optimal parameters.

Step 7: redefine the range of searching near the optimal parameters and reduce the search step; then go to step 4.

5. Data Analysis and Results

5.1. Model Performance Evaluation Using Statistical Indices. The effectiveness of the proposed modeling techniques was examined by comparing the forecasted river flow with the observed river flow data. It should be noted that the data used in this investigation was continuous and without any missing value.

The performance of the models in forecasting river flow one month ahead was forecasted and evaluated using several statistical metrics. Five statistical metrics were used to measure the performance of the predictive models in forecasting river flow during model testing, namely, Mean Error (ME), Root Mean Square Error (RMSE), Mean Absolute Error (MAE), Mean Percentage Error (MPE), Mean Absolute Percentage Error (MAPE), and Coefficient of Determination (R^2) [66, 67]. These statistical metrics were widely used by researchers to evaluate the performance of predictive models in hydrological and machine learning models [68]. These measurements are considered a good indicator of the accuracy and robustness of the model:

$$\begin{aligned}
\mathrm{ME} &= \frac{\sum_{i=1}^{N} y_o - y_p}{N}, \\
\mathrm{RMSE} &= \sqrt{\sum_{i=1}^{N} \frac{\left(y_o - y_p\right)^2}{N}}, \\
\mathrm{MAE} &= \frac{\sum_{i=1}^{N} \left|y_o - y_p\right|}{N}, \\
\mathrm{MPE} &= \frac{1}{N} \sum_{i=1}^{N} \frac{y_o - y_p}{y_o}, \\
\mathrm{MAPE} &= \frac{1}{N} \sum_{i=1}^{N} \frac{\left|y_o - y_p\right|}{y_o}, \\
R^2 &= \left(\frac{\sum_{i=1}^{N} \left(y_o - \ddot{y}_o\right) \sum_{i=1}^{N} \left(y_p - \ddot{y}_p\right)}{\sqrt{\sum_{i=1}^{N} \left(y_o - \ddot{y}_o\right)^2 \sum_{i=1}^{N} \left(y_p - \ddot{y}_p\right)^2}} \right)^2,
\end{aligned} \tag{6}$$

where N is the length of the testing data set. y_o and y_p are the actual and forecasted river flow data. $\ddot{y}_o$ and $\ddot{y}_p$ are the mean values of the actual and forecasted river flow data.

Tables 1–3 present the statistical performance indicators (i.e., ME, RMSE, MAE, MPE, MAPE, and R^2) for the five constructed input combinations, training and testing phases, and the three data division scenarios. The tables showed that all the four hybrid ML models (ANN-GA, SVR-GA, Grid-SVR, and Grid-RF) are performed in a general good performance. However, they are varied from one input combination to another. That totally depends on the historical data memory provided by the lead time "antecedent river flow values." A notable enhancement is achieved using the hybridized SVR-GA which collaborates with the findings of several other studies established over the literature within hydrological engineering [69–72]. It is observed that the data division plays an essential role in the learning process of the developed ML models. Apparently, increasing the span of the training phase contributes to model predictability enhancement. In quantitative terms, the best results of forecasting are attained for the SVR-GA with (RMSE = 0.04, MAE = 0.03, and $R^2 = 0.95$). The SVR-GA model indicated boosting in forecasting accuracy; although, the other ML models obtained a reasonable prediction accuracy. This observation approved the capacity of the hybrid SVR-GA model to solve the complexity of river flow located in semiarid environment. The Coefficient of Determination (R^2) was achieved more than 0.90 for almost all the input combinations over the using the SVR-GA model although the performance of the SVR-GA model over the training phase was not superior (Table 3). This can explain the feasibility of the SVR-GA to be more potent.

5.2. Models Graphical Evaluation. Two different graphical presentations are hereby presented for the evaluation of the performance of the proposed models. The actual and the forecasted values of the river flow for Tigris River are presented using scatter plots and Taylor diagram. The scatter plots for the three modeling scenarios of data division (70%–30%, 80%–20, and 90%–10%) and the four developed ML models (ANN-GA, SVR-GA, Grid-SVR, and Grid-RF) are illustrated in Figures 10–12. It can be clearly observed that the 90%–10% data division scenario using the SVR-GA model attained the best match between the observed and forecasted river based on four-month antecedent values. For this particular data division and based on this lead time, the observed and the forecasted values by all the models were found to follow the similar trends. However, the matching between the observed and the forecasted values was found to be the best for SVR-GA model. To assess the efficacy of the models, it was justifiable to investigate the linear relationship between the time series of observed and the forecasted river flows for the testing period. The uniformity plot of river flow forecasted by SVR-GA attained the maximum determination coefficient ($R^2 = 0.96$).

Another graphical presentation that was investigated for the applied predictive models was Taylor diagram [73] (Figures 13–15). It is a distinguished two-dimension graphical presentation that accompanied three statistical metrics including RMSE, correlation, and standard deviation. In harmony with the presented statistical results and the scatter plot presentation, using four-month lead time predictors for the one month ahead river flow, the SVR-GA model indicated the best forecasting value owing to the location of the model results on the Taylor map for the 90%–10% data division scenario.

Table 1: The statistical performance metrics for the developed hybrid ML models over the 70–30% modeling data division scenario.

	ME	RMSE	MAE	MPE	MAPE	R^2
Model I						
			Training phase			
ANN-GA	59.32	256.43	175.66	−1261.38	1549.29	0.63
SVR-GA	10.34	247.05	154.56	−862.91	1285.20	0.68
Grid-RF	−2.33	123.24	77.09	−264.95	527.544	0.92
Grid-SVR	−15.35	254.68	159.67	−576.68	1198.01	0.58
			Testing phase			
ANN-GA	66.05	205.10	163.48	−1632.74	1886.53	0.69
SVR-GA	7.83	157.47	124.27	−806.19	1270.95	0.78
Grid-RF	−3.25	138.48	108.65	−380.57	977.75	0.80
Grid-SVR	−5.68	128.32	91.09	−338.22	751.28	0.91
Model II						
			Training phase			
ANN-GA	−33.47	331.87	211.77	−1370.87	1938.01	0.46
SVR-GA	−10.54	235.56	142.34	−664.55	1183.01	0.72
Grid-RF	−7.59	116.75	71.18	205.18	490.95	0.93
Grid-SVR	−5.96	234.96	141.50	−516.18	1057.58	0.72
			Testing phase			
ANN-GA	13.75	194.68	137.36	−744.31	1242.38	0.56
SVR-GA	11.80	133.54	108.60	−506.76	941.08	0.79
Grid-RF	−14.79	160.42	119.92	−335.94	936.55	0.73
Grid-SVR	42.39	136.07	106.04	−782.93	1098.75	0.77
Model III						
			Training phase			
ANN-GA	−44.17	245.56	150.87	−218.53	921.87	0.65
SVR-GA	−9.11	236.37	143.78	−815.63	1334.09	0.72
Grid-RF	7.27	125.03	83.15	−454.79	921.87	0.91
Grid-SVR	−33.94	273.67	174.09	−862.27	1445.52	0.64
			Testing phase			
ANN-GA	21.40	164.3153	124.08	−856.11	1274.74	0.80
SVR-GA	27.02	142.074	115.56	−804.35	1138.05	0.87
Grid-RF	0.97	143.7111	110.28	−400.61	958.01	0.82
Grid-SVR	32.84	152.1099	105.33	−836.43	1173.84	0.38
Model IV						
			Training phase			
ANN-GA	21.40	164.36	124.08	−856.11	1274.74	0.67
SVR-GA	27.02	142.07	115.57	−804.35	1138.05	0.69
Grid-RF	9.78	143.711	110.28	−400.61	958.01	0.94
Grid-SVR	32.84	152.11	105.34	−836.43	1173.84	0.75
			Testing phase			
ANN-GA	21.40	164.31	124.09	−856.11	1274.74	0.79
SVR-GA	27.02	142.07	115.56	−804.35	1138.05	0.82
Grid-RF	9.78	143.71	110.28	−400.61	958.01	0.76
Grid-SVR	32.84	152.11	105.34	−836.43	1173.84	0.76
Model V						
			Training phase			
ANN-GA	−2.65	212.08	159.06	−318.12	1537.58	0.63
SVR-GA	−10.60	238.59	132.55	−583.22	1113.42	0.66
Grid-RF	−21.21	132.55	79.53	−397.65	662.75	0.9
Grid-SVR	−23.86	185.57	106.04	−371.14	901.34	0.83
			Testing phase			
ANN-GA	26.51	185.57	132.55	1166.44	1564.09	0.83
SVR-GA	18.56	159.06	106.04	−715.77	1086.91	0.83
Grid-RF	2.65	132.55	106.04	−450.67	954.36	0.67
Grid-SVR	−7.95	106.04	79.53	−212.08	715.77	0.75

The minimum instream environmental flow for the Tigris River was calculated on the basis of the SVR-GA model's mean forecast flow obtained during the dry season. The minimum environmental flow was 215.46 $m^3\ s^{-1}$ (based on 19.22 percent of the average flow 1121 $m^3\ s^{-1}$). This flow refers to the minimum instream environmental flow required to maintain the organisms in the river [13].

Table 2: The statistical performance metrics for the developed hybrid ML models over the 80–20% modeling data division scenario.

	ME	RMSE	MAE	MPE	MAPE	R^2
Model I						
			Training phase			
ANN-GA	−38.54	252.65	154.75	−363.45	1060.36	0.65
SVR-GA	−9.52	244.25	154.08	−766.23	1293.02	0.69
Grid-RF	32.83	256.13	170.43	−877.83	1365.77	0.65
Grid-SVR	−17.71	243.98	151.04	−531.12	1127.40	0.66
			Testing phase			
ANN-GA	27.193	199.25	154.61	−394.37	767.53	0.84
SVR-GA	38.94	198.88	157.71	−585.79	952.09	0.72
Grid-RF	28.12	209.33	168.85	−577.06	1064.34	0.76
Grid-SVR	6.38	187.98	145.17	−531.11	779.82	0.89
Model II						
			Training phase			
ANN-GA	11.19	244.34	152.65	−2214.68	1275.26	0.66
SVR-GA	16.59	237.26	148.64	−2134.11	2628.70	0.685
Grid-RF	14.91	251.78	152.43	−736.97	1441.17	0.66
Grid-SVR	−11.58	228.31	135.41	−1862.16	2420.91	0.72
			Testing phase			
ANN-GA	21.89	154.13	118.15	−682.55	1102.56	0.80
SVR-GA	33.23	134.97	113.16	−1104.83	1417.38	0.83
Grid-RF	26.17	140.25	109.19	−578.82	1000.16	0.65
Grid-SVR	6.38	187.98	145.17	−531.12	779.825	0.75
Model III						
			Training phase			
ANN-GA	30.35	247.37	163.25	−1009.14	1386.72	0.67
SVR-GA	3.59	235.55	147.26	−761.82	1255.21	0.69
Grid-RF	−2.70	155.95	99.25	−536.86	855.20	0.86
Grid-SVR	−31.80	268.65	169.28	−800.78	1380.50	0.62
			Testing phase			
ANN-GA	93.78	154.59	124.46	−1037.85	1178.38	0.45
SVR-GA	23.51	142.13	112.42	−723.81	1071.39	0.80
Grid-RF	35.81	126.91	102.84	−662.98	966.92	0.81
Grid-SVR	18.62	135.36	96.18	−800.78	1176.49	0.54
Model IV						
			Training phase			
ANN-GA	−113.06	269.44	171.97	432.71	994.68	0.61
SVR-GA	−6.04	236.42	149.41	−800.34	1333.56	0.66
Grid-RF	−2.23	130.28	78.18	−436.18	686.68	0.90
Grid-SVR	−54.99	303.65	191.10	−950.77	1615.86	0.51
			Testing phase			
ANN-GA	−72.62	139.88	115.74	423.35	1070.50	0.71
SVR-GA	12.64	113.96	92.45	−420.64	749.46	0.92
Grid-RF	−26.20	153.04	118.39	−217.54	862.89	0.81
Grid-SVR	33.19	125.64	97.16	−926.32	1208.60	0.65
Model V						
			Training phase			
ANN-GA	−24.92	230.48	141.42	−642.60	1227.55	0.72
SVR-GA	−15.24	230.22	143.09	−631.34	1192.60	0.71
Grid-RF	−5.14	142.65	83.66	−317.06	592.59	0.89
Grid-SVR	−22.75	176.60	106.58	−330.21	860.40	0.83
			Testing phase			
ANN-GA	−38.02	149.35	119.27	−53.29	793.33	0.64
SVR-GA	23.04	138.42	105.01	−616.43	1093.90	0.74
Grid-RF	9.44	145.23	95.98	−469.15	896.69	0.44
Grid-SVR	17.41	133.36	94.31	−723.81	1214.13	0.55

Table 3: The statistical performance metrics for the developed hybrid ML models over the 90–10% modeling data division scenario.

	ME	RMSE	MAE	MPE	MAPE	R^2
Model I						
			Training phase			
ANN-GA	−43.82	250.85	156.29	−521.03	1181.23	0.64
SVR-GA	−8.58	234.82	148.27	−629.26	1166.91	0.67
Grid-RF	14.09	234.43	151.84	−822.16	1297.23	0.69
Grid-SVR	−15.84	233.79	146.80	−656.04	1215.01	0.69
			Testing phase			
ANN-GA	10.08	106.21	82.72	−312.59	684.22	0.88
SVR-GA	16.46	100.58	81.27	−954.43	1332.15	0.92
Grid-RF	18.98	84.577	71.86	−275.80	622.07	0.79
Grid-SVR	16.46	100.58	81.27	−954.43	1332.15	0.92
Model II						
			Training phase			
ANN-GA	−71.45	244.98	150.23	−44.06	970.63	0.66
SVR-GA	5.20	229.71	147.46	−813.07	1290.19	0.69
Grid-RF	−3.26	138.91	84.65	−404.59	718.67	0.89
Grid-SVR	−7.78	221.91	134.74	−627.86	1156.57	0.73
			Testing phase			
ANN-GA	−27.24	110.15	79.18	19.78	657.83	0.61
SVR-GA	44.15	106.22	85.60	−754.08	977.85	0.91
Grid-RF	16.26	116.19	91.95	−757.04	1163.95	0.77
Grid-SVR	40.57	75.62	64.78	−710.36	894.09	0.71
Model III						
			Training phase			
ANN-GA	−28.96	279.03	173.82	−901.58	1455.28	0.55
SVR-GA	7.97	231.47	148.60	−839.83	1316.29	0.70
Grid-RF	−6.04	143.03	89.34	−459.07	769.44	0.88
Grid-SVR	−42.45	266.44	165.71	−734.56	1350.49	0.59
			Testing phase			
ANN-GA	29.79	147.39	116.93	−889.74	1306.29	0.71
SVR-GA	48.075	88.21	72.67	−703.78	841.28	0.67
Grid-RF	−20.47	100.62	79.93	−18.08	592.86	0.71
Grid-SVR	−7.54	96.34	76.34	−483.47	931.94	0.75
Model IV						
			Training phase			
ANN-GA	−26.51	238.59	159.06	−503.69	1219.46	0.66
SVR-GA	−2.65	212.08	132.55	−715.77	1245.97	0.66
Grid-RF	−10.60	132.55	79.53	−371.14	689.26	0.89
Grid-SVR	−31.81	238.59	185.57	−477.18	1272.48	0.61
			Testing phase			
ANN-GA	−13.55	140.20	116.22	−583.19	1233.32	0.86
SVR-GA	−14.73	100.78	81.585	−214.02	670.30	0.96
Grid-RF	16.86	85.65	76.07	−375.48	739.69	0.83
Grid-SVR	17.86	82.19	62.39	−675.72	751.89	0.63
Model V						
			Training phase			
ANN-GA	−74.23	238.59	159.06	−291.61	1139.93	0.66
SVR-GA	−13.25	212.08	132.55	−715.77	1245.97	0.70
Grid-RF	−10.60	132.55	79.53	−397.65	662.75	0.90
Grid-SVR	−15.91	185.57	106.04	−556.71	1086.91	0.79
			Testing phase			
ANN-GA	7.953	106.04	79.53	−1113.42	1537.58	0.82
SVR-GA	10.604	79.53	53.02	−238.59	636.24	0.93
Grid-RF	−15.906	106.04	79.53	−212.08	715.77	0.50
Grid-SVR	5.302	87.48	106.04	−291.61	768.79	0.74

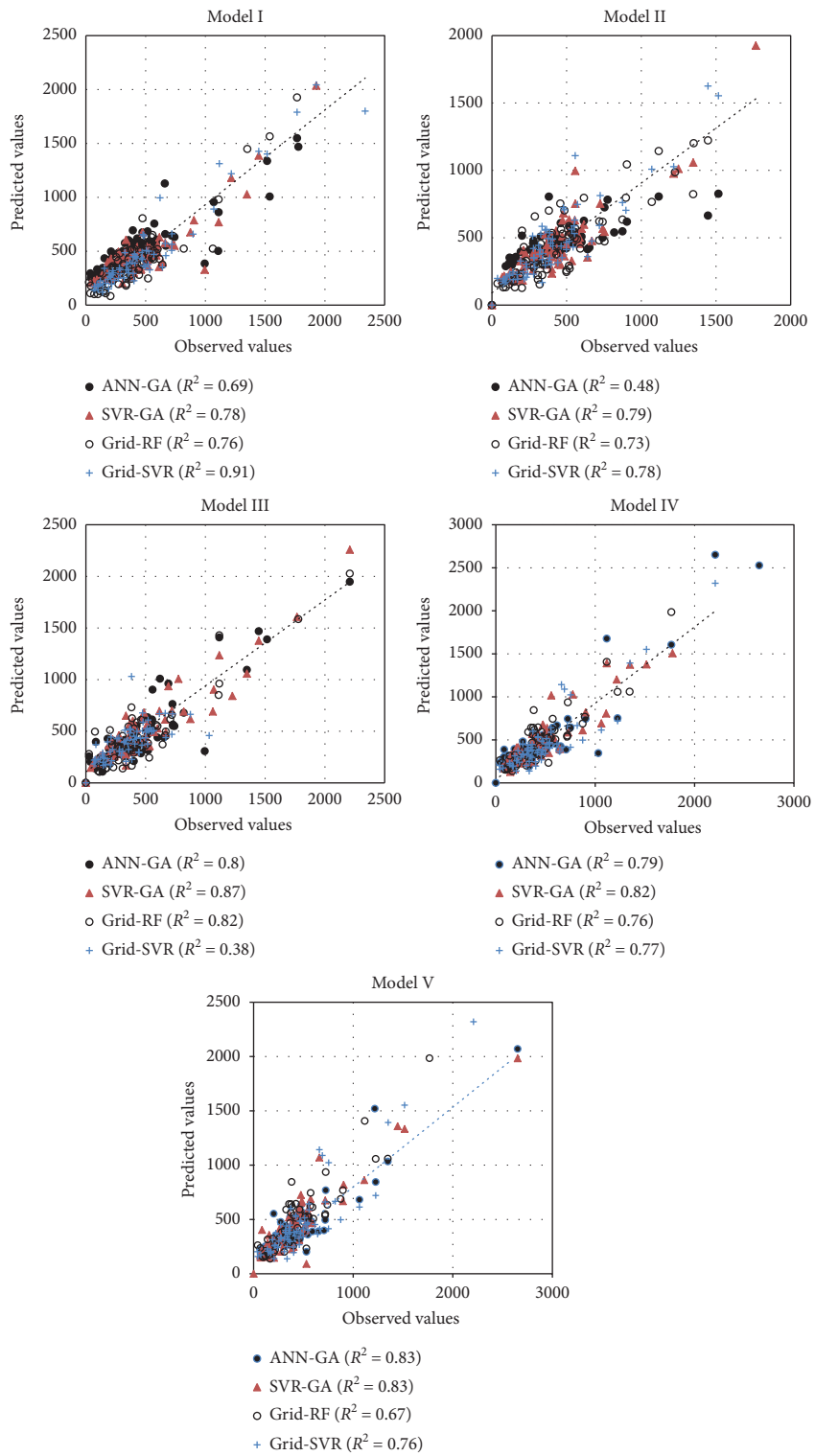

Figure 10: The scatter plot between the observed and forecasted river flow using the developed ML models and for the modeling scenario data division (70%–30%).

6. Discussion and Possible Future Research Directions

The results indicate that the proposed hybrid ML models can provide high accuracy in forecasting river flows for the studied Tigris River where the variability of river flow is less. Among all the developed four models, it was noticed that SVR-GA was superior to the other models. The model revealed the ability to solve complex process related to engineering problem. SVR-GA achieved a high Coefficient

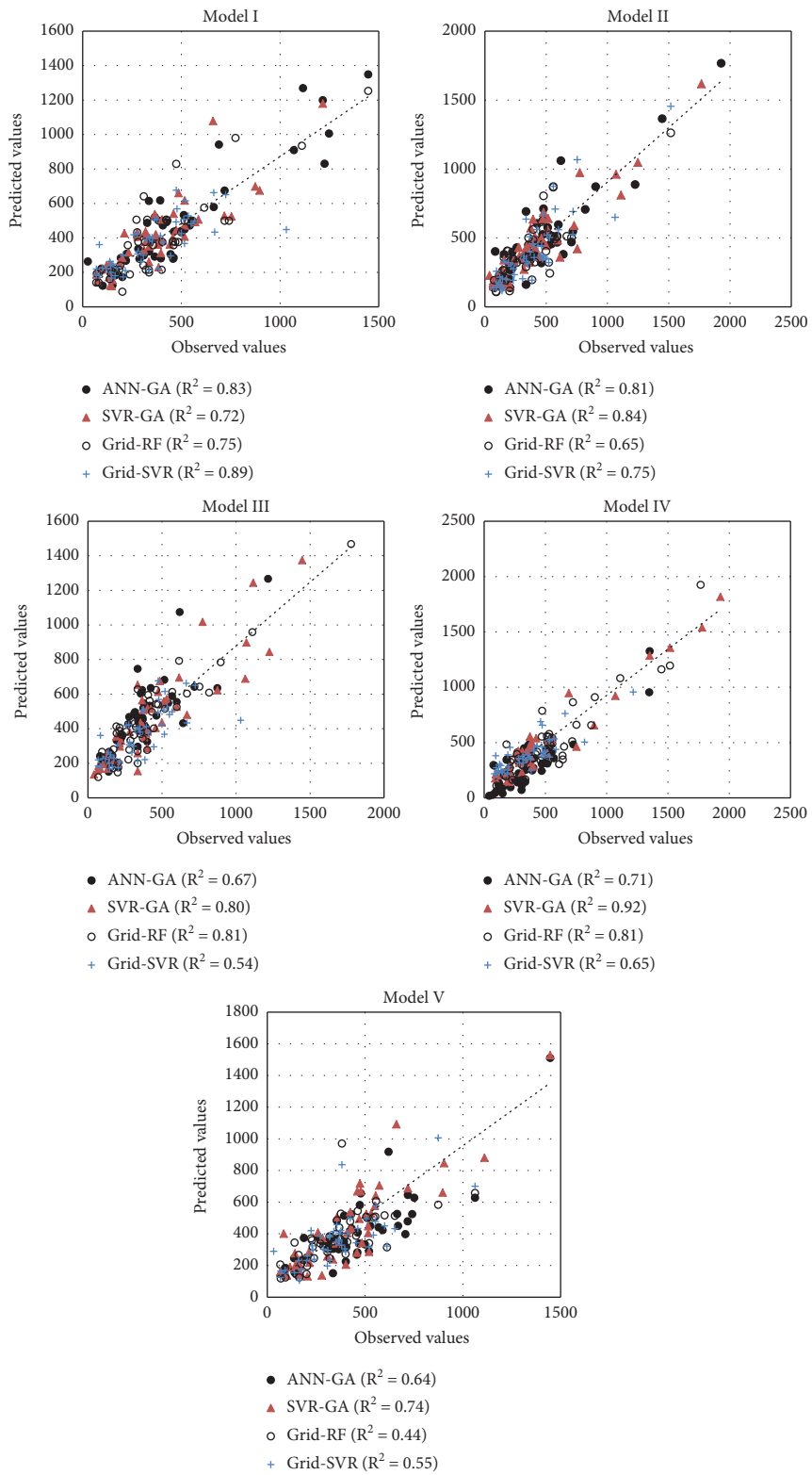

Figure 11: The scatter plot between the observed and forecasted river flow using the developed ML models and for the modeling scenario data division (80%–20%).

of Determination for almost all the input combinations for streamflow forecasting. It can be concluded that SVR-GA has the potential to deal with dynamics and chaotic environment with high accuracy in forecasting process.

In the current study, a type of forecasting is based on univariate modeling procedure where only river flow historical data was intercepted in the model development. In such case, it is suggested to use other variables such as

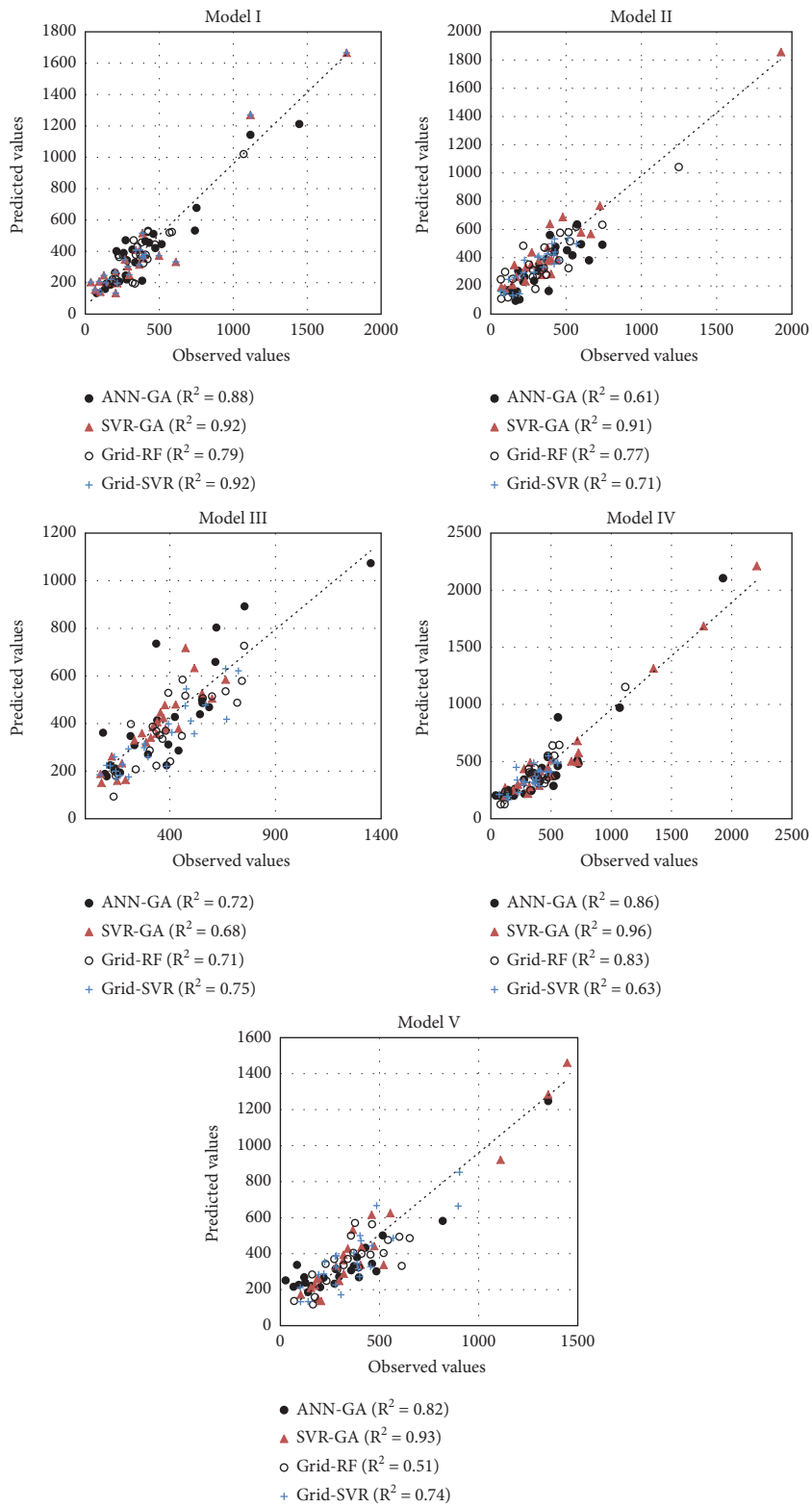

Figure 12: The scatter plot between the observed and forecasted river flow using the developed ML models and for the modeling scenario data division (90%–10%).

rainfall, humidity, temperature, or even evaporation rate to have a strong relationship with river flow. However, it is worth highlighting that the proposed models demonstrated an efficient soft computing model to capture the actual trend of the river flow time series. This is highly essential for several water and environmental engineering applications and particularly for management and monitoring of flooding and mitigations events.

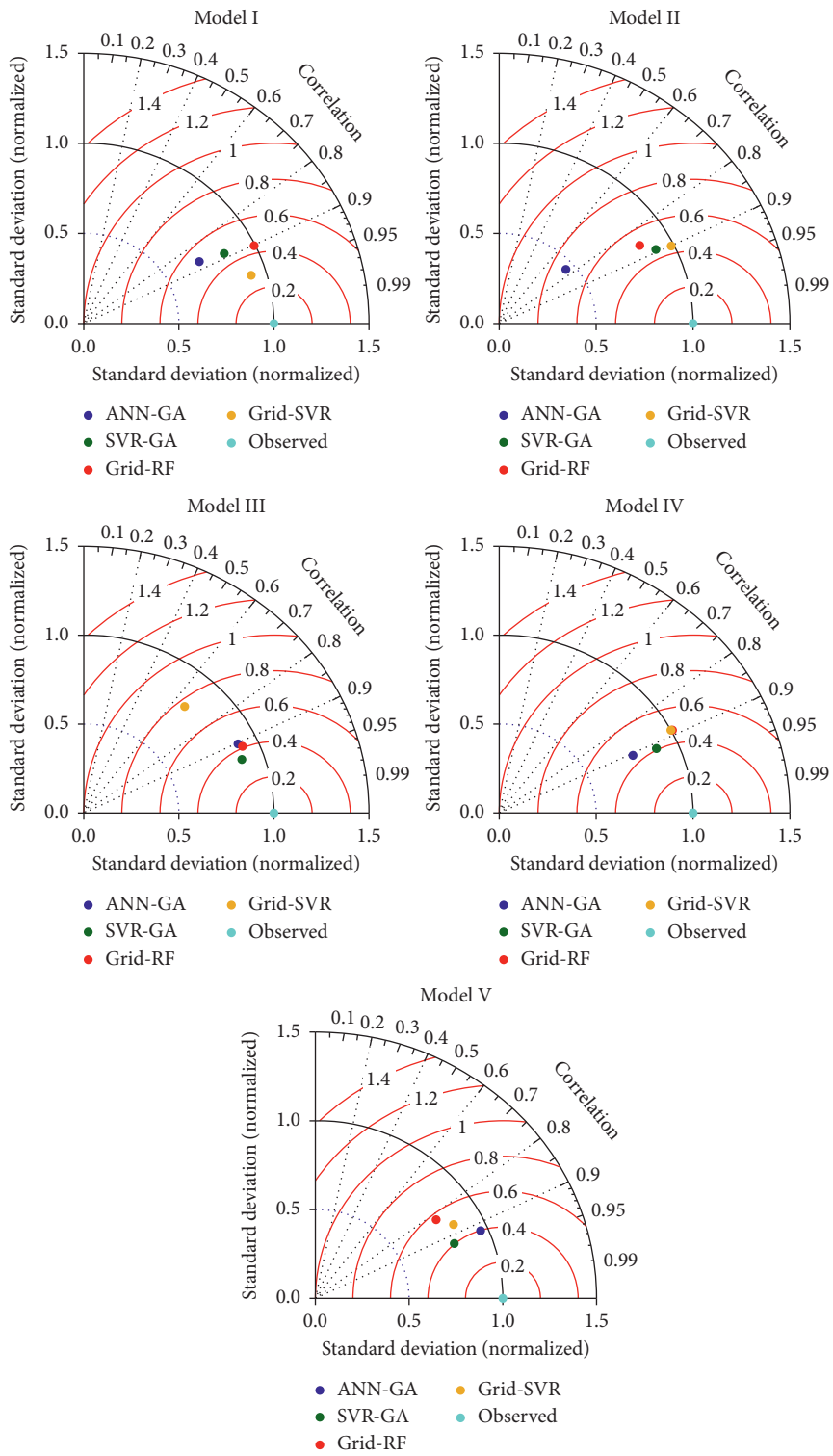

Figure 13: The Taylor diagram of the developed ML models and for the modeling scenario data division (70%–30%).

Based on the reported results, it was observed that using 20-year river flow data is sufficient for the development of the forecasting model. However, the length of the data span used for the modeling learning process has a considerable effect on the accuracy of model performance. Therefore, this is the essential finding of the hypotheses data division scenarios on the capacity of the machine learning models. Indeed, serious attention should be given in selecting the length of data for training the models. Selecting the length of data in an appropriate way reduces underfitting and helps the modeler to choose the best size of training data. This is due to the fact that the training stage should experience the majority of river flow

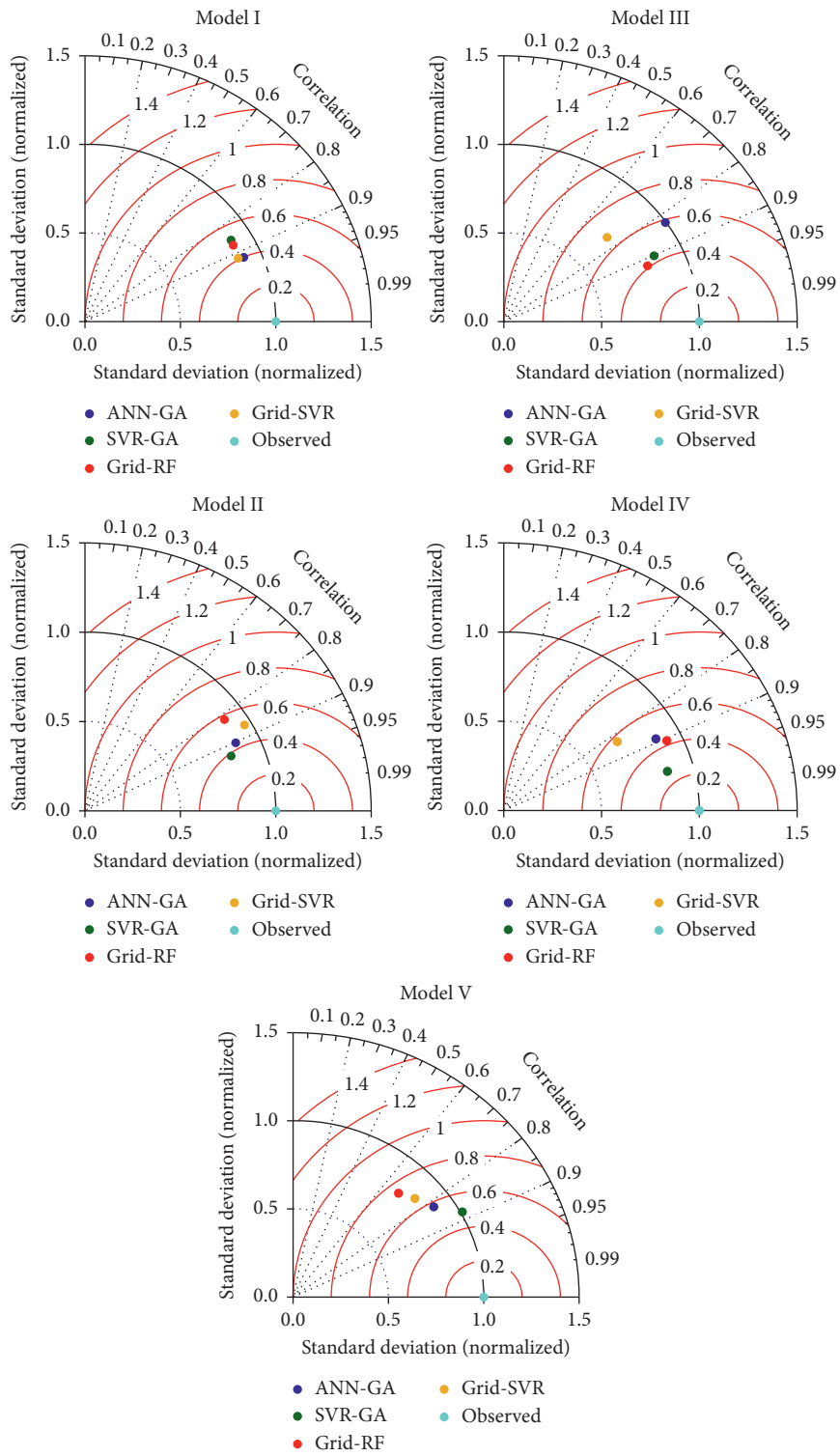

Figure 14: The Taylor diagram of the developed ML models and for the modeling scenario data division (80%–20%).

patterns to allow the models in the testing session to forecast river flow with an acceptable level of accuracy. The present study indicates that 20-year river flow data is enough to provide an acceptable accuracy in forecasting river flow.

Another significant aspect which can improve the predictability of the applied predictive models is the optimum selection of the lead times correlated to the targeted variable. Mutual information (MI) statistical approach potentially can be integrated as a prior stage of the forecasting model development process to abstract the highly associated information. The approach is based on the information theory and the notion of entropy [74].

It is worth highlighting that there is a need to extract the highly correlated features (the correlated lead times)

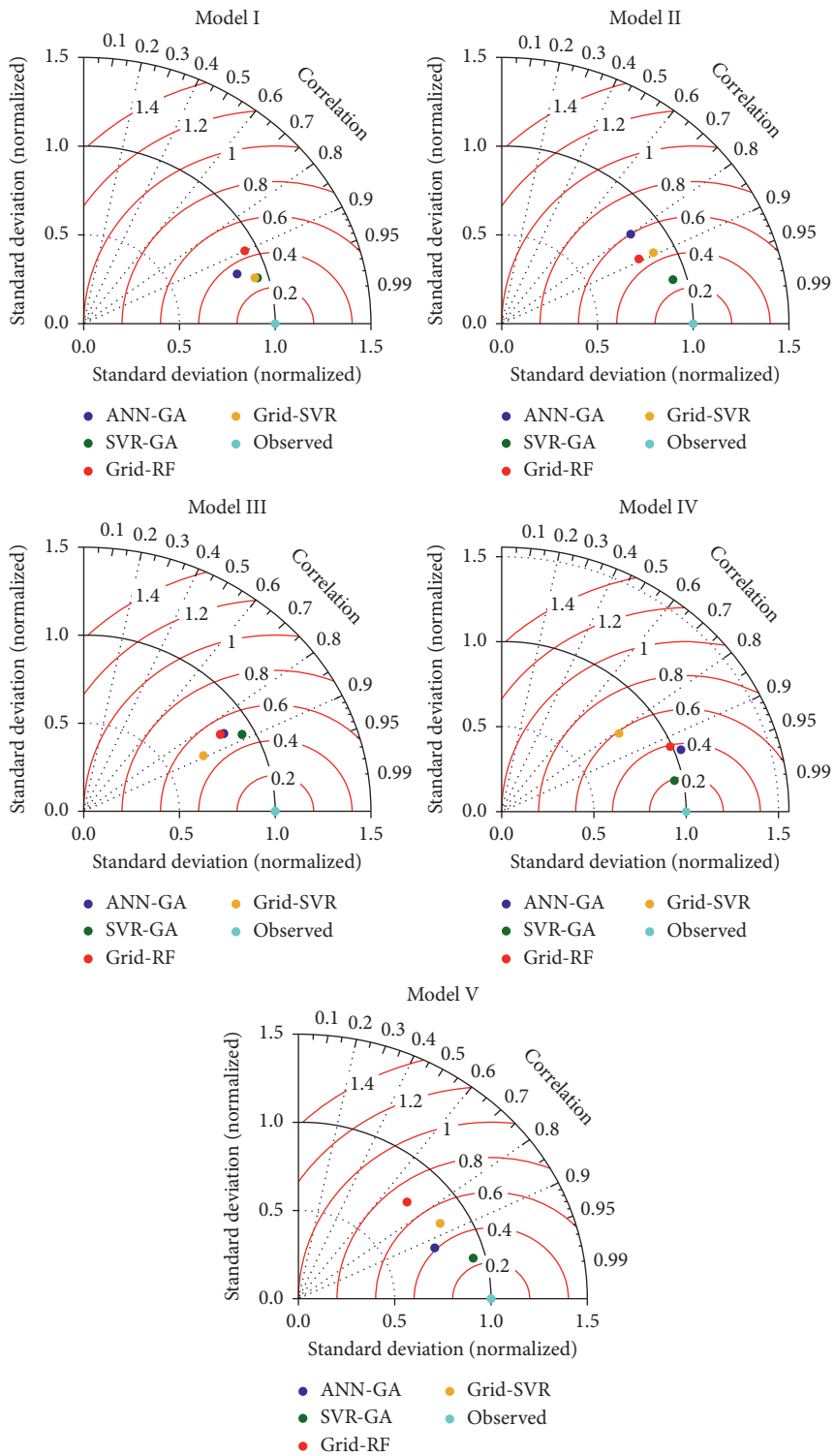

Figure 15: The Taylor diagram of the developed ML models and for the modeling scenario data division (90%–10%).

for the development of similar developed hybrid machine learning. Hence, the deep learning model has the advantage of deploying the hidden layers to automatically extract the features. The hydrological process is linked to typical time-sequential data [75] and therefore, the forecasting of hydrological time series is based on a fixed number of previous steps selected based on correlation. For such a case, deep learning model can be trained to learn time-varying or sequential patterns by facilitating time delay units through feedback connections for the selection of antecedent values as input. The suitability of the deep learning model for hydrological application relies on its capability of providing accurate and timely time-series prediction in the systems.

7. Conclusion

The motivation for the current research was to forecast monthly river flow in semiarid environment. Four hybrid ML models (i.e., ANN-GA, SVR-GA, Grid-SVR, and Grid-RF) were developed for this purpose. Three data division modeling scenarios (i.e., 70%–30%, 80%–20, and 90%–10%) were proposed and inspected for the model's performance predictability. The architecture of the applied ML models was established based on several antecedent values of the river flow in accordance with the correlation analysis. The performance of the models was assessed using a number of numerical skill indicators and graphical presentations. In general, the results demonstrated that the SVR-GA model achieved the highest ability in forecasting monthly river flow with significant accuracy. Therefore, it is possible to improve the river flow forecasting ability using the proposed hybrid machine learning model. In addition, the results indicated that building the predictive based on 90%–10% training-testing dataset attained better prediction capability. The results indicated that using 20 years of river flow data is sufficient for the development of the forecasting model. The study concluded that the size of the training data has a significant effect on the accuracy of the predicted model. The study revealed that the data division has an important role in the learning process of the developed ML models. The results demonstrated that increasing the span of the training phase can enhance the accuracy of model performance. The current research is possible to be further extended for the forecasting enhancement of river flow by including more information on river flow patterns through the inclusion of climate parameters such as rainfall, humidity, and temperature as an input. The models in the present study were developed for the forecasting of only one-step-ahead river flow. However, multiple-month ahead forecasting models are important for water resources planning and management. Although the success of SVR-GA model in forecasting one-step-ahead river flow indicates its capability in longer time-step ahead river flow forecasting, it is still necessary to examine the ability of SVR-GA model in multiple-month ahead forecasting. The study recommended using mutual information (MI) statistical approach as a prior stage of the forecasting model development process to extract the highly associated information.

Data Availability

The data used in the study are available upon request from the corresponding author.

Conflicts of Interest

The authors have no conflicts of interest to declare.

Acknowledgments

This study was funded by theLulea University of Technology. In addition, the authors acknowledge the support received from the Key Research and Development Program in Shaanxi Province (2020GY-078).

References

[1] J. Quilty and J. Adamowski, "A stochastic wavelet-based data-driven framework for forecasting uncertain multiscale hydrological and water resources processes," *Environmental Modelling & Software*, vol. 130, Article ID 104718, 2020.

[2] K. Lee, H. Gao, M. Huang, J. Sheffield, and X. Shi, "Development and application of improved long-term datasets of surface hydrology for Texas," *Advances in Meteorology*, vol. 2017, Article ID 8485130, 13 pages, 2017.

[3] M. Lefebvre and F. Bensalma, "An application of filtered renewal processes in hydrology," *International Journal of Engineering Mathematics*, vol. 2014, Article ID 593243, 9 pages, 2014.

[4] F. B. Hamzah, F. MohdHamzah, S. F. Mohd Razali, O. Jaafar, and N. AbdulJamil, "Imputation methods for recovering streamflow observation: a methodological review," *Cogent Environmental Science*, vol. 6, no. 1, 2020.

[5] Z. M. Yaseen, O. Kisi, and V. Demir, "Enhancing long-term streamflow forecasting and predicting using periodicity data component: application of artificial intelligence," *Water Resources Management*, vol. 30, no. 12, pp. 4125–4151, 2016.

[6] Z. M. Yaseen, S. R. Naganna, Z. Sa'adi et al., "Hourly river flow forecasting: application of emotional neural network versus multiple machine learning paradigms," *Water Resources Management*, vol. 34, no. 3, pp. 1075–1091, 2020.

[7] Z. Yaseen, W. H. M. W. Mohtar, A. M. S. Ameen et al., "Implementation of univariate paradigm for streamflow simulation using hybrid data-driven model: case study in tropical region," *IEEE Access*, vol. 7, pp. 74471–74481, 2019.

[8] A. H. El-Shafie and M. S. El-Manadely, "An integrated neural network stochastic dynamic programming model for optimizing the operation policy of Aswan High Dam," *Hydrology Research*, vol. 42, no. 1, pp. 50–67, 2011.

[9] H. Singh and A. Sankarasubramanian, "Systematic uncertainty reduction strategies for developing streamflow forecasts utilizing multiple climate models and hydrologic models," *Water Resources Research*, vol. 50, no. 2, pp. 1288–1307, 2014.

[10] M. Fu, T. Fan, Z. Ding, S. Q. Salih, N. Al-ansari, and Z. M. Yaseen, "Deep learning data-intelligence model based on adjusted forecasting window scale: application in daily streamflow simulation," *IEEE Access*, vol. 8, pp. 32632–32651, 2020.

[11] T. Asefa, M. Kemblowski, M. McKee, and A. Khalil, "Multi-time scale stream flow predictions: the support vector machines approach," *Journal of Hydrology*, vol. 318, no. 1–4, pp. 7–16, 2006.

[12] P. A. Kagoda, J. Ndiritu, C. Ntuli, and B. Mwaka, "Application of radial basis function neural networks to short-term streamflow forecasting," *Physics and Chemistry of the Earth, Parts A/B/C*, vol. 35, no. 13-14, pp. 571–581, 2010.

[13] F. Li, Q. Cai, X. Fu, and J. Liu, "Construction of habitat suitability models (HSMs) for benthic macroinvertebrate and their applications to instream environmental flows: a case study in Xiangxi River of Three Gorges Reservior region, China," *Progress in Natural Science*, vol. 19, no. 3, p. 359, 2009.

[14] C. Shen, "A transdisciplinary review of deep learning research and its relevance for water resources scientists," *Water Resources Research*, vol. 54, no. 11, pp. 8558–8593, 2018.

[15] R. C. Mamat, A. M. Samad, A. Kasa, S. F. M. Razali, A. Ramli, and M. B. H. C. Omar, "Slope stability prediction of road

embankment on soft ground treated with prefabricated vertical drains using artificial neural network," *IAES International Journal of Artificial Intelligence*, vol. 9, no. 2, pp. 236–243, 2020.

[16] Z. Sheikh Khozani, M. J. S. Safari, A. Danandeh Mehr, and W. H. M. Wan Mohtar, "An ensemble genetic programming approach to develop incipient sediment motion models in rectangular channels," *Journal of Hydrology*, vol. 584, Article ID 124753, 2020.

[17] Z. S. Khozani, K. Khosravi, B. T. Pham et al., "Determination of compound channel apparent shear stress: application of novel data mining models," *Journal of Hydroinformatics*, vol. 21, no. 5, pp. 798–811, 2019.

[18] Z. M. Yaseen, I. Ebtehaj, S. Kim, and H. Sanikhani, "Novel hybrid data-intelligence model for forecasting monthly rainfall with uncertainty analysis," *Water*, vol. 11, no. 3, 2019.

[19] H. Zhang, H. A. Loáiciga, F. Ren, Q. Du, and D. Ha, "Semi-empirical prediction method for monthly precipitation prediction based on environmental factors and comparison with stochastic and machine learning models," *Hydrological Sciences Journal*, vol. 65, no. 11, p. 1928, 2020.

[20] Z. M. Yaseen, S. O. Sulaiman, R. C. Deo, and K.-W. Chau, "An enhanced extreme learning machine model for river flow forecasting: state-of-the-art, practical applications in water resource engineering area and future research direction," *Journal of Hydrology*, vol. 569, pp. 387–408, 2019.

[21] V. Nourani, A. Hosseini Baghanam, J. Adamowski, and O. Kisi, "Applications of hybrid wavelet-artificial intelligence models in hydrology: a review," *Journal of Hydrology*, vol. 514, pp. 358–377, 2014.

[22] H. R. Maier, Z. Kapelan, J. Kasprzyk et al., "Evolutionary algorithms and other metaheuristics in water resources: current status, research challenges and future directions," *Environmental Modelling & Software*, vol. 62, pp. 271–299, 2014.

[23] M. Ehteram, S. Q. Salih, and Z. M. Yaseen, "Efficiency evaluation of reverse osmosis desalination plant using hybridized multilayer perceptron with particle swarm optimization," *Environmental Science and Pollution Research*, vol. 27, no. 13, p. 15278, 2020.

[24] G. Zhao, B. Pang, Z. Xu, and L. Xu, "A hybrid machine learning framework for real-time water level prediction in high sediment load reaches," *Journal of Hydrology*, vol. 581, Article ID 124422, 2020.

[25] S. Shamshirband, S. Hashemi, H. Salimi et al., "Predicting standardized streamflow index for hydrological drought using machine learning models," *Engineering Applications of Computational Fluid Mechanics*, vol. 14, no. 1, p. 339, 2020.

[26] M. B. Kia, S. Pirasteh, B. Pradhan, A. R. Mahmud, W. N. A. Sulaiman, and A. Moradi, "An artificial neural network model for flood simulation using GIS: Johor river basin, Malaysia," *Environmental Earth Sciences*, vol. 67, no. 1, p. 251, 2012.

[27] Y. Shao and R. S. Lunetta, "Comparison of support vector machine, neural network, and CART algorithms for the land-cover classification using limited training data points," *ISPRS Journal of Photogrammetry and Remote Sensing*, vol. 70, pp. 78–87, 2012.

[28] Z. M. Yaseen, H. Faris, and N. Al-Ansari, "Hybridized extreme learning machine model with Salp Swarm algorithm: a novel predictive model for hydrological application," *Complexity*, vol. 2020, Article ID 8206245, 14 pages, 2020.

[29] S. O. Sulaiman, J. Shiri, H. Shiralizadeh, O. Kisi, and Z. M. Yaseen, "Precipitation pattern modeling using cross-station perception: regional investigation," *Environmental Earth Sciences*, vol. 77, no. 19, p. 709, 2018.

[30] D. K. Saleh, *Stream Gage Descriptions and Streamflow Statistics for Sites in the Tigris River and Euphrates River Basins, Iraq*, US Department of the Interior, US Geological Survey, Reston, VA, USA, 2010.

[31] Z. M. Yaseen, S. M. Awadh, A. Sharafati, and S. Shahid, "Complementary data-intelligence model for river flow simulation," *Journal of Hydrology*, vol. 567, pp. 180–190, 2018.

[32] O. Kisi, S. Heddam, and Z. M. Yaseen, "The implementation of univariable scheme-based air temperature for solar radiation prediction: new development of dynamic evolving neural-fuzzy inference system model," *Applied Energy*, vol. 241, pp. 184–195, 2019.

[33] M. Firat, "Comparison of artificial intelligence techniques for river flow forecasting," *Hydrology and Earth System Sciences*, vol. 12, no. 1, pp. 123–139, 2008.

[34] K. Mohammadi, H. R. Eslami, and R. Kahawita, "Parameter estimation of an ARMA model for river flow forecasting using goal programming," *Journal of Hydrology*, vol. 331, no. 1-2, pp. 293–299, 2006.

[35] R. Burget, J. Karasek, Z. Smékal, V. Uher, and O. Dostal, "Rapidminer image processing extension: a platform for collaborative research," in *Proceedings of the 33rd International Conference on Telecommunication and Signal Processing TSP*, Vienna, Austria, 2010.

[36] D. E. Rumelhart, G. E. Hinton, and R. J. Williams, "Learning representations by back-propagating errors," *Nature*, vol. 323, no. 6088, p. 533, 1986.

[37] S. Zaza and M. Al-Emran, "Mining and exploration of credit cards data in UAE," in *Proceedings of the 2015 5th International Conference on E-Learning, ECONF 2015*, Manama, Bahrain, 2015.

[38] S. Naganna, P. Deka, M. Ghorbani, S. Biazar, N. Al-Ansari, and Z. Yaseen, "Dew point temperature estimation: application of artificial intelligence model integrated with nature-inspired optimization algorithms," *Water*, vol. 11, p. 742, 2019.

[39] D. E. Rumelhart, G. E. Hinton, and R. J. Williams, *Learning Internal Representations by Error Propagation*, Institute for Cognitive Science, University of California, San Diego, CA, USA, 1985.

[40] M. Kubat, "The genetic algorithm," *An Introduction to Machine Learning*, Springer, Berlin, Germany, 2017.

[41] I. Arpaci, S. Alshehabi, M. Al-Emran et al., "Analysis of twitter data using evolutionary clustering during the COVID-19 pandemic," *Computers, Materials & Continua*, vol. 65, no. 1, p. 193, 2020.

[42] S. Q. Salih, A. Sharafati, I. Ebtehaj et al., "Integrative stochastic model standardization with genetic algorithm for rainfall pattern forecasting in tropical and semi-arid environments," *Hydrological Sciences Journal*, vol. 65, 2020.

[43] M. E. A. B. Seghier, B. Keshtegar, K. F. Tee, T. Zayed, R. Abbassi, and N. T. Trung, "Prediction of maximum pitting corrosion depth in oil and gas pipelines," *Engineering Failure Analysis*, vol. 112, Article ID 104505, 2020.

[44] M. Jahandideh-Tehrani, G. Jenkins, and F. Helfer, "A comparison of particle swarm optimization and genetic algorithm for daily rainfall-runoff modelling: a case study for southeast Queensland, Australia," *Optimization and Engineering*, 2020.

[45] M. Zounemat-Kermani, E. Matta, A. Cominola et al., "Neurocomputing in surface water hydrology and hydraulics: a review of two decades retrospective, current status and

future prospects," *Journal of Hydrology*, vol. 588, Article ID 125085, 2020.

[46] M. E. A. Ben Seghier, H. Carvalho, B. Keshtegar, J. A. F. O. Correia, and F. Berto, "Novel hybridized adaptive neuro-fuzzy inference system models based particle swarm optimization and genetic algorithms for accurate prediction of stress intensity factor," *Fatigue & Fracture of Engineering Materials & Structures*, vol. 43, no. 11, pp. 2653–2667, 2020.

[47] S. H. Mai, M. E. A. B. Seghier, P. L. Nguyen, J. Jafari-Asl, and D.-K. Thai, "A hybrid model for predicting the axial compression capacity of square concrete-filled steel tubular columns," *Engineering with Computers*, pp. 1–18, 2020.

[48] A. A. Saa, M. Al-Emran, and K. Shaalan, "Mining student information system records to predict students' academic performance," *Advances in Intelligent Systems and Computing*, Springer, Berlin, Germany, 2020.

[49] L. Breiman, *Random Forest.Pdf*, Kluwer Academic Publishers, Dordrecht, Netherlands, 2001.

[50] C. Qi, W. Zhou, X. Lu, H. Luo, B. T. Pham, and Z. M. Yaseen, "Particulate matter concentration from open-cut coal mines: a hybrid machine learning estimation," *Environmental Pollution*, vol. 263, Article ID 114517, 2020.

[51] Z. M. Yaseen, S. Naghshara, S. Q. Salih, S. Kim, A. Malik, and M. A. Ghorbani, "Lake water level modeling using newly developed hybrid data intelligence model," *Theoretical and Applied Climatology*, vol. 141, no. 3-4, p. 1285, 2020.

[52] M. Ali, R. Prasad, Y. Xiang, and Z. M. Yaseen, "Complete ensemble empirical mode decomposition hybridized with random forest and kernel ridge regression model for monthly rainfall forecasts," *Journal of Hydrology*, vol. 584, Article ID 124647, 2020.

[53] Y. Tang, S. Krasser, Y. He, W. Yang, and D. Alperovitch, "Support vector machines and random forests modeling for spam senders behavior analysis," in *Proceedings of the 2008 IEEE Global Telecommunications Conference*, New Orleans, LA, USA, 2008.

[54] I. Arpaci, M. Al-Emran, M. A. Al-Sharafi, and K. Shaalan, "A novel approach for predicting the adoption of smartwatches using machine learning algorithms," *Studies in Systems, Decision and Control*, Springer, Berlin, Germany, 2021.

[55] L. Breiman, "Random forests," *Machine Learning*, vol. 45, no. 1, pp. 5–32, 2001.

[56] V. F. Rodriguez-Galiano, B. Ghimire, J. Rogan, M. Chica-Olmo, and J. P. Rigol-Sanchez, "An assessment of the effectiveness of a random forest classifier for land-cover classification," *ISPRS Journal of Photogrammetry and Remote Sensing*, vol. 67, pp. 93–104, 2012.

[57] V. Vapnik, *The Nature of Statistical Learning Theory*, Springer Science & Business Media, Berlin, Germany, 2013.

[58] N. Cristianini and J. Shawe-Taylor, *An Introduction to Support Vector Machines and Other Kernel-Based Learning Methods*, Cambridge University Press, Cambridge, UK, 2000.

[59] Z. M. Yaseen, R. C. Deo, A. Hilal et al., "Predicting compressive strength of lightweight foamed concrete using extreme learning machine model," *Advances in Engineering Software*, vol. 115, pp. 112–125, 2018.

[60] S. Belaid and A. Mellit, "Prediction of daily and mean monthly global solar radiation using support vector machine in an arid climate," *Energy Conversion and Management*, vol. 118, pp. 105–118, 2016.

[61] T. T. M. Tiyasha, T. M. Tung, and Z. M. Yaseen, "A survey on river water quality modelling using artificial intelligence models: 2000–2020," *Journal of Hydrology*, vol. 585, Article ID 124670, 2020.

[62] S. K. Bhagat, T. M. Tung, and Z. M. Yaseen, "Development of artificial intelligence for modeling wastewater heavy metal removal: state of the art, application assessment and possible future research," *Journal of Cleaner Production*, vol. 250, Article ID 119473, 2019.

[63] K. S. Sajan, V. Kumar, and B. Tyagi, "Genetic algorithm based support vector machine for on-line voltage stability monitoring," *International Journal of Electrical Power & Energy Systems*, vol. 73, p. 200, 2015.

[64] K.-P. Wu and S.-D. Wang, "Choosing the kernel parameters for support vector machines by the inter-cluster distance in the feature space," *Pattern Recognition*, vol. 42, no. 5, pp. 710–717, 2009.

[65] Q. Huang, J. Mao, and Y. Liu, "An improved grid search algorithm of SVR parameters optimization," in *Proceedings of the 2012 International Conference on Communication Technology Proceedings ICCT*, Chengdu, China, 2012.

[66] K. Khosravi, L. Mao, O. Kisi, Z. M. Yaseen, and S. Shahid, "Quantifying hourly suspended sediment load using data mining models: case study of a glacierized Andean catchment in Chile," *Journal of Hydrology*, vol. 567, pp. 165–179, 2018.

[67] O. Kisi and Z. M. Yaseen, "The potential of hybrid evolutionary fuzzy intelligence model for suspended sediment concentration prediction," *CATENA*, vol. 174, pp. 11–23, 2019.

[68] D. R. Legates and G. J. McCabe, "Evaluating the use of "goodness-of-fit" measures in hydrologic and hydroclimatic model validation," *Water Resources Research*, vol. 35, no. 1, pp. 233–241, 1999.

[69] M. Zounemat-Kermani, A. Mahdavi-Meymand, M. Alizamir, S. Adarsh, and Z. M. Yaseen, "On the complexities of sediment load modeling using integrative machine learning: application of the great river of Loíza in Puerto Rico," *Journal of Hydrology*, vol. 585, Article ID 124759, 2020.

[70] Y. Tikhamarine, A. Malik, D. Souag-Gamane, and O. Kisi, "Artificial intelligence models versus empirical equations for modeling monthly reference evapotranspiration," *Environmental Science and Pollution Research*, vol. 27, no. 24, p. 30001, 2020.

[71] Y. Seo, S. Kim, and V. P. Singh, "Physical interpretation of river stage forecasting using soft computing and optimization algorithms," *Advances in Intelligent Systems and Computing*, Springer, Berlin, Germany, 2016.

[72] B. Yaghoubi, S. A. Hosseini, and S. Nazif, "Monthly prediction of streamflow using data-driven models," *Journal of Earth System Science*, vol. 128, no. 6, 2019.

[73] K. E. Taylor, "Summarizing multiple aspects of model performance in a single diagram," *Journal of Geophysical Research: Atmospheres*, vol. 106, no. D7, pp. 7183–7192, 2001.

[74] C. E. Shannon, "The mathematical theory of communication," *The Bell System Technical Journal*, vol. 27, pp. 379–423, 1948.

[75] N. Rusk, "Deep learning," *Nature Methods*, vol. 13, no. 1, p. 35, 2015.

Hindawi
Complexity
Volume 2020, Article ID 7146593, 13 pages
https://doi.org/10.1155/2020/7146593

Review Article

Comparison of Statistical, Graphical, and Wavelet Transform Analyses for Rainfall Trends and Patterns in Badulu Oya Catchment, Sri Lanka

Ashika M. Ruwangika,[1] Anushka Perera,[2] and Upaka Rathnayake[2]

[1]*Department of Physical Science and Technology, Faculty of Applied Sciences, Sabaragamuwa University of Sri Lanka, Belihuloya, Sri Lanka*
[2]*Department of Civil Engineering, Faculty of Engineering, Sri Lanka Institute of Information Technology, Malabe, Sri Lanka*

Correspondence should be addressed to Upaka Rathnayake; upakasanjeewa@gmail.com

Received 4 August 2020; Revised 7 September 2020; Accepted 28 September 2020; Published 21 October 2020

Academic Editor: Shamsuddin Shahid

Climate change has adversely influenced many activities. It has increased the intensified precipitation events in some places and decreased the precipitation in some other places. In addition, some research studies revealed that the climate change has moved seasons in the temporal scale. Therefore, the changes can be seen in both spatial and temporal scales. Thus, analyzing climate change in the localized environments is highly essential. Rainfall trend analysis in a localized catchment can improve many aspects of water resource management not only to the catchment itself but also to some of the related other catchments. This research is carried to identify the rainfall trends in Badulu Oya catchment, Sri Lanka. The catchment is important as it is in the intermediate climate zone and rich in agricultural productions. Four rain gauges (namely, *Badulla, Kandekatiya, Lower Spring Valley, and Ledgerwatte Estate*) were used to analyze the rainfalls in the resolutions of monthly, seasonally, and annually. 30-year monthly cumulative rainfall data for the above four gauging stations are analyzed using various standard tests. Nonparametric tests including Mann–Kendall test and sequential Mann–Kendall test and innovative trend analysis methods are used to identify the potential rainfall trends in Badulu Oya catchment. In addition, continuous wavelet transforms and discrete wavelet transforms tests are carried out to check the patterns on rainfall to the catchment. The trend analysis methods are compared against each other to identify the better technique. The results reveal that the nonparametric Mann–Kendall test is powerful to produce the statistically significant rainfall trends in qualitative and quantitative manner. Mann–Kendall analysis shows a positive trend to Ledgerwatte Estate in monthly (3.7 mm *in February and* 7.4 mm *in October*), seasonal (6.9 mm *in the 2nd intermonsoon*), and annual (3 mm *annually*) scales. However, the analysis records one decreasing rainfall trend to Kandekatiya (8.1 mm *in December*) only in monthly scale. Nevertheless, it was found that the graphical method can be easily used in qualitative analysis, while discrete wavelet transformations are efficient in identifying the rainfall patterns effectively.

1. Introduction

Catchments in intermediate climatic zones are interesting to analyze for the water resources management [1]. These zones are neither the wet zones, where they have plenty of water resources, nor the arid zones, where there are enough water scarcities. Water sustainability can be achieved in these intermediate zones, only if the water resources are properly managed. The availability of water resources in these intermediate zones is highly influenced by the seasonal rainfall. However, there are many arguments on the changes and variations in seasonal rainfall in most of the countries due to ongoing climate changes.

When some countries have more than the usual annual rainfalls and rainfall intensities (*sometimes snowfalls*) [2–6], some other countries face more arid times leading to water scarcities [7–9]. Therefore, it is highly important to understand the spatial variation in various climatic

characteristics due to ongoing climate change in the local resolutions rather the global resolution. The best would be the catchment scale spatial resolution; thus, the local climate change scenarios can be easily acknowledged. As a result, the required adaptation processes (*whether they are structural or nonstructural*) in the catchment scales can be implemented.

Researchers used several methods to understand climate change and its impact on the precipitation (rainfall). Precipitation has taken more attention due to its driving capacity of the hydrological cycle, which is the life of the Earth [10, 11]. Among many empirical climate models, past recorded climate data analyses have taken much attention from most of the researchers. This can be due to the usual unpredictability of the climate scenarios; however, there may be some periodic characteristics behind the measured data. Therefore, statistical tests are frequently used in measured climate data analyses. Parametric and nonparametric statistical tests are used to detect climatic trends. Even though the parametric tests (*t*-test and linear regression) are powerful in statistical analyses, they need the tested data to be independent and normally distributed [12]. However, most of the climatic data are not normally distributed. Therefore, nonparametric tests like Mann–Kendall test [13–16] and sequential Mann–Kendall test [17–21] are common in climatic trend detection. Not only the statistical analysis but also some innovative methods like innovative trend analysis techniques [22] [23–26] are often used to identify the trends in climatic time series.

In addition to the trend analysis, wavelet analysis [27–31] can be observed in the climatic time series analysis for pattern detection. Various methods have their own advantages and disadvantages; however, a collection of these tests would receive a better outcome to the stakeholders. Therefore, comparison analyses using a collection of these parametric, nonparametric, innovative trend analysis, and wavelet analysis are common [24, 32–34]. However, the application of these climatic analyses is now moved to a localized area rather to the globe. As it was stated, identifying localized climatic trends are important in many planning activities [35–38]. Even though these rainfall trends may not perfectly be identified, acceptable identification is highly desirable for future planning activities, like irrigation scheduling, water supply systems design, and upgrading. Therefore, it is understood to be essential to a catchment, which is based on agriculture, not only to supply the food for the localized environment but to the whole Sri Lanka. Badulu Oya catchment in Sri Lanka is a catchment in the intermediate climate zone; however, it receives a significant amount of annual rainfall to cater the paddy and vegetable cultivation. The catchment produces more than 25% of the country's vegetable need. Several related research can be found in the context of Sri Lanka [24, 39–43]. However, no research is found in the literature for identifying the rainfall trends in the catchment to guide the planners. Therefore, the presented work herein reveals the rainfall trends to Badulu Oya catchment. Several methods, including the Mann–Kendall test, sequential Mann–Kendall test, innovative trend analysis, and wavelets, are used to analyze the rainfall trends, and the results are compared to each other in seeking the better method. The advantages and drawbacks of each method are discussed in relevant sections, and the importance of such study is well established and stated in Discussion.

2. Study Area: Badulu Oya Catchment

Badulu Oya starts from Namunukula mountain range and flows from the eastern slopes of the central highlands to reach Mahaweli River, which is the longest river in Sri Lanka. It is one of the most important tributaries of the Mahaweli River. The terrain, in which Badulu Oya flows, is in the intermediate climatic zone of the country [44], and therefore, a significant amount of annual rainfall is seen in the catchment (1500–2000 mm). The catchment receives its major rainfall in the months of October to March (during the northeast monsoon and 1st intermonsoon), whereas it has a drier period during April-September months. However, convection rainfalls are common during the drier months. Therefore, the catchment has a rich water capacity.

The catchment area of Badulu Oya is around 318 km^2 (refer Figure 1), and it is placed adjacent to the Uma Oya catchment from its left and Gal Oya catchment from its right. Intensive agricultural activities are taken place in Badulu Oya catchment [46]; therefore, various land-uses over the time can be observed. Some of the forest areas have been changed to urban, suburban, and agricultural areas over the last decades [46]. Most of the forest areas were converted into tea plantations during the British ruling era [47], while other land-use activities have been happened during the 20th century. Therefore, the surface water and groundwater availability have been severely impacted. Hence, it is timely important to observe the rainfall trends in the catchment using the recorded data.

Four rain gauging stations including Badulla (6.980 N, 81.050 E), Lower Spring Valley (6.920 N, 81.10 E), Ledgerwatte Estate (7.030 N, 81.020 E) and Kandekatiya (7.170 N, 81.020 E) were selected for this analysis.

3. Nonparametric Tests in Climatic Trends

Nonparametric tests are widely used to identify climate trends [48–51]. Nonparametric tests are widely used not only to identify the climatic trends but also to detect the trends in other temporal variations like stream flow trends [52, 53] and water quality trends in streams and rivers [54]. Several nonparametric tests can be found in the literature including Mann–Kendall test, Spearman's rho test [55, 56], and Hotelling–Pabst test [57, 58]. However, Mann–Kendall test and its modifications are widely used in the literature for trend analysis [41, 59, 60].

3.1. Mann–Kendall Test and Sen's Slope Estimator. Mann–Kendall test is used to identify monotonically increasing and decreasing trends in a climate data series. The test was initially proposed by Mann [61] and improved by Kendall [62]. The test was further improved to consider the seasonal effects by Hirsch et al. [63]. The test calculates Kendall's tau between two data samples based on the ranks. These samples were assumed to be independent. The alternative hypotheses from the test have three outcomes,

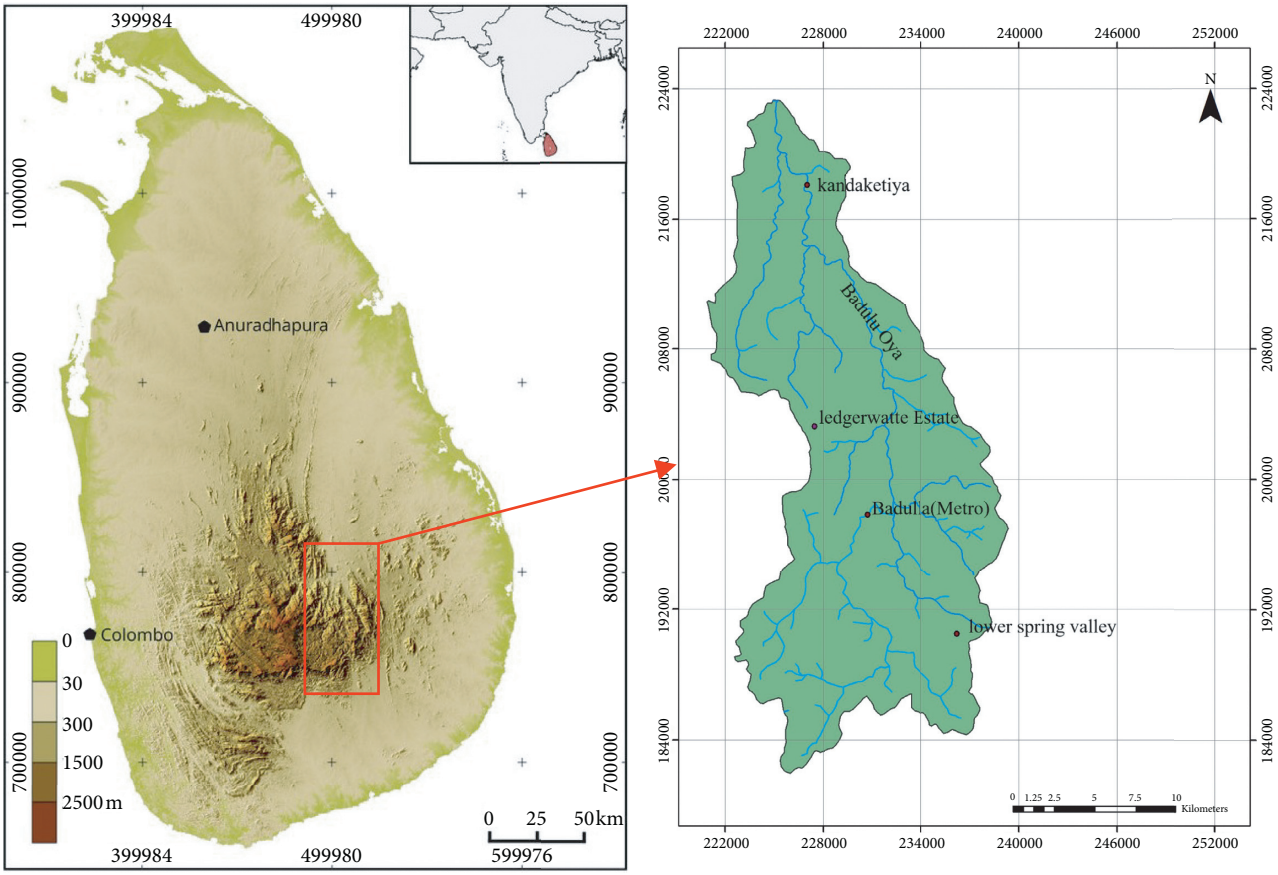

FIGURE 1: Badulu Oya catchment (*Sri Lanka topography map was extracted from* [45]).

negative trend, no trend, and positive trend. The mathematical formulations of calculating Mann–Kendall statistics S, variance $V(S)$, and standard test statistics Z_{MK} are given in the following equations:

$$S = \sum_{i-1}^{n-1} \sum_{j=i+1}^{n} \operatorname{sgn}\left(x_j - x_i\right), \tag{1}$$

$$\operatorname{sgn}\left(x_j - x_i\right) = \begin{cases} +1, & \text{if}\left(x_j - x_i\right) > 0, \\ 0, & \text{if}\left(x_j - x_i\right) = 0, \\ -1, & \text{if}\left(x_j - x_i\right) < 0, \end{cases} \tag{2}$$

$$V(S) = \frac{1}{18}\left[n(n-1)(2n+5) - \sum_{p=1}^{q} t_p\left(t_p - 1\right)\left(2t_p + 5\right)\right], \tag{3}$$

$$Z_{\mathrm{MK}} = \begin{cases} \dfrac{S-1}{\sqrt{V(S)}}, & \text{if } S > 0, \\ 0, & \text{if } S = 0, \\ \dfrac{S+1}{\sqrt{V(S)}}, & \text{if } S < 0, \end{cases} \tag{4}$$

where x_i and x_j are chronological time series observations, n is the length of the time series, t_p is the number of ties for the pth value, and q is the number of tied values in the above stated equations. An upward trend in the climatological series is given by a positive Z_{MK} value, whereas a downward trend is given by a negative Z_{MK} value. More details of the Mann–Kendall test can be found in Ahamed et al. [55] and Rathnayake [24].

Sen's slope estimator is usually used to quantify the meteorological trends identified from Mann–Kendall test [13–16]. Sen's slope estimator calculated the gradient of the trend line; therefore, it presents the linear magnitude of the trend. Sen's slope calculates the slopes (m_i) of all data pairs considered using the following equation:

$$m_i = \frac{x_j - x_k}{j - k}, \quad \text{for } i = 1, 2, \ldots, N, \tag{5}$$

where N is the number of data points in the climate time series and x_j and x_k are data values at time j and k (where $j > k$), respectively. The mean value of all slopes is Sen's slope and calculated as given in the following equation:

$$\beta = \begin{cases} m_{((N+1/2))}, & \text{if } N \text{ is odd}, \\ \dfrac{1}{2}\left(m_{(N/2)} + m_{((N+1/2))}\right), & \text{if } N \text{ is even}. \end{cases} \tag{6}$$

The trend can be detected as an upward or downward trend based on the + or–behavior of the β.

3.2. Sequential Mann–Kendall Test (SQMK Test). Not only the monotonic trend and its magnitude but also the starting time of the trend is important. In addition, identification of the changes in trends over the time is highly important [64]. Therefore, the sequential Mann–Kendall test is widely used in such cases [17–21]. Sneyers [65] has introduced sequential and partial values from the usual Mann–Kendall test. The test sets up two climatic time series: one for the progressive series $(u(t))$ and the other one is for the backward series $(u'(t))$. The $u(t)$ is a standardized variable, which has a zero mean and unit standard deviation. The test also considers the relative values of all terms in the time series. The following steps and equations (7)–(10)) give the mathematical forms of the SQMK test.

The values of annual mean time series (x_j) are compared against the time series (x_k), and they are denoted by n_j, when $x_j > x_k$. The test statistics (t_j) is calculated using the following equation:

$$t_j = \sum_{1}^{j} n_j. \tag{7}$$

Mean $(E(t_j))$ and the variance $(V(t_j))$ of the t_j are then calculated by the following equations:

$$E(t_j) = \frac{j(j-1)}{4}, \tag{8}$$

$$V(t_j) = \frac{j(j-1)(2j+5)}{72}. \tag{9}$$

Finally, the $u(t)$ values are calculated using the following equation:

$$u(t) = \frac{t_j - E(t_j)}{\sqrt{V(t_j)}}. \tag{10}$$

The same procedure is repeated for the $u'(t)$ time series using backward data. The intersection of the $u(t)$ and $u'(t)$ illustrates the stating of the climatic trend. More details of the SQMK test can be found in Zarenistanak et al. [66].

4. Graphical Trend Analysis (Innovative Trend Analysis)

Sen [67] has introduced an innovative but very simple method to detect the trends in time series. The technique was applied to many climates related research studies in identifying trends [22–26]. However, the technique only proposes a qualitative analysis without any quantitative or numerical significance of the identified trend. The test simply checks the comparative analysis of two halves of the time series prepared at ascending order. The main climatic data set is first divided into two halves and arranged them in the ascending order. These two sets are compared against each other, and there is no trend if the second half aligns in $\pm$ 5% of 45° degree line drawn to data series. However, if the second half aligns above the 5% of the 45^0 degree line, a positive trend is proposed. In contrast, if the second half aligns below the −5% of the 45° degree line, a negative trend is proposed. More information on this method can be found in Sen [67].

5. Wavelet Transformation

Wavelet transformation is a relatively new tool, which is widely used to detect the climatic trends [64, 68]. Not only in rainfall trends but also wavelet analysis is popular in many other trend detections, including freak waves in the ocean [69], water levels in rivers and reservoirs [79], and droughts [70]. A time series can be easily decomposed into several smaller time series based on time and frequency. Climatic trends, periodicity, various discontinuities, and changing points in climate series can be detected from wavelet transformation analysis [27–31]. Fourier analysis is used to break a signal into smaller but smooth sinusoids. A wavelet is a mathematical expression to localize the function in the spatial and temporal scales. Continuous and discrete wavelet transforms are two types of wavelet analysis used in the literature to identify the climatic trends.

5.1. Continuous Wavelet Transforms (CWTs). Continuous wavelet transforms use discrete wavelets in the continuous time scale $(x(t))$. Mathematically, the wavelet function $(\Psi(\eta))$ in CWT can be represented as given in equations (11)–(12). More information on these can be found in Chen et al. [71], Nalley et al. [72], and Partal and Küçük [30] study:

$$\Psi(\eta) = \Psi(s^*, \gamma) = \frac{1}{\sqrt{s^*}} \Psi \frac{t-\gamma}{s^*}, \tag{11}$$

where η, γ, and s^* are the nondimensional parameter and the translation factor (time shift) of the wavelet over the time series and the wavelet scale, respectively. The wavelet coefficients $(W_\Psi(s^*, \gamma))$ can be found from equation (12). Ψ^* is the complex conjugate function. A scalogram can be produced if the translation factor and the wavelet scale changed smoothly with the time. Therefore, calculations can be done to identify the amplitude of a particular scale and its fluctuations with time:

$$W_\Psi(s^*, \gamma) = \frac{1}{\sqrt{s^*}} \int_{-\infty}^{\infty} x(t) \Psi^* \left(\frac{t-\gamma}{s^*}\right) \mathrm{dt}. \tag{12}$$

5.2. Discrete Wavelet Transforms (DWTs). CWT can be effectively used to identify specific event, which is not obvious; however, construction of CWT is more complex [72]. In addition, CWT produces many coefficients and makes the problem more complicated. Therefore, discrete wavelet transforms (DWTs) are popular in trend identification. DWT simplifies the problem; nevertheless, they produce accurate and reliable answers [30]. DWT uses a dyadic calculation procedure; thus, it simplifies the problem [73]. Discrete wavelet transforms can be mathematically

represented in the following equations (refer equations (13) and (14)):

$$\Psi_{(a,b)}\left(\frac{t-\gamma}{s^*}\right) = \frac{1}{(s_0)^{a/2}}\Psi\left(\frac{t-b\gamma_0 s_0^a}{s_0^a}\right), \quad (13)$$

where Ψ, γ_0, and s_0 are mother wavelet, translation of the wavelet, and dilation step (>1), respectively. a and b are integers which are used to represent the dilation and translation of the wavelet. The wavelet coefficients are calculated using the following equation:

$$W_\Psi(a,b) = \frac{1}{2^{a/2}}\sum_{t=0}^{N-1} x(t)\Psi\left(\frac{t}{2^a}-b\right). \quad (14)$$

More information on DWT can be found in Nalley et al. [72].

6. Climatic Analysis in Badulu Oya Catchment

As it was stated in Section 2, four rain gauging stations (Badulla, Lower Spring Valley, Ledgerwatte Estate, and Kandekatiya) were selected to the analysis. These stations were selected due to the data scarcity of the catchment. Monthly rainfall data for 30 years (Jan/1990 to Dec/2019) for the above stations were purchased from the Department of Meteorology, Sri Lanka. There are no other rainfall gauging stations in the catchment according to the Department of Meteorology, Sri Lanka. There were several other older stations in the catchment; however, they are not functioned according to the Department of Meteorology, Sri Lanka (*Department of Meteorology, Sri Lanka holds the sole responsibility of meteorological data collection in the whole Sri Lanka*). There were few missing data, and their percentages were minimum (Kandekatiya, 1.67%; Ledgerwatte Estate, 1.67%; Lower Spring Valley, 1.1%; and Badulla, 0.28%). Therefore, the missing data were filled using the normal ratio method. The rainfall data series were tested for the homogeneity using Pettit's test, SNHT test, and Buishand's test and found they were homogeneous. Therefore, the quality of the data series was rich.

The monthly rainfall data were sorted to four rainfall seasons (northeast monsoon, December to February; 1st intermonsoon, March to April; southwest monsoon, May to September; 2nd intermonsoon, October to November) and annual cumulative rainfalls. The rainfall data were then processed for the Mann–Kendall test in monthly, seasonal, and annual resolutions. After that, the sequential Mann–Kendall test was carried out to identify the locations of the trends in seasonal and annual resolutions. The innovative method was also processed to develop the graphical trends for monthly, seasonal, and annual resolutions for all four rain gauges.

Finally, wavelet analysis from CWT and DWT was carried out to the monthly, seasonal, and annual resolutions. Morlet wavelet and Daubechies wavelet (db) were used to carry out the CWT and DWT analyses, respectively. Morlet wavelet is sine-shaped Gaussian, and more details on this are discussed in the relevant Results section. On the contrary, Daubechies wavelet is commonly used in hydrometeorological studies as it has a smooth mother wavelet [74–78]. These tests were carried out in the Matlab mathematical package. The moderately large number of data points was used in this study from the monthly and annual precipitation datasets. The precipitation data were analyzed for the period 1990–2019. Therefore, there were 360 (12×30) data points for the monthly sets. First, the decomposition levels were determined to avoid unnecessary levels of data decomposition of these larger datasets. Finally, comparative analyses were conducted to identify a better technique in identifying the rainfall trends of the Badulu Oya catchment.

7. Results and Discussion

7.1. Mann–Kendall Trend Analysis Results. Table 1 presents the trend analysis results from the MK test. No significant trends were identified for the Badulla rain gauge for the 30-year rainfall analysis in the monthly (January to December separately), seasonal (4 seasons), and annual resolutions. However, a decreasing trend was identified in Kandekatiya rain gauge for the month of December. Nevertheless, month December is treated to be one of the most rainfalls receiving months to Badulu Oya catchment. However, this trend identification was not justified in seasonal and annual trend analysis. Similar observation: however, an increasing trend in the month of May can be found for the rain gauge in Lower Spring Valley.

7.2. Sequential Mann–Kendall Trend Analysis Results. Figure 2 presents the graphical trend analysis results for annual (Figure 2(a)) and seasonal (Figures 2(b)–2(e)) from the SQMK test. The standard value of Z for the significance level of 0.05 ($p = 0.05$ or 5%) is ± 1.96, and these boundary lines are shown in bold black straight lines of all figures. Mann–Kendall Z values greater than the upper bound ($Z > 1.96$) propose an upward trend, while lower than the lower bound ($Z < -1.96$) propose a downward trend. Figure 2(a) clearly shows an upward rainfall trend for Ledgerwatte Estate rain gauge and that is from 2007 onwards. Lower Spring Valley rain gauge also indicates Z values above the upper bound in years 2011 and 2014; however, these years may not be considered for upward trends. Soon after the Z value variation crosses the +1.96 line, it comes down. Therefore, it is not considered a significant upward trend. However, the other two rain gauges in Badulla and Kandekatiya have not shown upward or downward trends.

Similarly, upward trends can be seen in Figures 2(b) and 2(c). Ledgerwatte Estate shows a positive rainfall trend for northeast monsoon (*in year* 2011), whereas it shows an upward trend in year 2008 for the 1st intermonsoon. In addition, Lower Spring Valley and Badulla gauging stations show upward rainfall trends in years 2003 and 2010, respectively. However, no upward or downward trends were found in southeast monsoon and 2nd intermonsoon seasons (refer Figures 2(d) and 2(e)).

Table 1: Trend analysis results from the MK test.

Temporal resolution	Rain gauge			
	Badulla	Kandekatiya	Lower spring valley	Ledgerwatte estate
Monthly	No trend	Decreasing trend (8.1 mm) in December	Increasing trend (4.9 mm) in May	Increasing trends: 3.7 mm in February and 7.4 mm in October
Seasonal	No trend	No trend	No trend	Increasing trends (6.9 mm) in the 2nd intermonsoon
Annual	No trend	No trend	No trend	Increasing trend (3 mm)

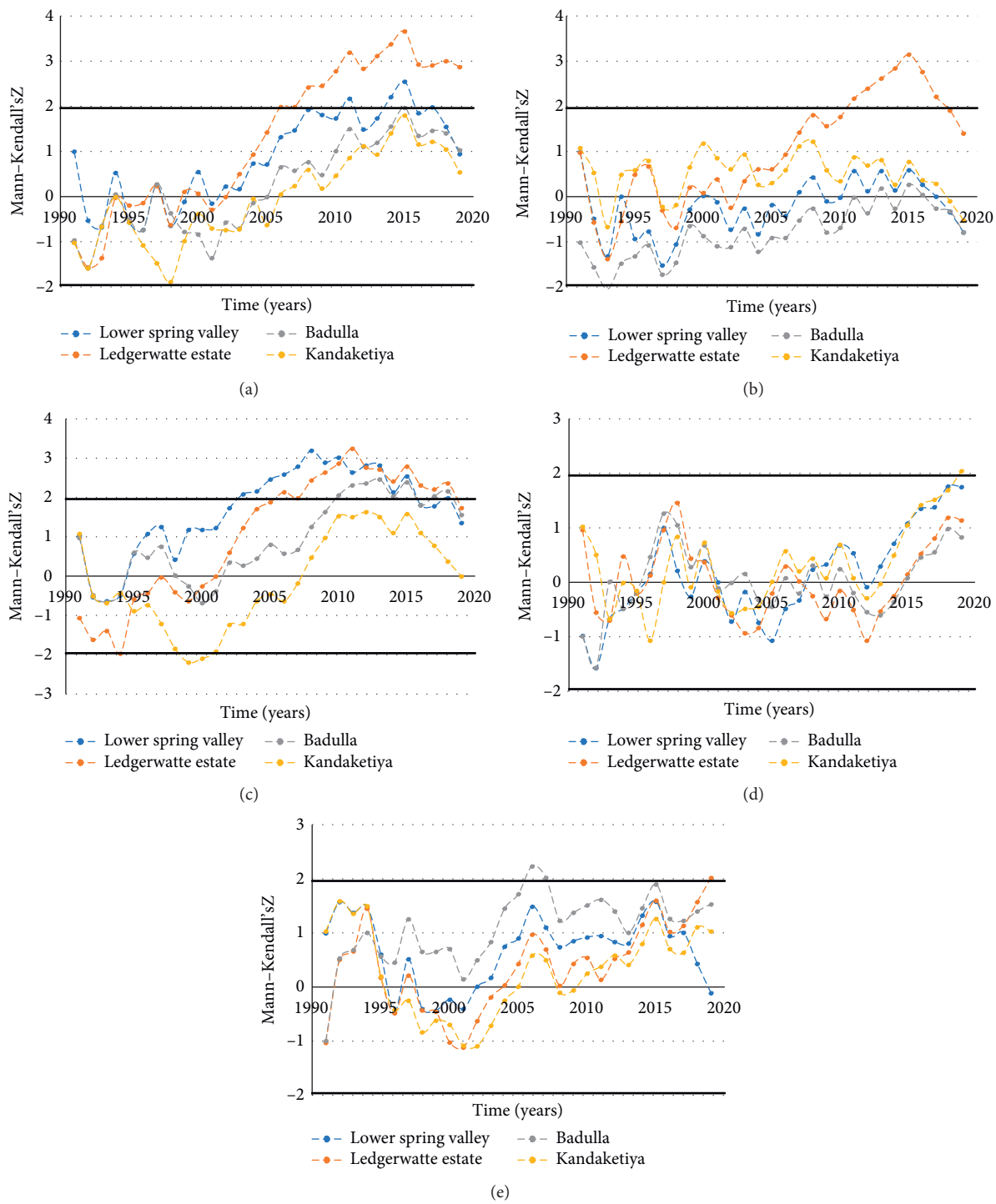

Figure 2: Trend analysis results from the SQMK test: (a) for annual rainfall; (b) for northeast monsoon; (c) for the 1st intermonsoon; (d) for southwest monsoon; (e) for the 2nd intermonsoon.

7.3. Graphical Trend (ITA) Analysis Results. Table 2 shows trend analysis results from innovative trend analysis. Several positive trends were identified from the graphical (innovative) analysis. Monthly analysis shows positive trends in the months of March and October for Badulla. A positive trend in October was supported by the corresponding seasonal analysis where a positive trend was identified in the 2nd intermonsoon. However, the positive trend in March was not supported by the seasonal analysis. Positive trends were found in May, October, and December for Ledgerwatte Estate, and they were supported by the seasonal and annual trends. Similar observation can be seen in Kandekatiya. However, the positive trend identified in Lower Spring Valley for May was not supported by any lower resolution rainfall patterns.

Graphical results of Badulla (Figures 3(a) and 3(b)) and Ledgerwatte Estate (Figures 3(c) and 3(d)) can be seen in Figure 3. Identification of positive trends can be clearly seen from the data scatter and the trend line drawn for data scatter.

7.4. CWT Analysis Results. Wavelet maps are generated from the CWT analysis. The wavelet map is a graphical illustration of the continuous wavelet coefficients C, which signifies how closely related the wavelet with each section of the signal is. The continuous wavelet coefficients of the signals have been calculated at real, positive scales (8 voices), using the Morlet wavelet.

Morlet wavelet is often used in the rainfall analysis due to its sine-shaped Gaussian, and it has several advantages in climatic time series analysis. Gaussian shaped in the frequency domain is one advantage. It minimizes the sharp edges; therefore, the ripple effects can be ignored (these ripples can be misinterpreted as the oscillations). In addition, the results of the Morlet wavelet convolution retain the temporal resolution of the original signal. Moreover, it is computationally efficient and requires less computational cost. Therefore, many wavelet analyses tend to use Morlet wavelets.

The analyses for seasonal and annual resolutions do not show any pattern, and the data points were not enough to generate a pattern. However, if the monthly rainfall for 30 years was considered as a continuous series, interesting patterns can be observed, and they are shown in Figure 4 (4(a)–4(d)).

Figure 4(a) illustrates the continuous wavelet results from monthly rainfall for Badulla from January 1990 to December 2019 (360 data points). Several important observations are identified, and they are presented by part I to part VI. Times corresponding to part I to part VI are 05/1990–03/1995, 09/1998–06/2006, 01/2011–08/2015, 01/2018–08/2019, 07/1993–06/2003, and 11/2009–12/2017, respectively. The periodicity was changed from 7 to 11 months in the first identified time zone (05/1990–03/1995). Then, a 5-month cycle was found for the 2nd time zone, 4-month cycle for the 3rd, 7–11 month for the 4th, 14-month for the 5th, and 18-month for the 6th time zone. Similarly, patterns were identified in other rain gauges, and they are shown by the corresponding boxes. Interestingly, 6 different patterns were identified from the 4 rain gauges. Closer observation of the CWT analyses gives the corresponding time slots in the patterns are somewhat similar. Therefore, this can be an indication of the similar temporal variation in the rainfalls to the Badulu Oya catchment. Nevertheless, more analysis should be required for a solid conclusion. However, cyclic patterns of the rainfall can be easily identified from the CWT analysis.

7.5. DWT Analysis Results. Figure 5 shows the decomposed level for annual and monthly rainfall time series using DWT. The monthly rainfall series was decomposed into six lower resolution levels using the DWT approach. It can be seen herein that the decomposed levels have lower frequencies. This shows the changes in periodicity. The 2, 4, 6, 16, 32, and 64 monthly periodicities are given by d1–d6, as shown in Figures 5(a)–5(d). The corresponding approximation component is a6 shows the long-term change in trend. Lower frequency in a6 approximation component represents the slowly changing component of the time series. However, the annual time series was decomposed into three detailed components (d1–d3) for 2, 4, and 8 years and one approximation component (a3). The annual DWT analysis results are given in Figures 5(e) and 5(f) for Badulla and Ledgerwatte Estate, respectively. The patterns herein (DWT) are much clearer in comparison to CWT. Therefore, as usual, DWT is preferred for the analysis.

7.6. Summary of the Results. Table 3 presents the summary of various rainfall trend analysis results. Interesting findings are presented here. Several months were identified with positive trends by all tested methods, and these monthly trends were supported by the seasonal and annual trend analysis. However, other than one month from one test (*Kandekatiya downward trend in December by the MK test*), all other identified trends were positive trends. Similar analysis can be found in the literature, as it was already stated in a handful research studies in the context of Sri Lanka. Therefore, this analysis would be interested by the water resources planners in the country.

As it was stated, the Mann–Kendall test is a nonparametric test where the concept of it is simple. It assumes a joint distribution of the data, and therefore, the results are minimally affected due to the normality of the series. However, one of the most important drawbacks of the test is the null hypothesis. The test assumes the data are independent and identically distributed. Therefore, nonacceptance of null hypothesis in theoretical view and application view are different. It is assumed to have a trend in application, whereas the theoretical view says the data are not independent and not identically distributed. Therefore, the results of the test may be confusing.

However, on the contrary, the sequential MK test can be effectively used to detect the changing points or events in the long-term time series. Therefore, this is important in the

Table 2: Results from innovative trend analysis.

Time series	Badulla	Ledgerwatte estate	Lower spring valley	Kandekatiya
January	—	—	—	—
February	—	—	—	—
March	Up	—	—	—
April	—	—	—	—
May	—	Up	Up	—
June	—	—	—	—
July	—	—	—	—
August	—	—	—	—
September	—	—	—	—
October	Up	Up	—	Up
November	—	—	—	—
December	—	Up	—	—
Annual	—	Up	—	—
Northeast monsoon	—	Up	—	—
1st intermonsoon	—	Up	—	—
Southwest monsoon	—	—	—	Up
2nd intermonsoon	Up	Up	—	—

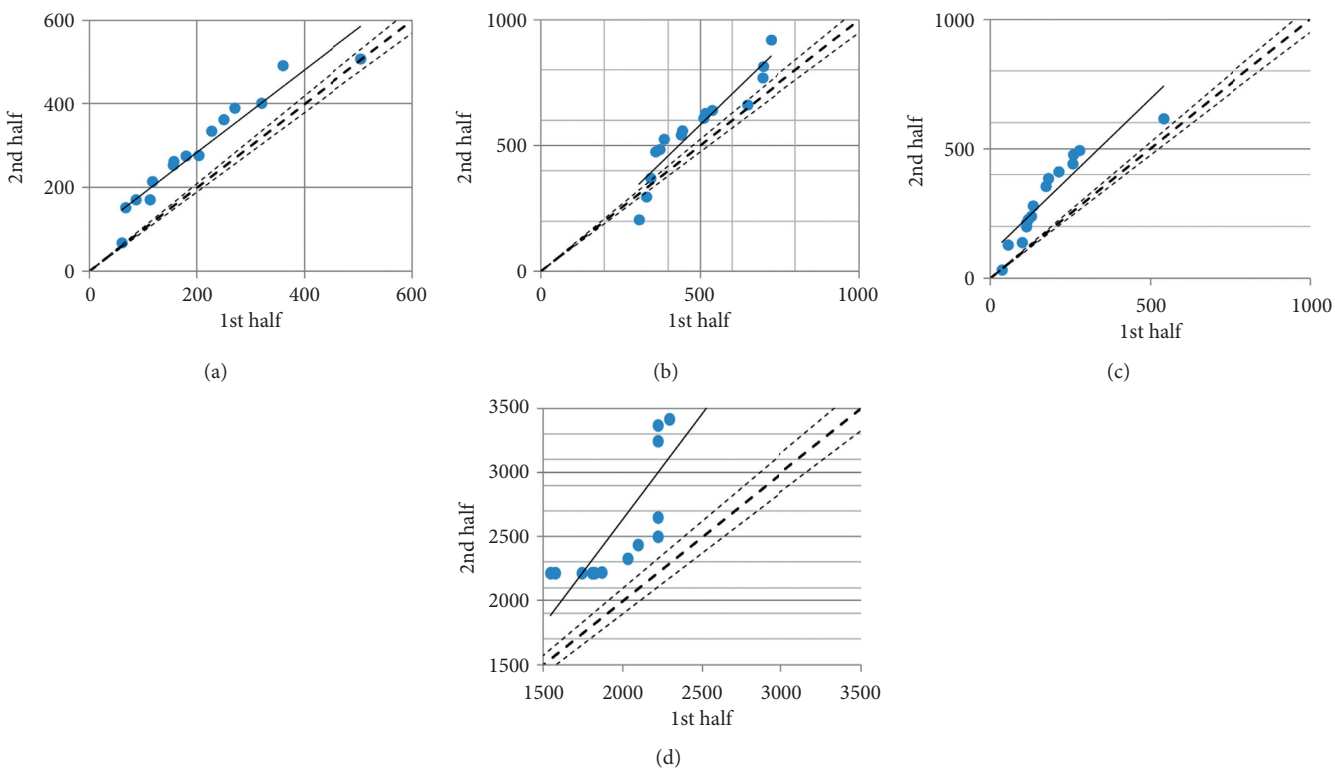

Figure 3: Graphical trend analysis results from ITA: (a) for Badulla–October; (b) for Badulla–2nd intermonsoon; (c) for Ledgerwatte Estate–October; (d) for Ledgerwatte Estate–annual.

analysis to have the potential trend from the MK test and the changing event from the SQMK test. Therefore, coupling both tests (MK and SQMK) would give a better picture to the stakeholders. In addition, ITA is much simpler than any other method in trend detention. It is, however, a qualitative analysis, rather a quantitative analysis. Therefore, researchers can use ITA as an initial step to detect the potential trends and then move to solid statistical tests for quantitative trends. Even though CWT and DWT have advantages, they are more complex analyses compared to simple statistical analyses. Therefore, the stakeholders would not be much interested, unless they are given a clear idea and the physical meaning of these CWT and DWT analyses. However, they are highly sophisticated methods in climate time series analysis in the research point of view.

Therefore, the comparison of various methods in rainfall time series analysis for Badulu Oya catchment requires much attention, depending on the stakeholders'

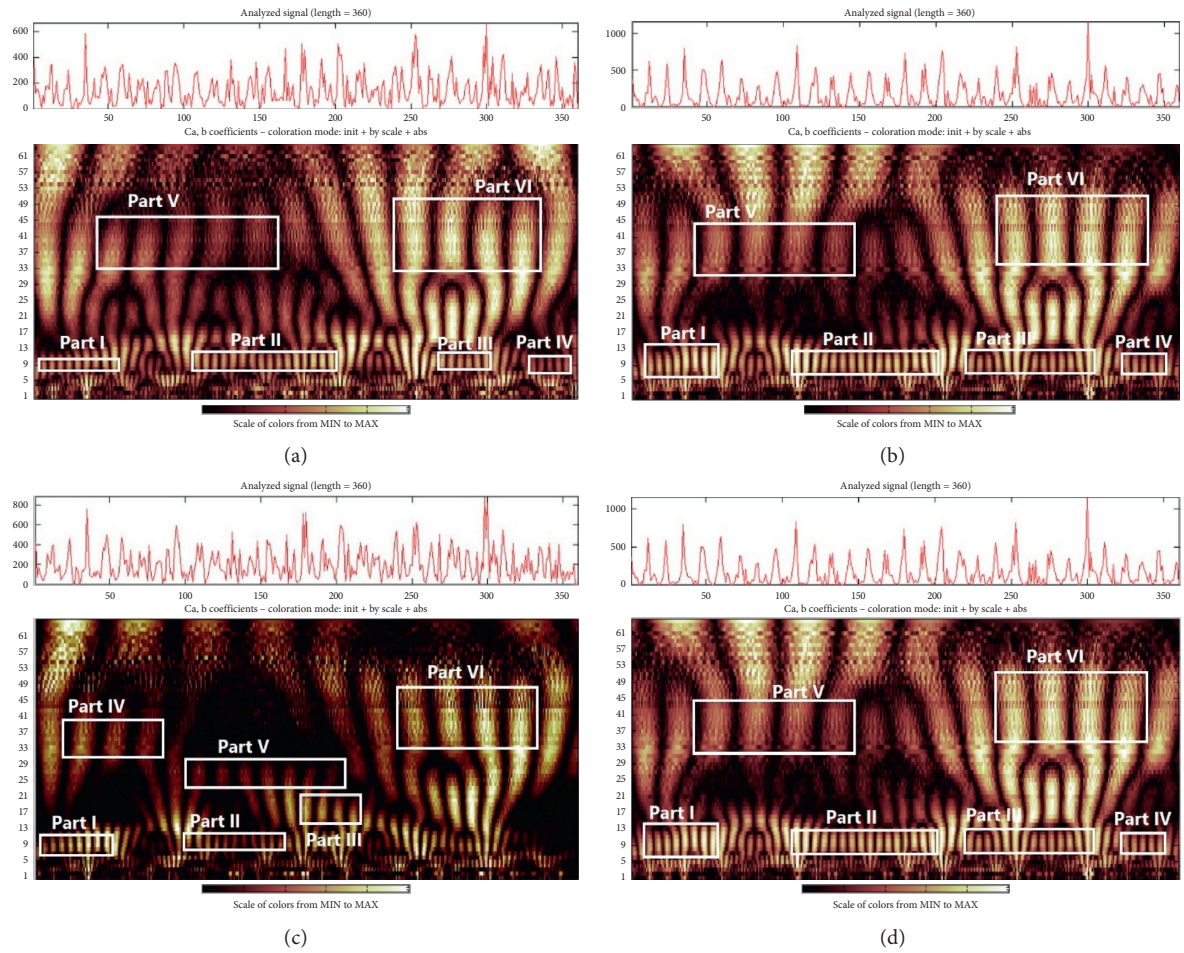

Figure 4: Continuous wavelet transform results for monthly rainfall: (a) for Badulla; (b) for Ledgerwatte Estate; (c) for Lower Spring Valley; (d) For Kandekatiya.

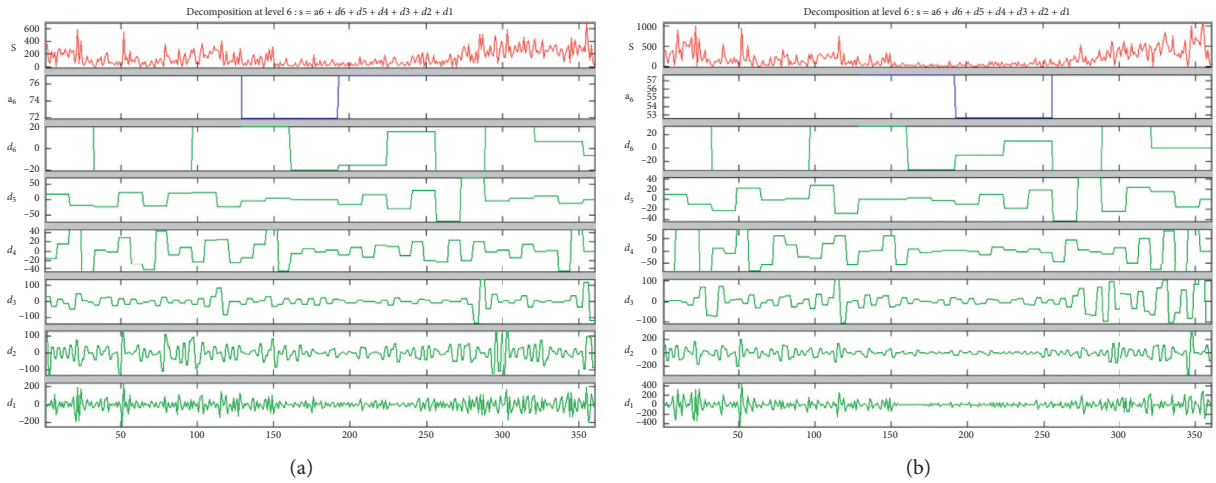

Figure 5: Continued.

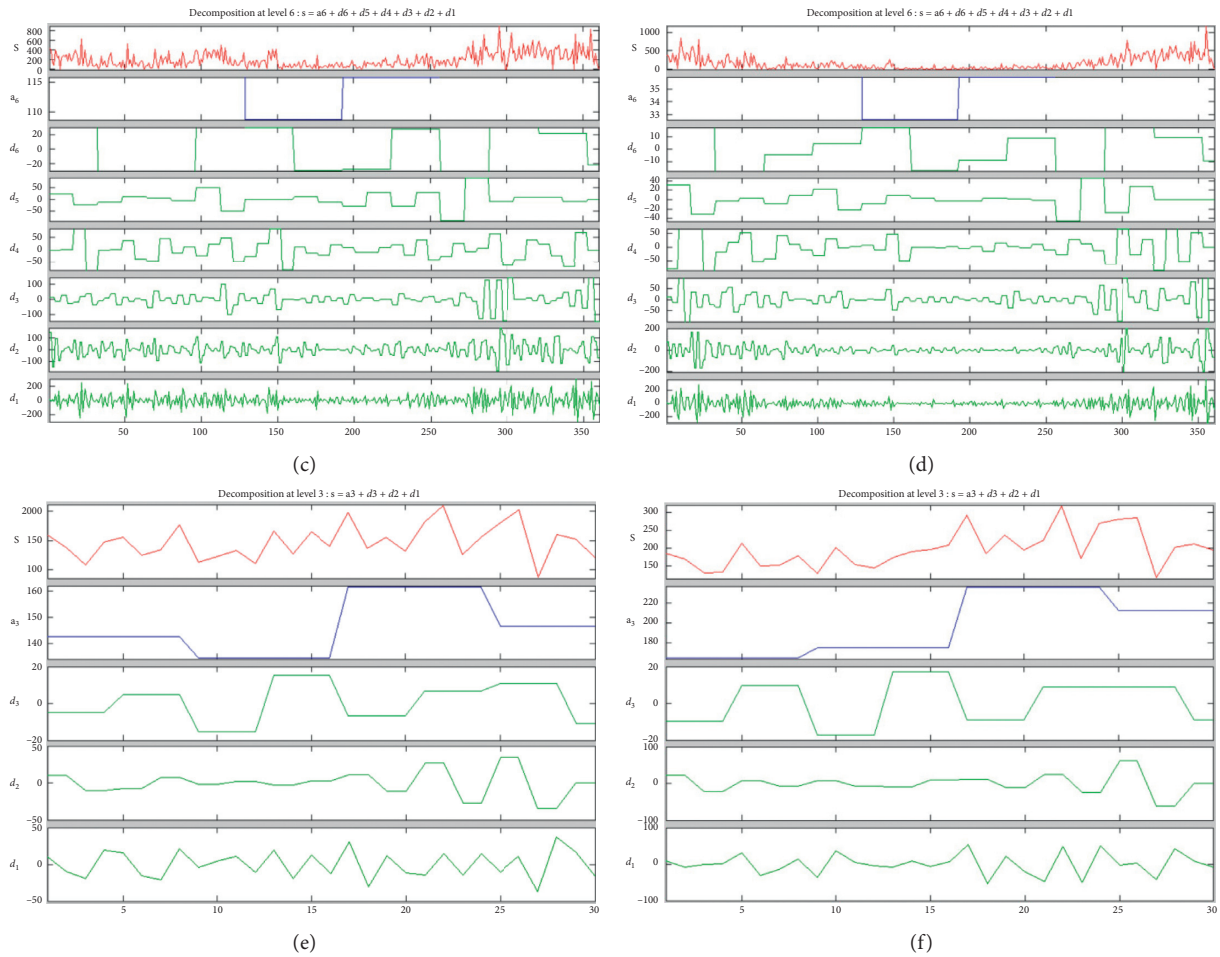

Figure 5: Discrete wavelet transform results for monthly rainfall: (a) for Badulla (monthly); (b) for Ledgerwatte Estate (monthly); (c) for Lower Spring Valley (monthly); (d) for Kandekatiya (monthly); (e) for Badulla (annual); (f) for Ledgerwatte Estate (annual).

Table 3: Comparison of trend analysis.

Test	Monthly	Seasonal	Annual
MK	Ledgerwatte Estate: Feb ↑ and Oct ↑; Lower Spring Valley: May ↑; Kandekatiya: Dec ↓	Ledgerwatte Estate: upward, 2nd ↑	Ledgerwatte Estate: ↑
SQMK	NA	Badulla: 1st ↑; Ledgerwatte Estate: NE ↑ and 1st ↑; Lower spring valley: 1st ↑	Ledgerwatte Estate: ↑
ITA	Badulla: Mar ↑ and Oct ↑; Ledgerwatte Estate: May ↑, Oct ↑, and Dec ↑; Lower Spring Valley: May ↑; Kandekatiya: Oct ↑	Badulla: 2nd ↑; Ledgerwatte Estate: NE ↑, 1st ↑, and 2nd ↑; Kandekatiya: SW ↑	Ledgerwatte Estate: ↑
CWT	Cyclic patterns in all four gauges	NA	NA
DWT	Cyclic patterns in all four gauges	Cyclic patterns in all four gauges	Cyclic patterns in all four gauges

interest. Majority of the farmers would have their famous question: "would there be enough water to harvest for the next term?". This would be a million-dollar question to answer. However, the farmers can be advised not only for the potential climatic trends but also cyclic patterns (*using CWT and DWT*) of the rainfall to the Badulu Oya catchment using this analysis.

8. Conclusions

The results revealed positive rainfall trends in Badulu Oya catchment. Farming community in the Badulla district would be interested on the finding. Therefore, it can be predicted that there would not be water scarcities in the catchment in coming recent future. As usual, the MK test

combined with Sen's slope is proved to be highly efficient in finding the quantitative and qualitative analyses of rainfall trends. However, graphical trends (ITA) provided a quick qualitative view of the trends at a lower computational cost. Therefore, ITA can be considered for similar analysis as the first step in searching rainfall trends. In addition, as it is expected DWT outperformed the CWT. The complexity and computational cost are going to be two important factors for the successful application of the DWT. Therefore, the rainfall patterns can be easily identified by DWT. Therefore, as a summary, rainfall trends for Badulu Oya catchment were successfully presented from this paper while comparing the available trend analysis methods. The authors would like to recommend a set of tests rather a single test in identifying rainfall trends to local catchment to enhance the analysis. Thus, the outcome would be much beneficial to the relevant stakeholders. In addition, it is highly advised to do continuous analysis for the localized catchments while identifying the importance of the climate with the local interest.

Data Availability

The climatic data and the analysis data are available from the corresponding author upon request.

Disclosure

The research was carried out in the Sabaragamuwa University, Belihuloya, Sri Lanka, and Sri Lanka Institute of Information Technology, Malabe, Sri Lanka environments. No specific funds were received to carry out this research.

Conflicts of Interest

The authors declare that they have no conflicts of interest.

Acknowledgments

The authors would like to acknowledge the support they have received from their home universities.

References

[1] S. Withanachchi, S. Köpke, C. Withanachchi, R. Pathiranage, and A. Ploeger, "Water Resource Management in Dry Zonal Paddy Cultivation in Mahaweli River Basin, Sri Lanka: An Analysis of Spatial and Temporal Climate Change Impacts and Traditional Knowledge," *Climate*, vol. 2, no. 4, pp. 329–354, 2014.

[2] C. M. Dunning, E. Black, and R. P. Allan, "Later Wet Seasons with More Intense Rainfall over Africa under Future Climate Change," *Journal of Climate*, vol. 31, no. 23, pp. 9719–9738, 2018.

[3] H. J. Fowler and M. Ekström, "Multi-model ensemble estimates of climate change impacts on UK seasonal precipitation extremes," *International Journal of Climatology*, vol. 29, no. 3, pp. 385–416, 2009.

[4] M. K. Van Aalst, "The impacts of climate change on the risk of natural disasters," *Disasters*, vol. 30, no. 1, pp. 5–18, 2006.

[5] D. Waters, W. E. Watt, J. Marsalek, and B. C. Anderson, "Adaptation of a Storm Drainage System to Accommodate Increased Rainfall Resulting from Climate Change," *Journal of Environmental Planning and Management*, vol. 46, no. 5, pp. 755–770, 2003.

[6] R. L. Wilby, K. J. Beven, and N. S. Reynard, "Climate change and fluvial flood risk in the UK: more of the same?" *Hydrological Processes*, vol. 22, no. 14, pp. 2511–2523, 2008.

[7] J. Huang, M. Ji, Y. Xie, S. Wang, Y. He, and J. Ran, "Global semi-arid climate change over last 60 years," *Climate Dynamics*, vol. 46, no. 3-4, pp. 1131–1150, 2015.

[8] P. Molnar, "Climate change, flooding in arid environments, and erosion rates," *Geology*, vol. 29, no. 12, pp. 1071–1074, 2001.

[9] R. Seager, M. Ting, I. Held et al., "Model Projections of an Imminent Transition to a More Arid Climate in Southwestern North America," *Science*, vol. 316, no. 5828, pp. 1181–1184, 2007.

[10] L. Gimeno, M. Vázquez, J. Eiras-Barca et al., "Recent progress on the sources of continental precipitation as revealed by moisture transport analysis," *Earth-Science Reviews*, vol. 201, p. 103070, 2020.

[11] K. E. Trenberth, "Conceptual Framework for Changes of Rainfall and Extremes of the Hydrological Cycle with Climate Change," *PAGES news*, vol. 8, no. 1, pp. 12-13, 2000.

[12] M. Tsagris, A. Alenazi, K.-M. Verrou, and N. Pandis, "Hypothesis testing for two population means: parametric or non-parametric test?" *Journal of Statistical Computation and Simulation*, vol. 90, no. 2, pp. 252–270, 2019.

[13] N. S. Abeysingha and U. R. L. N. Rajapaksha, "SPI-Based Spatiotemporal Drought over Sri Lanka," *Advances in Meteorology*, vol. 2020, pp. 1–10, Article ID 9753279, 2020.

[14] M. Amirabadizadeh, Y. F. Huang, and T. S. Lee, "Recent Trends in Temperature and Precipitation in the Langat River Basin, Malaysia," *Advances in Meteorology*, vol. 2015, pp. 1–16, Article ID 579437, 2015.

[15] T. Merabtene, M. Siddique, and A. Shanableh, "Assessment of Seasonal and Annual Rainfall Trends and Variability in Sharjah City, UAE," *Advances in Meteorology*, vol. 2016, Article ID 6206238, 13 pages, 2016.

[16] X. Song, J. Zhang, C. Zhang, and X. Zou, "A Comprehensive Analysis of the Changes in Precipitation Patterns over Beijing during 1960-2012," *Advances in Meteorology*, vol. 2019, pp. 1–22, Article ID 6364040, 2019.

[17] P. Datta and S. Das, "Analysis of long-term seasonal and annual temperature trends in North Bengal, India," *Spatial Information Research*, vol. 27, no. 4, pp. 475–496, 2019.

[18] L. Mumo, J. Yu, and B. Ayugi, "Evaluation of spatiotemporal variability of rainfall over Kenya from 1979 to 2017," *Journal of Atmospheric and Solar-Terrestrial Physics*, vol. 194, p. 105097, 2019.

[19] S. Salehi, M. Dehghani, S. M. Mortazavi, and V. P. Singh, "Trend analysis and change point detection of seasonal and annual precipitation in Iran," *International Journal of Climatology*, vol. 40, no. 1, pp. 308–323, 2019.

[20] S. Sharma and P. K. Singh, "Spatial trends in rainfall seasonality: a case study in Jharkhand, India," *Weather*, vol. 74, no. 1, pp. 31–39, 2018.

[21] S. Shrestha, T. Yao, and T. R. Adhikari, "Analysis of rainfall trends of two complex mountain river basins on the southern slopes of the Central Himalayas," *Atmospheric Research*, vol. 215, pp. 99–115, 2019.

[22] T. Caloiero, "Evaluation of rainfall trends in the South Island of New Zealand through the innovative trend analysis (ITA),"

Theoretical and Applied Climatology2019, vol. 139, no. 1-2, pp. 493–504.

[23] W.D.S. Nisansala, N.S. Abeysingha, A. Islam, and A.M.K.R. Bandara, "Recent rainfall trend over Sri Lanka (1987-2017)," *International Journal of Climatology*, vol. 40, no. 7, p. 3417, 2019.

[24] U. Rathnayake, "Comparison of Statistical Methods to Graphical Methods in Rainfall Trend Analysis: Case Studies from Tropical Catchments," *Advances in Meteorology*, vol. 2019, Article ID 8603586, 1 page, 2019.

[25] Y. Wang, Y. Xu, H. Tabari et al., "Innovative trend analysis of annual and seasonal rainfall in the Yangtze River Delta, eastern China," *Atmospheric Research2020*, vol. 231, Article ID 104673.

[26] H Wu and H Qian, "Innovative trend analysis of annual and seasonal rainfall and extreme values in Shaanxi, China, since the 1950s," *International Journal of Climatology*, vol. 37, no. 5, pp. 2582–2592, 2016.

[27] N. Joshi, D. Gupta, S. Suryavanshi, J. Adamowski, and C. A. Madramootoo, "Analysis of trends and dominant periodicities in drought variables in India: A wavelet transform based approach," *Atmospheric Research*, vol. 182, pp. 200–220, 2016.

[28] D. Labat, J. Ronchail, and J. Guyot, "Recent advances in wavelet analyses: Part 2—Amazon, Parana, Orinoco and Congo discharges time scale variability," *Journal of Hydrology*, vol. 314, no. 1-4, pp. 289–311, 2005.

[29] P. P. Nikhil Raj and P. A. Azeez, "Trend analysis of rainfall in Bharathapuzha River basin, Kerala, India," *International Journal of Climatology*, vol. 32, no. 4, pp. 533–539, 2011.

[30] T. Partal and M. Küçük, "Long-term trend analysis using discrete wavelet components of annual precipitations measurements in Marmara region (Turkey)," *Physics and Chemistry of the Earth, Parts A/B/C*, vol. 31, no. 18, pp. 1189–1200, 2006.

[31] Y.-F. Sang, D. Wang, J.-C. Wu, Q.-P. Zhu, and L. Wang, "Entropy-Based Wavelet De-noising Method for Time Series Analysis," *Entropy*, vol. 11, no. 4, pp. 1123–1147, 2009.

[32] R. Mahmood, S. Jia, and W. Zhu, "Analysis of climate variability, trends, and prediction in the most active parts of the Lake Chad basin, Africa," *Scientific Reports*, vol. 9, no. 1, 2019.

[33] M. Mudelsee, "Trend analysis of climate time series: A review of methods," *Earth-Science Reviews*, vol. 190, pp. 310–322, 2019.

[34] N. Phojanamongkolkij, S. Kato, B. A. Wielicki, P. C. Taylor, and M. G. Mlynczak, "A Comparison of Climate Signal Trend Detection Uncertainty Analysis Methods," *Journal of Climate*, vol. 27, no. 9, pp. 3363–3376, 2014.

[35] C. R. Groves, E. T. Game, M. G. Anderson et al., "Incorporating climate change into systematic conservation planning," *Biodiversity and Conservation*, vol. 21, no. 7, pp. 1651–1671, 2012.

[36] K. E. McNamara and H. J. Des Combes, "Planning for Community Relocations Due to Climate Change in Fiji," *International Journal of Disaster Risk Science*, vol. 6, no. 3, pp. 315–319, 2015.

[37] A. E. Reside, N. Butt, and V. M. Adams, "Adapting systematic conservation planning for climate change," *Biodiversity and Conservation*, vol. 27, no. 1, pp. 1–29, 2017.

[38] E. L. Rowland, J. E. Davison, and L. J. Graumlich, "Approaches to Evaluating Climate Change Impacts on Species: A Guide to Initiating the Adaptation Planning Process," *Environmental Management*, vol. 47, no. 3, pp. 322–337, 2011.

[39] S. Herath and U. Ratnayake, "Monitoring rainfall trends to predict adverse impacts-a case study from Sri Lanka (1964-1993)," *Global Environmental Change*, vol. 14, pp. 71–79, 2004.

[40] H. Jayawardene, D. Sonnadara, and D. Jayewardene, "Trends of Rainfall in Sri Lanka over the Last Century," *Sri Lankan Journal of Physics*, vol. 6, pp. 7–17, 2005.

[41] B. Khaniya, I. Jayanayaka, P. Jayasanka, and U. Rathnayake, "Rainfall Trend Analysis in Uma Oya Basin, Sri Lanka, and Future Water Scarcity Problems in Perspective of Climate Variability," *Advances in Meteorology*, vol. 2019, pp. 1–10, Article ID 3636158, 2019.

[42] B. Khaniya, H. G. Priyantha, N. Baduge, H. M. Azamathulla, and U. Rathnayake, "Impact of climate variability on hydropower generation: A case study from Sri Lanka," *ISH Journal of Hydraulic Engineering*, vol. 26, no. 3, pp. 301–309, 2018.

[43] P. Wickramagamage, "Spatial and temporal variation of rainfall trends of Sri Lanka," *Theoretical and Applied Climatology*, vol. 125, no. 3-4, pp. 427–438, 2015.

[44] P. Ranasinghe, G. Fernando, C. Dissanayake, M. Rupasinghe, and D. Witter, "Statistical evaluation of stream sediment geochemistry in interpreting the river catchment of high-grade metamorphic terrains," *Journal of Geochemical Exploration*, vol. 103, no. 2-3, pp. 97–114, 2009.

[45] T. Wagalawatta, W. Bebermeier, D. Knitter, K. Kohlmeyer, and B. Schütt, "Ancient rock quarries in Anuradhapura, Sri Lanka," *Journal for Ancient Studies*, vol. 4, pp. 48–65, 2015.

[46] W. D. T. M. Gunawardhana, J. M. C. K. Jayawardhana, E. P. N. Udayakumara, and S. Malavipathirana, "Spatio-temporal variation of water quality and bio indicators of the Badulu Oya in Sri Lanka due to catchment disturbances," *Journal of the National Science Foundation of Sri Lanka*, vol. 46, no. 1, pp. 51–67, 2018.

[47] P. Wickramagamage, "Large-scale deforestation for plantation agriculture in the hill country of Sri Lanka and its impacts," *Hydrological Processes*, vol. 12, no. 13-14, pp. 2015–2028, 1998.

[48] D. Amara, K. Ullah, and Z. Yushu, "Rainfall erosivity estimation for Sierra Leone using non-parametric indices," *Theoretical and Applied Climatology*, vol. 139, no. 1-2, pp. 221–236, 2019.

[49] Y. Güçlü, "Improved visualization for trend analysis by comparing with classical Mann-Kendall test and ITA," *Journal of Hydrology*, vol. 584, no. 24674, 2020.

[50] A. Malik and A. Kumar, "Spatio-temporal trend analysis of rainfall using parametric and non-parametric tests: case study in Uttarakhand, India," *Theoretical and Applied Climatology*, vol. 140, no. 1-2, pp. 183–207, 2020.

[51] S. Meshram, E. Kahya, C. Meshram, M. Ghorbani, B. Ambade, and R. Mirabbasi, "Long-term temperature trend analysis associated with agriculture crops," *Theoretical and Applied Climatology*, vol. 140, no. 3-4, pp. 1139–1159, 2020.

[52] A. Malik, A. Kumar, A. Najah Ahmed et al., "Application of non-parametric approaches to identify trend in streamflow during 1976-2007 (Naula watershed)," *Alexandria Engineering Journal*, vol. 59, no. 3, pp. 1595–1606, 2020.

[53] A. Y. Sönmez and S. Kale, "Climate change effects on annual streamflow of Filyos River (Turkey)," *Journal of Water and Climate Change*, vol. 11, no. 2, pp. 420–433, 2018.

[54] D. Berryman, B. Bobée, D. Cluis, and J. Haemmerli, "Non-parametric tests for trend detection in water quality time series," *Journal of the American Water Resources Association*, vol. 24, no. 3, pp. 545–556, 1988.

[55] I. Ahmad, D. Tang, T. Wang, M. Wang, and B. Wagan, "Precipitation Trends over Time Using Mann-Kendall and Spearman's rho Tests in Swat River Basin, Pakistan," *Advances in Meteorology*, vol. 2015, pp. 1–15, Article ID 431860, 2015.

[56] K. H. Hamed, "The distribution of Spearman's rho trend statistic for persistent hydrologic data," *Hydrological Sciences Journal*, vol. 61, no. 1, pp. 214–223, 2015.

[57] D. Machiwal and M. Jha, "Trend and homogeneity in subsurface hydrologic variables: case study in a hard-rock aquifer of western india," *Hydrologic Time Series Analysis: Theory and Practice*, pp. 165–180, Springer, Berlin, Germany, 2012.

[58] Y. Ryu, H. Shin, S. Kim, and J.-H. Heo, "Power Test of Trend Analysis using Simulation Experiment," *Journal of Korea Water Resources Association*, vol. 46, no. 3, pp. 219–227, 2013.

[59] G. Naveendrakumar, M. Vithanage, H.-H. Kwon, M. C. M. Iqbal, S. Pathmarajah, and J. Obeysekera, "Five Decadal Trends in Averages and Extremes of Rainfall and Temperature in Sri Lanka," *Advances in Meteorology*, vol. 2018, pp. 1–13, Article ID 4217917, 2018.

[60] A. Panda and N. Sahu, "Trend analysis of seasonal rainfall and temperature pattern in Kalahandi, Bolangir and Koraput districts of Odisha, India," *Atmospheric Science Letters*, vol. 20, no. 10, pp. 1–10, 2019.

[61] H. B. Mann, "Nonparametric Tests Against Trend," *Econometrica*, vol. 13, no. 3, pp. 245–259, 1945.

[62] M. G. Kendall, *Rank Correlation Methods*, Griffin, London, UK, 1975.

[63] R. M. Hirsch and J. R. Slack, "A Nonparametric Trend Test for Seasonal Data With Serial Dependence," *Water Resources Research*, vol. 20, no. 6, pp. 107–121, 1984.

[64] S. Adarsh and M. Janga Reddy, "Trend analysis of rainfall in four meteorological subdivisions of southern India using nonparametric methods and discrete wavelet transforms," *International Journal of Climatology*, vol. 35, no. 6, pp. 1107–1124, 2014.

[65] R. Sneyers, *On the Statistical Analysis of Series of Observations*, Technical Note 143, WMO-No. 415, p. 192, World Meteorological Organization (WMO), Geneva, Switzerland, 1990.

[66] M. Zarenistanak, A. G. Dhorde, and R. H. Kripalani, "Trend analysis and change point detection of annual and seasonal precipitation and temperature series over southwest Iran," *Journal of Earth System Science*, vol. 123, no. 2, pp. 281–295, 2014.

[67] Z. Sen, "Innovative Trend Analysis Methodology," *Journal of Hydrologic Engineering*, vol. 17, pp. 1042–1046, 2012.

[68] B. K. Pandey, H. Tiwari, and D. Khare, "Trend analysis using discrete wavelet transform (DWT) for long-term precipitation (1851-2006) over India," *Hydrological Sciences Journal*, vol. 62, no. 13, pp. 2187–2208, 2017.

[69] E.-B. Lin and P. C. Liu, "A discrete wavelet analysis of freak waves in the ocean," *Journal of Applied Mathematics*, vol. 2004, no. 5, pp. 379–394, 2004.

[70] H. Jia and D. Pan, "Drought Risk Assessment in Yunnan Province of China Based on Wavelet Analysis," *Advances in Meteorology*, vol. 2016, pp. 1–10, Article ID 1579415, 2016.

[71] Y. Chen, Y. Guan, G. Shao, and D. Zhang, "Investigating Trends in Streamflow and Precipitation in Huangfuchuan Basin with Wavelet Analysis and the Mann-Kendall Test," *Water*, vol. 8, no. 3-77, pp. 1–32, 2016.

[72] D. Nalley, J. Adamowski, and B. Khalil, "Using discrete wavelet transforms to analyze trends in streamflow and precipitation in Quebec and Ontario (1954-2008)," *Journal of Hydrology*, vol. 475, pp. 204–228, 2012.

[73] C. Chou, "Applying multi-resolution analysis to differential hydrological grey models with dual series," *Journal of Hydrology*, vol. 332, no. 1-2, pp. 174–186, 2007.

[74] C. A. Guimarães Santos and G. B. L. d. Silva, "Daily streamflow forecasting using a wavelet transform and artificial neural network hybrid models," *Hydrological Sciences Journal*, vol. 59, no. 2, pp. 312–324, 2014.

[75] C. Santos, P. Freire, R. Silva, and S. Akrami, "Hybrid Wavelet Neural Network Approach for Daily Inflow Forecasting Using Tropical Rainfall Measuring Mission Data," *Journal of Hydrologic Engineering*, vol. 24, no. 2, Article ID 04018062, 2019.

[76] S. Sharma, D. Nalley, and N. Subedi, "Characterization of Temporal and Spatial Variability of Phosphorus Loading to Lake Erie from the Western Basin Using Wavelet Transform Methods," *Hydrology*, vol. 5, no. 3-50, pp. 1–28, 2018.

[77] M. Yang, Y. Sang, C. Liu, and Z. Wang, "Discussion on the Choice of Decomposition Level for Wavelet Based Hydrological Time Series Modeling," *Water*, vol. 8, no. 5-197, pp. 1–11, 2016.

[78] F. Zhang, H. Dai, and D. Tang, "A Conjunction Method of Wavelet Transform-Particle Swarm Optimization-Support Vector Machine for Streamflow Forecasting," *Journal of Applied Mathematics*, vol. 2014, Article ID 910196, 10 pages, 2014.

[79] T. Zhao, L. Wu, D. Li, and Y. Ding, "Multifractal Analysis of Hydrologic Data Using Wavelet Methods and Fluctuation Analysis," *Discrete Dynamics in Nature and Society*, vol. 2017, Article ID 3148257, 18 pages, 2017.